Sant'Anna
School of Advanced Studies – Pisa

Academic Year 2018/2019

Phd Course
Emerging Digital Technologies

A Photonics based Multiple Input Multiple Output Coherent Radar Network for Maritime Surveillance and High Resolution Applications

Author
Leonardo LEMBO

Supervisor
Antonella BOGONI

Tutor
Antonio MALACARNE

ISBN: XXXXXXXXXXXX

This page was intentionally left blank

CONTENT

ACRONYM LIST

ADC *Analog-to-Digital Converter*
AM *Amplitude Modulation*
AWGN *Additive White Gaussian Noise*
BB *Band Band*
BPF *Band Pass Filter*
BF *Beam Forming*
BW *Bandwidth*
CA-CFAR *Cell Average Constant False Alarm Rate*
CDM *Code Division Multiplexing*
CFAR *Constant False Alarm Rate*
CH *Channel*
COHO *Coherent Oscillator*
CPI *Coherent Processing Interval*
CUT *Cell Under Test*
CW *Continuous-Wave*
DAC *Digital-to-Analog Converter*
DDS *Direct Digital Synthesizer*
DFB *Distributed Feed-Back*
DFBG *Dual Fiber Bragg Grating*
DM *Direct Modulation*
SSB *Double Side-Band*
ECM *Electronic Counter Measure*
EDFA *Erbium-Doped Fiber Amplifier*
EHF *Extremely High Frequency*
EM *Electromagnetic*
EMI *Electromagnetic Interference*
EMI *Electromagnetic Interference*
ENOB *Effective Number of Bits*
E\O *Electro-Optical*
EOM *Electro-Optical Modulator*
ESM *Electronic Static Measure*
EW *Electronic Warfare*
EWS *Electronic Warfare System*
FA *False Alarm*
FBG *Fiber Bragg Grating*
FDM *Frequency Division Multiplexing*
FFT *Fast Fourier Transform*
FM *Frequency Modulation*
FP Fabry-Perot
GPS *Global Positioning System*
GPSDO *Global Positioning System Disciplined Oscillator*
GUI *Graphical User Interface*
HFSS *High Frequency Electromagnetic Field Simulator*
HPBW *Half Power Beam Width*
HW *Hardware*
IF *Intermediate Frequency*
IL *Injection Locking*
IMDD *Intensity Modulation Direct Detection*
IR *Infra Red*
ISAR *Inverse Synthetic Aperture Radar*

LIDAR *Light Detection and Ranging*
LO *Local Oscillator*
LW-VCSEL Long Wavelength Vertical Cavity Surface Emitting Lasers
MIMO *Multiple Input Multiple Output*
MLL *Mode Locked Laser*
MMB *Millimeter Band*
MZM *Mach Zehnder Modulator*
MTI *Moving Target Indicator*
MRR Microring Resonator
MTD *Moving Target Detector*
MWP *Microwave Photonics*
NF *Noise Figure*
ODL *Optical Delay Line*
OF *Optical Fiber*
OFDM *Orthogonal Frequency Division Multiplexing*
O\E *Opto- Electrical*
OEO *Opto- Electrical Oscillator*
PAA *Phased Array Antenna*
PADC *Photonic Analog to Digital Converter*
PC *Photonic Core*
PCB Printed Circuit Board
PD *Photodiode*
PN *Phase Noise*
PRF *Pulse Repetition Frequency*
PRI *Pulse Repetition Interval*
PSD *Power Spectral Density*
PSLR *Peak Side Lobe Ratio*
PW *Pulse Width*
RADAR *Radio Detection and Ranging*
RCS *Radar Cross Section*
RIN *Relative Intensity Noise*
RoF *Radio over Fiber*
RF *Radio Frequency*
RP *Radar Peripheral*
RX *Receiver*
SAR *Synthetic Aperture Radar*
SDR *Software Defined Radio*
SFDR *Spurious-Free Dynamic Range*
SIMO *Single Input Multiple Output*
SMF *Single Mode Fiber*
SNR *Signal-to-Noise Ratio*
SOA *Semiconductor Optical Amplifier*
SSB *Single Side-Band*
STALO *Stabilized Local Oscillator*
SW *Software*
TDM *Time Division Multiplexing*
TLS *Tuneable Laser Source*
TTD *True Time Delay*
TX *Transmitter*
TXCO *Temperature Controlled Oscillator*
VCO *Voltage Controlled Oscillator*
VCSEL Vertical Cavity Surface Emitting Lasers

UHF *Ultra High Frequency*
UWB *Ultra Wide Band*
WDM *Wavelength Division Multiplexing*

LIST OF FIGURES

LIST OF TABLES

This page was intentionally left blank

INTRODUCTION

After more than a century since its invention mankind needs radars more than ever for manifold applications ranging from long-established air surveillance to pollution control via satellite observations, driving assistance, bio-medical purposes or even more innovative applications. No other sensing system including high resolution cameras, infrared (IR) sensors and light detection and ranging (LIDAR), has the same efficiency and reliability as radar systems have. Other technologies, in fact, do not ensure "all day" and "all weather" operability thus radars still represent the leading solution for sensing applications. Although each application has its unique requirements, a general trend towards higher performance standards is clearly recognizable. Military as well as commercial applications, in fact, already claim better and better performance especially in terms of resolution capability.

In the last decades the geopolitical scenario has rapidly changed and accordingly defence policy has evolved in order to face new security challenges. Nowadays, security concerns are focused on asymmetric warfare, since the main threat are terroristic attacks. Consequently, the challenge now is to individuate small objects such as drones, jet skies and missiles, which likely could be used by terrorists. A precise and accurate localization as well as a rapid detection are essential for an effective reaction. Moreover, in overcrowded scenarios high resolution facilitates target classification and identification, therefore providing a superior situation awareness.

Similarly, new generation civil applications are pushing the bar towards higher sensing standards. Sophisticated applications such as, for instance, autonomous driving, definitely demand a reliable, detailed and possibly real-time picture of the environment surrounding the vehicle. In absence of this precondition there is no way for artificial intelligence algorithms to ensure safe driving.

Notoriously, in a conventional monostatic radar, range resolution depends on the signal bandwidth, whereas angular resolution on the antenna features. In general, angular resolution is rather modest with respect to range resolution, therefore in the last decades diverse processing techniques have been developed to address this critical aspect. The most known and effective is Synthetic Aperture Radar (SAR), based on a coherent data fusion of samples acquired sequentially while the platform carrying the radar system is moving. SAR processing is generally used for spaceborne or airborne earth observations. Unfortunately, small or no platform speed as well as constraints descending from the size of the area to monitor, which has a direct implication on the maximum pulse repetition frequency (PRF), hinder to extend the approach to ground-based applications. Inverse Synthetic Aperture Radar (ISAR) has been developed with the specific aim to apply the SAR principle also for naval or air surveillance purposes, exploiting essentially target motion rather than platform motion. ISAR can ensure a remarkable target resolution, however data processing is complex and what's worst, the approach is not very robust as it leverages on unknown target movements, out of direct control.

Albeit range resolution is far better than angular resolution, it is undeniable that there are wide margins for the improvement of this primary radar feature. However, due to spectrum erosion and difficulties to efficiently manage signals with high fractional bandwidths in the radio frequency (RF) domain it is foreseeable that next generation systems cannot just rely on broader radar waveforms to fulfil the ever growing claim for high resolution target detection. In fact, despite different portions of the RF spectrum are reserved either for telecommunication or radar purposes, the RF spectrum is already overcrowded and, as modern applications all demand to use larger and larger signal bandwidths, conflicts are inevitable.

In this framework the only possible alternative is to change the paradigm of current radar systems from conventional monostatic, stand-alone and with limited integration skills, as we are used to know them, to unprecedented network-centric spatial distributed systems constituted by multiple intrinsically highly integrated sensors. In other words, modern systems should profit more from information acquired in spatial diversity rather than leveraging exclusively on frequency diversity.

Recently a novel class of multistatic radar systems has been proposed named Multiple Input Multiple Output (MIMO) radars. This class of new generation radars derives from the transposition to the radar world of the well known MIMO principle underpinning current communication standards, such as IEEE 802.11 (Wi-Fi) and Long Term Evolution (LTE) 4/5G, where space diversity is exploited specifically to increment signal coverage and data transmission throughput. The basic idea is that spatial diversity can enhance system performance regardless of the application field. Unlike multistatic radars, which can be imagined as constituted by multiple monostatic or bi-static independent radars (each one composed by one transmitter and one receiver), MIMO radars consist of multiple bi-static synergistically operating radars. By definition, in fact, a MIMO radar is a radar system employing multiple transmit waveforms and having the ability to jointly process all signals received by multiple antennas. The enormous advantage of a MIMO architecture compared to a multistatic one is evident: fixed for both configurations the same number of transmitters (TXs), N_{TX}=M and receivers (RXs), N_{RX}=M, a multiple bi-static radar configuration can exploit for detection only M received signals, while a MIMO configuration can exploit for the same purpose M^2 signals.

MIMO radars are increasingly studied, especially in the automotive sector, where high angular resolutions are necessary and the whole design process is highly cost-driven. Thanks to the MIMO principle, indeed, by using only M+N antennas (respectively M in TX and N in RX) a virtual array formed by MxN antennas can be synthesized. Therefore, the same angular resolution assured by a real antenna with MxN array elements can be achieved using a considerably lower number of antenna elements.

In this work we focus specifically on MIMO radars with widely separated antennas which can provide diversity gain, useful when targets with low radar cross section (RCS) or high angular RCS variability have to be detected, and super-resolution, (i.e. a resolution in cross-range better than range resolution). Moreover, slow moving targets can be better located and the area of interest can be continuously monitored. Despite all those benefits, manifold issues, yet unsolved in the RF domain, still impede the realization of large coherent MIMO radar networks. Depending on the adopted network topology, different issues have to be solved. In particular, an efficient signal distribution is crucial in case a centralized radar network is preferred, which consists of a core in charge of signal generation and elaboration and several peripherals which either transmit or receive multiple orthogonal waveforms in order to jointly elaborate them. Unfortunately, large networks are unconceivable since signal attenuation in the RF domain is significant. In addition, signal distribution experiences an important distortion when high fractional bandwidths are transmitted, as it happens in MIMO operations. Instead a correct time and phase synchronization among all nodes of the network is the foremost issue to solve when a distributed network solution is adopted. In this case each node performs a local pre-processing (e.g., detection, tracking), and then sends the results to a master node for final data fusion. Hence only a limited amount of data are exchanged, whereas usually complex synchronization algorithms are employed to permit an efficient final data fusion.

Microwave photonics (MWP) is a branch of photonics whose ambition is to find suitable technological solutions in the optical domain expressly for microwave applications. Switching to photonics often consents to overcome limitations existing or hard to deal with in the RF domain.

The maturity reached in this field is noteworthy. The Sant'Anna School of Advanced Studies together with the National Inter-University Consortium for Telecommunications have developed in 2012 the first photonics-based radar, which has been successfully tested in naval and air scenarios. The peculiarity of the demonstrator is that signal generation, elaboration (i.e. modulation, up/down conversion) and distribution is effectuated by means of optical devices, thus ensuring a remarkable frequency flexibility, an effective signal distribution over long distances as well as an excellent phase stability. Those features match exactly the system requirements necessary for a MIMO radar network

with widely separated antennas. For this reason, we have started investigating the feasibility of a photonics-based coherent MIMO radar network.

Unlike a conventional monostatic radar, several parameters such as antenna geometry, radar waveforms, oscillator stability and signal-to-noise ratio (SNR) have a strong impact on the radar cross-ambiguity function. Therefore, with the twofold purpose to set-up preliminary MIMO detection algorithms and better understand how the aforementioned parameters affect detection performance an ad-hoc MIMO scenario simulator has been developed.

Thanks to an extensive use of the self-developed design tool, 3 different scenarios have been deeply analysed. Two simulative analysis out of the three carried out are similar as they both consider a maritime scenario, whereas the remaining study examines a completely different scenario as it concerns an automotive application. Despite the enormous difference of system parameters, the MIMO approach, as results from the numerical analysis conducted, is indicated in all these situations and empowers high resolution target detection. The simulative study is incremental in the sense that results emerged for a scenario, previously examined, are extended to the subsequent scenarios, so that different aspects can be better addressed.

The first simulative outcomes presented refer to a coastal scenario. Nevertheless, from MIMO theory the superiority of coherent detection is well-known, first of all a comparison between a coherent and a non-coherent MIMO processing is made finalized to assess the improvement resulting from coherent operations. Following the impact of various MIMO parameters on the detection cross-ambiguity function and the detrimental effects caused by network phase noise are evaluated. While for the coastal scenario mainly theoretical aspects are covered, in the ensuing naval scenario a concrete installation solution is studied. MIMO antennas are assumed to be placed along the ship hull of a frigate and after a coarse power budget check, useful to establish if the solution under exam is feasible or not, an optimal antenna disposition is identified. In real installations, physical constraints hinder to uniformly distributed antenna elements on the whole antenna aperture, thus a genetic algorithm is employed for antenna geometry optimization. Furthermore, the network phase stability ensured by different centralized hardware (HW) architectures is investigated, as well as the robustness to sensor displacement errors, imputable to ship deformations.

Ultimately, an automotive case is examined in order to verify if a MIMO approach can be extended also to this area of application, safeguarding high angular resolutions with few antenna elements.

From the simulative analysis clearly emerges that the main drawback of MIMO detection are troublesome side lobes of the cross-ambiguity function. Consequently, with the aim to cope this critical issue, two alternative possibilities are investigated: a SAR-like approach which as standard SAR processing leverages on the relative motion between the target and the MIMO antenna configuration and a multiband MIMO system, where additional frequency diversity is exploited to further enhance side lobe suppression.

In light of the outcomes obtained from the simulative analysis and thanks to the lessons learnt during a field trial campaign, executed at the facilities of the Italian Navy in Tirrenia (Pisa), a 2 TXs x 2 RXs photonics-based MIMO radar network has been designed, built and successfully tested. Outdoor tests, which are reported in the final part of this thesis, appear very promising. Despite the minimal MIMO architecture used for the experiment, accountable for considerable side lobes around the target and the difficulties, typical of an outdoor trial, a collaborative target, carried by a drone, has been correctly located. Moreover, test involving multiple targets have permitted to verify the remarkable angular resolution capability of the photonics-based demonstrator.

A further test activity has been conducted indoor deploying a MIMO 2 TXs x 4 RXs radar network which exploits photonics, essentially, for signal distribution to all antennas. The test activity is still ongoing and has already consented to assess the notable detection accuracy and resolution capability and to validate the self-developed MIMO scenario simulator.

Additional tests are planned involving multiple targets, more antennas and larger signal bandwidths in order to confirm the huge potential arising from the use of a photonic approach for the implementation of a MIMO radar network with widely separated antennas.

The work is structured as follows. An overview on MIMO radars is presented in Chapter I, focusing on advantages and technological restrictions existing in the RF domain which currently impede to realize coherent MIMO radar networks with widely separated antennas. In the final part of the Chapter the MIMO scenario simulator developed by the author is described in detail. Chapter II is dedicated to the review of the main existing microwave photonic techniques, highlighting the effectiveness of signal distribution realized in the optical domain. In Chapter III the outcomes of the numerical analysis conducted on the three scenarios introduced above are discussed. Finally, before drawing the conclusions, the results obtained processing real data sets, which have been acquired during both indoor and outdoor experimental activities employing, as mentioned, two different centralized photonics-based coherent MIMO architectures are outlined in Chapter IV.

1. MULTIPLE INPUT MULTIPLE OUTPUT RADARS

A multistatic radar is defined as a radar that obtains information on a target by means of simultaneous processing of signals from several spatially separated transmitting, receiving or transceiving positions [1]. Multistatic radars offer several advantages in terms of resolution capability, robustness to interference, area coverage, continuous monitoring or system reliability. Conversely all this benefits entail a higher system complexity compared to monostatic radar systems, where the transmitter and the receiver are located in the same place. For this reasons, even tough bi-static radars have been used since World War II especially for air surveillance [2], technical difficulties hard to cope in the RF domain have hindered until today a widespread use of this class of radars and, whenever possible, monostatic solutions have been preferred. As far as we know, in fact, exception made for some research project, such as NetRad, finalized to provide a bi-static sea clutter and vessel reflectivity database [3][4] no multistatic radar system has been yet implemented for maritime surveillance.

In this Chapter we examine MIMO radars, which are a subset of multistatic radars. The basic principle of operation will be introduced, enhancing the strengths and the weaknesses of the MIMO approach and in the last part a MIMO scenario simulator developed by the author is described. The concepts discussed are useful to clarify MIMO principles and are also propaedeutic to understand the numerical analysis reported in Chapter III.

1.1. MULTISTATIC RADARS

Since its invention in 1904, attributed to the German scientist Hulsmeyer[1], radar requirements have enormously changed: more than a century ago, as the acronym RaDaR (Radio Detection and Ranging) suggests, the only required functions were radio detection and ranging. The ancestors of modern radars, despite modest technological resources of the past, could assure those simple requirements adopting mono-static or bi-static radar configurations and using lower RF frequencies (in order to overcome power budget issues as well as technological limitations existing at that time) than standard frequencies used nowadays for radar applications. New operative scenarios are more challenging: detecting the presence of a metallic object is not sufficient anymore; end-users want also classify and eventually identify targets. Then, once completed the identification process, objects of interest have to be tracked and resulting tracks handed to Situation Awareness Centres, where information coming from heterogeneous sensors (i.e. lidars, radars, IR sensors or cameras) are jointly evaluated. In addition, recently the trend is that manifold tasks previously carried out by specific systems are ensured by a single radar system obtaining in this way an enhanced functional system integration. The foremost drawback of multi-functional radars is that the same shared hardware has to satisfy all assignments. Subsequently, when computational resources are insufficient, it is

[1] Hertian-wave Projecting and Receiving Apparatus Adapted to indicate or Give Warning of the presence of metallic body such Ship or train, in the line of Projecting of Such waves.

inevitable to separate tasks in the time domain and find an appropriate policy to prioritize critical functions [5]. Unfortunately, although it is evident that this approach is inefficient, when a conventional monostatic radar architecture is adopted there is no better solution.

Besides unrestrainable demand of target detection improvement, better tracking and imaging capabilities, more accurate parameter estimation and reliable target identification and classification, demonstrate that, despite the recent advancements in components technology, traditional single-operating monostatic or bistatic radars, in which only a single transmitter and a single receiver are used cannot meet anymore modern system requirements, imposed by novel operative scenarios [6]. Therefore, the concept of multistatic radar as well as multiband radar is gaining more and more attention [7]. Multistatic radars, as said, employ several spatially distributed transmitting and receiving nodes, capable of granting radar coverage of extended areas. Thanks to hardware and software developments (e.g. multichannel antennas with electronic beam steering, high speed digital processors and computers, high capacity communication links, and precise synchronization systems, such as the Global Positioning System (GPS)), the transition from single-sensor to multi-sensor systems has been enabled [8].

1.2. CENTRALIZED AND DISTRIBUTED RADAR NETWORKS

Radar networks, depending on where the signal generation and processing is made, can be divided into centralized and distributed networks [9][10]. As shown in Figure 1-1 the main difference between cited architectures is that in a distributed configuration each remote node provides to autonomous signal generation and elaboration while in a centralized scheme only the Master node carries out those functions. Furthermore, while in distributed networks data fusion is performed on already pre-processed data (at plot level) by the Master Node, in centralized networks this operation is done on raw data (at signal level).

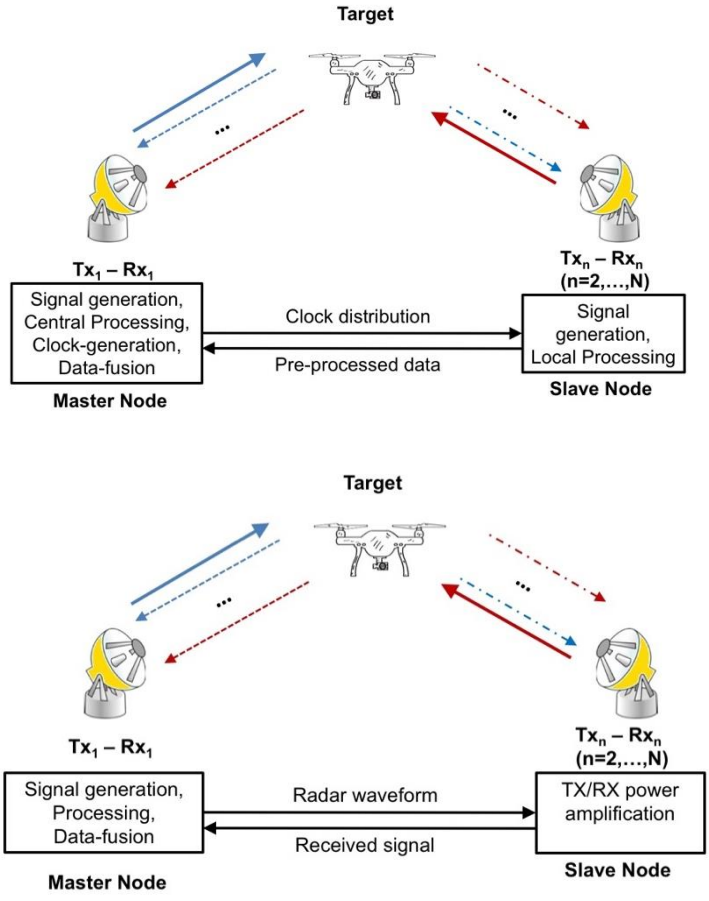

Figure 1-1: Distributed network architecture (top); Centralized network architecture (bottom)

Leaving the conventional monostatic radar paradigm for an innovative multistatic approach, able to satisfy current radar requirements, implies first of all the resolution of several technological issues summarized in Table 1-1.

Network type	Coherent Mode	Non-Coherent Mode
Distributed	Time and phase synchronization	Time synchronization
Centralized	Efficient signal distribution (low attenuation, high capacity data links) Phase compensated links	Efficient signal distribution (low attenuation, high capacity data links)

Table 1-1: Centralized and distributed architecture main radar network requirements

To overcome demanding requirements in the RF domain (i.e. low signal attenuation links, high capacity data links) usually incoherent distributed radar networks are preferred over coherent centralized networks. However, this shortcut determines a significant reduction of detection performance caused by the fact that data fusion is performed on already pre-processed data. Accordingly, pre-processing implies that a certain amount of information is inevitably lost leading to worse overall performance. As will be better clarified in next paragraphs, distributed radar networks operating coherently can be realized, provided that dedicated synchronization signals are sent to all nodes or complex synchronization algorithms are applied afterwards in order to align in time and phase acquired data prior to their data fusion. It has to be pointed out that a misalignment would have dramatic consequences on detection, as for instance, the same target would be detected more than once as direct consequence of the fact that each monostatic/bi-static radar part of the network would locate the target in a different range or angular cell.

Despite a more demanding system requirement on signal links, centralized networks are intrinsically coherent, since the whole network shares a unique oscillator. Accordingly, those architectures only need phase compensated links to preserve phase coherence during signal distribution between the Master and all remote Slave nodes. The challenge in this case is to ensure an efficient signal distribution among all sub-systems part of the network. In particular, low attenuation and low distortion links occur to transfer waveforms form the Master node towards all Slave nodes and, on the contrary, high capacity data links are necessary to convoy digitized data from the Slave nodes to the Master node for final data fusion.

1.3. PHASE NOISE AND RADARS

Phase Noise (PN) and its temporal equivalent timing jitter represent the utmost parameters for an oscillator as they furnish an indication on its stability. An insufficient stability can have an extreme negative impact on radar performance, especially on the detection of slow-moving targets. The aim of the present paragraph is to furnish a quick insight on PN so that data and results presented in the following can be better understood.

It is well known that at difference to incoherent radar systems where the target information lays in the amplitude of the backscattered echo, coherent radars leverage on phase information of the received signal. In this way it is possible to determine in addition to the target position also its radial speed and consequently stationary targets or unwanted clutter can be effectively filtered out, by removing the zero Doppler spectral component. However, this is possible only if the oscillator coherence is good enough. Otherwise, also stationary clutter undergoes a phase modulation, induced by phase noise, which is deleterious as resulting modulated spectral clutter components overlap with potential slow moving targets having a small Doppler frequency. Consequently it is not possible anymore either distinguish slow-moving targets from stationary clutter or individuate the correct radial speed associated to a moving object. Since, in general, the stability heavily depends on the

oscillator frequency, in other words the higher the oscillator frequency the higher the instability, a conventional coherent radar scheme foresees two oscillators a STAbilized Local Oscillator (STALO) and a COHerent Oscillator (COHO), which satisfy different stability requirements. The STALO has to ensure coherence over a pulse repetition interval (PRI), while the COHO has to ensure coherence over the coherent processing interval (CPI), which is N times longer than the PRI. Accordingly, for the reason given above that a higher working frequency in general implies a worse stability, it is evident that usually the COHO works at much lower frequencies than those generated by the STALO.

To explain what PN is, it is helpful consider an oscillator as a filtered noise generator in the sense that an ideal RF tone suffers a random amplitude (AM) and frequency modulation (FM). Therefore, if we would represent an oscillator on a phasor diagram, we could observe that the phasor wanders randomly in a certain region of the plane. Since noise is a statistically process, the phase is uniformly random but the amplitude of noise can be described through a probability distribution function. PN, in fact, can be defined as the one-sided spectral density of a signal phase deviation and is generally measured in dBc/Hz at a given offset from the desired carrier frequency. Expressed in a different way, PN represents the noise power relative to the carrier contained in a 1 Hz bandwidth centered at a certain offset from the carrier frequency.

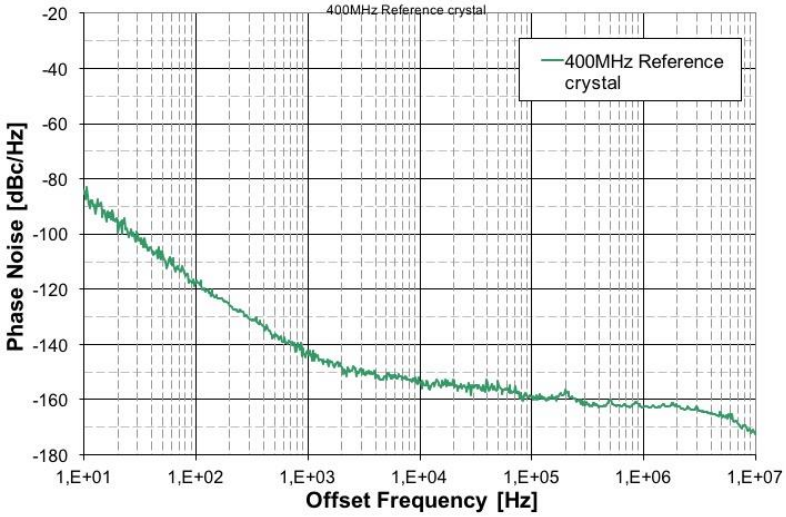

Figure 1-2: Phase Noise curve of a 400 MHz RF crystal oscillator

In Figure 1-2 a typical PN curve of a 400 MHz RF oscillator is reported.

In general, as mentioned, high frequency oscillators are characterized by higher PN curves; if a frequency multiplication technique is adopted to get high RF frequencies each multiplication by a factor 2 implies a 6 dB increase in the PN curve levels. Hence for frequencies commonly used in radar applications (i.e. C or X-band) it is convenient to use RF filters or loops in order to reach much lower PN values. In [11] the importance of this parameter on radar detection is highlighted as a -5 dB phase noise enhancement from -120 dBc to -125 dBc of the oscillator consents a 45% improvement of the detection probability.

Often the stability of an oscillator is described in terms of temporal jitter, which is defined as the unwanted temporal fluctuations of a timing signal. However, it has to be noticed that this parameter represents the time-domain perspective of the same general phenomena, while PN represents its frequency domain perspective. This explains perfectly why integrating the PN curve the temporal or the angular jitter variance can be determined [12] and why PN entails a lower accuracy in range estimation.

1.4. SYNCHRONIZATION ISSUES

After having examined the importance of oscillator stability for a conventional monostatic radar system, here, we briefly address time and phase synchronization requirements for radar networks. First time synchronization essential for incoherent radar networks is analysed and, afterwards, phase synchronization indispensable for coherent operation mode is discussed.

1.4.1. Time synchronization

Essentially radar ranging is based on the measure of the elapsed time between the transmitted signal and the backscattered return echo. Hence it is evident that a correct timing is a key factor in radar signal processing. In fact, as it is reported in

Table 1-1, in distributed networks time synchronization is a mandatory requirement both for coherent and non coherent mode. However, at the state of the art time synchronization is not an issue anymore and compared to phase synchronization results a much more affordable requirement.

An insufficient time synchronization is accountable for an incorrect data fusion with a detrimental effect on overall detection performance. A common data fusion approach employed when radar networks with multiple bi-static or monostatic radars are deployed are multilateration algorithms. Aforesaid algorithms are applicable, provided that range cells associated to each node of the network are correctly aligned, else, depending on the entity of the synchronization error, a target is located in a shifted range cell. Subsequently, either the target is not detected at all or the same target is detected multiple times in different locations, since some nodes individuate the target in the correct range cell, whereas other nodes spot it in shifted cells.

A practical design rule for an appropriate network timing consists of selecting for the implementation of the radar network, oscillators that have a precision indicatively of one tenth of the pulse width of the radar waveform. Therefore, considering that the typical radar pulse lengths for maritime applications are of the order of μs, local oscillators have to assure a time stability better than 0.1 μs equivalent to 100 ns for non coherent operations. Common quartz oscillators satisfy the above specified requirement as they usually provide in a scan period, typically of the order of tens of seconds, a timing accuracy ($\Delta\tau$) of ns (i.e. clock stabilities of 10^{-8} in 10s) [6]. Accordingly, a possible way to provide a good time synchronization among all nodes is to install in each node identical oscillators, which are periodically synchronized so that residual slow time drifts can be recovered. Another valid solution is to select, as oscillator sources, GPS disciplined oscillators (GPSDO) which receive a synchronization signal exploiting the GPS system. Ultimately, it is also possible to use different oscillators provided that time synchronism is recovered through direct synchronization signals sent to all nodes via dedicated radio or cable links.

1.4.2. Phase synchronization

Phase synchronization is an essential factor to implement a distributed coherent radar network and is much more complex to realize with respect to time synchronism. The reason cause phase synchronization is more challenging to implement descends from the high RF frequencies typically utilized for radar applications (i.e. GHz). For instance in maritime applications usually carrier frequencies in the range 1-10 GHz are used, hence an instability of 10^{-9} (10^{-3} ppm), assuming to work at 1 GHz and a CPI equal to 1 s determines a disastrous phase shift of 2π which is not acceptable. Phase synchronization is still an open issue [13][14][15][16] [17] in the implementation of distributed coherent radar networks. As already seen for timing purposes, also for phase synchronization a direct approach (i.e. wired or RF links) or an indirect approach (i.e. GPS synchronization) can be considered. The phase stability requirement can be expressed by the relation detailed in Eq. 1-1:

$$\Delta\theta = 2\pi f T_{CPI} < \theta_{MAX} \qquad \textbf{Eq. 1-1}$$

In a given integration interval T_{CPI} , the phase error, $\Delta\theta$, has to be lower than a maximum tolerable phase deviation indicated with θ_{MAX}. It is clear that by reducing the integration time, the phase stability requirement becomes less demanding as the phase error, $\Delta\theta$, assumes a lower value. Inversely, at higher frequencies, f, the phase shift is higher; hence superior stabilities are necessary. At the state of the art temperature controlled oscillators (TXCO) can guarantee an oscillator stability of 10^{-12} over 1 s. Conversely, if phase stability has to be assured over longer time intervals or higher carrier frequencies are adopted, even those oscillators could result inappropriate. A further analysis is beyond the scope of this work. However, we conclude pointing out that recently photonic circuits have been tested for synchronization scopes and that an incredible oscillator stability of 10^{-14} over 100 s has been demonstrated [18][19]. This unprecedented oscillator stability opens new intriguing perspectives for modern radar applications.

1.5. EFFICIENT SIGNAL DISTRIBUTION

In the RF domain high signal attenuation limits the maximum possible distance of wired signal distribution. As can be noticed from Table 1-2, the attenuation of a coaxial cable at 2 GHz carrier frequency is about 360dB Km^{-1} [20]. Accordingly, a signal distribution on large distances via RF cables, for instance, for a coastal surveillance application, where the distances to cover between network nodes are of the order of hundreds of meters, is obviously unfeasible.

Another critical aspect in the RF domain is handle signals with high fractional bandwidths (BWs) as well as preserve signal coherence of those wide band signals during signal distribution, due to the fact that RF cables introduce a significant signal distortion, especially on longer distances. Instead, as can be noticed from Table 1-2 optical fiber (O.F.) has an attenuation of a fraction of dB per Km and can manage with negligible distortion high fractional BWs. Hence in the optical domain an efficient signal distribution can be accomplished even on extremely long distances. The low distortion ensured is a direct consequence of the high carrier frequencies typically used by optical signals, laying around 200 Thz (i.e. corresponding to a wavelength of 1500 nm). Accordingly, a signal with a bandwidth of 2 GHz represents only the 0.00001% of the optical carrier frequency, while in the RF domain, assuming a 10 GHz carrier frequency, the same bandwidth represents the 10% of aforementioned carrier frequency. For this reason, OF links preserve an excellent phase stability when they are employed for radar applications and, unlike ordinary RF technology, can handle high BWs on extremely long distances. OF, indeed, is employed for high capacity transoceanic telecommunication backbones working at tens of Tb/s thus it is not surprising that even low cost optical solutions can easily transfer signals of some GHz back and forth between all nodes of the centralized multistatic radar network. Furthermore, OF compared to RF cable has many other advantages, which are summarized in Table 1-2.

Parameter	RF Cable	Optical Fiber
Weight	570 Kg/Km	1,7 Kg/Km
Attenuation	360 dB/Km (@2GHz)	0.2 dB/Km
Carrier frequency	2 GHz	200 THz
Bandwidth	10 MHz	10 GHz
Cost	6 $ per m	<10 cents per m
Installation	Heavy/Thick/Not flexible	Light/Thin/Flexible
Size Diameter	2 cm	1 cm (with jacket)

Table 1-2: Optical Fiber (OF) and RF cable comparison

For all these reasons, an efficient signal distribution over large distances, can be ensured in the optical domain and, without any doubt, photonics can represent an enabling technology for the realization of centralized coherent MIMO radar networks.

1.6. MIMO RADARS

A particular sort of multistatic radars are MIMO radars. The MIMO concept is a crucial element for IEEE 802.11 (Wi-Fi) and LTE 4G and 5G standards. Thanks to multipath propagation higher capacity links can be implemented and a better signal coverage is achievable too. In the last decades the MIMO approach has been extended also to radars and, as for communication applications, the basic idea is that spatial diversity can enhance detection performance.

At difference to multistatic radars, which can be considered composed by multiple monostatic or bi-static independent radars, each one with its exclusive transmitter and receiver, MIMO radars are multiple bi-static radar networks. In a MIMO configuration, in fact, whichever transmitter-receiver couple yields to a bi-static radar combination. Accordingly, assuming that the MIMO architecture has M transmitters and N receivers in total MxN bi-static radar channels can be exploited for detection. In Figure 1-3 the MIMO concept is clarified: in a MIMO configuration both receiving antennas collect the signal sent from the corresponding transmitter and also from the transmitter virtually associated to the other receiver.

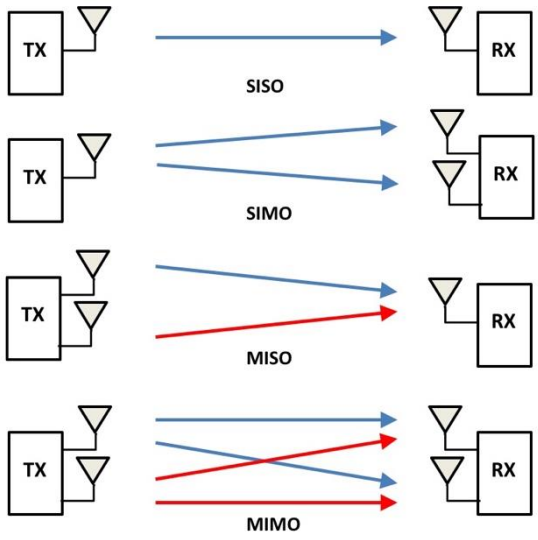

Figure 1-3: single input single output (SISO), single input multiple output (SIMO), multiple input single output (MISO) and multiple input multiple output (MIMO) architectures

The enormous advantage is manifest, in fact, given for both configurations the same number of transmitters and receivers, M=N, a multiple monostatic radar configuration can use for detection M received signals, while a MIMO configuration can exploit for the same purpose M^2 received signals.

A MIMO radar is defined as a radar system employing multiple transmit waveforms and having the ability to jointly process signals received by multiple antennas [21].

MIMO radars are indicated for high resolution applications as, for instance, for automotive purposes. It has to be pointed out that, when a MIMO radar having 2xM antennas (respectively M TXs and M RXs) is deployed, as will be shown in next paragraph, a virtual array formed by M^2 antenna elements is synthesized. Furthermore, assuming that the antenna elements are opportunely placed so that the resulting virtual array coincides with a phased array antenna, the same angular resolution ensured by an ordinary phased array antenna can be obtained using, in total, 2xM rather than M^2 antenna elements.

1.6.1. Orthogonal waveforms

Signal orthogonality is a pillar of the MIMO approach, as it allows to distinguish the source of each received signal. However, this key factor represents a main disadvantage in detection performance perspective. The orthogonality, indeed, leads to a non coherent summation on the target of M uncorrelated signals. Subsequently, the resulting SNR compared to a classical phased array antenna with the same number of elements, is M times lower. Luckily, this loss can be easily compensated by increasing the target observation time. This can be done as MIMO radars rely on large aperture antennas so that all antennas can simultaneously observe the area of interest. Hence, unlike conventional radars based on rotating or electronically beam scanning antennas, theoretically the integration time is unlimited thanks to the distinctive feature to cover the area to monitor with a wide illuminating beam and perform beam forming on reception. However, in practice due to limited target coherence it is not plausible exceed a fixed integration time limit. Therefore, depending on the antenna elements the resulting energy compensation can be total or only partial. As assessed in [22], if M is lower than 25/30 elements full compensation can be accomplished; while for higher values the compensation is only partial. In [23] in addition to cell migration considered in [22] also Doppler frequency is identified as a limiting factor for possible signal time integration, due to phase shifts, which are proportional to the target speed and the selected carrier frequency.

Orthogonality can be achieved in several ways: time-domain multiplexing (TDM), frequency-domain multiplexing (FDM) or code-domain multiplexing (CDM) are all possible solutions. The TDM approach reduces the number of pulses that can be integrated within a CPI, because a single PRI, Tr, is divided into M sub-PRIs of duration Tr/M so that each of the M transmitters can irradiate its signal while the others are silent. As a direct consequence, assuming to use a chirp modulation or a pulsed modulation having a pulse width (PW) scaled by a factor M as the PRI, the resulting SNR level gets also reduced by a factor M. Instead FDM an CDM approaches do not have any detrimental impact on SNR, hence those are better options.

1.6.2. Basic principle

The minimal geometry necessary for an angular estimation is constituted by a configuration formed, at least, by 1 TX and 2 RXs and, as described in [24], by measuring the phase difference between the received signals at the 2 receivers, distant *d* one from another the direction of arrival can be individuated (see Figure 1-4). The following well known formula can be used to estimate the direction of arrival of the signal:

$$\theta = \sin^{-1}\left(\frac{\omega\lambda}{2\pi * d}\right) \qquad \textbf{Eq. 1-2}$$

where ω represents the phase difference of the signals acquired by the two receivers.

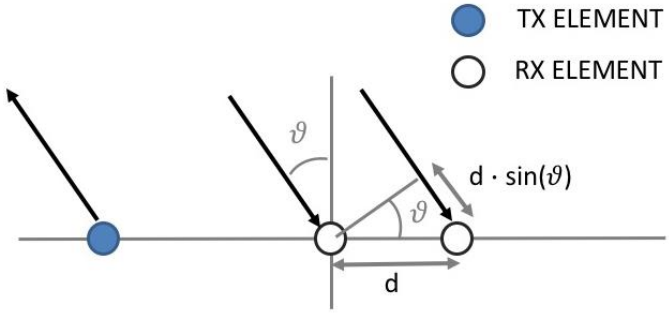

Figure 1-4 Direction of arrival estimation with 1 TX and 2 RXs

Expanding the model to N equidistant receiving antennas entails that the phase shift at each antenna increases by a factor ω with respect to the previous antenna. An estimation of the phase shift ω can be easily accomplished sampling at each antenna the signal and performing a Fast Fourier Transform (FFT) in the spatial domain. This intuitively explains why more receiving antennas can provide a better angular resolution (since their FFT has sharper peaks, enhancing so angular resolution).

Until now only 1 TX (i.e. a Single Input Multiple Output configuration) has been considered, if we add another transmitter to the previous geometry distant 3d from the first transmitter and another receiving antenna, as shown in Figure 1-5, we realize a virtual array of 6 elements (i.e. 2 TXs x 3 RXs MIMO configuration). The receivers, in fact, collect signals with phase shifts equal to [0ω 1ω 2ω] associated to TX1 and phase shifts equal to [3ω 4ω 5ω] associated to TX2. This demonstrates that the configuration is perfectly equivalent to an 6-element equidistant receiving array.

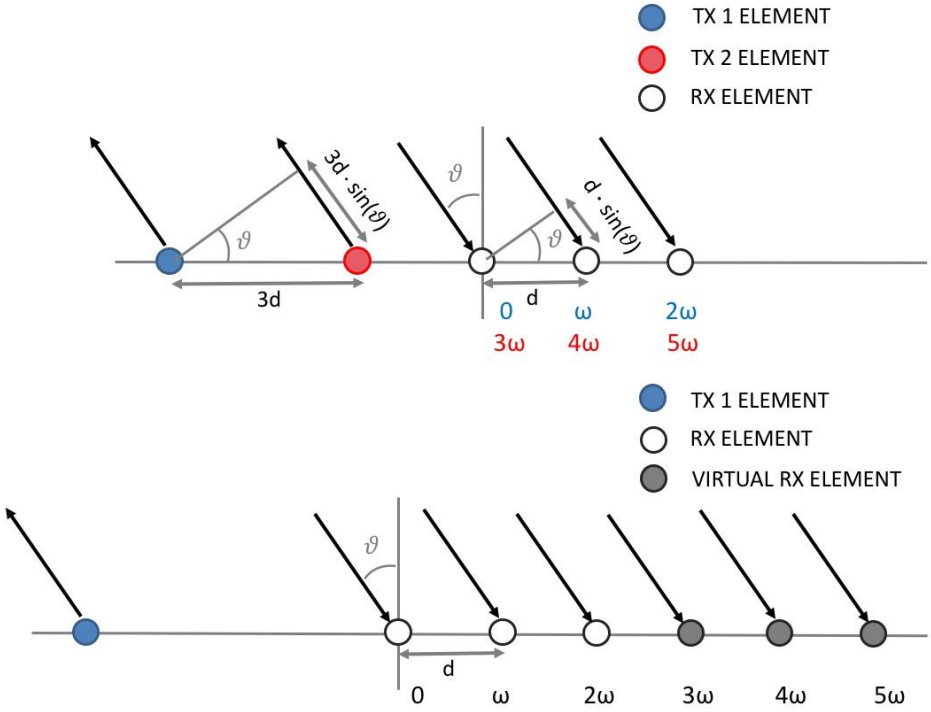

Figure 1-5 MIMO radar principle 2 TXs and 3 RXs: real array (top) and virtual equivalent array (bottom)

1.6.3. Co-located MIMO & MIMO with widely separated antennas

MIMO radars can be classified depending on their antenna disposition into MIMO with co-located or widely separated antennas [25]. In this study we will focus merely on the latter MIMO type.

Before giving a rigorous mathematical criterion, we prefer introduce a qualitative definition useful to distinguish abovementioned radar architectures: a MIMO configuration is classified as an architecture with widely separated antennas if each element views a different aspect (side) of the target. Expressed in a different way, if the distributed target cannot illuminate with the same beam aperture two antennas of the radar architecture the information content received by spatial distributed antennas is decorrelated. On the other hand, when all antennas observe the same target side co-located MIMO theory should be applied, which corresponds to ordinary array antenna theory if MIMO inter-element spacing is exactly half carrier wavelength.

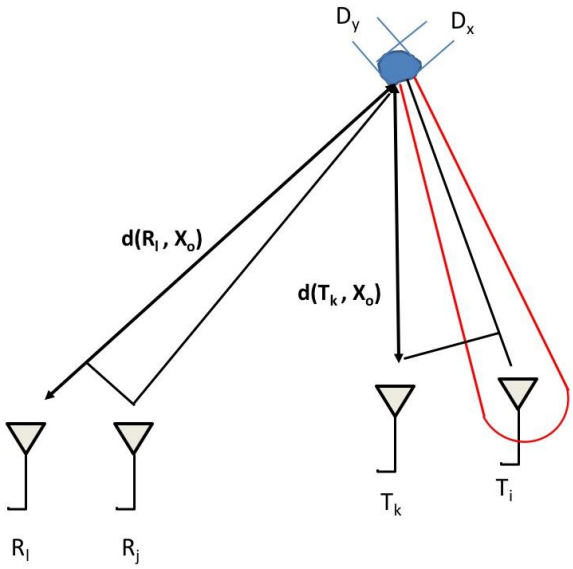

Figure 1-6: MIMO radar with widely separated antennas

Observing Figure 1-6 it is evident that the essential factors to determine whether for a specific scenario co-locate or widely separated theory is applicable are following: the antenna geometry, the target distance and the target dimension. MIMO theory for widely separated antennas reviewed in [25] can be applied provided that, at least, one of the following inequality is verified since this implies that signals received by different antennas are not correlated.

$$\frac{x_{tk}}{d(T_{k,}X_0)} - \frac{x_{ti}}{d(T_{i,}X_0)} > \frac{\lambda}{D_x}$$

$$\frac{y_{tk}}{d(T_{k,}X_0)} - \frac{y_{ti}}{d(T_{i,}X_0)} > \frac{\lambda}{D_y}$$

$$\frac{x_{rl}}{d(R_{l,}X_0)} - \frac{x_{rj}}{d(R_{j,}X_0)} > \frac{\lambda}{D_x}$$

$$\frac{y_{rl}}{d(R_{l,}X_0)} - \frac{y_{rj}}{d(R_{j,}X_0)} > \frac{\lambda}{D_y}$$

Eq. 1-3

In Eq. 1-3 (x_{tk}, y_{tk}) and (x_{ti}, y_{ti}) indicate the coordinates of the transmitting antennas T_k and T_i, while the notation (x_{rl}, y_{rl}) and (x_{rj}, y_{rj}) refers to the coordinates of the receiving antennas R_l and R_j and $d(T_K,X_0)$ to the distance between the antenna position T_k and the target position X_0 and, as usual, λ is the carrier wavelength.

If the antenna target geometry satisfies the above reported condition widely separated transmit and receive antennas can capture the spatial diversity of the target RCS. Conversely, when the antenna distances are small compared to the target distance we are observing the target under the same angle of view; thus the backscattered energy for all channels (i.e. any transmitter-receiver combination) is proportional to the monostatic RCS. That is always true exception made for the situation where the target is so large that the right term of the inequality in Eq. 1-3 tends to 0 and the inequality is again verified. In this case, although the target is far away from all antennas, due to its considerable size the application of MIMO processing for widely separated antennas is appropriate.

1.6.4. Main MIMO radar network with widely separated antennas benefits

In this paragraph we briefly outline the foremost advantages related to MIMO radar networks with widely separated antennas.

Diversity Gain

Combining radar returns obtained by independent target illumination provides a gain analogous to the diversity gain exploited in telecommunication for the resolution of the fading channel issue. Likewise, starting from the assumption that, especially for complex targets, the RCS has a high angular variability the probability that the RCS is very small, hindering so detection, can be reduced by increasing the number of "looks" at the target.

It must be specified that for MIMO architectures with widely separated antennas, as sketched in Figure 1-7, the transmitters and receivers view the target from different aspect angles. Subsequently each receiving antenna collects the signal retro-scattered in its direction which does not coincide with the energy back-scattered towards the illuminating source. In fact, as for bi-static radars, bi-static RCS has to be considered rather than conventional monostatic RCS. While RCS target models (i.e. Swerling models) have been developed and largely validated for the monostatic case, only limited data on bi-static and multi-static RCS measures are available. However, further simulations and bi-static RCS measures, as those reported in [26] [27], are necessary before reliable mathematical models can be formulated.

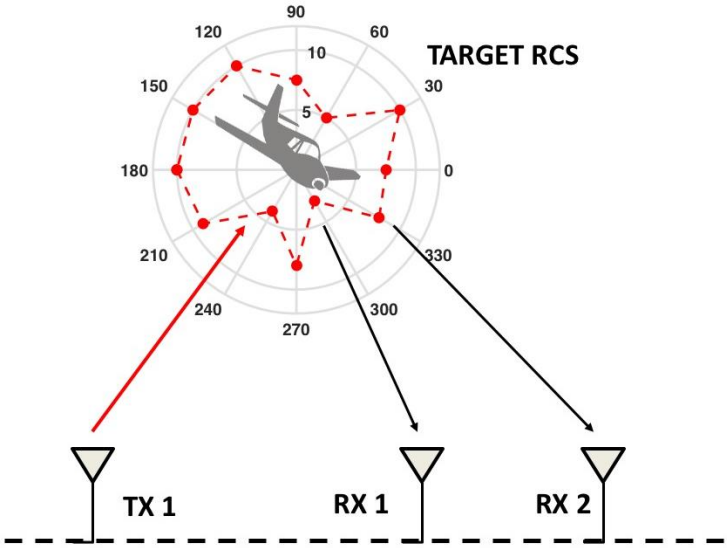

Figure 1-7: Multi bi-static RCS concept

Despite the lack of models concerning bi-static RCS, the potential profit achievable when the same target is observed from multiple aspect angles is undeniable. Thanks to information acquired in spatial diversity some classes of objects arduous to detect with monostatic radars, such as drones or stealth targets, can be better spotted. Many objects, as for instance ships, have a small frontal RCS signature while the same objects "looked" from a different viewpoint (i.e. lateral) has a higher RCS even by tens of dBs, which, as said, could contribute to facilitate its detection. Morevover, even military targets designed explicitly to be invisible to enemy radars (i.e. stealth targets), when observed from multiple observation points, can be better individuated since, typically, they convey the incident electromagnetic (EM) energy in expendable sectors, not coincident with the illuminating sectors.

To profit from diversity gain sensors need to have a common time reference, but phase synchronization is not required; assuming orthogonality between transmitted signals, the Newman Pearson optimum detector assumes following form:

$$\|y(X)\|^2 \underset{H0}{\overset{H1}{\gtrless}} \gamma \qquad \textbf{Eq. 1-4}$$

In Eq. 1-4 ||.|| denotes the Euclidean norm, while, as usual, H1 and H0 represent respectively the hypothesis of target present and target not present and γ indicates the decision statistic threshold. y(X) instead represents the vector having MxN (i.e. M = number of transmitters and N number of receivers) vector components $y_{kl}(X)$, each obtained filtering with a matched filter the received signals sampled at an opportune time delay corresponding to the location X= (x, y) in the target plane. Given that the transmitted signals are orthogonal also $y_{kl}(X)$ vector components are orthogonal. Hence the Euclidean norm becomes the sum of MxN $|y_{kl}(X)|^2$ terms. Accordingly, the optimal detector test statistic can be calculated by a central processor just summing all amplitude contributes $|y_{kl}(X)|^2$ received by the N receivers, which implies that data fusion can be performed through a non-coherent combiner.

Slow moving target detection and accurate Doppler frequency estimation

Objects with a radial speed can be easily detected applying a moving target indicator (MTI) or moving target detector (MTD) processing. The impact on radar performance is remarkable as stationary clutter (i.e. hills, buildings) can effortlessly be filtered out as their Doppler speed is much lower than the one associated to moving targets. A standard Range-Doppler processing allows to individuate moving targets, which have non-zero spectral Doppler components and notoriously the Doppler frequency shift is proportional to the radial speed of the target according to following relation valid for the monostatic case:

$$f_D = \frac{2v_R}{\lambda} \qquad \textbf{Eq. 1-5}$$

Instead for a bistatic radar configuration, assuming that the target and the transmitter are aligned on the x-axis and that the receiver forms with the target transmitter axis an angle equal to θ as shown in Figure 1-8, the Doppler shift recasts as follows.

$$\mathrm{f_{bi-Doppler}} = \frac{\mathrm{v_x}}{\lambda}(1+\cos\theta) + \frac{\mathrm{v_y}}{\lambda}(\sin\theta) \qquad \textbf{Eq. 1-6}$$

Further details can be found in [25].

From the above reported bi-static Doppler formulation we can infer that, provided that the transmitter and the receiver are not aligned both on the x-axis (i.e. in this case all 3 elements TX, RX and target would be aligned, which would cause in above made assumptions that θ is equal to 0 and that Eq. 1-6 degenerates to the mono-static Doppler relation reported in Eq. 1-6), it is possible to appreciate both the x and the y components of the target's speed vector. Besides another direct consequence is that slow moving targets can be better individuated, as they cause a more evident Doppler shift (i.e. proportional to θ which ultimately depends on the baseline extension).

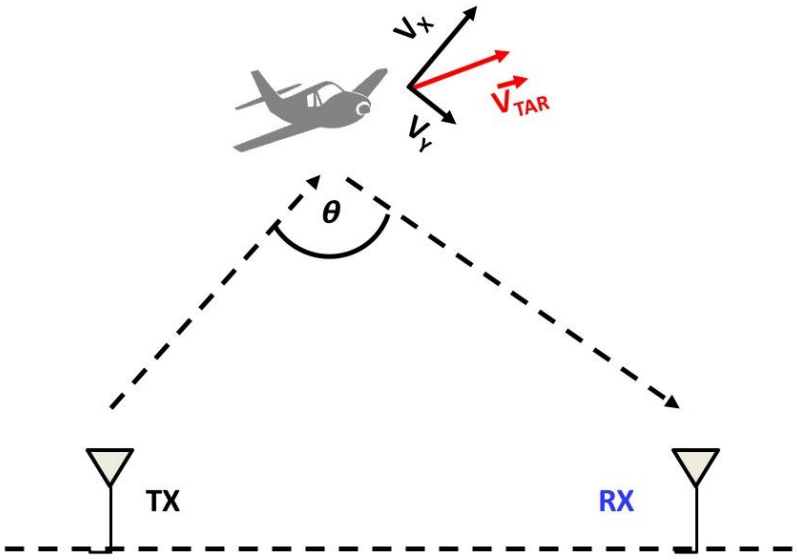

Figure 1-8: Bi-static Doppler geometry

High angular resolution (Super-Resolution)

The most interesting aspect, which will be deeply examined in this dissertation, is definitively the high angular resolution achievable when MIMO radar networks with widely separated antennas are deployed. Exploiting the spatial information collected by multiple bi-static channels, a resolution better than the one associated to the employed signal BW can be reached. For this reason, in the following this feature is also referred to as super-resolution underscoring the remarkable positive impact on radar resolution. First of all, a higher resolution consents to better locate a pre-detected target, secondly when multiple small targets are present in an area they can be resolved (i.e. distinguished as two separate targets) and finally in case of distributed targets, which occupy more than a single resolution cell, a high resolution image can be obtained, which is advantageous for an ensuing target classification and, eventually, for its identification.

Notoriously, radar range resolution is limited by the signal BW of the radar waveform (i.e. $\Delta r = \frac{c}{2B}$), whereas the cross-range resolution (also referred to as azimuth resolution) depends on the antenna beam aperture and the target distance and, coarsely, can be determined through following relation:

$$\Delta r_{az} = \frac{\lambda}{D} R \qquad \textbf{Eq. 1-7}$$

where λ indicates the carrier wavelength, R the target distance and D the physical dimension of the antenna in the considered plane. From Eq. 1-7 it is evident that, as the distance increases, though the angular antenna beam aperture remains constant, the cross-range cell dimension increases linearly. Although unavoidable when monostatic radars are employed, cited angular resolution limitation is unacceptable either for high resolution applications as well as for ordinary surveillance purposes, as results evident from the following example.

Assuming a maritime scenario and, in particular, a naval X-band radar operating at 10 GHz (i.e. λ=0.03 m) using a planar array antenna having a horizontal dimension of 3 m, from Eq. 1-7 results that the angular resolution is 0.01 rad corresponding to 0.6°. Accordingly, at 20 Km the range cell has an azimuth size of circa 200 m, which is certainly not suitable for tracking functions in a maritime scenario and can result inadequate even for surveillance operations.

In [28] a coherent processing approach applicable to MIMO configurations with widely separated antennas is reported. The simulated results show that, thanks to spatial diversity and a coherent processing scheme, the radar cross-range ambiguity function can be significantly enhanced

compared to the cross-range ambiguity function determined through a non-coherent approach. In particular, simulations done considering a 9 TXs x 9 RXs MIMO architecture, presented in [28], prove that a distributed target constituted by 4 ideal point-like scatterers, spaced by 6 λ both in range and in cross range, can be correctly detected, resolving successfully all scatterers.

Aforementioned study is based on two papers [29][30] concerning an analysis on side lobe reduction in random array antennas. From these analysis emerges that the peak to side lobe ratio (PSLR) is influenced dominantly, namely linearly, by the number of elements N, used for the realization of the random array. Whereas other parameters such as the carrier wavelength, the array size and the signal BW have only a logarithmic effect on side lobes. In particular, the theory developed in [30] shows that wide-band frequency diversity reduces the high side lobe level of random thinned arrays. Besides coherence offers the advantage to reduce the average level of distant side lobes and, as reported in Figure 1-9, in case $Q<\frac{L}{\lambda}$, where Q is the reciprocal fractional BW (i.e. $Q=\frac{f_C}{BW}$) and L is the array length, the PSL/ASL (peak side lobe over the average side lobe) is proportional to ln Q [30].

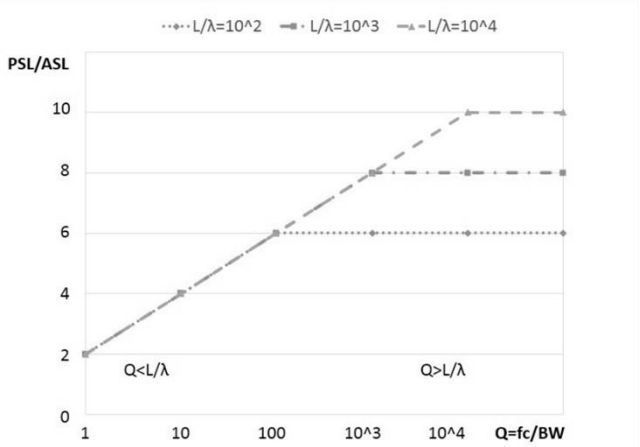

Figure 1-9: Peak Side Lobe/Average Side lobe in function of Q (inverse fractional BW) and array size length (L/λ)

At this point it is opportune to check what are the expectable PSL values, according to the above recap theory for a maritime scenario. Assuming to implement a MIMO radar geometry with widely separated antennas, equivalent to a virtual sparse array having a baseline of 3 Km working at 10 GHz, it turns out that $\frac{L}{\lambda}$ is equal to 10^5, which becomes 500 in a naval case, assuming a baseline length of about 150 m. Instead, considering the signal BWs, typically used for aforementioned applications (i.e. 10MHz:100MHz), for a 10 GHz carrier frequency, Q assumes a value in the range [100:1000]. As Q is lower than $\frac{L}{\lambda}$, according to the graph depicted in Figure 1-9, the expected PSL on the average side lobe (ASL) is proportional to ln Q, which means that in this case the lower the Q, the lower the PSL. The result confirms that MIMO theory can be applied to maritime scenarios and, as will be confirmed in Chapter III, that higher BWs (i.e. lower Q) entail lower PSL.

In conclusion, a resolution in the cross-range dimension (i.e. perpendicular to the range dimension) higher than the resolution assured by the BW in the range dimension is possible provided that:

- High fractional BWs are used and the antenna geometry (L) is large measured in terms of wavelength so that $Q<\frac{L}{\lambda}$;
- Transmitted signals are orthogonal, otherwise receivers are not able to distinguish which transmitter originated the signal;
- Signal coherence is guaranteed.

System advantages

A MIMO radar, as already discussed, consents to obtain manifold performance benefits ranging from diversity gain to enhanced angular resolution. However, this innovative radar class is convenient also for its system architecture. In the following the main positive repercussion descending from the spatial distributed system architecture are listed:

- Spatial sensor distribution allows to solve electromagnetic interference (EMI) issues between conflicting systems (i.e. EMI optimization);
- Large aperture antennas assure a better area coverage and perhaps a continuous surveillance unlike conventional radars with rotating or electronically beam scanning antennas, where monitoring is discontinuous (ubiquitous monitoring) [31];
- Lower interceptability probability, due to the use of multiple receivers and coherent integration on long CPIs. Thus higher SNRs can be obtained and consequently lower peak powers are necessary [31];
- Better fault tolerance and graceful degradation, due to the system architecture based on multiple distributed TXs and RXs.

1.7. MIMO SIMULATOR SIGNAL MODEL

Prior to describe in next paragraph the developed MIMO scenario simulator, it is opportune outline the considered signal model.

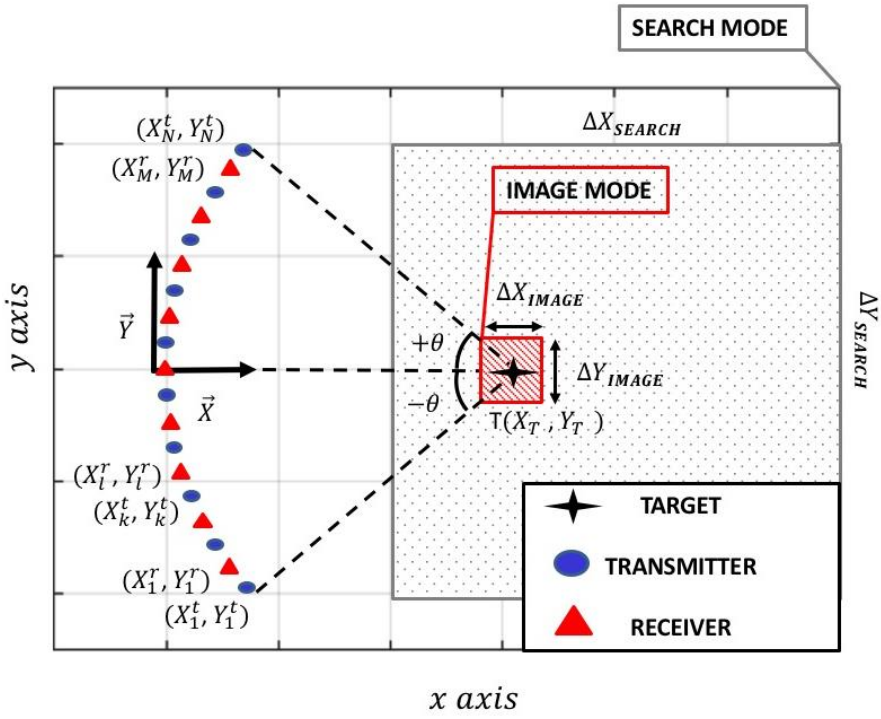

Figure 1-10: MIMO reference scenario

The reference scenario, represented in Figure 1-10, has an antenna configuration of M transmitters and N receivers and all sensors are assumed to be equidistant from the target and equally spaced on an angular sector, 2θ. The M receivers and the N transmitters are identified by the coordinates (X_l^r, Y_l^r) and (X_k^t, Y_k^t) respectively, whereas the target is an ideal point-like scatterer placed in position T = (X_T, Y_T) and assuming to use wide beam antennas so that the target is in the Field of

View of each antenna (e.g. using horn antennas). Differently than a monostatic radar a common reference system for all bi-static radar combinations has to be individuated. In the rest of the dissertation, as shown in Figure 1-10, the y-axis always individuates the cross-range direction and is oriented as the antenna baseline, instead the x-axis, perpendicular to the baseline, individuates the range direction. A further assumption is that the transmitted signals s_k are orthonormal.

Neglecting all possible sources of noise, the signal received by the l-th receiver, as defined in [25] can be expressed as follows:

$$r_{k,l}(t) = a s_k(t - \tau_{k,l}(x,y)) \qquad \textbf{Eq. 1-8}$$

where s_k is the signal transmitted by the k-th transmitter, and a is an amplitude factor, depending on the specific channel power budget[2] (i.e. a channel is any TX-RX combination). Instead, $\tau_{k,l}$ indicates the time delay between the transmitted and received signal and depends only on the location of the target and of the k-th transmitter and l-th receiver. Eq. 1-8 is valid in ideal noiseless conditions, however, in real case, amplitude and PN contributes have to be taken into account. As usually the amplitude noise contribute can be modelled as an additive white Gaussian noise (AWGN) so that the signal model becomes:

$$r_{k,l}(t) = a s_k\left(t - \tau_{k,l}(x,y)\right) + n_{k,l}(t) \qquad \textbf{Eq. 1-9}$$

where the term $n_{k,l}(t)$ represents the noise contribute related to the signal associated to the k-th transmitter and l-th receiver. Instead, in presence of PN, the received signal recast as follows:

$$r_{k,l}(t) = a s_k(t - \tau_{k,l}(x,y)) e^{j(\theta(t-\tau kl) - \theta_{PN}(t))} \qquad \textbf{Eq. 1-10}$$

where $\theta_{PN}(t)$ represents a phase shift caused by the oscillator instability (i.e. angular jitter obtained integrating the phase noise curve of the oscillator over the spectral window of interest).

If the angular jitter is below 0.1 rad, as stated in [32], the phase noise influence on the received signal is negligible (i.e. in Eq. 1-10 the factor $e^{j(\theta(t-\tau kl)-\theta(t))}$ is equal to $e^{j(\theta(t-\tau kl))}$), therefore, the following log-likelihood function described in [25] appropriate for a coherent MIMO detection can be used:

$$\ln f\big(r(t)\big|(x,y)\big) = c' \left| \sum_{k=1}^{M} \sum_{l=1}^{N} e^{-j2\pi f_c \tau_{k,l}} \int r_{k,l}^{b*}(t)\; s_k^b\big(t - \tau_{k,l}\big) dt \right| + c'' \qquad \textbf{Eq. 1-11}$$

According to the formula in Eq. 1-10, for each possible target location having coordinates (x,y) the decision statistic is computed determining for all M transmitters and N receivers the correlation between the received and transmitted signal at baseband. Afterwards, a phase compensation term compensates the phase shift due to the time delay $\tau_{k,l}$, which differs for each possible target location (x,y) and considered transmitter (X_t,Y_t) and receiver (X_r,Y_r) couple. Completed the re-phasing of each term, all MxN correlation contributes can be coherently added up. For further details (i.e., for constants c' and c'') see Eq. 6 in [25].

From the exponential term in Eq. 1-10 it is clear that the resolution cell has to be really small, in fact, for points just one wavelength distant, the phase compensation values change by 4π. Hence, as pointed out in [33], in order to have an acceptable computational complexity it is opportune to split the surveillance function into two steps. Primarily in "search mode" for all points, laying in an area

[2]the amplitude factor a depends on all factors included in the radar equation (the RCS of the scatterer, the transmitted signal, the distance of the target, the antenna gain, the loss factors and the utilized carrier wavelength).

of size ΔX_{SEARCH} x ΔY_{SEARCH} targets are pre-located using low resolution cells then only on limited portions of the scenario, as shown in Figure 1-10 , high resolution "image mode" is performed on a rectangular area of size ΔX_{IMAGE} x ΔY_{IMAGE} around the position occupied by the target T. Consequently, as the area on which the detection statistic, reported in Eq. 1-10, has to be calculate is much smaller, a fine range/cross-range resolution can be ensured which is appropriate to resolve the presence of multiple targets, to classify and, eventually, identify already pre-located targets.

1.8. MIMO SCENARIO SIMULATOR

Differently than a conventional radar system when a MIMO radar is employed several parameters, such as the number of transmitters and receivers, the radar waveform fractional BW and the adopted antenna geometry, have all a deep impact on overall radar performance. In particular, minimal system changes can cause significant variations in the shape of the radar cross-ambiguity function rising the false alarm rate and changing the angular resolution capability of the system.

For this reason, a 2-D MIMO scenario simulator has been developed with the twofold intent to understand how aforesaid parameters influence radar performance and the detrimental effect of oscillator instability. As will be evident in the rest of the dissertation, the simulator is useful either to get precious design indications for the realization of a MIMO coherent radar network and to set-up and test processing algorithms on simulated data set before using them on real data.

The simulator has been developed in MATLAB and is structured as sketched in the block diagram depicted in Figure 1-11. From a functional perspective all SW module can be divided into two classes: modules propaedeutic to the generation of the received signal and modules whose task is to compute the MIMO ambiguity function. It has to be pointed out that, while for the simulative analysis examined in Chapter III both functions of the simulator have been exploited, the results presented in Chapter IV, related to real data processing, have been obtained exploiting exclusively the detection function SW modules.

Before describing in detail the implemented detection blocks it is useful to furnish a brief explanation of the simulation process and the interactions among all modules. First of all, a MIMO geometry and a target need to be specified, these parameters can be specified by the user thanks to the user defined MIMO geometry and target model SW block. In order to get the received signal matrix further parameters such as, for instance, the radar waveforms, the sampling rate, the desired orthogonality type (i.e. TDM, CDM, FDM) need to be defined by the user. In ideal noiseless conditions, the resulting matrix constituted by MxN arrays, each having S samples, is directly passed to the detection blocks. In case a more realistic scenario has to be simulated the White Gaussian Noise Source and the Phase Noise Source can generate apposite random noise contributes. Those two contributes emulate respectively the additive noise contribute indicated with $n_{k,l}(t)$ in Eq. 1-9 and the term $\theta_{PN}(t)$ present in Eq. 1-10, due to oscillator instability. In total MxN random arrays having S samples are generated by both modules.

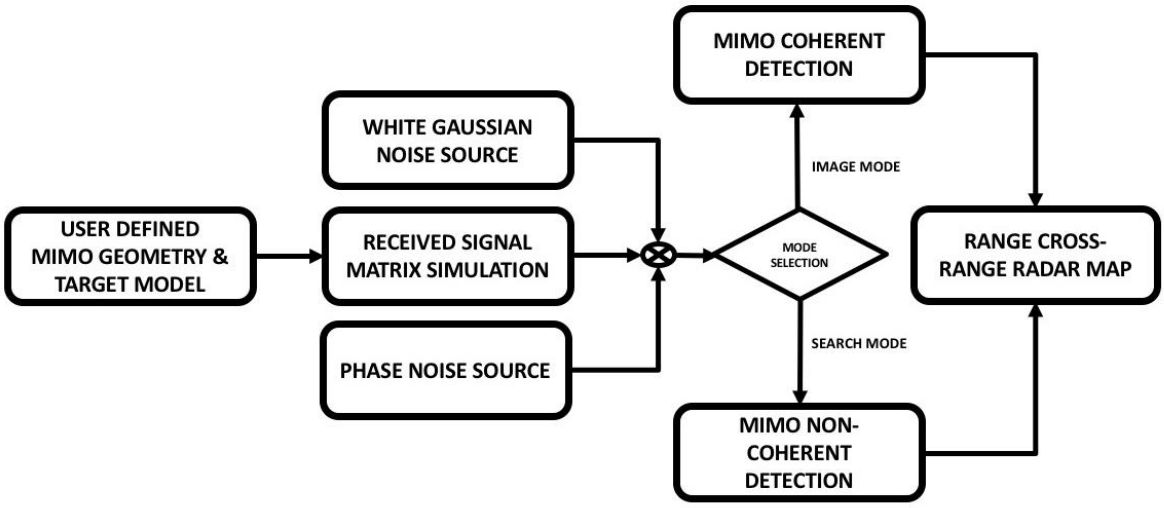

Figure 1-11: MIMO simulator SW block diagram

However, the matrix related to the additive noise phenomenon is added to the noiseless received signal matrix, instead to generate the signal matrix corrupted by phase noise a scalar product between the output matrix of the phase noise source block and the noiseless received signal matrix is executed.

In

Table 1-3 a exhaustive functional description of each developed SW block is given.

Block	Function
USER-DEFINED MIMO GEOMETRY AND TARGET MODEL	Defines the geometry of the scenario: antenna location, target position and area of interest (size and spatial sampling rate). The output of this block are 4 matrixes: one for the TX, the RX and the target coordinates and one with the coordinates of the points on which the MIMO ambiguity function has to be computed.
RECEIVED SIGNAL MATRIX SIMULATION	Based on the waveforms used by the transmitters and according to Eq. 1-8, the received signals at each receiver are simulated. In particular, in case of a multitarget scenario the received signal is obtained as the sum of the echoes associated to all targets assumed on the scene. The output of this module is a 3-D matrix having dimension M (number of transmitters) x N (number of receivers) x S (number of temporal samples).
WHITE GAUSSIAN NOISE SOURCE	Generates a random noise contribute; the random variable has a Gaussian distribution and a uniform power spectral density. The total power of the process depends on the environmental conditions and on the assumed receiver characteristics. The output of this module is a 3-D matrix having dimension M (number of transmitters) x N (number of receivers) x S (number of temporal samples).
PHASE NOISE SOURCE	The purpose of this module is to emulate the effect of oscillator instability. First a random complex noise array is generated then the resulting sequence is filtered with a filter having the spectral shape of the considered oscillator Phase Noise (coloured noise). Finally, the resulting random phase variations $\theta_{PN}(k)$ are exploited to get according to Eq. 1-10 the complex sample array. The output of this

	module is a 3-D matrix having dimension M (number of transmitters) x N (number of receivers) x S(number of temporal samples).
MIMO COHERENT DETECTION	According to the formula reported in Eq. 1-10, the block computes the MIMO coherent ambiguity function (image mode) on a defined number of points. The output of this block is a 2D matrix of size M_X (range samples) x M_Y (cross-range samples).
MIMO NON COHERENT DETECTION	Computes the MIMO non coherent ambiguity function (search mode) on a defined number of points. Aforesaid function is determined according to the formula reported in Eq. 1-10, without compensating the path delay phase shifts (for all channels and for all points of interest the term $e^{-j2\pi f_c \tau_{k,l}}$ is assumed to be equal to 1). The output of this block is a 2D matrix of size M_X (range samples) x M_Y (cross-range samples).
RANGE CROSS-RANGE RADAR MAP	This block receives the ambiguity function matrix obtained in image or search mode and consents to represent the range cross-range map related to a specific area or user-defined range cross-range plots. The module consents to extract essential features, such as peak side lobe ratio, range resolution, angular resolution and export, or, save files of interest.

Table 1-3: MIMO simulator block description

For sake of clarity, in Figure 1-12 the outputs of the various SW modules included in the block diagram depicted in Figure 1-11 are shown.

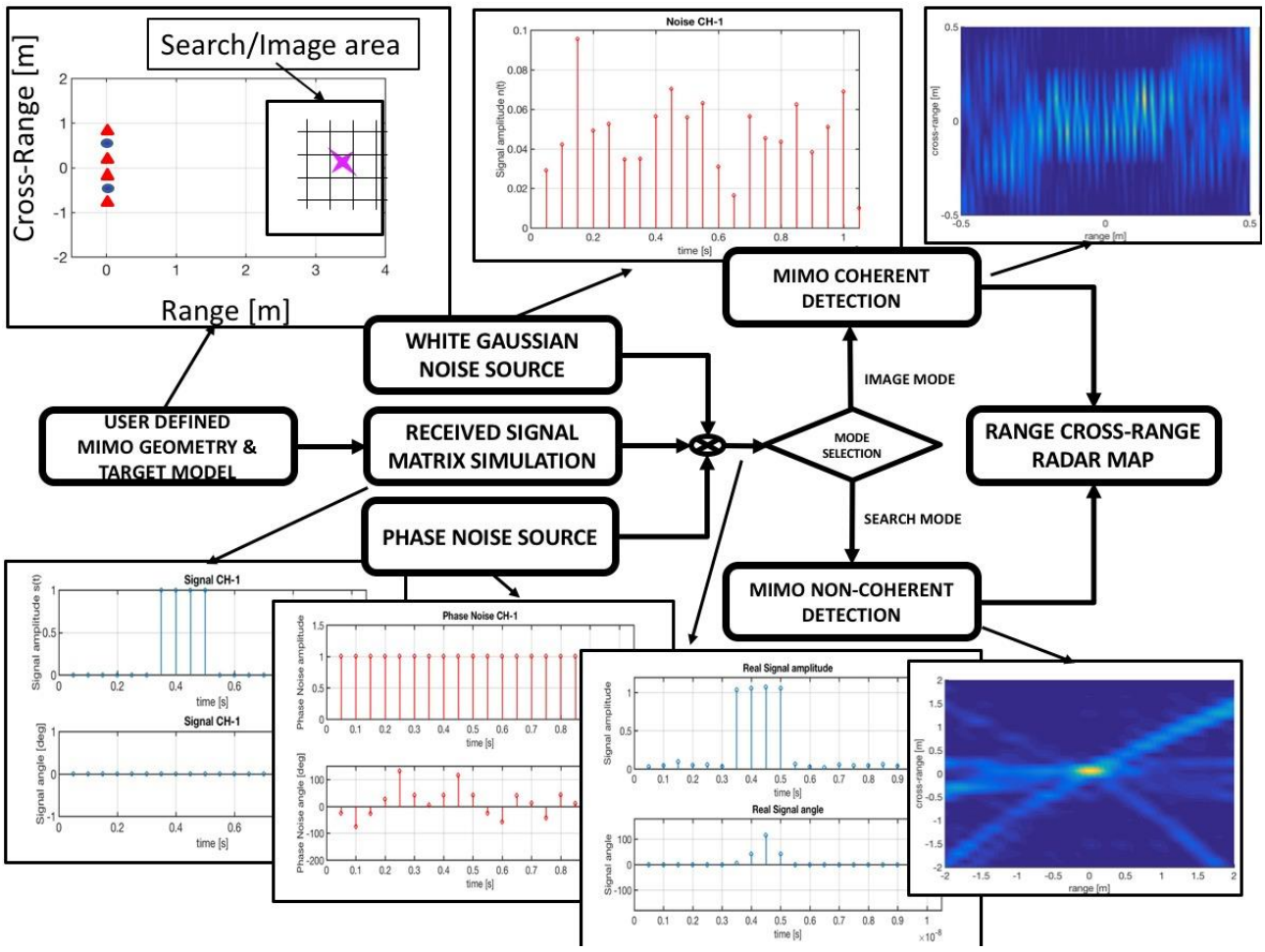

Figure 1-12: MIMO coherent and non coherent simulator outputs

In the flow chart in Figure 1-13 the sequence of mathematical operations performed by the MIMO detection blocks on acquired or simulated data sets are represented. The M transmitters and N receivers generate MxN data arrays, those arrays are the result of the cross-correlations operated between the received signals at BB and the transmitted reference signals at BB. Once the antenna positions are known each cross-correlation function can be mapped on a specific area having M_X x M_Y points, spaced respectively by Δx and Δy, obtaining so a mono-channel range cross-range map. As already stated, it is convenient explore in non coherent search mode a large area with a low spatial sampling rate. In this way the number of resulting sampling points M_X x M_Y is adequate. Conversely, in image mode the sampling rate has to be much higher in order to ensure a better resolution; however, by reducing the area to investigate the computational burden can be kept at acceptable levels.

Furthermore, in search mode also a non coherent processing is sufficient, therefore Non Coherent Maps can be directly added up without effectuating any phase alignment or, as represented in the flow chart diagram, this can be achieved performing a scalar product between cited maps and a matrix of all ones having the same size as the Non Compensated (NC) Map matrix. In image mode, instead, each point of the NC Map matrix has to be phase aligned thus, for each channel a Phase Compensation map is calculated. In this case the scalar product between aforesaid map and the associated NC Map originates a phase aligned map, where the phase shifts induced by transmitter-target and receiver-target path delays have been corrected. The resulting MxN rephased maps, eventually, can be added up coherently obtaining so a high-resolution map with the MIMO coherent ambiguity function on a specific area and with the selected sampling spacing.

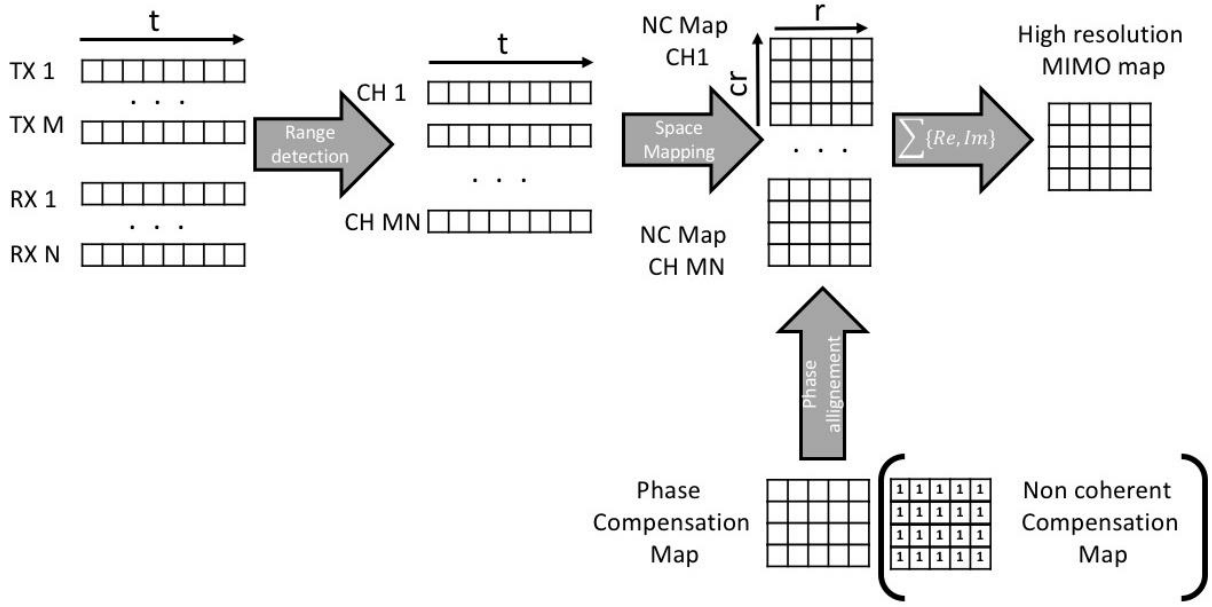

Figure 1-13: MIMO coherent and non coherent detection flow chart

2. MICROWAVE PHOTONICS

This Chapter is dedicated to Microwave Photonics which, as already stated, can represent an enabling technology for MIMO radars with widely separated antennas. The purpose is to furnish a quick overview on existing techniques and their benefits with respect to conventional microwave devices. Before discussing the foremost optical solutions suitable for radar applications, techniques exploitable also by different microwave applications are addressed, pointing out advantages and drawbacks. In the final part of the Chapter it we examine why photonics can be considered an enabling technology for the realization of coherent MIMO radar networks and describe the first photonics-based radar prototype.

2.1. MICROWAVE PHOTONICS

MWP is a branch of photonics that studies photonic devices for microwave applications in order to consent functions otherwise hard to realize in the RF domain. In Figure 2-1 the E/M spectrum is depicted showing the different frequency ranges typically employed by microwave (electronics) and optical (photonics) devices.

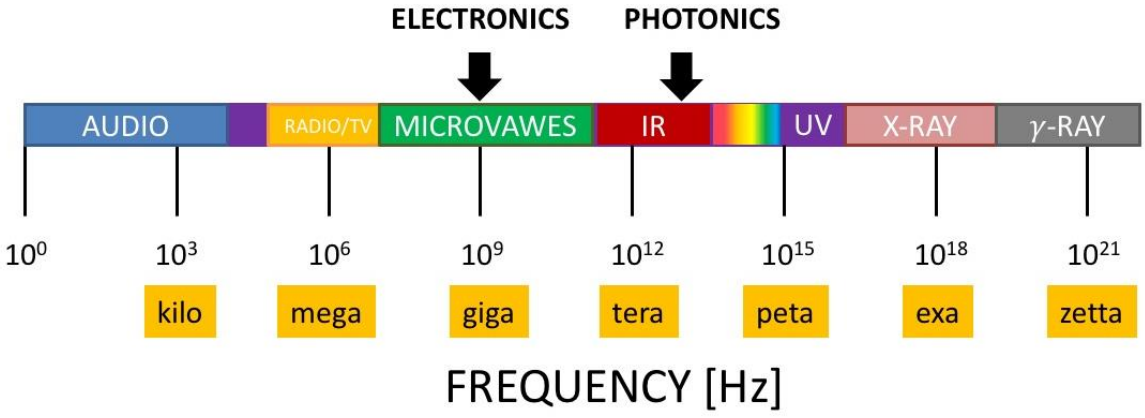

Figure 2-1: EM spectrum

MWP compared to conventional RF technology presents following valuable advantages:

- Reduced size, weight, cost and power consumption (SWAP);
- High-capacity data link;
- E/M immunity;
- Low signal attenuation;
- Low signal distortion.

In Table 1-2 a comparison between RF cable and equivalent OF parameters has already been made. The remarkable features of OF reported there perfectly explicate why photonics is largely adopted for data transmission. Moreover, thanks to continuously increasing features of optical devices (i.e. sources, photodetectors, modulators etc.), ever growing world wide data stream demand can be satisfied [34]. In the following the main MWP techniques are summarized; those interested in further details can find them in [35].

2.1.1. Radio over fibre

As already mentioned, data transmission is much more convenient in the optical domain than using conventional RF standards, consequently one of the most common MWP applications is Radio-over-Fiber (RoF), where optical devices are employed for RF signal distribution.

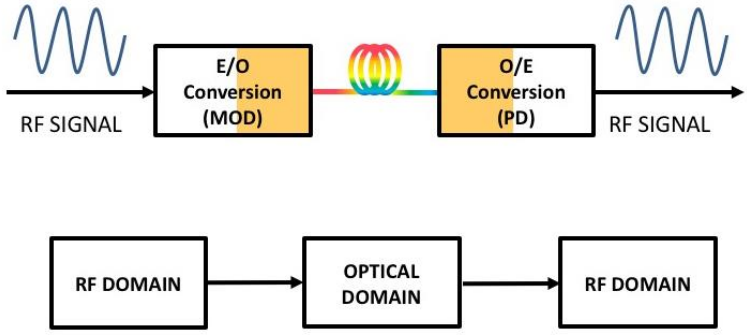

Figure 2-2: RF over fibre (RoF) scheme

An RoF system, as schematically shown in Figure 2-2, first converts an RF signal from the electrical domain to the optical domain; then transmits via optical fiber the signal to the desired location. There an optoelectronic conversion converts the signal back from the optical to the electrical domain. In this way great distances can be covered as well as signal with high bandwidths can be effectively transferred.

2.1.1. Beam forming

Another noteworthy MWP application is beam forming (BF). Leveraging on opportune phase shifts introduced in different elements part of an array antenna both the beam shape can be modified (beam shaping) and the pointing angle can be controlled (beam steering). Although RF solutions generally based on RF phase shifters exist, those solutions present numerous disadvantages respect BF realized through photonics. In particular squint[3] effect afflicts RF BF and therefore, RF BF is not indicated in case of wideband applications. On the contrary, photonic true time delay (TTD) solutions ensure wide band operations and offer some further benefits such as fast tuneability, higher precision and also EMI immunity.

2.1.2. Signal processing

MWP can be used also to facilitate RF signal processing. In fact, following three aspects have been extensively studied in the last decades:

[3] the steering angle or the antenna pattern depends on the RF frequency due to the fact that RF phase shifters transfer function changes for different frequencies;

- Photonic filtering;
- RF signal analog-to-digital conversion;
- Waveform generation.

Photonic filtering

RF filtering at high frequencies is not easy in the RF domain: RF filters have a modest tuneability and limited Q factors. Hence RF systems traditionally down-convert signals from RF to lower IF frequencies, where filtering operations are more affordable. Photonics-based solutions instead have a much larger range of tuneability (i.e. 10 MHz: 20 GHz) and can reach Q factors as high as 40dB. The high tuneability is a direct consequence of the superior carrier frequency approximately equal to 200 THz used in the optic domain. Accordingly, 20 GHz represent only the 0.0001% of the carrier frequency.

Analog to digital converters

Unfortunately, down-conversion from RF to IF stage is still unavoidable, due to existing sampling speed limitations. At the state of the art, in fact, the maximum available sampling speed of electronic analog to digital converters (ADCs), indeed, is limited to 100GS/s due to jitter effects on system clocks and still open issues in the realizations of interleaved ADC configurations. A solution to this bottleneck can originate from photonics: a technique known as time stretch slows down the electrical signal, so that a single ADC can sample and digitize the whole signal.

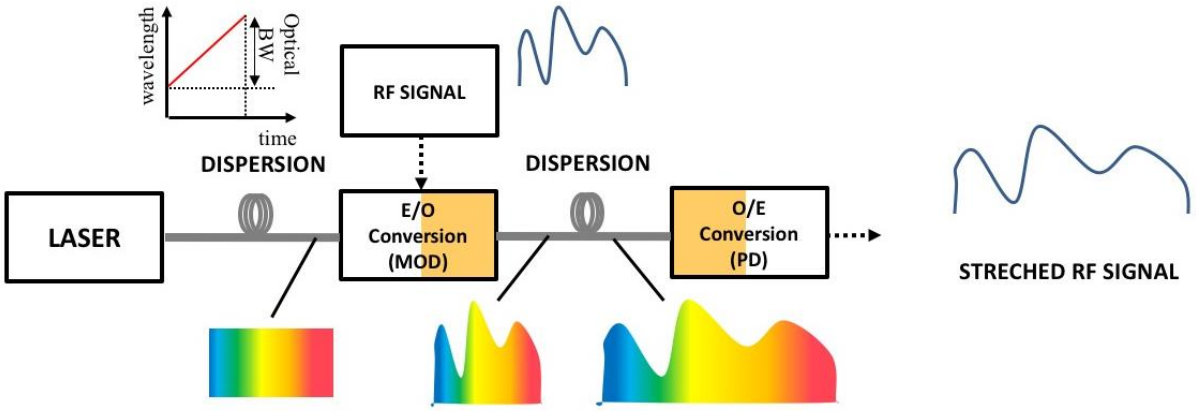

Figure 2-3: Photonic time stretch technique scheme

The technique as represented in Figure 2-3 is composed by 3 main steps [36] :

1. time-to-wavelength transformation;
2. wavelength domain processing;
3. wavelength-to-time mapping.

Signal generation

Next generation signal generation systems have to ensure a high degree of system configurability and flexibility; the goal is to have the possibility to change parameters such as signal BW, carrier frequency or even power dynamically selecting always the best set of parameters required by the current situation. This task can be guaranteed, provided that software defined RF signal generators are employed. At the state of the art, Direct Digital Synthesizer (DDS) generation is limited

to few GHz so up-conversion is necessary to reach the desired carrier frequency with detrimental effects on PN. A solution also to this pitfall can come from photonics: several techniques have already been experimented for ultra wide band (UWB) signal generation and signals up to tens of GHz have been successfully synthetized. In Figure 2-4 , for instance, the block diagram of a coherent UWB radar using a radar signal having a BW of 12.5 GHz is sketched [37].

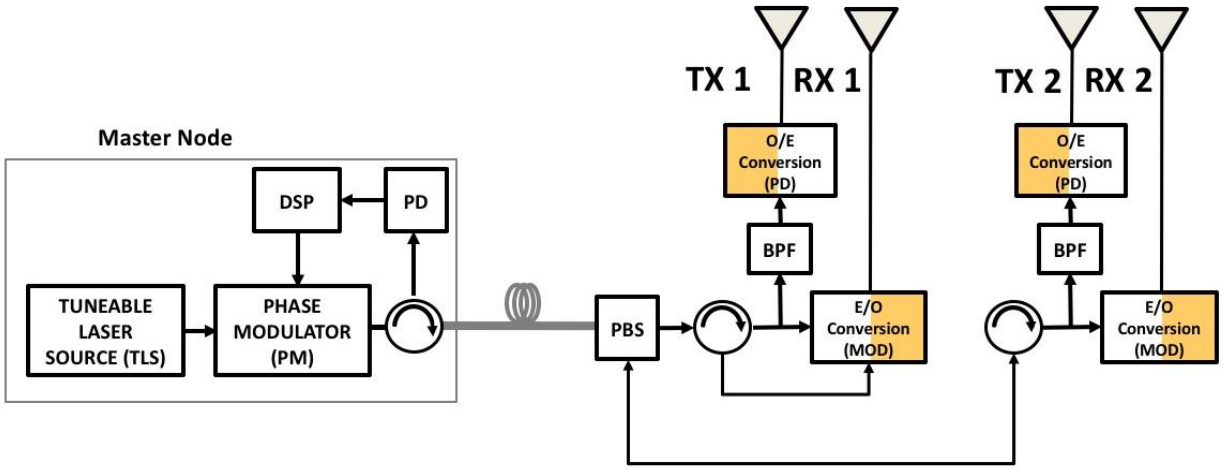

Figure 2-4: Schematic diagram a fiber-distributed UWB radar based on OTDM. TLS: tuneable laser source; PM: phase modulator PD: photodiode; DSP digital signal generation and processing; PBS: polarization beam splitter; BPF: band pass filter; EOM/MOD: electro optical modulator

2.2. MICROWAVE PHOTONICS FOR RADAR APPLICATIONS

In the previous paragraph the universal benefits of MWP have been introduced, here we focus on MWP solutions suitable exclusively for radar applications with the aim to furnish an outline of the state of the art. In particular, technological solutions, selected for the realization of the first photonic based radar are examined, in order to facilitate, afterwards, the comprehension of its principle of operation.

In Figure 2-5 the block diagram of a radar system is shown, highlighting which functions could be implemented in new generation systems through optical devices and which through electronic components.

From the figure we infer that essentially 4 functions can be implemented in the optical domain:

- RF signal generation and up-conversion;
- RF signal detection and down-conversion;
- RF filtering/processing;
- RF signal distribution.

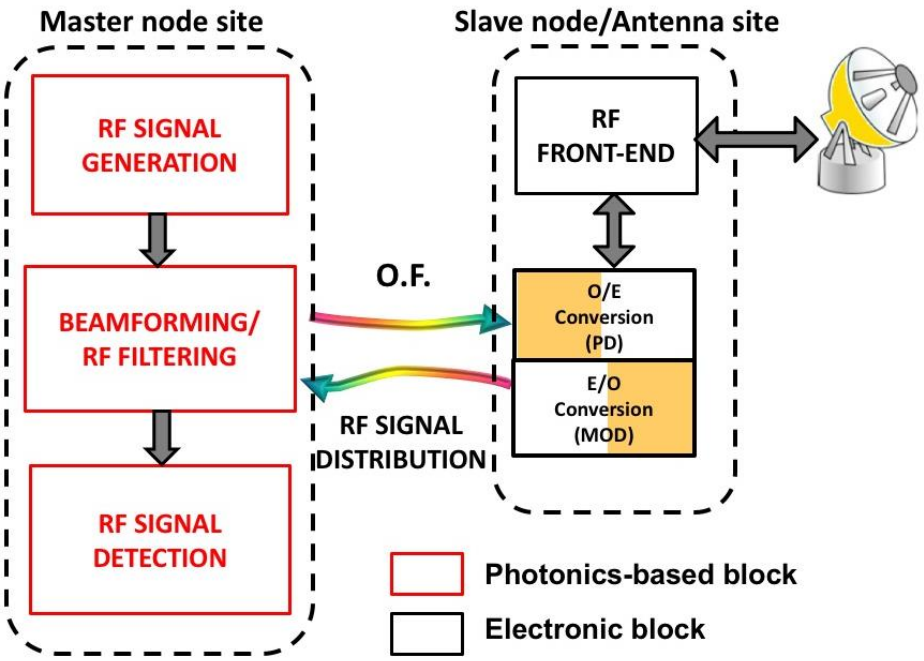

Figure 2-5: Possible radar functions realizable by the means of MWP

Before analysing in next paragraphs some specific scheme for the realization of the above listed functions appropriate for radar applications, we summarize the advantages brought by photonics dividing those benefits into two classes: benefits related to the transceiver and benefits associated to signal distribution.

Realizing a photonic transceiver (i.e. RF signal generation, reception and filtering in the optical domain) is convenient for the motives listed in the following:

- Low phase noise: lasers are characterized by extremely low noise (amplitude or phase noise, summarized in the parameter of the laser linewidth); they can be used to generate or detect RF signals with an excellent stability, in particular in terms of phase noise.
- Wide bandwidth: the technological advancements of optical communications has lead to the development of devices that allow loading broadband signals on optical carriers. Therefore new generation MWP devices can manage RF signals with BWs up to tens of GHz.
- Easy tuneability: lasers and other devices, as optical filters, are easily tuneable thus it is conceivable, built radars with an excellent frequency flexibility so that radar parameters can dynamically be adapted to the current scenario.

The main advantages of RF signal distribution are instead:

- Low-loss and low-distortion propagation: these are fundamental properties of optical fibers, and among the reasons for their worldwide adoption for communications. These features can result extremely useful also for long–range signal distribution in radar networks, avoiding so the significant attenuation and bandwidth limitations of RF waveguides and cables.
- EMI immunity: this peculiarity of optical transmission can be clearly of uppermost importance for RF systems operating in harsh conditions, as, for instance, happens in a naval installation where multiple radiating systems must cooperate jointly.

2.2.1. Photonics-based RF generation and up-conversion

Conventional generation of RF signals is generally realized through multiple electronic up-conversion stages; each stage, as shown in Figure 2-6, is constituted by an electronic local oscillator (LO) followed by a band pass filter (BPF) with the function to select the up-converted signal and suppress the image frequency. Unfortunately, each up-conversion stage introduces a non-negligible phase and amplitude noise, due to phase drifts of the local oscillators and the nonlinearities of the active electronic mixers. Moreover, the phase stability of the LOs decreases as the RF increases and the tuneability of the above described generation scheme is rather poor.

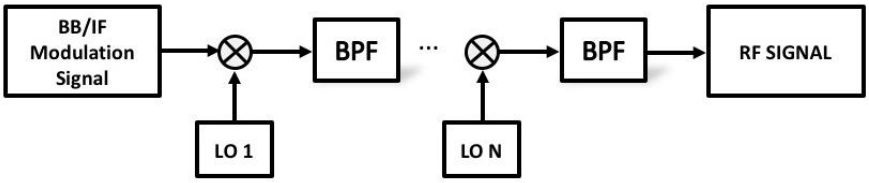

Figure 2-6: Conventional high frequency RF generation

Instead in Figure 2-7 a photonics based high frequency RF generation circuit is reported. It is based on the concept of heterodyning (i.e. detecting two laser signals in a photodiode). In this way a RF signal proportional to the square of the optical input fields is generated. Assuming that the two lasers emit ideal continuous wave optical signals, when they are coupled together and received by a photodiode (PD), the PD generates an electrical current (the RF signal) that can be expressed as the square of the two inputs:

$$S_{RF}(t) \sim [S_1(t) + S_2(t)]^2 \qquad \textbf{Eq. 2-1}$$

Neglecting the direct-current components and the components at twice the optical frequency, which are not detected by the PD, the above detailed formula recasts as follows:

$$S_{RF}(t) \sim A\cos(2\pi f_{RF}(t) + \Delta(\phi)) \qquad \textbf{Eq. 2-2}$$

Therefore, a RF signal is generated, whose frequency, f_{RF}, is equal to the detuning between the two lasers (i.e. $f_{RF}=f_{laser2}-f_{laser1}$).

If one of the two lasers is modulated, for example, with an external optical modulator (EOM), driven by a modulation signal at BB or at IF, as it is the case for Laser 1 in Figure 2-7, the heterodyning process transfers also the modulation to the RF carrier frequency resulting from the laser detuning. Since the optical communications field has brought to the market optical modulators with electro-optical bandwidths up to 40 GHz, photonics allows the generation of ultra-broad bandwidth RF signals with carrier frequencies up to 100GHz.

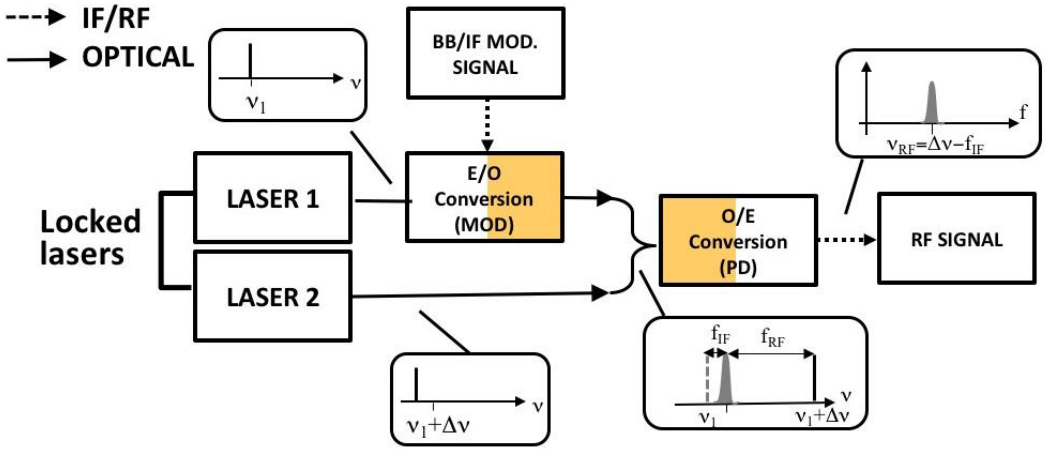

Figure 2-7: Photonics-based high frequency RF generation

A key parameter for an oscillator is phase stability (see paragraph 1.3). It has to be remarked that in the photonics-based scheme, the phase stability depends only on the reciprocal phase behaviour of the two beating optical signals, as can be noticed from the term $\Delta\phi$ in formula Eq. 2-2. From the equation it is evident that, if the two lasers have ideally no phase noise, then the optically generated RF signal has no phase noise as well. Unfortunately, lasers always have a certain amount of phase noise, and two independent beating lasers generate a RF signal with a phase term equal to the difference of the lasers phase noise processes, as expressed in Eq. 2-3:

$$\Delta_\phi = N_{\phi 1}(t) - N_{\phi 2}(t) \qquad \textbf{Eq. 2-3}$$

where $N_{\phi 1}(t)$ and $N_{\phi 2}(t)$ are the phase noise terms of the lasers involved in signal generation. However, if the two lasers are not independent, for instance, they have the same time-varying phase noise process $N_\phi(t)$ then the phase term is canceled, and a RF signal, ideally, free from phase noise can be generated. The action of forcing the two oscillators to have the same phase noise is possible in photonics and is referred to as phase locking.

The most common and effective techniques for obtaining phase locked lasers suitable to be used for photonics-based RF signal generation are: generation of phase locked lasers through RF modulation, injection locking (IL), opto-electronic oscillators (OEO) and Mode Locked Lasers (MLL). In the next section only MLLs are described, since this type of optical oscillators is employed by the first photonics-based radar described hereafter.

Mode locked lasers

MLLs generate pulses by forcing the modes of an optical cavity to have exactly the same phase (mode locking), so that the optical signal can be described as a sum of several cavity modes, all in-phase to each other, which gives as an output an optical pulse train at a repetition rate equal to the mode spacing. The optical spectrum of these lasers presents a large number of equally spaced modes, all with the same phase, and the spacing $\Delta\nu$ depends on the cavity length:

$$\Delta\nu = \frac{c_n}{L_{RT}} \qquad \textbf{Eq. 2-4}$$

with c_n equal to the speed of the light in the medium, and L_{RT} the round-trip length of the cavity (i.e. in case of a ring laser, L is the length of the ring; in the case of a linear cavity, L is twice the length of the cavity).

The basic scheme of a MLL ring cavity is reported in Figure 2-8: at steady state, a single optical pulse is circulating in the ring, and the saturable absorber (SA) lets the peak of the pulse pass with low attenuation. In other terms the saturable absorber modulates the attenuation of the cavity, forcing the modes to assume the same phase (i.e., all the modes are modulated by the saturable absorber in order to see a reduced cavity loss at the same instant). Finally, an optical coupler extracts a portion of the optical power to make it available to the end-user.

Starting from the base configuration described above, several architectural modifications can be implemented. For example, a piezo-activated tuneable delay can be inserted in the cavity to lock the MLL repetition rate to an external clock, and an optical filter can be inserted to force the MLL to oscillate in a specific spectral region.

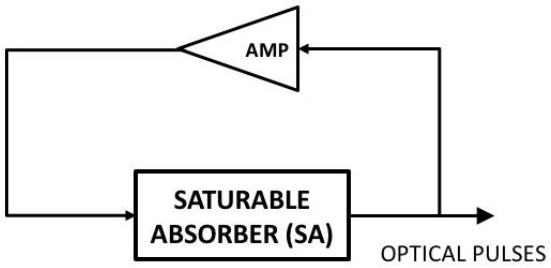

Figure 2-8: Basic scheme of a passive mode-locked laser

MLLs have demonstrated to have a good stability, therefore they have been largely proposed for the generation of RF signals. At difference to OEOs which ensure an excellent stability too, MLLs can generate virtually any RF signal with a frequency multiple of the repetition frequency [38], [39],[40],[41],[42]. It has to be underscored that all the RF signals generated by the same MLL are coherent with each other (i.e. they have exactly the same phase), and their phase noise shows the same behaviour. Clearly, since all the possibly generated RF signals are multiples of the RF signal at the MLL repetition rate (i.e. $RF_n = n \cdot RF$) the phase noise is multiplied as well. This is evident from the measures reported in Figure 2-9, where RF signals at 10, 20, 30, 40 and 50 GHz have been generated from a MLL at 10 GHz. Their phase noise shows the same shape, but the curves appear translated 6 dB for every frequency doubling [43][44].

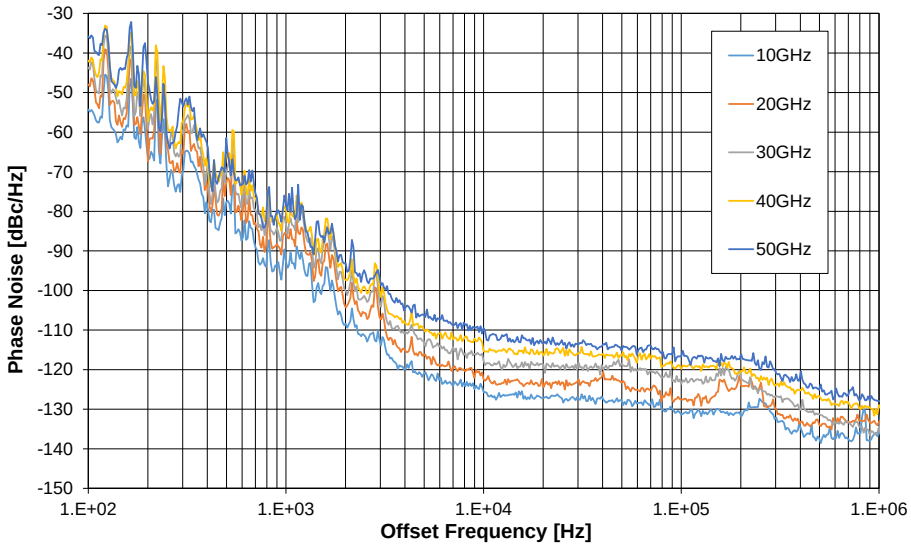

Figure 2-9: Measured phase noise of RF signals at 10, 20, 30, 40, 50 GHz generated by a regenerative fiber-based MLL at 10 GHz repetition rate

2.2.2. Photonics-based RF detection and down-conversion

The detection of RF signals in a software-defined way would require the availability of ADCs with an input bandwidth extending from DC to, at least, tens of GHz, with a consequently extreme fast sampling rate. Real time oscilloscopes are now available with an input bandwidth up to 100 GHz and a sampling rate as high as 240 GSps. Unfortunately, the architectural complexity required for reaching such high sampling rates limits the maximum SNR of the detected signals to about 30 dB, and as SNR has a huge variability, aforesaid signal dynamic is insufficient for the realization of a radar system. This explains why the detection of RF signals is still managed exploiting ordinary RF signal down-conversion followed by ADCs working at much slower sampling rates.

Figure 2-10 shows the conventional scheme used for a RF down-conversion. As for the RF up-conversion scheme, it exploits multiple stages, in order to move the detected signals into the bandwidth of the ADCs and each of these stages introduces phase and amplitude noise, so in general the total noise increases with the detected frequency. Moreover, this architecture is very frequency-specific, and allows a limited frequency flexibility.

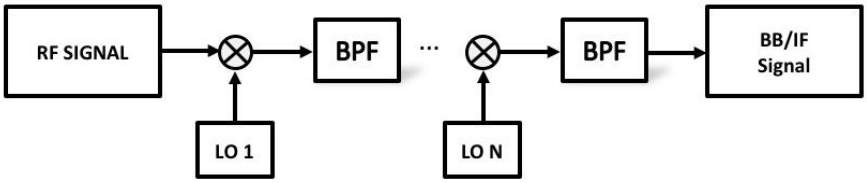

Figure 2-10: Conventional RF down-conversion scheme

The photonics-based RF detection leverages on the enormous electro-optical bandwidth of optical modulators, as the RF signal is first translated to the optical domain and then back to the electrical domain. This operation facilitates the acquisition and digitization which can be realized with more flexibility and precision [45][46][47][48][49]. Several different schemes for RF receivers have been proposed so far. In the following, we review the main techniques, used by the photonics-based radar demonstrators, described later on in this Chapter.

Photonics-based RF detection

The detection of RF signal can be implemented through direct down-conversion exploiting, as for up-conversion, the concept of heterodyning [50], combined with the generation of phase locked laser lines, as schematically sketched in Figure 2-11 a).

Instead in the scheme, reported in Figure 2-11 b), every comb laser (i.e. mode of the MLL) is modulated by the RF signal, generating multiple sidebands at f_{RF} from each optical carrier. Sidebands are detuned f_{IF} from the closest comb line thus, when the entire spectrum is detected with a photodiode, all the modulation sidebands beat with its closest laser line, generating a contribution at f_{IF}. All these contributions sum up in phase at the output of the PD, giving the direct down-conversion of the detected RF signal to IF. Finally, after a low-pass filter, the down-converted signal can be digitized by an electrical ADC. This operation is therefore a form of under sampling, translated in the photonics domain. With this approach, RF signals with carrier frequencies up to 40 GHz and bandwidth of 20 MHz have been correctly digitized by ADC working at 100 MSps with an effective number of bit (ENOB) equal to 7 [51].

The optical pulses from a MLL can also be used as a high-rate sampling system to directly sample broadband and high-frequency RF signals [52][53][54]. With respect to the direct RF sampling, this technique shows a larger RF input bandwidth, and can reach a much lower sampling jitter (which is the limiting factor in electronic ADCs). As an example, Figure 2-11 c) shows the sampling scheme used in [54][55]: the optical sampling occurs when the RF signal modulates the MLL pulses; from that moment, the amplitude of the modulated pulses represent the optical samples

(the sampling rate and its jitter are given by the MLL). In order to digitize the samples by means of precise ADCs, the optical samples are then demultiplexed in the time domain in a fast optical switching matrix, in order to parallelize the samples to lower sample trains that are synchronously digitized by precise electronic ADCs. The acquired samples must then be interleaved in the digital domain. With this technique, a signal-to-noise ratio higher than 42dB has been demonstrated for signals at 40 GHz [55].

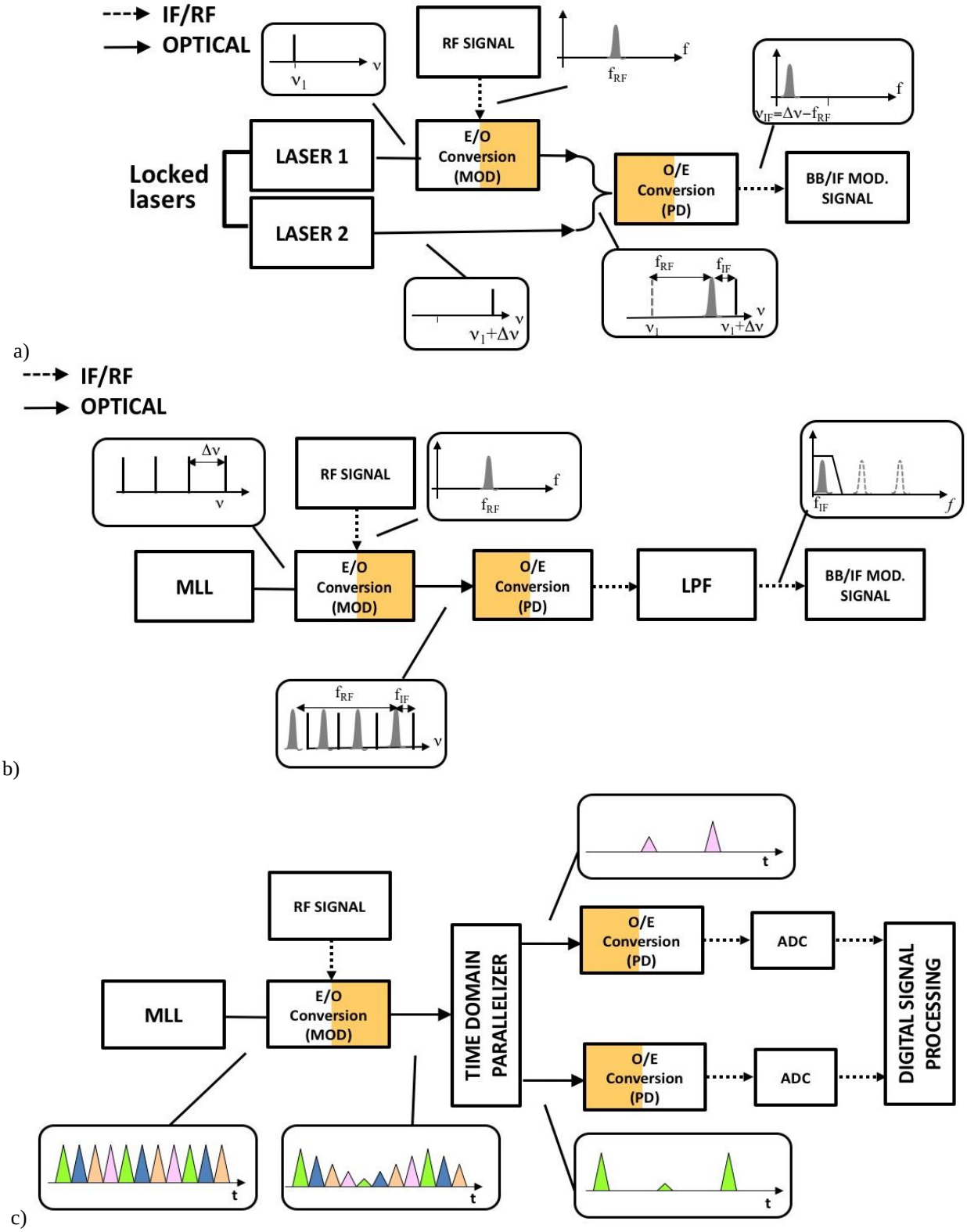

Figure 2-11: a) RF detection based on photonic down-conversion. b) RF detection based on photonic under sampling. c) RF detection based on photonic sampling and time-demultiplexing

2.2.3. RF filtering

Filtering is an essential operation performed on RF signals. While electronic filtering is a simple function for low frequency signals, when the signal frequency increases it becomes a complex issue. In fact, filters parameters such as the flatness, the edge steepness, and the out-of-band rejection worsen as the central frequency becomes higher. Therefore, high-performing cavity filters become necessary to get the desired features at high frequencies: usually aforesaid filters are not tuneable and accordingly the resulting system flexibility is reduced.

On the other hand, tuning a filter in the photonic domain is much easier. This is evident as the optical filter selects an electromagnetic field (i.e., the optical signal) with a carrier frequency close to 200 THz, whereas the maximum required filter tuning range for microwave photonics applications extends for few tens of GHz. Subsequently, the required tuneability is only a small fraction (in the order of 10^{-4}) of the filter central frequency.

The generic scheme of a microwave photonic filter is sketched in Figure 2-12. The RF signal is first transferred to the optical domain modulating a laser. Accordingly, the spectrum of the modulated optical signal is composed by the carrier and the modulation sideband, which is a copy of the RF signal translated to an optical frequency. An optical tuneable filter then is used to select a portion of the modulation sideband. After re-introducing the optical carrier and heterodyning, the photodiode gives back the RF signal filtered by the optical filter.

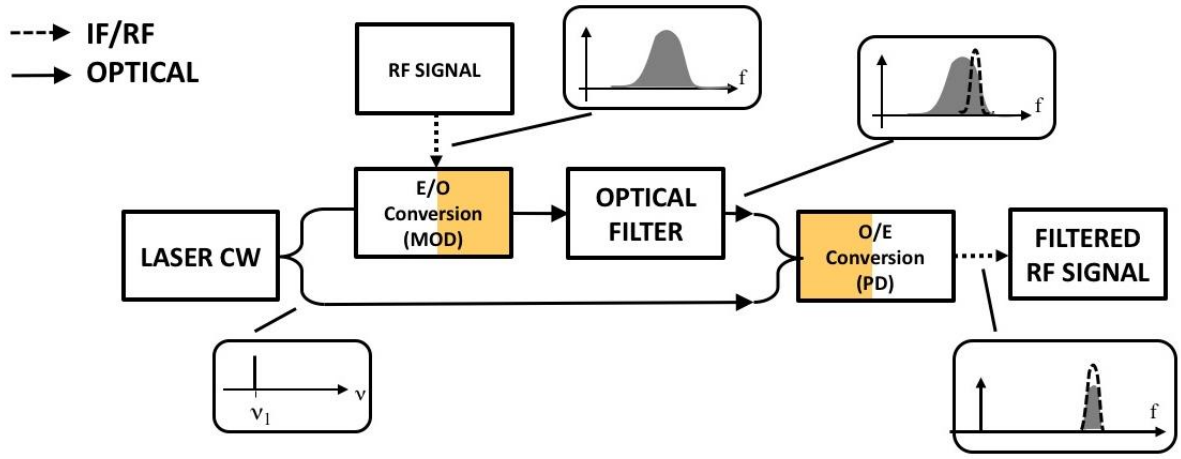

Figure 2-12: Basic scheme of a microwave photonic filter

The optical filter can be easily tuned changing some of the physical characteristics in the filter structure. This can be done, for example, exploiting the thermal effect (with tuning times in the order of few hundreds of microsecond) or changing the wavelength of the laser, while keeping fixed the filter position.

The equivalent shape of the microwave filters follows the shape of the optical filters. Therefore, the optical filter must fulfil the filtering requirement of the RF application. Unfortunately, except for tuneability, which is a simple feature to achieve with photonics, several other requirements can be very challenging for an optical filter, considering that its central frequency is in the order of 200 THz, for instance, realizing a filter with a bandwidth of 1 GHz corresponds to a quality factor of about $2*10^5$.

To reach the technical specifications required for RF systems, microwave photonic filters are commonly implemented by interferometric structures [56]. Typical examples of optical filters are Fabry-Perot (FP) filter, fiber Bragg gratings (FBGs) or microring resonator (MRR), which consists of a waveguide in ring configuration, that is weakly coupled to a feeding waveguide as sketched in Figure 2-13.

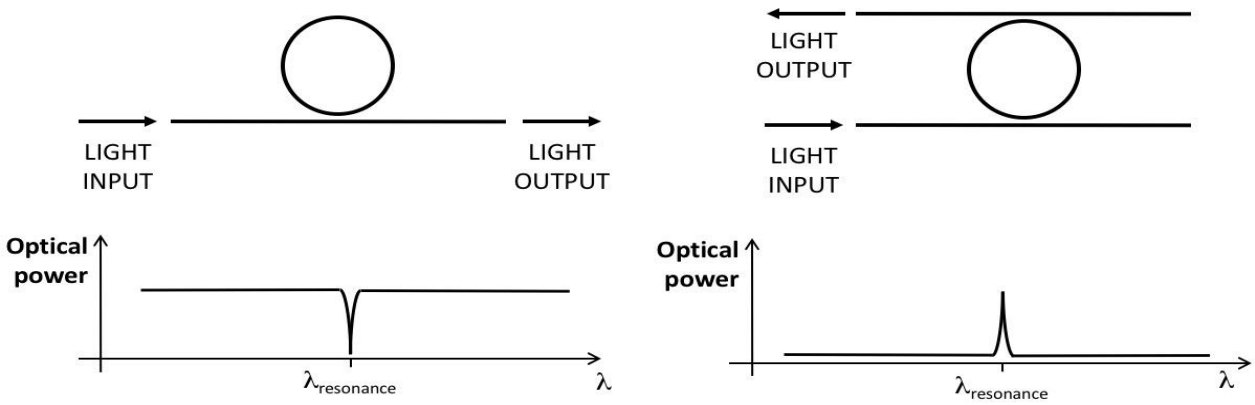

Figure 2-13: Scheme of a MRR: a) in all-pass filter configuration, and b) in add/drop configuration

Moreover, it is opportune point out that filter structures, formed by cascades of MRR, can be quickly reconfigured, implementing software defined microwave filters that can tune in frequency and also in shape [57]. This is a unique feature that photonics can bring to radar applications, and could open up completely novel and unexplored possibilities.

2.2.4. RF signal distribution

Once the RF signal is loaded on an optical carrier, it becomes convenient exploit optical fibers for an efficient signal distribution, implementing so a RoF system. In fact, fiber transmission as said, is broadband, low-loss (as low as 0.2 dB/km, while RF waveguides have a propagation loss in the order of several dB/m), and immune to EM interference (EMI free). Moreover, optical fiber allows transporting the RF signal over long distances without significant distortions, which could be fundamental, for example, in order to remote control antennas in a multistatic radar system. Finally, optical fiber is light, small, and flexible, and therefore can be installed in complex and narrow sites, such as unmanned vehicles or satellites.

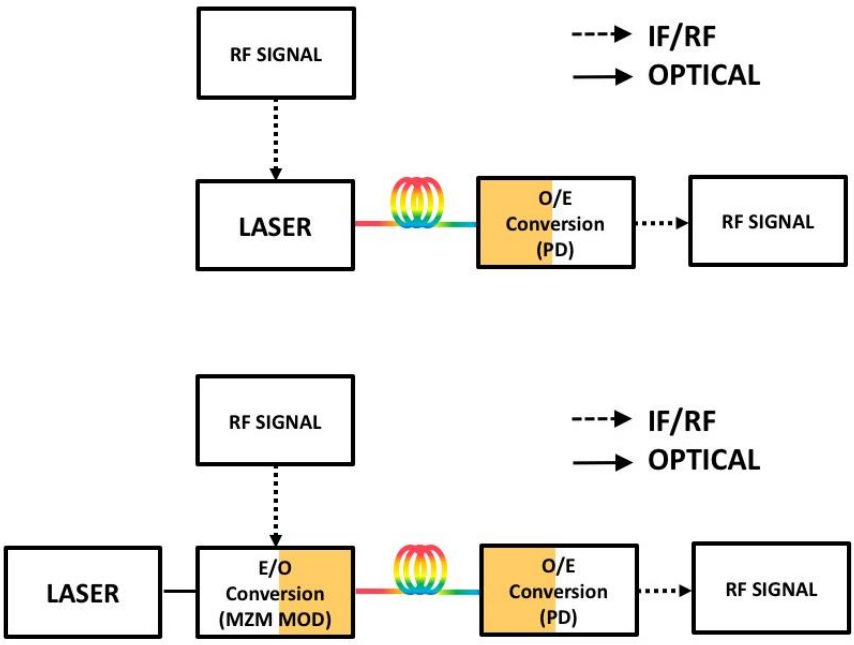

Figure 2-14: Scheme of a RoF system based on: a) direct modulation (top); b) external modulation (bottom)

The basic RoF scheme is implemented by modulating the RF signal on a laser, sending it through optical fiber, and detecting it directly with a PD at the other end of the fiber link. This technique is called intensity modulation-direct detection (IMDD). The amplitude modulation can be realized either by direct modulation of the laser source Figure 2-14 a), or by external modulation through a Mach Zehnder modulator (MZM), as shown in Figure 2-14 b).

Up to now the standard gain range in the order of <-20dB in case neither electrical nor optical amplification is used. The achievable gain in directly modulated links is limited by the laser modulation efficiency (which ranges around 0.1-0.3 W/A). In externally modulated links, instead, the gain can be increased acting mainly on the laser power, and on the modulator's on–off switching voltage (usually referred to as Vπ). By exploiting high power lasers and low Vπ modulators, modulation efficiency higher than 10 W/A and positive link gain were reported [58].

The noise figure (NF) strongly depends on the link gain and on the intrinsic noise characteristics of the components (e.g., the laser relative intensity noise, RIN). If a low noise amplifier is introduced in the scheme before the link, a significant improvement in NF and a positive link gain can be obtained. Signal-to-noise ratio is affected by the noise sources present in the link, mainly the RIN of the laser, the shot noise of the PD, and the thermal noise. At high photocurrents (i.e., at high optical powers), the SNR turns out to be limited by the laser RIN characteristics.

Signal distribution for MIMO radars

A different approach for signal distribution, convenient for coherent spatial distributed MIMO operations consist of a distributed up and down-conversion. Essentially the electro-optic and opto-electronic signal conversions can be managed through the up- and down-conversion schemes, already described respectively in paragraph 2.2.1 and 2.2.2, with the shrewdness to place the modulator inside the master node and a wideband photodiode at the remote antenna site for up-conversion and vice versa (the modulator at the antenna site and the photodiode inside the master node for down-conversion).

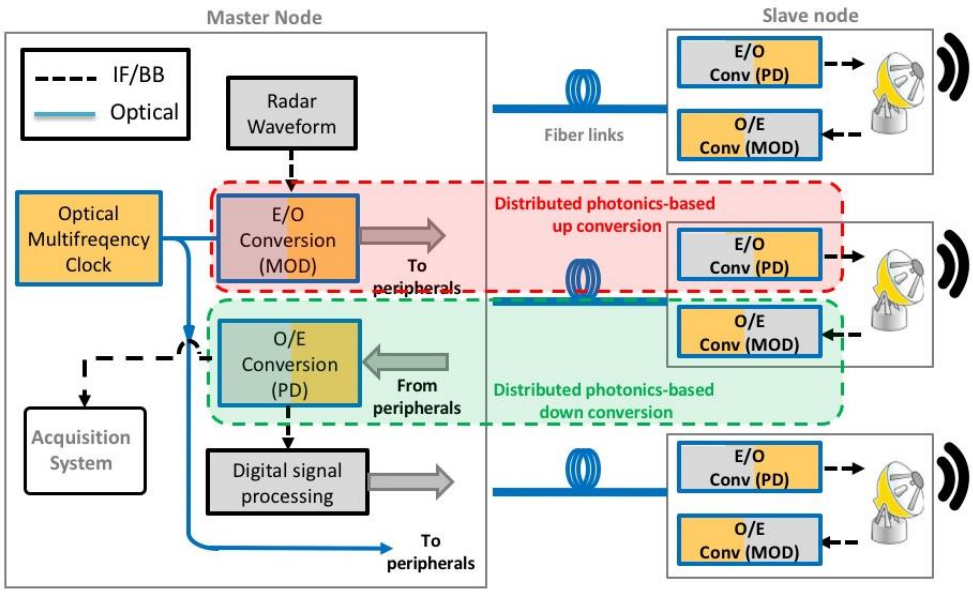

Figure 2-15: MIMO radar signal distribution block diagram: distributed up/down conversion

This architecture, represented in Figure 2-15 has multiple positive implications. From a system perspective the proposed solution leads to a significant simplification of slave nodes at the antenna sites, since optical sources are all kept at the master node in charge to send the unmodulated optical carrier to the antenna through a dedicated optical fiber link. The resulting network coherence is also

increased as the same shared optical source can be exploited both for up and for down conversion. Finally, even though the master node and the slave node are far from each other, there is no detrimental repercussion on network phase stability. In other terms, the source has to guarantee a sufficient stability in the span of time that elapses between the transmitted and the received signal, exactly as conventional monostatic radars do. Instead, if a normal RoF system had been used in order to implement coherent detection the oscillator would have to ensure a sufficient phase stability in the span of time that elapses between the transmitted and the received signal plus the amount of time to distribute the signal from the master node to the remote antennas in transmission and from the remote nodes to the master node in reception.

The proposed signal distribution scheme requires 3 optical fiber links for each slave node: an optical fiber for up-conversion, one for down-conversion and an additional link to send the optical source to all modulators to consent coherent down-conversion. A further simplification can be obtained replacing aforementioned links with a single link, exploiting wavelength division multiplexing (WDM). WDM consent, in fact, to sent multiple signals on a single O.F. multiplexing them in wavelength domain.

Due to a fading effect induced by chromatic OF dispersion, for signal distribution in radar applications a single side band (SSB) modulation rather than a double side band (DSB) modulation is preferable. In this way considering to use also optical amplifiers, such as semiconductor optical amplifiers (SOA) or erbium-doped fiber amplifiers (EDFAs), distances as long as several hundreds of km can be covered [59].

2.3. MICROWAVE PHOTONICS ENABLING TECHNOLOGY FOR MIMO RADARS

In Chapter I MIMO radars have been introduced and, in particular, configurations with widely separated antennas have been examined, which can considerably enhance radar detection. Here benefits and obstacles hindering the implementation of MIMO spatial distributed radar networks are briefly recap.

Following benefits descend immediately, when multiple radar echoes backscattered by the same object and acquired in spatial diversity are available for data processing:

- Diversity gain;
- Slow moving target detection/accurate Doppler estimation;
- Super-resolution (enhanced angular resolution)
- System advantages (see section 1.6.4).

However, to collect above listed benefits several issues need to be overcome, which are hard to solve in the RF domain. The most demanding issues are summarized below:

- Efficient signal distribution over long distances;
- Systems capable to deal signals with high fractional BWs;
- Signal coherence (low PN in generation and coherence maintenance during signal distribution);
- Generate orthogonal radar waveforms to transmit.

As seen in paragraph 2.2, photonic generation and detection schemes, permits the generation of signals with low PN (i.e. MLL beating) and can manage high fractional BWs. In addition, photonic distribution ensures an efficient signal distribution (low attenuation) and coherence preservation (low distortion). Besides orthogonality between transmitted signals can be easily achieved in time diversity (TDM) by the means of optical delay lines (ODL): a cheap but effective way to realize ODL is

through fiber spools with an opportune length. In conclusion, issues hard to solve in the RF domain are successfully coped in the optical domain. Hence photonics can undoubdtedly be considered, an enabling technology underpinning the development of coherent MIMO radar networks with widely separated antennas.

2.4. PHODIR: THE FIRST PHOTONICS-BASED RADAR

The aim of this paragraph is to furnish evidence that the use of MWP solutions for radar applications is a concrete reality and not a questionable innovation, which still needs to be further investigated. Though the disruptive potential of photonics is evident, an initial resistance to innovation is comprehensible. However, as the components necessary to realize the circuits described in previous paragraphs are off the shelf components commonly used for telecommunication purposes, it is expectable that the realization of new generation photonics-based radar systems is destined to spread rapidly.

Here we describe, in fact, the first photonics-based radar ever built developed in 2012 at TECIP Institute of Sant'Anna School in Pisa. The demonstrator has been realized combining some of the MWP techniques described above, taking so advantage of the peculiar features brought about by photonics.

At this point, it is opportune to underscore that, despite a significant research activity has interested specific photonics-based functionalities, only few examples of complete photonics-based RF transceivers have been presented so far, in particular related to radar [60][61] as well as for wireless communication [62][63].

The basic idea of the PHODIR project ('Photonics-based fully digital radar') project, which has led to the realization of the first photonic radar demonstrator, is to use a single MLL for the implementation of both the RF generation and the sampling of the received signal. In the work reported in [60] a MLL with a repetition rate of 400 MHz has been used as the master clock of the photonic transceiver governing the radar system in X-band (9.9 GHz). The radar block diagram, sketched in Figure 2-16 [60] shows clearly that the same MLL is exploited for signal up and down-conversion as well as for signal sampling.

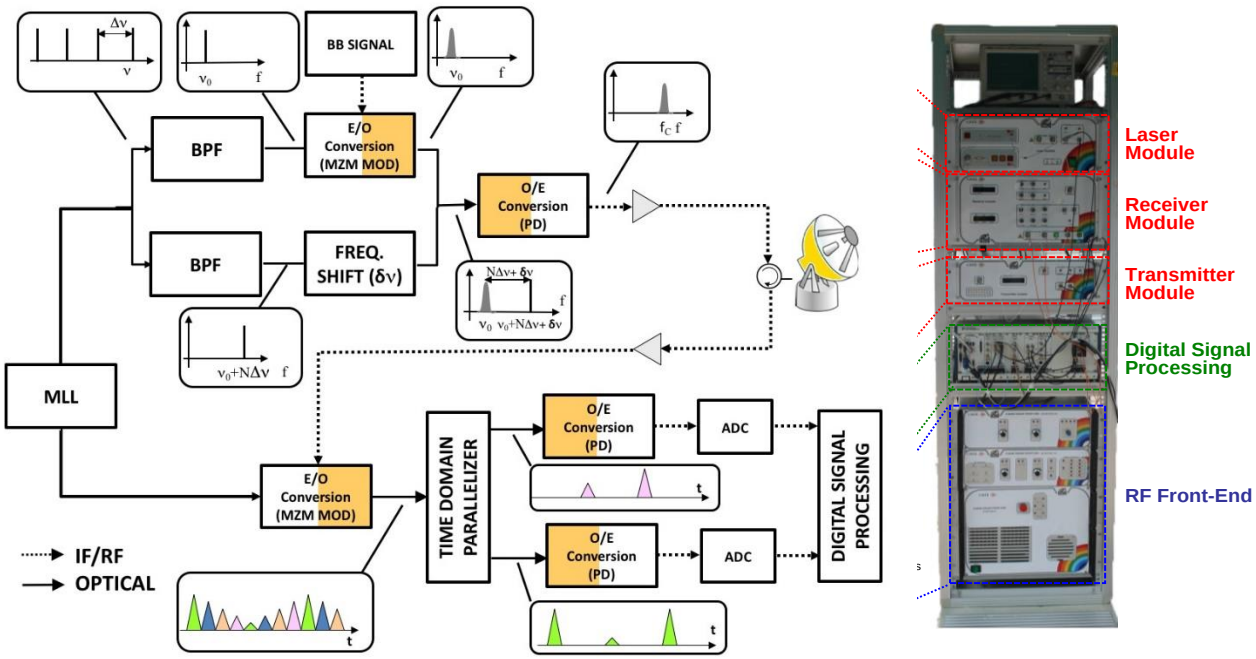

Figure 2-16: Architecture of the first photonics-based radar PHODIR (left) and a picture of the demonstrator (right)

The radar signal to transmit is digitally generated at base band frequency (BB), and fed into the RF port of an electro-optical modulator to modulate the MLL output providing so, as already discussed in paragraph 2.2.1, a signal up-conversion from BB to RF. From sampling theory, it is well known that the sampling frequency has to be, at least, twice the BW of the signal and that, in addition, the carrier frequency should not be a multiple of the sampling frequency. For this reasons, in the generation stage before heterodyning, one of the two modes of the MLL is shifted in frequency by a factor $\delta\nu$. In this way the final carrier frequency *fc* after beating in the PD is shifted by the same amount fulfilling so both above specified requirements. In fact, as already seen in par 2.2.1, the beating products generated by the detection process in the PD create a replica of the radar waveform at frequency *fc* , which corresponds to the frequency shift between the modulated and unmodulated MLL mode (i.e. $fc=\nu_0+N\Delta\nu+\delta\nu-\nu_0$).

In the receiving stage, as discussed in paragraph 2.2.2 , optical sampling, based on photonic sampling and time-demultiplexing, is performed. In particular, the optical pulses from the MLL are amplitude-modulated in a MZM, driven by the received RF signal. The resulting modulated signal is then parallelized in a serial-to parallel converter into multiple lower-rate sample streams. Finally, by the means of multiple electronic ADCs, having low sampling frequency and high precision, the RF signal can be effectively digitized.

Parameter	**Photonics-based transceiver**	**State of the art**
Carrier frequency	< 40 GHz (direct)	Direct < 2 GHz (up-conversions > 2 GHz)
TX Signal jitter[4]	< 15fs	Typical >20 fs
TX SNR	> 73dB/MHz	> 80dB/MHz
Signal BW	200 MHz	< 2GHz
RX Effective number of bits (ENOB)	> 7 for carrier frequency < 40GHz	< 8 for carrier frequency < 2GHz
RX Sampling jitter	<10fs	Typical >100fs

Table 2-1: Performance of the PHODIR transceiver and RF transceivers at the state of the art

The performance of the photonics-based transceiver presented in [60] are summarized in

Table 2-1 and are compared with the corresponding performance ensured by electronic transceivers at the state of the art. As can be noticed from the table, the photonic approach shows a significant advantage especially in terms of frequency flexibility, and in the precision of the digitization for any input frequency up to 40GHz, enabling so the software-defined radio concept.

The PHODIR demonstrator has been tested in different scenarios, proving the clear profit attainable when MWP solutions are extended to radar systems [64][65].

In 2015 a field trail has been run in collaboration with GEM, an Italian radar manufacturer specialized in naval radars, and a direct comparison with a commercial naval radar, SeaEagle, working also in X-band, has been done [65]. In Table 2-2 the main radar parameters related to the PHODIR demonstrator are compared with those of the SeaEagle commercial radar system. Due to a

[4] integrated on the interval [10kHz-10MHz]

higher noise figure the PHODIR demonstrator has a lower sensibility as the minimum detectable signal (MDS) is equal to -87 dBm while the commercial radar ensures -90 dBm. On the other hand, the PHODIR transceiver consents a greater waveform agility and potentially the implemented architecture can manage any carrier frequency as well as signals with a larger bandwidth, provided that different RF BPF, see Figure 2-16, are employed.

Parameters	***SEAEAGLE***	**PHODIR**
Peak Power	100W	50W
RF frequency (MHz)	9300÷9500 (step)	9880÷9920 (continuous)
Signal bandwidth	40MHz	40MHz
Noise figure	5.5dB	8dB
MDS	-90dBm@40MHz BW	-87dBm@40MHz BW
Max range	48NM (cargo target)	18NM (cargo target)
Pulse width	50nsec÷93µsec	0.2÷10µsec
PRF	350÷2500Hz	1÷12KHz
Modulation format	Chirp	Any

Table 2-2: Main PHODIR radar parameters

Although the PHODIR radar is only a demonstrator, while the SeaEagle is a fully developed product from the trials effectuated emerges that both systems have similar performance. For this reason, it is expectable that, in future, a fully refined photonics-based radar can easily outperform a conventional RF radar system in a maritime scenario.

2.5. MULTI-BAND PHOTONICS-BASED RADAR

The PHODIR single-band system has been upgraded in 2015 with a second front-end in the S-band for dual band functionality, exploiting the signal coherence provided by photonics-based signal generation. This new prototype has been named PANDORA (Photonics-based dual-band radar), and has been first characterized in a controlled environment [66] and afterwards tested in 2016 in a real environment scenario at the facilities of the CSSN Naval Research Centre in Livorno.
PANDORA leverages on the capability assured by a photonics-based signal generation by the means of MLL optical oscillator to generate and simultaneously detect multiple RF signals on different RF bands. Furthermore, since all RF signals are generated by the same MLL, they are all intrinsically phase locked to each other. Conversely, realizing an equivalent system employing RF technology would require a duplication of all circuits for each desired band. Instead the photonics-based approach consents to share several optical devices for both radar bands.

In Figure 2-17 the modified functional block diagram is sketched: the multi-band RF generator and the multi-band RF receiver both exploit the same MLL. A DDS provides simultaneous multiple signals at different intermediate frequencies (IF_i), which are sent to a MZM modulator followed by a

PD for signal up-conversion. As can be noticed from inset D in Figure 2-17, at the output of the PD, the multiple IF signals have generated multiple RF signals at different frequency bands. At this stage multiple pass band RF filters centered at different central frequencies (CF_i) can select the desired RF signals to transmit.

Similarly, the RF receiver block combines the multiple received RF echoes with the optical signal from the MLL, obtaining the simultaneous down-conversion of each detected RF signal to its original IF (see inset F) and finally a single ADC simultaneously digitizes all the received signals.

The scheme presented in [67] also includes a broadband front-end, constituted by a power amplifier at the transmitter side and a preamplifier at the receiver side. The broadband front-end supplies the multi-band photonics-based transceiver with the necessary frequency flexibility.

The field trials conducted at the facilities of the Naval Research Centre CSSN ITE in Livorno have essentially assessed the detection capability of the dual band radar in single band operation mode. Furthermore, thanks to the signal coherence provided by the innovative photonics-based signal generation scheme, a synthetic BW, given by the sum of the single BWs in X and in S band, has been demonstrated, ensuring so an enhanced range resolution with respect to the resolution achievable in single band operations.

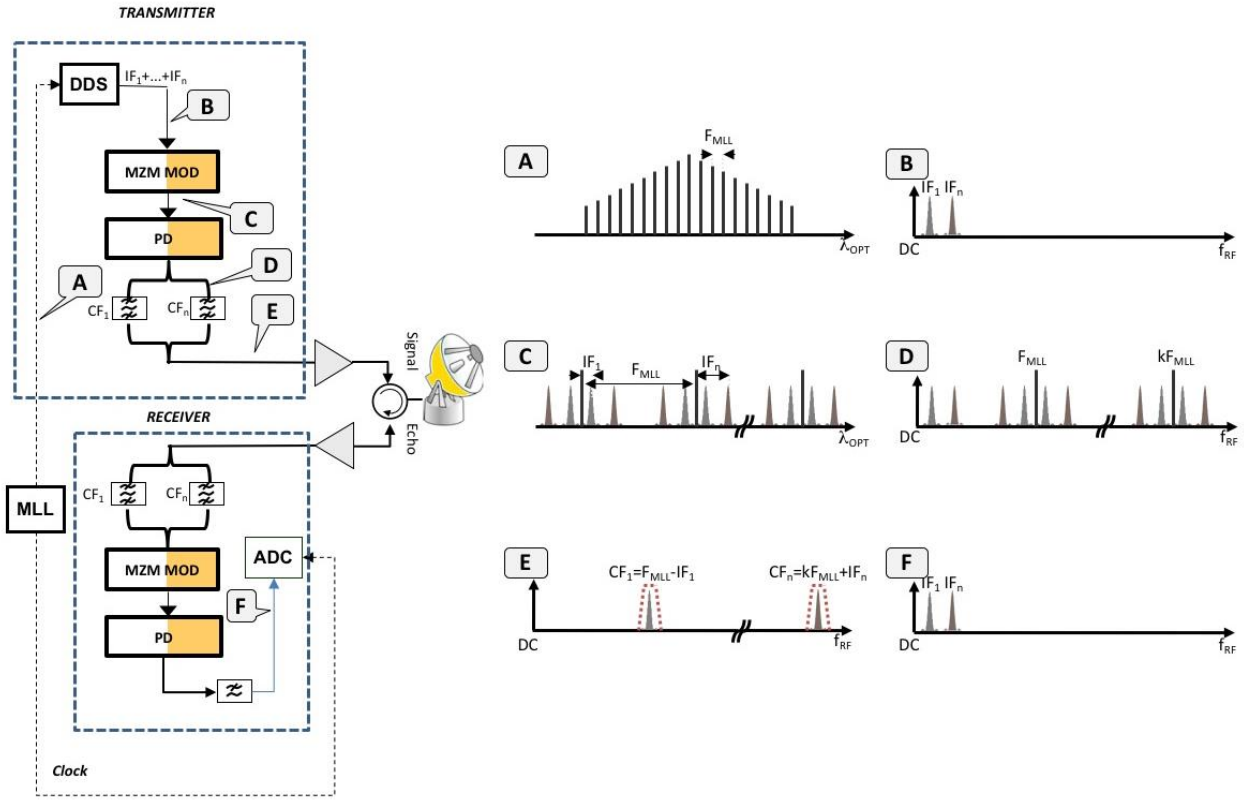

Figure 2-17: PANDORA multi-band photonics-based radar: block diagram and spectral outputs at different stages

3. SIMULATIVE ANALYSIS

MIMO radars are radar networks with multiple transmit and receive antennas which can jointly process all received signals thanks to the use of multiple orthogonal waveforms in transmission. Among MIMO radars the most promising are MIMO radars with widely separated antennas mostly for their enhanced cross-resolution capability and their aptitude to detect low RCS and stealth targets. However, unsolved issues in the RF domain have hindered, until now, the development of those kind of radar networks. As discussed in Chapter II, photonics compared to traditional RF technology has some valuable feature and could represent the enabling technology for the development of new generation MIMO radars. In the present Chapter in total 3 scenarios are examined with the primarily intent to individuate a suitable MIMO architecture for each analysed situation and verify that the expected performances are appropriate for the final applications. In particular, the first two scenarios are similar as they are both related to maritime scenarios, whereas the last scenario presented refers to an automotive application.

As already highlighted, despite various application fields have been addressed, the whole numerical analysis conducted is incremental, meaning that whenever possible outcomes found before are extended to the remaining situations. In this way, the focus can move to different aspects that can be covered in detail. Essentially, the main purpose for the coastal scenario, which is the first handled in chronological order, is to comprehend how MIMO parameters impact on the final radar cross-ambiguity function. Instead, the purpose of the naval scenario is to assess first of all if a MIMO solution can satisfy the power budget requirement and then find an optimal installation solution in terms of antenna geometry and network architecture. Ultimately, an automotive case is examined with the intent to verify if a MIMO approach can be adopted also for this emerging application field, ensuring the desired angular resolution with few antenna elements. In particular, the automotive scenario, in addition, to aspects already covered, investigates the possibility to employ a multiband MIMO radar system. Indeed, leveraging also on frequency diversity, a superior side lobe suppression can be guaranteed than the suppression ensured by minimal MIMO geometries that satisfy strict cost constraits. This analysis is extremely practical, especially when on board (on a car) systems are considered, as the baseline is small, indicatively 3 m long. For this reason, it is possible conduct indoor experiments using exactly the simulated baseline, avoiding so to implement down-scaled experiments as, for instance, has been done for the outdoor costal scenario field trials reported in Chapter IV.

It has to be underscored that all outcomes, exception made for those concerning the radar power budget analysis realized specifically for the naval case, have been obtained using the self-developed MIMO scenario simulator, introduced in Chapter I.

3.1. COASTAL SURVEILLANCE SCENARIO

The first analysed scenario is a coastal surveillance scenario (e.g. a port surveillance radar). Simulations have been executed considering as input parameters those individuated appropriate for the EU project Roborder. The main purpose of aforementioned research project, in fact, is to realize a multistatic radar network for border security, capable to ensure an efficient surveillance of land borders as well as sea boundaries and, in particular, port infrastructures preventing possible terroristic attacks. Although different aspects are examined for each scenario, we remark that design indications attained for a specific application are relevant also for all remaining scenarios discussed in this Chapter. Therefore, for sake of simplicity, during the dissertation some aspects are not examined when they have already been addressed previously and a plausible relationship has been individuated. In other words, the analysis is incremental in the sense that the outcomes of a scenario are extended to different situations. This is extremely convenient since the focus is directly put on salient features without starting the analysis from the beginning.

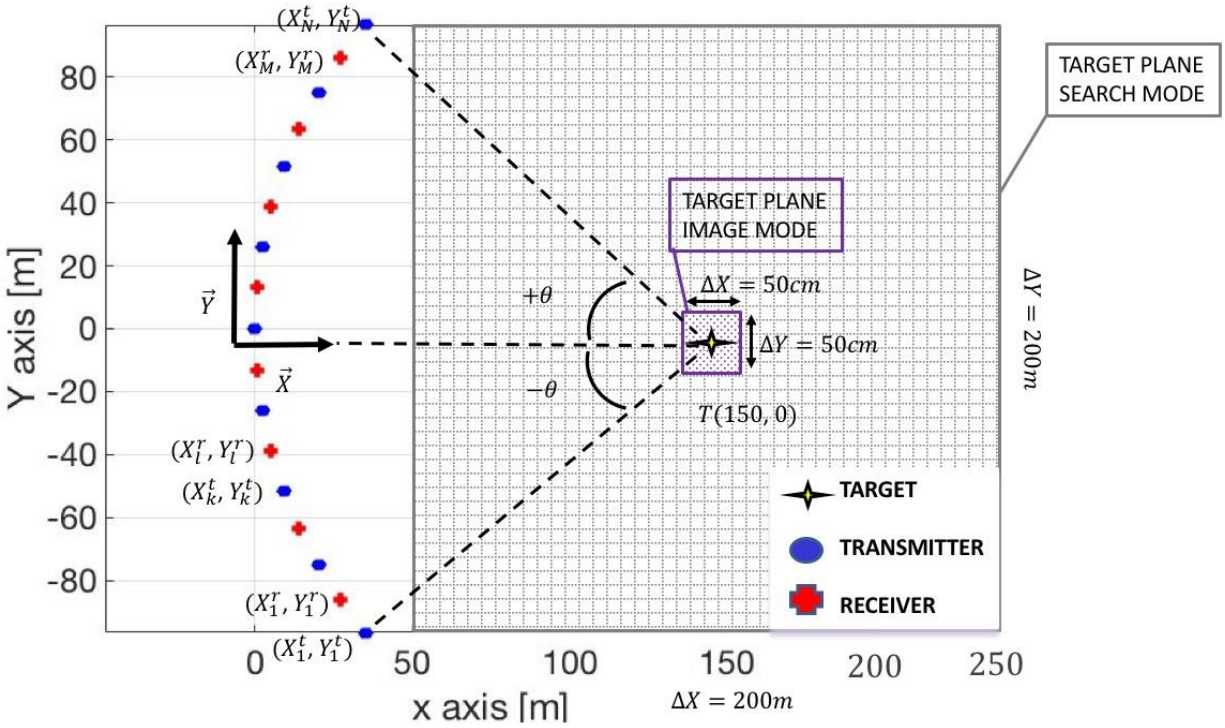

Figure 3-1: Coastal reference scenario

As shown in Figure 3-1, the considered coastal scenario has an antenna configuration of M transmitters and N receivers. All antennas are equidistant to the target, at a distance of 150 m from the target, which is placed in position T = (150 m, 0 m). The k-the transmitter and the l-th receiver antennas are located at angles θ_k^t and θ_l^r, respectively and all antennas occupy an angular sector of 2θ.

In the reference case, M=9 transmitters, N=8 receivers, and θ= 45° are considered. The M receivers and the N transmitters, identified by the coordinates (X_l^r, Y_l^r) and (X_k^t, Y_k^t) respectively, are always assumed to be equally spaced on the angular sector. The target is an ideal point scatterer and is assumed to be in the Field of View of all antennas (e.g. using horn antennas).
The reference signal parameters initially used to carry out simulations are listed in Table 3-1.

Parameter	Value
Carrier freq.	10 GHz
Signal Modulation	Pulse/Chirp
Bandwidth	1GHz
PRF	1KHz
Radar Cross Section (RCS)	0 dBsm
Channel SNR	18dB
Target distance	150m

Table 3-1: Coastal scenario simulation reference parameters

3.2. RESULTS COASTAL SCENARIO SIMULATIONS

Here we present the results reported in [33] emerging from the analysis of the above described coastal scenario. Since the finality is to understand how involved radar parameters impact on the detection performance of a MIMO radar system, multiple simulations have been run changing the antenna geometry as well as the radar waveform. In particular, after assessing the superiority of coherent over non coherent operations, a side lobe and a main lobe analysis have been effectuated changing the antenna disposition with respect to the reference scenario. Later on the received signals have been modified in terms of SNR and fractional bandwidth in order to determine the impact on the side lobe intensity of the MIMO radar cross-ambiguity function. Last but not least consequences of oscillator phase noise have been evaluated.

3.2.1. Coherent MIMO processing superiority

Three point scatterers have been simulated with the intent to evaluate the improvement resulting from a coherent processing with respect to a non coherent processing. Assuming the reference configuration, depicted in Figure 3-1, and the reference parameters listed in Table 3-1, first a coherent processing on an area of 200 m x 200 m using a high resolution cell and following a non coherent processing (in this case no rephasing has been executed and the exponential term in Eq. 1-11 has been set to 1) on the same area above detailed have been effectuated. From the comparison of the two radar cross-ambiguity functions determined, which are represented in Figure 3-2, the superiority of coherent MIMO processing is manifest. Phase information consents to considerably reduce detection ambiguity, in fact, in coherent mode, as shown in Figure 3-2 (right), all three simulated point scatterers are correctly individuated by point like areas on the range cross-range map. Conversely, when a non coherent processing is applied instead than narrow point like areas, elliptical crowns can be clearly noticed on the detection map, see Figure 3-2 (left). Those individuate all points of the plane with a total distance from the transmitter and the receiver (i.e. the foci of the ellipses) equal to the simulated target total path distance (i.e. transmitter-target plus target-receiver distance). Each ellipse is associated to a specific bistatic channels and targets are spotted where multiple ellipses intercept. Substantially, the non-coherent output coincides with the result achievable through a multilateration data fusion algorithm [33]. In conclusion, when also phase information is available the simulated scatterers are individuated with a much lower ambiguity and, as is evident, observing the range cross-range maps depicted, that a threshold detector would detect much more false alarms (FA) in a non coherent case than in the corresponding coherent case.

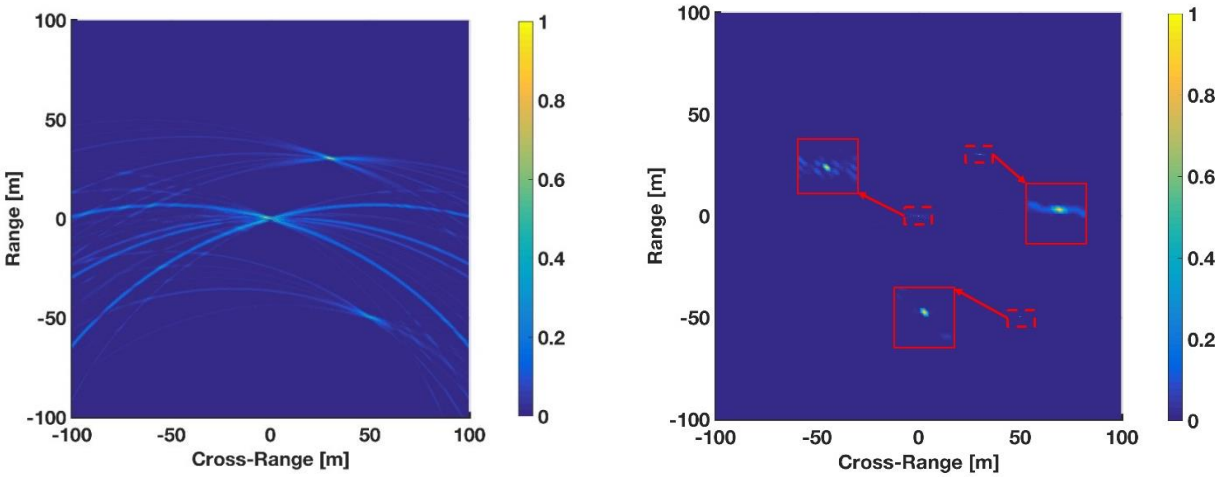

Figure 3-2: Search mode cross-ambiguity function comparison between non-coherent (left) and coherent (right) MIMO processing

3.2.2. Side lobe analysis

From MIMO theory it is well known that the number of antenna elements and their disposition have a deep impact on the radar cross-ambiguity function. Consequently, 8 simulations have been effectuated changing the number of antennas from the 9 TXs x 8 RXs reference geometry down to a minimal 2 TXs x 1 RX configuration in order to better understand the detrimental effect on side lobe amplitude. An ideal point-like scatterer target has been simulated in T and an image mode processing has been performed on an area of size 0.5 m x 0.5 m selecting a 3 mm x 3 mm resolution cell. In Figure 3-3 the cross-range profiles of the 8 simulations done decreasing the reference configuration step by step by one transmitter and one receiver are represented. It can be noticed how the side lobes, located initially at +/-18 cm from the center, where the target has been simulated, first start to increase in intensity and then further side lobes arise until the target barely can be distinguished as side lobes have reached the same amplitude associated to the main lobe.

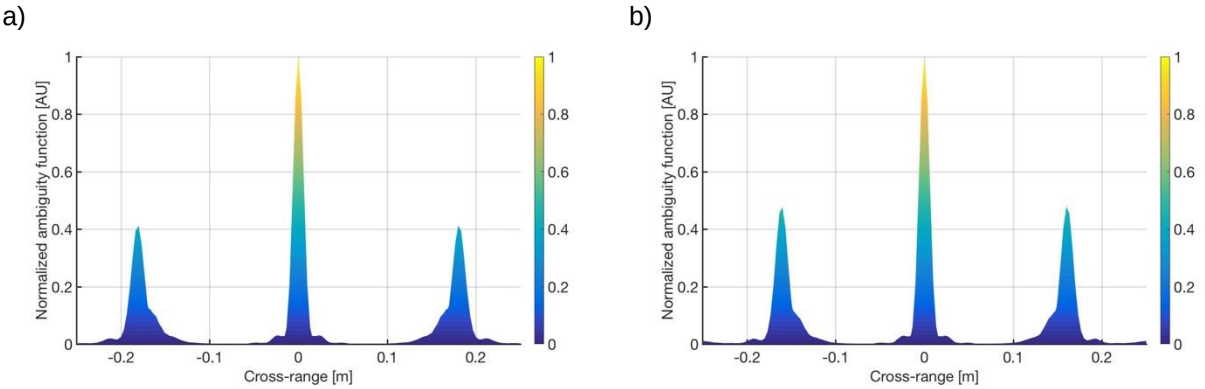

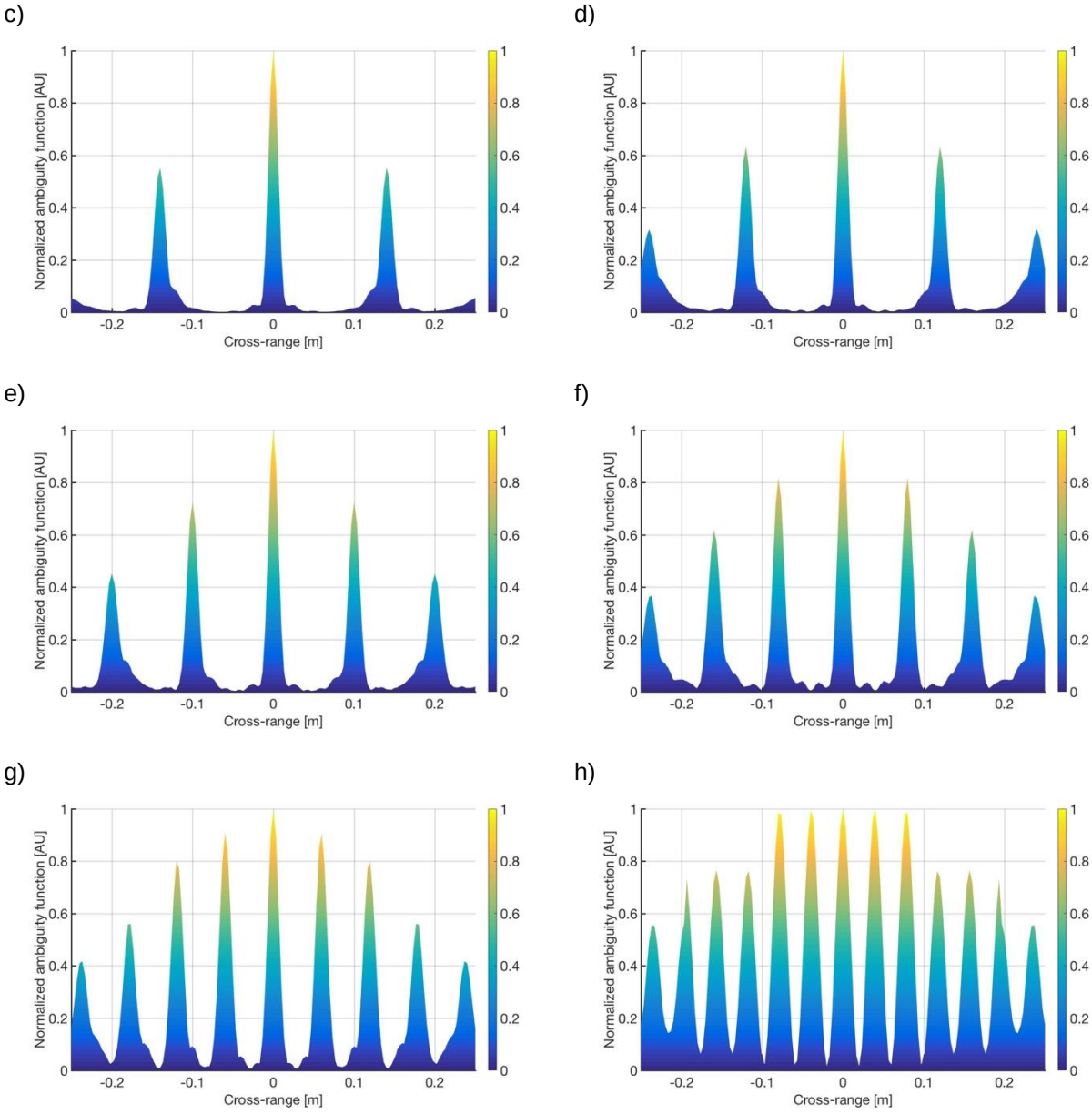

Figure 3-3: Image mode cross-range profile for a 9TXs x 8RXs (a), 8TXs x 7RXs (b), 7TXs x 6RXs (c), 6TXs x 5RXs (d), 5TXs x 4RXs (e), 4TXs x 3RXs (f), 3TXs x 2RXs (g), 2TXs x 1RXs (h) MIMO configuration

3.2.3. Main lobe analysis

After the side lobe analysis, another interesting aspect is to examine what happens to the main lobe as the MIMO configuration is altered. For this purpose, a target located in position T has been simulated and image mode with the same parameters used for the previous conducted side lobe analysis has been implemented. However, this time the number of elements (i.e. 9 TXs x 8 RXs) is fixed and instead their angular distribution has been changed. In total 4 simulation were done with $\theta = \pm 45; \pm 90; \pm 135; \pm 180$ (see Figure 3-1) the outcomes are reported in Figure 3-4. As the antenna geometry has a higher variability along the range dimension the impact on the range pattern is more evident than on the cross-range pattern. Thus at difference to the previous analysis it is opportune to show the evolution of the main lobes associated to the range profiles.

Observing aforementioned figure it is possible infer that the half power beam width (HPBW) of the main lobe decreases from 2.3 cm to 0.44 cm as the angular coverage increases from $2\theta=90°$ to $2\theta=360°$.

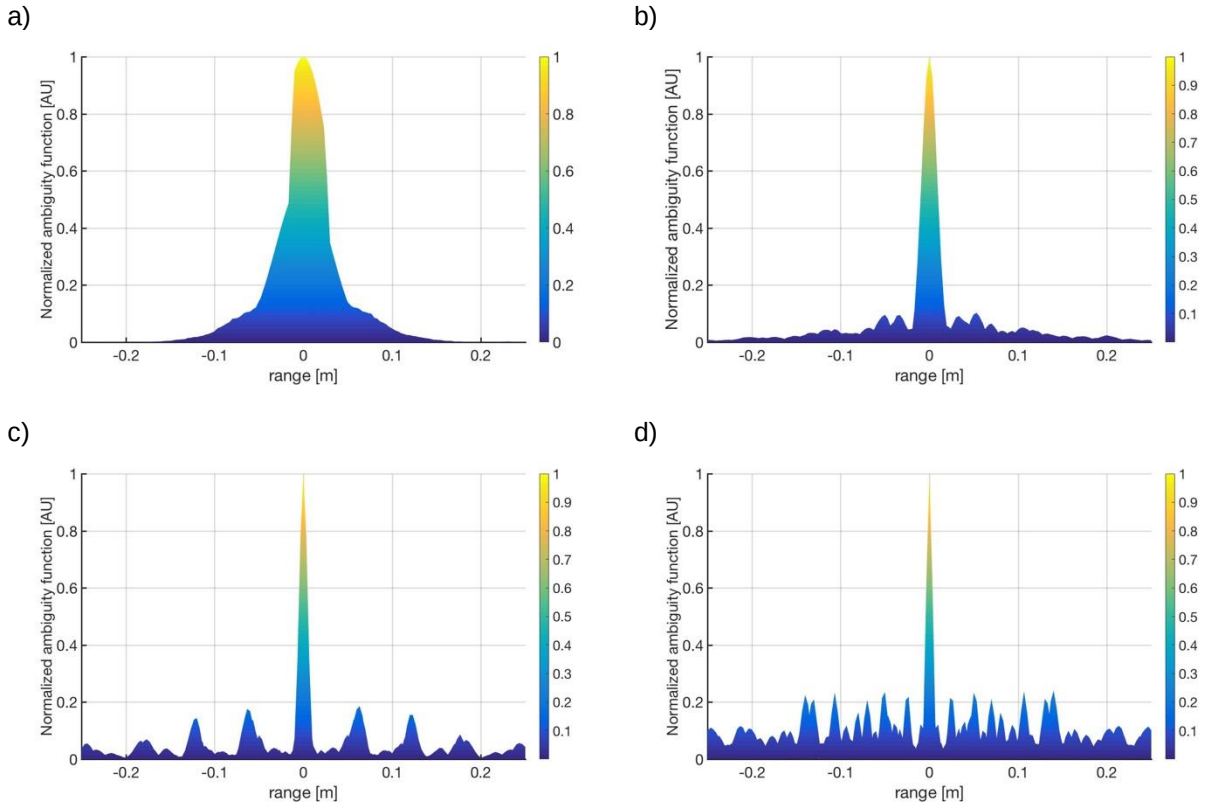

Figure 3-4: Image mode range profile 9TXx8RX for angular distribution ϑ=+/-45° (a), ϑ=+/-90° (b), ϑ=+/-135° (c), ϑ=+/-180° (d)

3.2.4. Resolution capability

The most interesting benefit that a MIMO coherent approach can provide is an enhanced cross-range resolution. In order to test this feature 2 point scatterers, distant 3 cm one from each other along cross-range, have been simulated. The cross-range profile in Figure 3-5, obtained in image mode, demonstrates that the 2 simulated targets, despite the fact that the signal BW is 1GHz to which corresponds a range resolution of 15 cm, can be clearly distinguished. Accordingly, the remarkable resolution capability of a coherent MIMO radar with widely separated antennas is definitively confirmed.

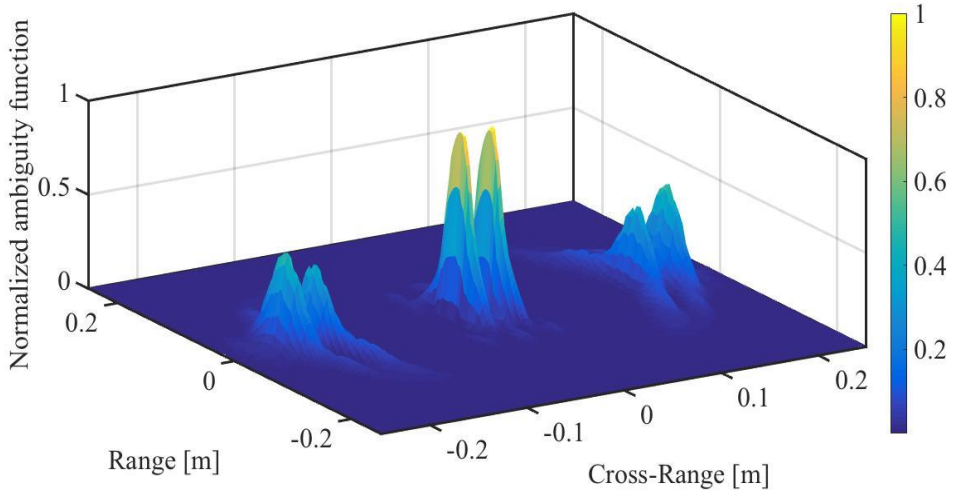

Figure 3-5: Image mode range cross-range map for 2 simulated targets 3 cm faraway in cross-range

3.2.5. Radar waveform fractional bandwidth

According to sparse array antenna theory, presented in paragraph 1.6.4 , in [30] it has been demonstrated that when the antenna dimension is large enough so that $Q<L/\lambda$, the PSLR is better as the Q factor decreases, where Q is the inverse of the fractional BW. Consequently, once fixed the carrier frequency, the PSLR decreases as radar waveforms having larger signal BWs are employed. Simulations done modifying the BW of the transmitted signal in the range [10MHz:1GHz] confirm this behaviour. As the curve plotted in Figure 3-6 reveals, indeed, the side lobe extinction ratio (1/PSLR) increases from less than 3 dB until almost 8 dB when the signal BW becomes 10% of the carrier frequency (BW/fc=0.1).

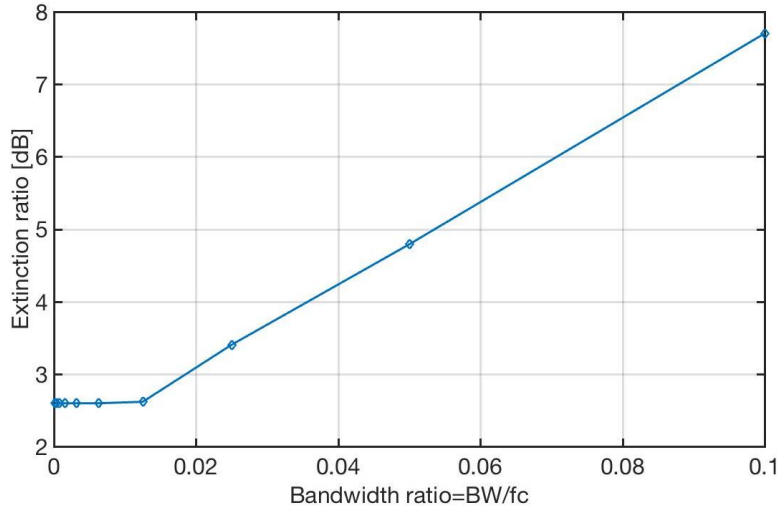

Figure 3-6: MIMO cross-ambiguity function extinction ratio in function of radar waveform BW ratio

3.2.6. Signal Phase Noise

Finally, the effect of oscillator phase noise has been evaluated. For this purpose, an object, constituted by 3 point-like scatterers, has been simulated and the received MIMO signal matrix has been computed assuming first, in ideal case, that signals are not afflicted by any phase noise and, afterwards, adding a strong random phase shift contribute, causes by limited oscillator stability. Processing in high resolution image mode the simulated data set not corrupted by random phase shifts all three scatterers are successfully detected (see Figure 3-7). Instead in case of a high PN contribute, as reported in Figure 3-7, one out of three targets (i.e. the target placed in position T3=(-0.1m, 0.1m)) is not detected anymore. In conclusion, this proves that phase instability can significantly worsen detection performance. Therefore, during the design process this element has to be carefully weighed and an appropriate oscillator has to be selected in order to guarantee an acceptable overall detection performance.

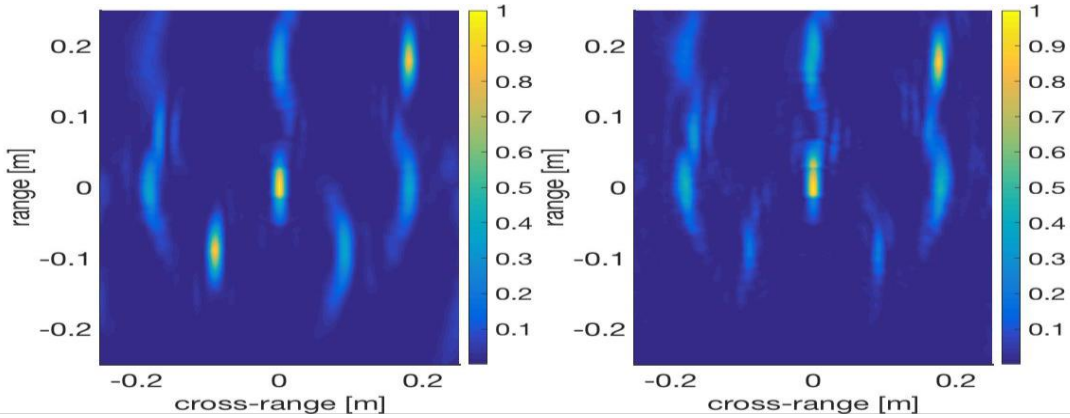

Figure 3-7: Image mode 3 targets detection in absence of PN (left) and in presence of high PN (right)

3.3. NAVAL SCENARIO

The simulative outcomes presented in the following are related to a naval scenario which presents several analogies with the coastal scenario discussed above in terms of assumptions made on the target as well as on the radar waveform, since substantially both are related to maritime applications. However, a major difference has to be found in the baseline constraints that are less challenging for a coastal radar network than they are for a naval one. In the naval case, in fact, the basic idea is to place MIMO antenna elements on the ship hull. Consequently, without considering at the moment further installation impediments, a direct implication is that the maximum baseline length has to be lower than the ship length. Furthermore, unlike conventional monostatic radars, where the shape of the ship is almost irrelevant, except for the antenna installation height, for MIMO radar networks with widely separated antennas, the antenna geometry is an essential aspect. As, in fact, results from the analysis carried out for the coastal scenario the antenna geometry impacts directly on the PSLR of the cros-ambiguity function, on the resolution capability (main lobe amplitude) and, eventually, on overall radar performance.

For this reason, in order to get realistic results, the assumption is to install the candidate MIMO system under investigation on a new generation frigate and that both transmitting and receiving antennas can be placed without any restriction on the whole ship hull. Besides for sake of simplicity, the assumption is to design a naval surveillance radar since this implies a clear simplification. In fact, in this case a MIMO 2-D model rather than a more complex 3-D model is sufficient, as all naval targets are on the see level (i.e. elevation=0°). From the analysis of the coastal scenario emerges that a longer baseline (larger spatial antenna distribution) entails a narrower main lobe of the MIMO cross-ambiguity function. Thus, observing the ship profile of a typical frigate, as the one depicted in Figure 3-8 the best installation options, since they ensure the longest baselines possible are listed in the following :

- CASE A: all antennas are placed on a straight line under the main deck at a height of 5m;
- CASE B: all antennas are placed on a straight line on the upper decks at a height of 12m.

Each use case has its advantages and drawbacks. A higher installation would be preferable since this consents to get a higher optical horizon value as will be discussed in next paragraph. Unfortunately, while for CASE A we can dispose the antennas on the whole ship length, indicatively 130 m long, CASE B presents some constraint, as sensors can be placed only on specific areas of the considered ship, ensuring so a baseline which is almost 70 m long. If we assume a reference system with center in O, placed half way of the maximum ship length, the two options identified recast as follows:

- CASE A: all antennas are at 5 m above the water line and in the interval [-65m: 65m];
- CASE B: all antennas are at 12m above the water line and lay in the interval:
    - BOW= [8m: 28m]
    - STERN= [-42m: -8m];

In Figure 3-8 the two alternative options are shown.

Figure 3-8: Naval scenario possible installation options suitable for a frigate

3.3.1. Optical horizon & Target Visibility

The two identified use cases, are both characterized by an antenna installation height, which is considerably lower, than the usual installation height of an antenna associated to a conventional monostatic radar (indicatively 20 m). Therefore, our analysis starts from a factor which is generally overlooked in the design process of a radar system: the evaluation of the optical horizon and the maximum target visibility.

Once fixed the antenna height h_B and the target height h_L both expressed in [m], applying the approximated formula in Eq. 3-1, the maximum target visibility D_{BL} expressed in [Km] can be calculated.

$$D_{BL} < 3.86\left(\sqrt{h_B} + \sqrt{h_L}\right) \qquad \textbf{Eq. 3-1}$$

The above reported inequality includes also the atmospheric refraction phenomenon. Otherwise the coefficient 3.86 in Eq. 3-1 would be equal to 3.57 which implies that without atmospheric refraction the theoretical target visibility is slightly smaller than in the previous case. Exploiting the same formula, just considering a target height of 0 m above the see level (hL = 0m) the optical horizon can be determined. In fact, the optical horizon is defined as the maximum distance at which an object at 0m above the see level can still be seen.

Typically, for a ship the antenna height, h_B, can assume values in the range between 0 m (i.e. if we install the antenna in correspondence of the ship waterline) to the maximum constructive height. For a frigate, it is reasonable to assume that this parameter can vary in the range [1m: 20m]. In Table 3-2 we show how the choice of the installation height impacts on the optical horizon and on the maximum detectable range, supposing a target height equal to 5m.

Both options result sub-optimal if we compare them to a conventional monostatic radar where the single TX/RX antenna is at 20 m above the waterline (i.e. at the top of the mast). However, from Table 3-2 results that for case A the optical horizon is about 9 Km and the maximum detectable range 17 Km. Instead for use case B, since antennas are placed at 12 m, those values increase and become respectively 13 Km and 22 Km. Aforementioned values apparently inadequate, at first glance, are acceptable, especially if we compare them with the optimal solution (optical horizon 17 Km and maximum detectable range 26 Km).

hB [m]	hLmin [m]	OPTICAL HORIZON [km]	MAXIMUM DETECTABLE DISTANCE [km]
5.00	5.00	8.63	17.26
12.00	5.00	13.37	22.00
20.00	5.00	17.26	25.89

Table 3-2: Optical horizon and maximum detectable range (assuming a target height of 5m above sea level) for different antenna installation heigths

3.3.1. Power Budget Analysis

For the power budget study, based on the results obtained from the previous analysis, it is reasonable to assume that the transmitted power (P_T) has to detect a 30 Km distant target. Higher values are useless, due to the fact that earth curvature hinders to spot targets, which are further away than the maximum detectable distance.

For MIMO radar networks, since the multiple transmitter-receiver combinations realize multiple bi-static channels, it is more convenient to use the bi-static expression of the well known radar equation reported in Eq. 3-2 :

$$SNR = \frac{P_T G^2 \sigma N G_{PC} \lambda^2}{(4\pi)^3 N_0 R^4 L} \quad \textbf{Eq. 3-2}$$

which becomes:

$$\mathrm{SNR} = \frac{\mathrm{P_T G_T G_R \sigma_B N G_{PC} \lambda^2}}{(4\pi)^3 \mathrm{N_0 R_T^2 R_R^2 L}} \quad \textbf{Eq. 3-3}$$

where:

SNR is the signal to noise ratio;

P_T is the radar peak power;

G_T and G_R are respectively the antenna gain in transmission and reception;

σ_B is the bi-static radar cross section;

N is the number of pulses which can be integrated;

G_{PC} is the compression gain, equal to Ti*B;

λ is the carrier wavelength;

N_0 is the spectral power density of noise at the input of the receiver;

R_T and R_R are respectively the target distance from the transmitting and receiving antenna;

and L are the specific loss factors for the radar system in exam.

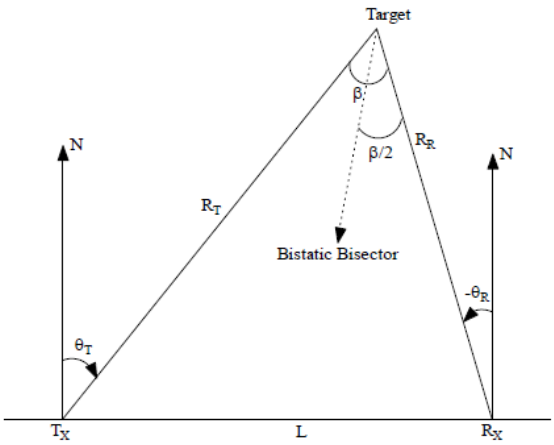

Figure 3-9: Bi-static radar geometry

The bi-static expression of the radar equation differs from the mono-static formulation in two points. First, a bi-static RCS value has to be considered rather than a monostatic RCS, in addition, as schematically shown in Figure 3-9, the antenna-target distance is different if we consider the TX-target path (R_T) or the target-RX path.

However, it has to be observed that in the worst case, namely in case the target is at the maximum distance (R=30 Km), even if the baseline, where the transmitters and the receivers are located, is 130 m long the bi-static angle β is only some mrad large. Thus $R_T \approx R_R$ and the RCS, σ_B, can be well approximated by the monostatic RCS, σ , cause all transmitters and receivers observe the target with the same observation angle. Thanks to this simplification, also the four Swerling target models are certainly valid.

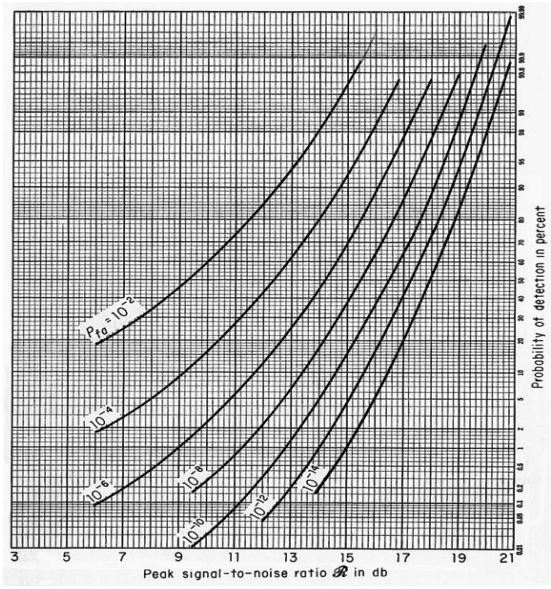

Figure 3-10: Single pulse detection characteristic for a fluctuating target type dominant plus Rayleigh (Swerling III) [68]

From Figure 3-10, applicable when the received signal has unknown phase and amplitude and the density distribution probability of the target RCS is type dominant plus Rayleigh, which is the most appropriate if we consider a naval target, we find out that to achieve the standard detection performance (P_D =80% and P_{FA} =10^{-6}) the signal to noise ratio has to be, at least, 18 dB (SNR=18dB). Moreover, under the assumption to use a coherent train of pulses, the SNR increases by a factor N, number of integrated pulses, without undergoing any integration loss (L4 =0dB). Otherwise, for an

incoherent train, under the assumption that the target is dominant plus Rayleigh fluctuating from scan to scan (Swerling model III) depending on the number of integrated pulses, as shown in Figure 3-11, an additional integration loss (L4) needs to be taken into account and compensated to get the same performance achievable by a coherent radar system.

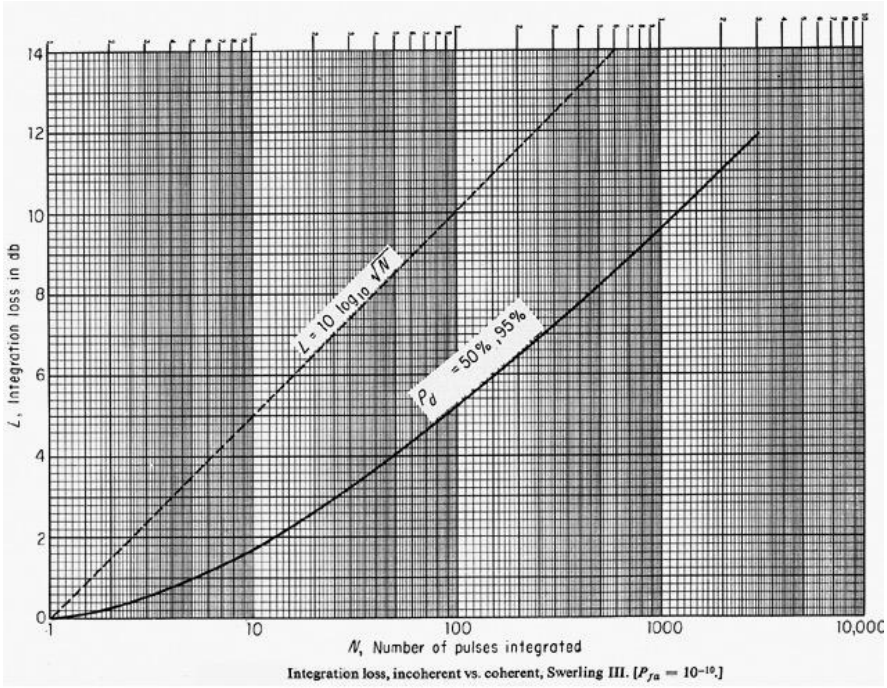

Figure 3-11: Integration Loss for a train of incoherent pulses Swerling III model [68]

For a MIMO configuration the number of integrable pulses N cannot be determined as usual by the relation T_{dwell} /T_r, where T_{dwell} represents the time that main lobe of the rotating antenna illuminates the target, and T_r the pulse repetition interval. A peculiarity of MIMO radar, in fact, is that all antennas can look at the target at the same time. Therefore, for a correct power budget design low antenna gains have to be considered. Conversely, it has to be reminded that this disadvantage can be partially compensated, thanks to the fact that the target can be illuminated for a longer amount of time. Unfortunately, even if the observation time, T_{obs}, is longer this does not mean that an infinite number of impulses can be integrated. While we illuminate the target with our MIMO architecture, the target, indeed, is moving, hence an adequate integration interval has to be found during which the target is assumed coherent. Of course this value depends heavily on the kinematic characteristics of the target. Luckily, naval targets are slow moving thus it is correct to assume a 100 ms long CPI, underscoring that this in a cautionary assumption, as results evident if we compare the given value with the standard Tdwell of a rotating antenna, typically, equal to 20 ms (e.g. assuming a rotating antenna speed of 50 rpm and -3 dB antenna aperture of 6°). Furthermore, assuming the values listed in

Table 3-3, when the compression gain is set to 1, we determine that the necessary signal peak power in transmission has to be about 50 W to detect at 30 Km with the given P_D and P_{FA} a target having a RCS of 100 m^2. Including also pulse compression, for instance, a chirp pulse with a compression gain equal to 100, the peak power drops to 0.5 W.

Although both power values are acceptable for a naval radar, it is opportune to relax the antenna gain requirement of 25 dB which is challenging for a low directivity antenna (i.e. horn or patch antenna). A trade-off solution could be to use 50 W of peak power along with 10 dB compression gain. In this way the two-way antenna gain can be reduced by 10 dB, so that both G_T and G_R can be reduced to 20 dB.

Parameter	Value
Radar Cross Section	100 m^2
Carrier Frequency	10 GHz (X-band)
Wavelength	0.03 m
Antenna Gain RX	25 dB
Antenna Gain TX	25 dB
Integrated Pulses (N)	200
Radar Range	30 Km
Compression gain	1:100
Total Loss L	9 dB
Receiver Noise Figure	4 dB
Pulse duration Ti	1 µs
Pulse rep. interval Tr	0.5 ms
Coherent Processing Interval	100 ms
Transmitted Peak Power	0.5 : 50 Watt
False Alarm Probability	10e-6
Detection Probability	80%
SNR (Dominant + Rayleigh @ PD=80% PFA=10^-6)	18 dB

Table 3-3: Naval scenario power budget radar parameters

Finally, it has to be remarked that the considered range of 30 Km is much higher than the maximum detectable range foreseen for case B (22 Km) and that the power budget analysis has been effectuated on a single channel. Conversely, a coherent MIMO radar exploits for target detection multiple channels (MxN), hence it is likely that even smaller targets with a lower RCS, can be detected at maximum radar range.

3.3.2. Signal choice

From the power budget analysis conducted, it it clear that a MIMO radar with the parameters, listed in

Table 3-3, is feasible for naval applications. The resulting peak power, in fact, is in the order of tens of Watt without pulse compression. However, to apply a coherent MIMO processing high fractional BWs should be used to mitigate the side lobe peaks (see paragraph 1.6.4) of the cross-

ambiguity function. The signal BW should lay between 0.1% and 1% of the carrier wavelength. Accordingly, for a 10 GHz carrier frequency, as in the present case, a radar waveform with a BW in the range from 10 MHz to 100 MHz is indicated. In order to preserve a good power budget, without increasing the peak power, pulse compression has to be employed. Diversely, the peak power raises, respectively, to 500 W and 5000 W, which are unacceptable values for the radar system in exam, as pulse duration has to diminish from initial 1 μs to 0.1 or 0.01 μs to satify above given BW requirement. In conclusion, a linear chirp pulse with a 100 MHz BW and a pulse wide of 1 μs seems to be a good compromise for the present application. Assuming to implement this modulation, the total compression gain is 100 and the necessary peak power is 50 W.
Once identified a suitable radar waveform for the MIMO radar network, the main radar parameters can be determined. Notoriously monostatic range resolution is given by:

$$\Delta r = \frac{c}{2B} \qquad \textbf{Eq. 3-4}$$

Instead for bi-static configurations Eq. 3-4 recasts as follows:

$$\Delta r_{bi} = \frac{\Delta r}{\cos(\frac{\beta}{2})} \qquad \textbf{Eq. 3-5}$$

where β is the bi-static angle formed by the TX-target segment and the target-RX segment, as shown in Figure 3-9. From Eq. 3-5 it is clear that the monostatic range resolution represents the lower limit for the corresponding bi-static range resolution. The signal specified above appears to be appropriate for the application under investigation, indeed, from Eq. 3-4 the monostatic resolution results to be equal to 1.5 m.

Although pulse compression technique allows to transmit even longer chirp pulses obtaining higher compression gains, this is not really indicated, because a negative implication is an increased blind range, which can be calculated through following relation:

$$r_{blind} = \frac{cTi}{2} \qquad \textbf{Eq. 3-6}$$

Accordingly, a pulse duration, Ti, of 1 μs causes a 150 m blind range, which results appropriate for the naval scenario in exam. Continuing the analysis of the parameters, reported in
Table 3-3, we notice a PRI of 0.5 ms, to which corresponds a non-ambiguous range of 75 Km, obtained thanks to ensuing relation:

$$r_{NA} = \frac{cTr}{2} \qquad \textbf{Eq. 3-7}$$

Nonetheless, the lower the PRI, the higher the number of integrable pulses, N, and the higher the available SNR, another aspect to carefully evaluate is range ambiguity. Decreasing the PRI to values close to the radar range can cause ambiguous echoes, hence 0.5 ms seems to be an appropriate value for this parameter.

3.3.3. Antenna selection

In the power budget analysis, antenna gain has been set to 20 dB as MIMO operations forsees that low directivity antennas are used so that all can simultaneously observe the area of interest. The purpose of the present section is to investigate some concrete solution and, among those which fulfil the given gain requirement, the most indicated for a naval scenario is identified.

As already emphasized, antenna gain is a weakness of the MIMO approach. In fact, unlike conventional radar systems, where the EM propagation attenuation (proportional to R^4 where R represents the target distance), can be compensated thanks to high antenna gains, MIMO radars cannot do the same, as low directivity antennas need to be employed so that, as said, all antennas can simultaneously "look" at the target. Based on this consideration, deliberately an intermediate antenna gain of 20 dB has been taken into account.

Aforementioned antenna gain, for instance, can be assured by horn antennas having a HPBM of about 20°. However, despite horn antennas are fit as they can provide the requested gain and directivity, a better solution, especially in system integration perspective, are patch antennas.

Patch antennas, in fact, can be better embedded in the ship's hull. Unfortunately, as can be noticed from Table 3-4 reporting the data sheet for a Sage model SAM-84 patch antenna, for this antenna class the gain is significantly lower. For instance, for aforesaid patch antenna the gain amounts to only 8 dBi. Consequently, multiple antenna elements can be organized in arrays, incrementing the total antenna gain to 20 dB, as assumed in the power budget analysis. In particular, in this case an array of 16 patch antennas is sufficient.

$$AF = e^{j(N-1)\frac{\psi}{2}} \frac{\sin(\frac{N\psi}{2})}{\sin(\frac{\psi}{2})} \qquad \textbf{Eq. 3-8}$$

In fact, for N=16, from the formula of the array factor reported in Eq. 3-8 we obtain that at the broadside (i.e. for ψ=0) the antenna gain is increased by 12 dB with respect to the case that only one antenna element is employed.

Parameter	Value
Frequency	8450 MHz
Gain	8dBi
HPBW	65°(vertical, E plane) x 65°(horizontal, H plane)
Power	50 W
Polarization	Linear

Table 3-4: Sage model SAM-84 patch antenna data sheet

A further analysis is beyond the scope of this study as the purpose of this paragraph, indeed, was to proof that low directivity antennas, like horn or patch antennas, are both valid solutions for the implementation of a naval MIMO radar network as they can provide appropriate antenna gains in X-band.

3.3.4. MIMO scenario simulations

The aim of simulations presented in the following is to individuate, given the signal obtained from the previous analysis, a feasible antenna architecture which can fulfil a fixed angular resolution requirement. At this point of the dissertation it is clear that an additional factor to consider carefully is the side lobe intensity of the cross-ambiguity function as higher side lobes have a detrimental effect on detection false alarm rate. Accordingly, in this phase of the design process a suitable antenna configuration, in terms of sensor numbers and geometry, has to be found that matches the resolution

requirement while suppressing adequately side lobes, so that an acceptable surveillance performance is safeguarded.

Once completed this step, the robustness of the architecture is tested introducing random errors in the sensor position and, eventually, different network topologies, supposing to use oscillators with variable stabilities, are evaluated. Thanks to aforementioned investigation, a potential HW architecture is identified, showing, at the same time, the importance of oscillator stability and network phase coherence preservation. All above listed design indications presented, hereinafter, have all been obtained using the MIMO 2-D scenario simulator presented in paragraph 1.8.

First of all, the desired angular resolution requirement, has to be set. This parameter along with all other relevant assumptions valid for MIMO simulations carried out are summarized in Table 3-5.

As reported there, an angular resolution requirement of 1 mrad has been set as desired design goal, which implies that at 5000 m, 2 objects distant 5 m one from another should be still distinguished. The assumption on the transmitted signals is to use a 100 MHz linear chirp waveform with a duration of 1 μs and a PRI of 0.5 ms. Prior to start the analysis it is advisable to verify that the problem is well formulated and the expectable PSLR values. From theory, recap in paragraph 1.6.4, the expected PSLR is proportional to ln Q (i.e. Q inverse fractional BW) in case $Q<L/\lambda$. As the fractional BW of the signal is equal to 100, whereas the sparse array has a dimension measured in wavelengths of about 200 or 400 depending on the considered concrete installation case (respectively case B and case A). Accordingly, a 20 dB side lobe suppression results achievable.

Furthermore, we assume that both targets have a cross-range dimension of 3 m so that the decorrelation condition in Eq. 1-3 is verified. Hence, MIMO theory with widely separated antennas can be applied.

Parameter	**Value**
Angular resolution requirement	1 mrad
Carrier Frequency	10 GHz (X-band)
Wavelength	0.03 m
Pulse type	Chirp
Signal BW	100 MHz
Pulse duration Ti	1 μs
Pulse rep. interval Tr	0.5 ms
Coherent Processing Interval	100 ms
Case A	BASELINE=[-65m:65m] HEIGHT=5m
Case B	BASELINE STERN= [-42m: -8m] BASELINE BOW= [8m: 28m] HEIGHT=12m
Target distance	5000 m
Target cross-range dimension	3 m

Table 3-5: MIMO naval scenario simulation parameters

The considered naval scenario is schematically sketched in Figure 3-12 and, as shown there, the MIMO detection statistic is calculated on an area of 100 m x 100 m around the simulated target position.

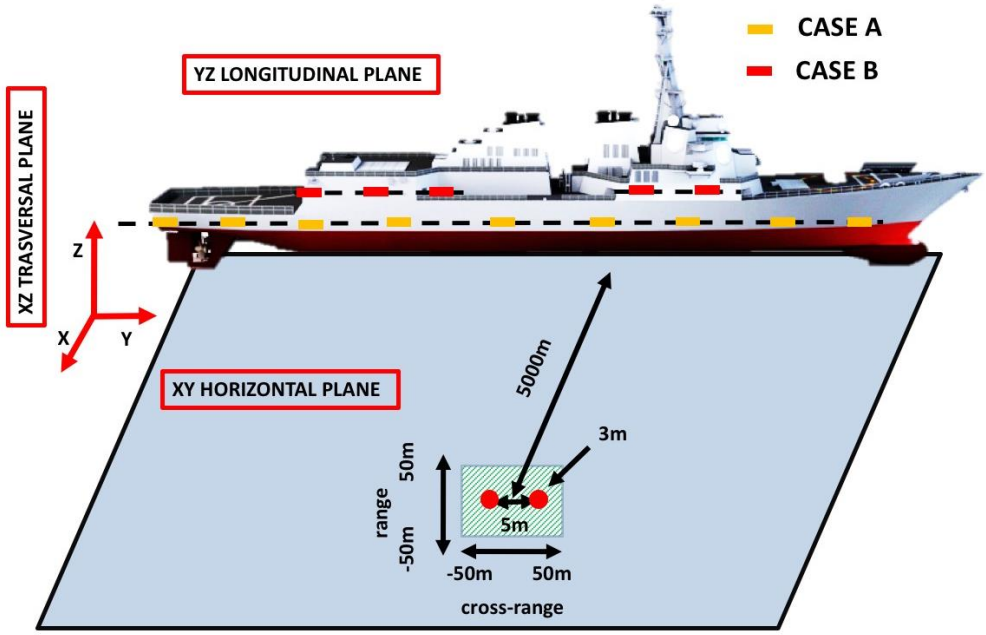

Figure 3-12: Naval Scenario

The analysis is structured as follows: first an apt number of TXs and RXs, which should constitute the MIMO architecture is found, then a preliminary check on the main lobe amplitude of the MIMO cross-ambiguity function is effectuated in order to be sure that the angular resolution requirement is fulfilled. At this point an antenna geometry optimization is addressed and, in particular, both a statistical and a genetic approach are explored. In the light that the sensor position can change, due to unknown ship deformations, the impact of unknown sensor displacements has been verified. The final part of the naval scenario study is dedicated to the description of the outcomes obtained in search and image mode and finalized to definitively assess that the the identified MIMO architecture meets the angular resolution requirement specified in Table 3-5.

3.3.5. MIMO antenna configuration: number of TX and RX antennas

As has already been verified for the coastal scenario analysed, changing the number of TXs and RXs has a deep impact on the PSLR. In addition, another factor that influences the PSLR is the fractional bandwidth of the selected radar waveforms. Spatial side lobes, like temporal side lobes, are extremely dangerous as they can lead either to the miss detection of targets with different RCS, as will be clarified in the following or to an intolerable rise in the false alarm rate.

Unfortunately, in radar applications the received signal dynamic is enormous for several factors such as high RCS variability (i.e. ship RCS can assume values which differ also by 40-50 dB). A common problem in radar detection consists of individuating close targets having a huge RCS difference. Essentially, the smaller lobe associated to the target with a lower RCS can be confused with a side lobe of the main target. Conversely, in case of multiple targets side lobes can sum up and determine fake targets. To avoid these unfavourable situations, radar waveforms are specifically designed to have an autocorrelation function as low as possible. This principle can be extended also to MIMO radar systems. Similarly, to range resolution of a monostatic radar, the lower side lobes of the cross-ambiguity function are, the better the radar detection and the achievable angular resolution

become. Known that the best Barker code assures a -23.3 dB side lobe suppression, a -20 dB suppression for MIMO cross-ambiguity side lobes seems reasonable.

In Figure 3-13, fixed the number of TXs, the extinction ratio (i.e. 1/PSLR) is plotted in function of different number of RXs (i.e. 1,2,3,5,10,15,20 receivers) is simulated. It has to be remarked that for this set of simulations realized with the aim to determine a suitable number of sensors and not to optimize their geometry, all sensors are assumed uniformly distributed.

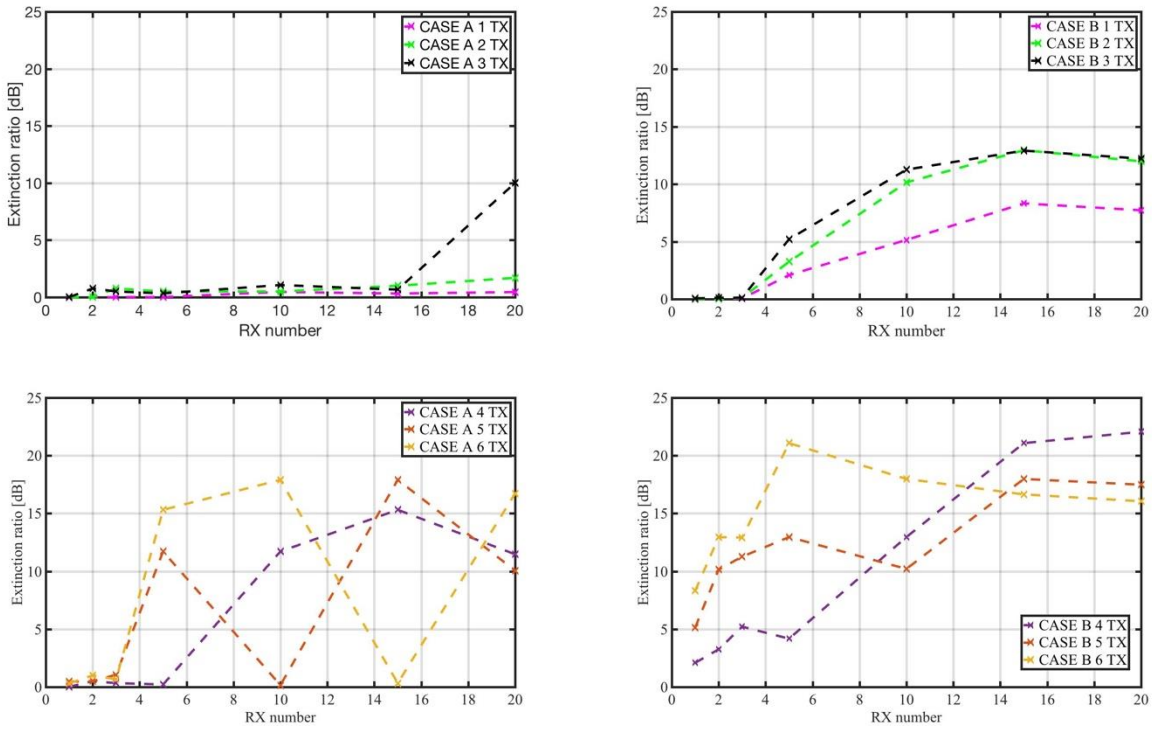

Figure 3-13: MIMO cross-ambiguity function extinction ratio for use case A (left) and B (right)

In both cases, as it was predictable, the trend is that by increasing the factor MxN the extinction ratio increases (i.e. the PSLR decreases). Furthermore, from simulations emerges that the curves do not increase monotonically, underpinning so the importance of antenna geometry, which will be discussed in detail later on.

From the results it is evident that in both cases to achieve a 20 dB side lobe suppression a 5 TXs x 20 RXs MIMO configuration (M=5, N=20) is appropriate.

3.3.6. MIMO antenna configuration: preliminary main lobe analysis

Although at this point the antenna geometry is not optimized and all TXs and RXs are uniformly distributed on the antenna aperture interval, it is opportune to verify that a MIMO 5TXs x 20 RXs antenna configuration satisfies the wanted 1 mrad angular resolution requirement. For this purpose, an ideal point-like scatterer has been simulated at a distance of 5000 m from the ship.

At first glance, both installation options (i.e. use case A and use case B) seem equivalent. In fact, observing the range cross-range maps, represented in Figure 3-14, the simulated target is clearly visible and no side lobe which attests that the suppression is significant. Instead, in Figure 3-15 the cross-range profiles for the simulated target are plotted. Comparing the two plots we can notice that for use case A the HPBW is equal to 60 cm, while for use case B the HPBW amounts to 70 cm. The better result obtained in the first case is comprehensible, since, from antenna theory, it is well-known that the linear length of the sparse array directly affects the HPBW extension. Anyway, we can

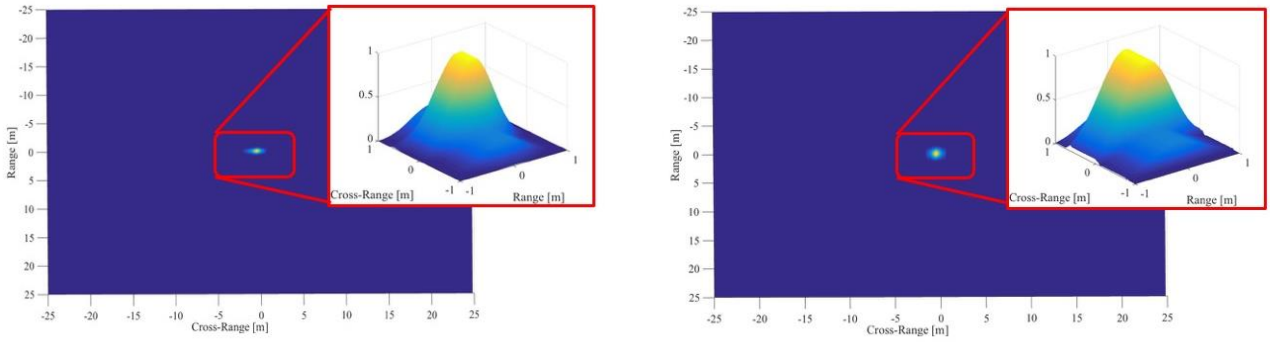

Figure 3-14: Range cross-range maps MIMO 5TXs x 20 RXs use case A (left) and use case B (right)

continue the analysis cause in both cases the cross-range resolution satisfies, by far, the specified angular resolution requirement.

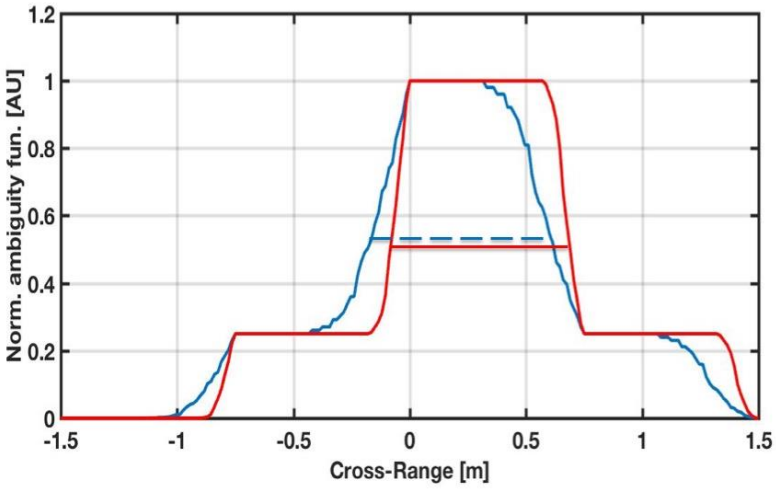

Figure 3-15: MIMO 5 TXs x 20 RXs antenna configuration cross-range pattern for use case A (red) and use case B (blue)

3.3.7. MIMO antenna configuration: geometry optimization

A MIMO antenna architecture is equivalent to a virtual array attainable as the convolution between the transmitter and the receiver positions. Therefore, typically the optimal solution in terms of PSLR is the one where all elements are equidistant and transmitters and receivers are interleaved. Unfortunately, this design rule can not always be applied due, for instance, to installative constraints (as it happens for use case B), or when interleaving transmitters and receivers is not possible, because they are not numerically equal. In all those situations it is opportune to realize an antenna geometry optimization, as unfavourable geometries can lead to virtual arrays with overlapping elements. When this happens spatial information results weakened and PSLR increases. Although the outcomes reported in Figure 3-13 refer to antenna configurations having a different number of sensors, the inexplicable non monotonically trend of PSLR, accentuated for use case A with 4 and 6 TX antennas, is imputable to non optimal geometries where, albeit more antenna elements are used, spatial information decreases. Consequently, once individuated a plausible antenna configuration in terms of number of TXs and RXs, it is convenient to effectuate an antenna geometry optimization.

The optimization problem has two degrees of freedom and can be recapped as follows: given M TX antennas and N RX antennas and a linear interval, on which those sensors can be positioned, find the best solution which minimizes the PSLR.

The antenna optimization problem has as many possible solutions as the combination without repetition of k elements extracted from a set of n elements, which can be calculated through the formula in Eq. 3-9. In the specific case in exam n is the number of possible antenna positions and k the number of antennas to be positioned.

$$\binom{k}{n} = \frac{n!}{(n-k)!\,k!} \qquad \text{Eq. 3-9}$$

If we divide the continuous interval where sensors can be placed in a discrete number of points spaced half carrier wavelength, the value of n is determined corresponding to a set of possible antenna positions (i.e. for case A=8666 points and for case B=3660 points). Instead k represents the number of TX and RX antennas and is in both cases equal to 25. From the formula we learn that for use case A the number of possible combinations is approximately 10^{100}, while for use case B only approximately 10^{90} combinations are possible! Hence it is obvious that an exhaustive optimization method can not be adopted and subsequently in the following two alternative optimization approaches are examined: a statistical approach and a more sophisticated genetic approach.

Statistical approach

A good strategy to solve the current optimization problem is to reduce the complexity by setting the position of the transmitters, so that they fill the whole interval where sensors can be positioned possibly equidistant. Fixed the transmitting antenna positions, different receiver positions can be randomly explored with the finality to find the best solution. Although the individuated solution is clearly suboptimal, due to the constraint imposed on transmitter sensors, the advantage of this method is that a solution good enough for the optimization problem in exam can be rapidly individuated.

In Figure 3-16 the histogram of 50 simulations effectuated applying the above explained optimization logic is reported. The extinction ratio variability is almost 10 dB, which implies that the best realization is 10 dB better than the worst one. Analysing the 5 best solutions out of the 50 simulations done, it seems that completely different RX antenna distributions can lead to the same result, consequently no relationship, helpful for a further PSLR enhancement, can be extracted. The optimal geometry achieved by the means of the proposed statistical approach ensures, for use case A, an extinction ratio of nearly 14 dB and for use case B of 18 dB.

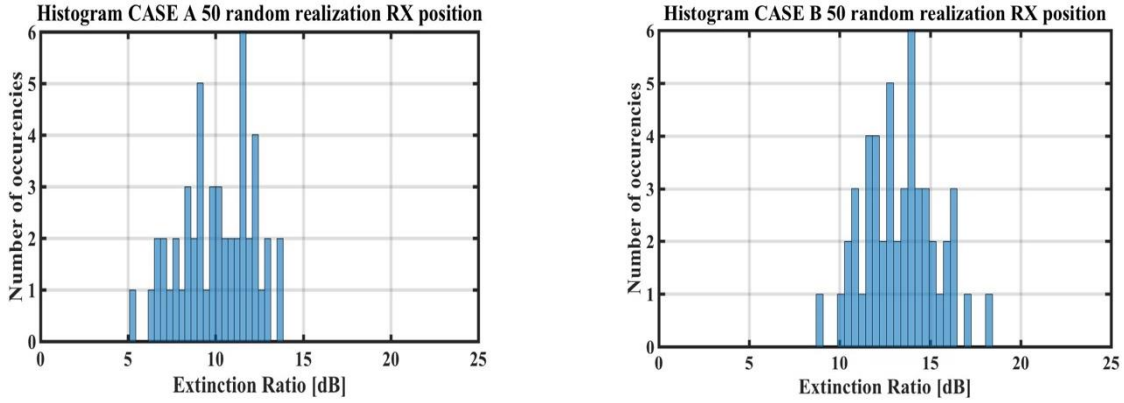

Figure 3-16: Extinction ratio histogram assuming equidistant TXs and 50 random RXs positions for use case A (left) and B (right)

Genetic algorithms

The purpose of this paragraph is to furnish some insight into genetic algorithms so that the steps of the optimization process developed and the results shown in next paragraph can be better understood.

Genetic algorithms are a branch of evolutionary computation generally applied to optimization problems, since this approach is much quicker compared to an exhaustive search of the optimal

solution and has the additional advantage that no extra information related to the optimization problem is requested. Accordingly, whenever an exhaustive search of the optimal solution is not feasible, due to the complexity of the assigned problem or when a good solution has to be quickly individuated it is convenient to employ this class of optimization algorithms. Genetic algorithms are based on Darwin's natural evolutionary theory: the main idea is that individuals which have a higher probability to survive in a certain context have a higher probability to transmit their genetic heritage to descendants. The terminology adopted for genetic algorithms coincides with the one adopted for evolutionary theory.
The first step for a genetic algorithm is to encode a potential solution; therefore, in case a problem has *Npar* dimensions, also the chromosome will have *Npar* genes:

$$\mathbf{Chromosome = [gene_1, gene_2, \ldots, gene_{Npar}];}$$

Although binary chromosomes are very common, genes can also be encoded using integers or real numbers. Then a selection rule (i.e. fitness/cost function) must be defined to determine which are the candidate chromosomes that are eligible for reproduction and an appropriate crossover strategy. The crossover strategy establishes how, once selected parents, new generations inherit the genes from their parents. Finally, as happens in nature, a random mutation function is needed to obtain chromosomes with some different genes.
Once defined all these functions, a genetic algorithm implements following steps:

1. An initial random population is selected;
2. The fitness function is evaluated for all chromosomes of the population;
3. Based on the fitness score obtained by each chromosome, parents are identified;
4. According to the crossover strategy, matings are performed;
5. Random mutations are introduced in the new population;
6. Steps 2 to 5 are iterated until a stop condition is reached (i.e. typically when a maximum number of iterations is elapsed or when the fitness function results better than a fixed threshold).

The algorithm is simple. However, parameters have to be chosen carefully then otherwise the risk is that the algorithm does not converge. Parameters choice often derives from a trade-off. For instance, a larger initial population ensures a better coverage of the solution space. Unfortunately, a large initial population converges only after numerous generations. In the same way, if a low percentage of population mutations is selected, the risk is that a local minimum of the cost function is found, whereas a too elevated value can cause instability, which hinders final algorithm convergence.

A classical example of a problem solvable by the means of a genetic algorithm is the travelling salesman problem. A salesman has to visit n cities across the country, he visits each city once and returns to the city, where he started the journey. The goal of the optimization problem is to determine the shortest route possible. In Figure 3-17 a solution to this problem, in case n is equal to 20, is shown. As can be noticed, the fitness function for the best solution (blue) and mean population (red) decreases generation after generation so that, after 100 generations, the algorithm converges and an optimal solution is individuated.

Readers interested in further details related to genetic algorithms can find them in [69].

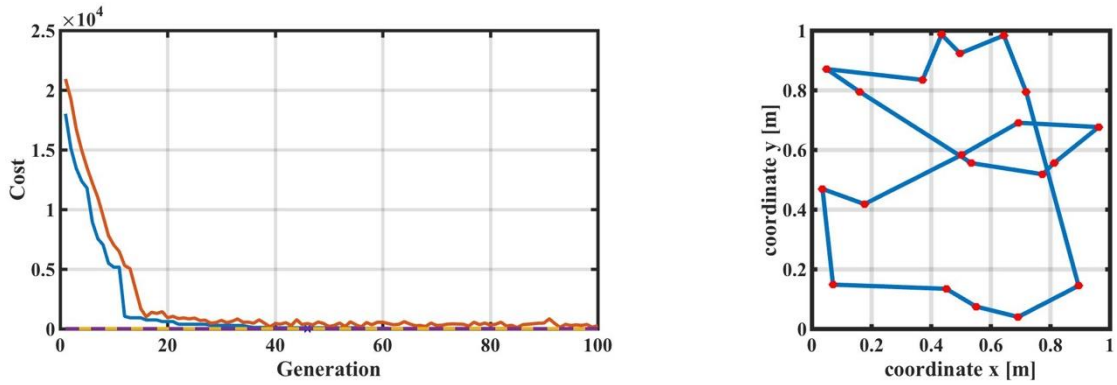

Figure 3-17: Salesman problem solved through a genetic approach: evolution of the cost function (left); optimal solution determined after 100 generations (right)

Optimization through genetic algorithms

Genetic algorithms are recommended for optimization problems, where as in the present case the cost function is unknown. The PSLR, in fact, is not known and each time computed for a specific antenna geometry through the MIMO scenario simulator, as described in [70]. In Table 3-6 all significant parameters used by the implemented genetic algorithm are listed.

The cost function seems to converge, in fact, as shown in Figure 3-18, after 50 generations the extinction ratio passes from 13.5 dB to 16.5 dB, for use case A, with an increment of circa 3 dB and from 15 dB to almost 20 dB, for use case B.

Parameter	Value
Max generations	50
Cost function	PSLR
Initial random population	10
Selected Population (survivor rate)	50%
Mutation rate	10%
Parent combining criteria	Single crossover permutation
Gene number	25

Table 3-6: Genetic algorithm settings

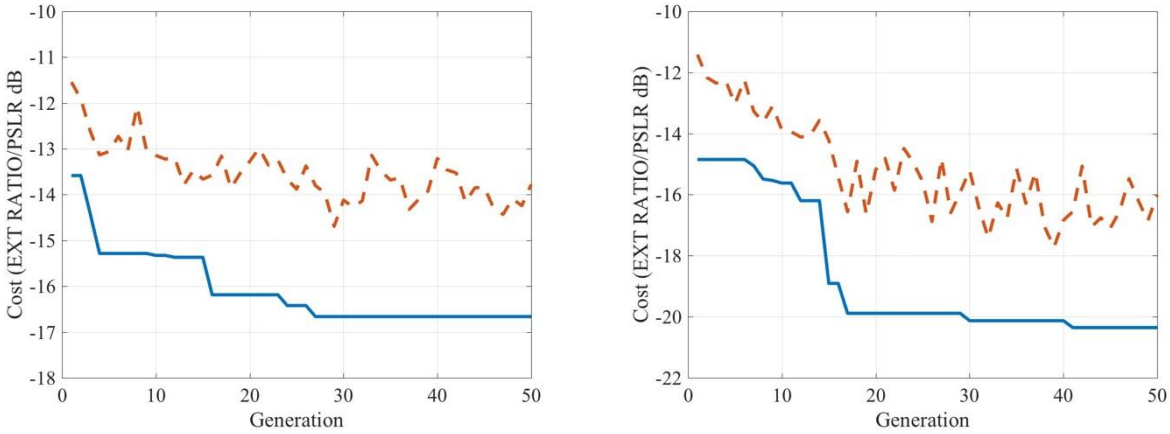

Figure 3-18: Genetic algorithm optimization population mean cost (red) and best solution cost (blue) for use case A (left) and B (right)

In conclusion, the optimal solutions individuated, thanks to the genetic algorithm, reported in Table **3-7** outperform the corresponding best solutions found through the statistical approach.

The 3 dB gap between the best solution for use case A and B probably depends on the fact that, for use case B, a better solution has been found; whereas, for use case A, after 50 generations only a local minimum has been discovered. However, the main aim of this analysis is principally to demonstrate the validity of the proposed genetic approach as the PSLR has been increased respectively by 4 dB and 2 dB. A further analysis is beyond the scope of this work.

ANTENNA NUMBER	1	2	3	4	5	6	7	8	9	10
	11	12	13	14	15	16	17	18	19	20
TX A [m]	**14.34**	**1.73**	**-34.72**	**-64.25**	**57.24**					
RX A [m]	**64.92**	**60.07**	**51.54**	**48.84**	**40.42**	**33.09**	**29.77**	**25.77**	**24.52**	**15.97**
	14.47	**-13.28**	**-19.51**	**-27.68**	**-30.27**	**-35.17**	**-37.23**	**-39.29**	**-43.84**	**-58.88**
TX B [m]	**11.25**	**-9.28**	**-13.36**	**-26.77**	**-36.00**					
RX B [m]	**27.47**	**26.43**	**24.66**	**21.20**	**19.50**	**16.08**	**16.02**	**11.99**	**11.10**	**10.89**
	-15.91	**-17.19**	**-18.99**	**-20.16**	**-21.70**	**-25.51**	**-29.01**	**-31.74**	**-35.58**	**-40.05**

Table 3-7: Optimum antenna geometry resulting from genetic algorithm

3.3.8. Displacement analysis

Phase compensation is the distinctive factor of a coherent MIMO processing. The precondition for this operation is that the MIMO geometry is perfectly known, which is not always true. Here, in fact, the impact of eventual sensor displacements errors on overall system performance is evaluated. In particular, in the following the impact on the PSLR of the cross-ambiguity function is evaluated when unknown spatial displacements affect sensor distribution.

At this point it is useful to remind that the sensors and the target are assumed to be all placed on the same horizontal plane, as schematically shown Figure 3-12 which is a legitimate assumption, since we are designing a MIMO coherent distributed radar network for naval surveillance applications. The developed 2-D simulator, given a Cartesian reference triad, as the one represented

in Figure 3-12,where x corresponds to the transversal axis of a ship, y to the horizontal and z to the longitudinal, assumes, in fact, that the longitudinal coordinate is equal to 0 (z=0) for all elements (i.e. antennas, targets).

Though longitudinal ship displacements are relevant (i.e. the maximum displacement for a frigate can reach also tens of cm) it is convenient briefly discuss which are the effects of such a dynamic platform deformation on our application.

The antenna elevation pattern of a conventional (i.e. monostatic) naval radar is not an essential design parameter, at difference to the azimuth pattern, which influences the number of integrable pulses N in a CPI, and defines the resolution capability in the azimuth dimension. The only requirement that an antenna has to satisfy in the elevation plane is to illuminate the potential target with an appropriate amount of energy and, since the aperture is large enough an eventual longitudinal displacement is not an issue. Conversely, for a distributed MIMO architecture a change in the element disposition determines a different ambiguity function. Furthermore, conscious that a variation of the array elements of an antenna along a certain axis reflects mainly on the antenna pattern coplanar with that axis, we can infer that a longitudinal displacement causes mainly a modification in the elevation pattern of the MIMO antenna configuration.

Nevertheless, provided that the target is within the antenna aperture in elevation, even in this case the effects on performance should be negligible. Assuming a sensor distribution in the longitudinal plane on an aperture of 30 cm (i.e. [-15cm +15cm]), which represent the maximum longitudinal deviation from the nominal position for a frigate and to use isotropic antenna elements, at 10 GHz the -3dB beam aperture turns out to be about 6° and is still adequate for a naval application.

At this point, clarified that longitudinal displacements are insignificant for the present study the focus passes to displacements laying in the horizontal plane, distinguishing between lateral (along the y axis) and transversal (along the x axis) displacements.

Unfortunately, naval design focuses principally on longitudinal deformation since in this direction stresses determined by still sea and wave loads are predominant and limited data are available for displacements in other directions. In general, exploiting a Finite Element Model (FEM) the maximum positive (bend) and negative (sag) deformations are calculated. The resulting deformations typically reach a maximum in the central region of the ship, whereas in correspondence of bow and stern the deformation is minimal and the relation is almost linear along the z axis. In absence of better data, a model based on the information valid for longitudinal displacement can be assumed. Therefore, taking into account also that solicitations in the transversal and horizontal plane are between 1% and 5% of corresponding longitudinal values, for the present analysis following assumptions are made on transversal (along x axis) and lateral (along y axis) displacements:

- Maximum sensor displacement between 3 mm (1% of 300mm) and 15 mm (5% of 300mm);
- Linear relation between sensor displacement likewise longitudinal ship deformation.

Given these assumptions, the displacement has been modelled in both dimensions as a random uniform distributed variable and we have also considered that the intensity of the displacement changes linearly in the same manner as the longitudinal displacement does, namely increases from stern or bow to the middle of the ship. For this analysis, a Monte Carlo approach would be more indicated, however, for the present purpose and with the intent to limit the computational complexity just ten realizations of the random process for each possible maximum sensor displacement value, which, as said, is assumed to be in the range [3mm: 15mm] have been done.

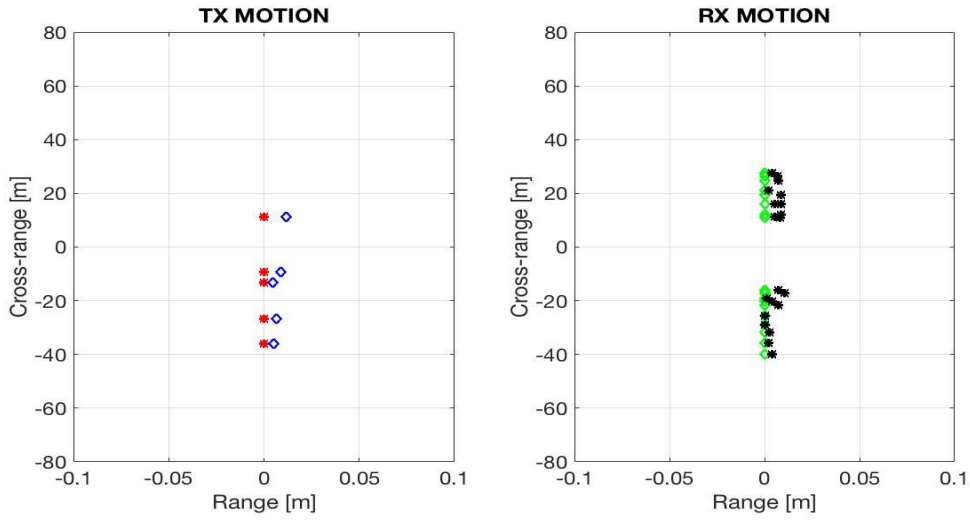

Figure 3-19: Random sensor displacement with linear relation TX elements (left) and RX elements (right) - (red dots nominal TX positions, blue circles displaced TX positions- green circles nominal RX positions, black dots displaced RX positions)

In total 100 run for each use case have been effectuated. From the scatterplots, depicted in Figure 3-20 and Figure 3-21, it is clear that the extinction ratio of the coherent MIMO cross-ambiguity function worsen, as the displacement increases. Errors below 8 mm can still be managed, while superior displacements completely spoil the detection capability. The outcome is consistent, since errors close to the carrier wavelength cause an incorrect phase compensation (see Eq. 1-11) with negative repercussions on the side lobe amplitude.

In conclusion, this aspect should be further investigated in future studies to determine whether the real displacement is low enough to assure good radar performance or calibration techniques and lower carrier frequencies need to be considered.

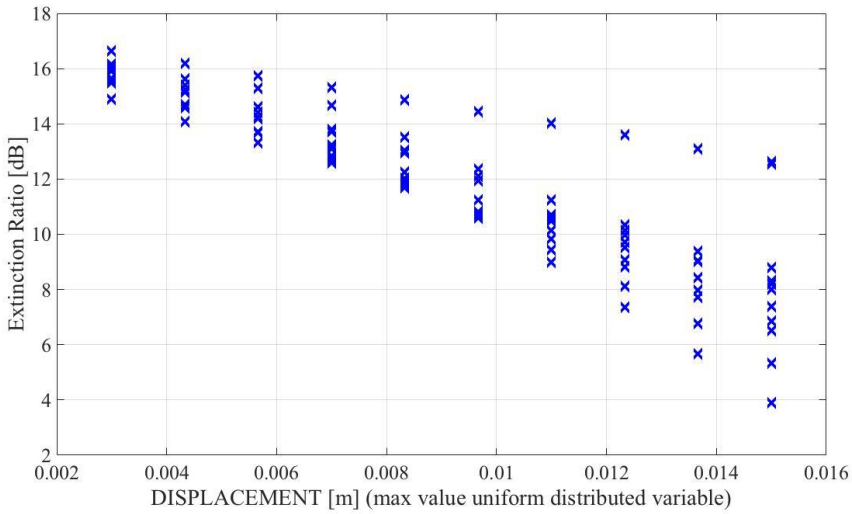

Figure 3-20: Side lobe extinction ratio scatterplot (10 random realizations) in function of the maximum sensor displacement for use case A

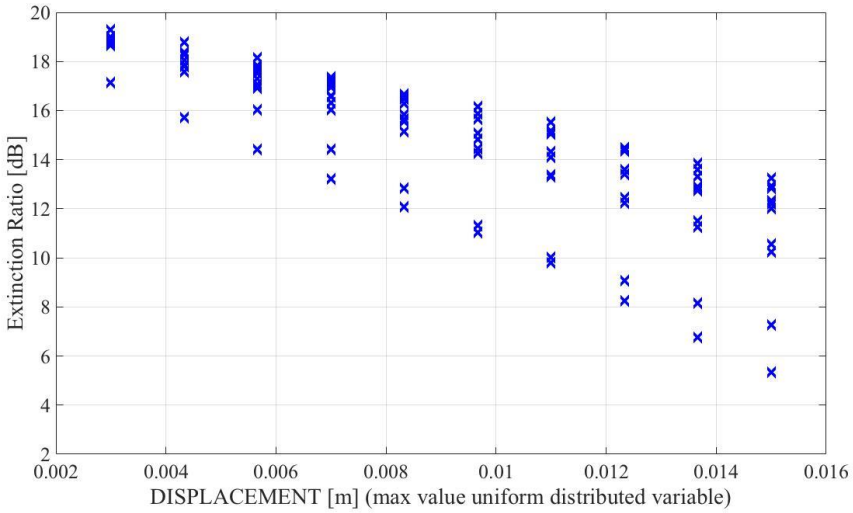

Figure 3-21: Side lobe extinction ratio scatterplot (10 random realizations) in function of the maximum sensor displacement for use case B

3.3.9. Phase noise analysis

A MIMO radar configuration can exploit multiple bistatic TX-RX combinations, provided that all transmitted signals are orthogonal. Thanks to orthogonality, in fact, the receivers can distinguish the transmitter that originated each contribute within the collected signal. Different approaches can be used to obtain signal orthogonality. The most promising is multiplying signals in the code domain. Nevertheless, the easiest way is to separate signals in time diversity, especially in the optical domain, even if this is the less efficient option because, fixed a CPI, the number of integrable pulses decreases. In the following two different HW architectures based on time diversity are examined and the requested oscillator phase stability for each solution is evaluated.

The first architecture, sketched in Figure 3-22 (left), is realized by the means of a single optical oscillator shared by the whole radar network configuration: signals are generated in the optical domain and distributed through optical fiber to the antenna peripherals. By inserting ODLs (i.e. spoon of OF), which delay the signal by an amount of time (l-1)*PRI, where l indicates the l-th transmitter, it is possible divide the system PRI in M sub-PRIs. In this manner each transmitter has its own time slot to transmits the same delayed signal, while the others are silent.

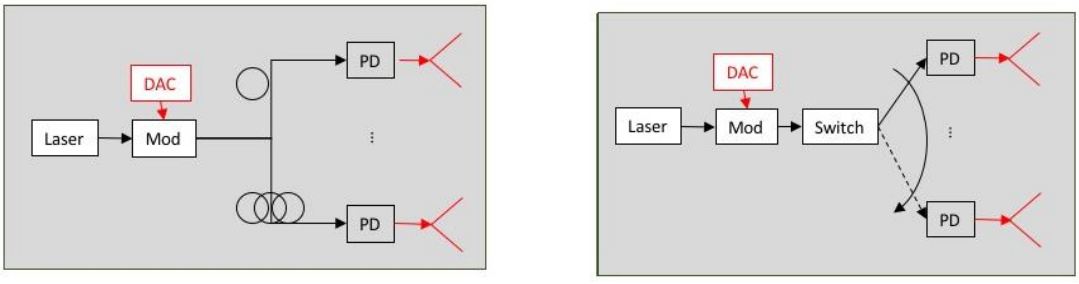

Figure 3-22: Photonic multi-transmitter architecture TDM-ODL solution (left) and TDM-switch solution (right)

Another possible solution similar to the previous one, as shown in Figure 3-22 (right), can be obtained substituting instead of multiple ODLs a switch which commutes in transmission the signals towards each antenna. The only difference with respect to the ODL solution is that, switching times are limited downwards by the features of the device and typically are higher than hundreds of ns.

Subsequently, the ODL solution assures a higher flexibility, due to the fact that the delays can be as short as desired; whereas a switch solution entails a minimum delay, defined by the selected RF component.

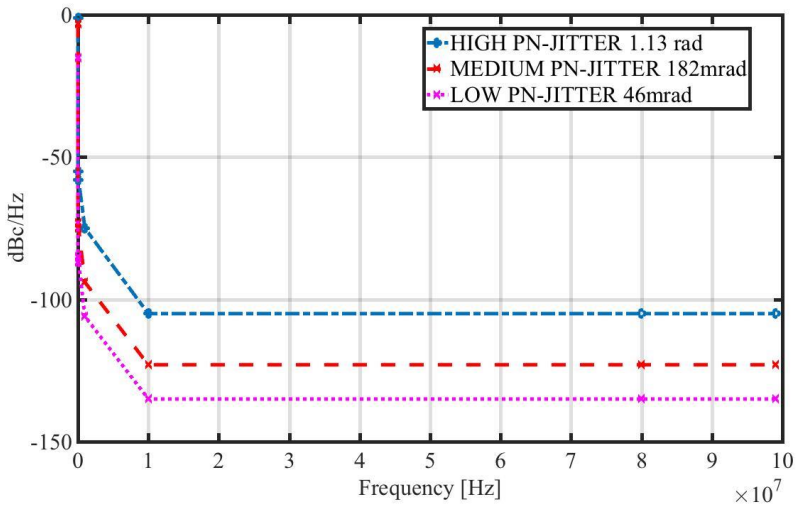

Figure 3-23: Oscillator Phase Noise curves low PN (pink), medium PN (red) and high PN (blue)

For simulations shown hereafter the optimal antenna distribution, resulting from the genetic algorithm discussed in paragraph 3.3.7, has been considered. Furthermore, the phase noise curves of the 3 oscillators, shown in Figure 3-23 related to an extreme precise RF oscillator, to an MLL optical oscillator, as the one used for the realization of the first photonics-based radar prototype, and to a low cost 10 GHz RF oscillator have been evaluated. In particular, on the spectral range of interest [10 Hz: 200MHz] aforementioned oscillators, respectively present an angular jitter of 46 mrad, 182 mrad and 1,13 rad.

For each HW solution and use case, 10 realizations per oscillator type have been executed, thus, in total, 120 simulations have been run which are summarized in the 4 scatterplots showing the side lobe extinction ratio of the coherent MIMO cross-ambiguity function for each oscillator.

It has to be remarked that simulations carried out differ profoundly. For the TDM-ODL configuration a single PN array has been generated; instead for the remaining configuration, multiple PN arrays have been simulated assuming that PN is uncorrelated, due to longer switching times. From Figure 3-24, where the scatterplots adopting a TDM-ODL HW solution are depicted, it is clear that only an extreme precise RF oscillator is eligible for the realization of coherent MIMO radar networks.

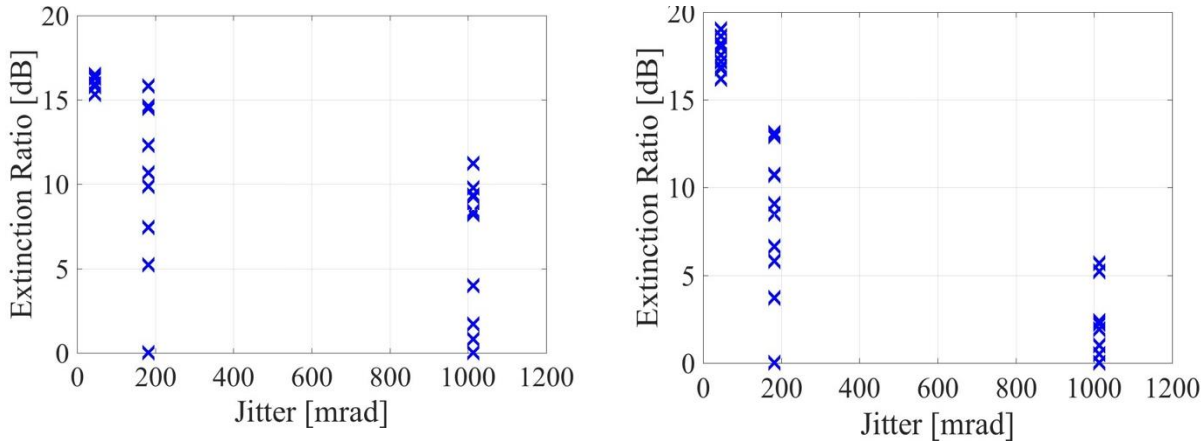

Figure 3-24: Extinction ratio scatterplot TDM-ODL option use case A (left) and use case B (right)

Instead, observing Figure 3-25 which shows the results obtained for the TDM-switch solution, it is evident that in this case also the MLL optical oscillator is appropriate to set up the radar network. The extinction ratio, indeed, compared to the ideal case without PN decreases by only 2 dB and hence an effective radar detection is conceivable.

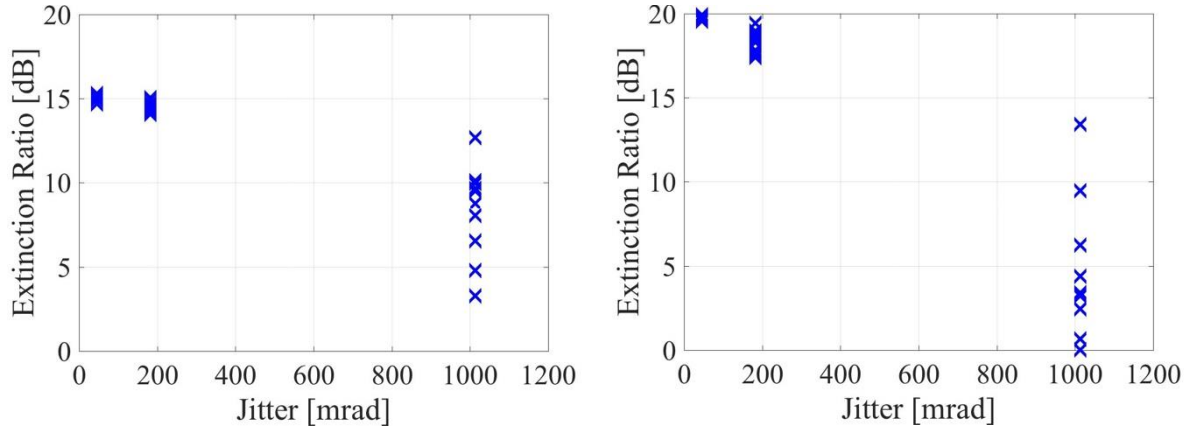

Figure 3-25: Extinction ratio scatterplot TDM-switch option use case A (left) and use case B (right)

3.3.10. Naval scenario target pre-localization and high resolution detection

The aim of this paragraph is to test that both identified concrete design solutions in terms of:

- Radar signal characteristics;
- MIMO number of TXs and RXs;
- MIMO geometry;
- TDM HW solution;
- Oscillator PN type;

are appropriate to assure the given angular resolution requirement of 1mrad.

Two ideal point-like scatterers located at a distance of 5000 m and spaced 5 m in cross-range (i.e. 1 mrad angular resolution) have been simulated and, unlike simulations previously discussed, in order to get more realistic outcomes this time the simulated MIMO signal matrix includes also amplitude and phase noise contributes. In Figure 3-26 and in Figure 3-27 the range cross-range maps, computed in search mode on an area of 2 Km x 2 Km with a resolution cell of 30 cm x 30 cm, are represented, respectively, for use case A and for use case B. In both cases search mode consents to successfully locate an area of interest centered around T= (5000m, 0m). However, due to the low resolution sampling, only one peak is visible rather than the expected two peaks.

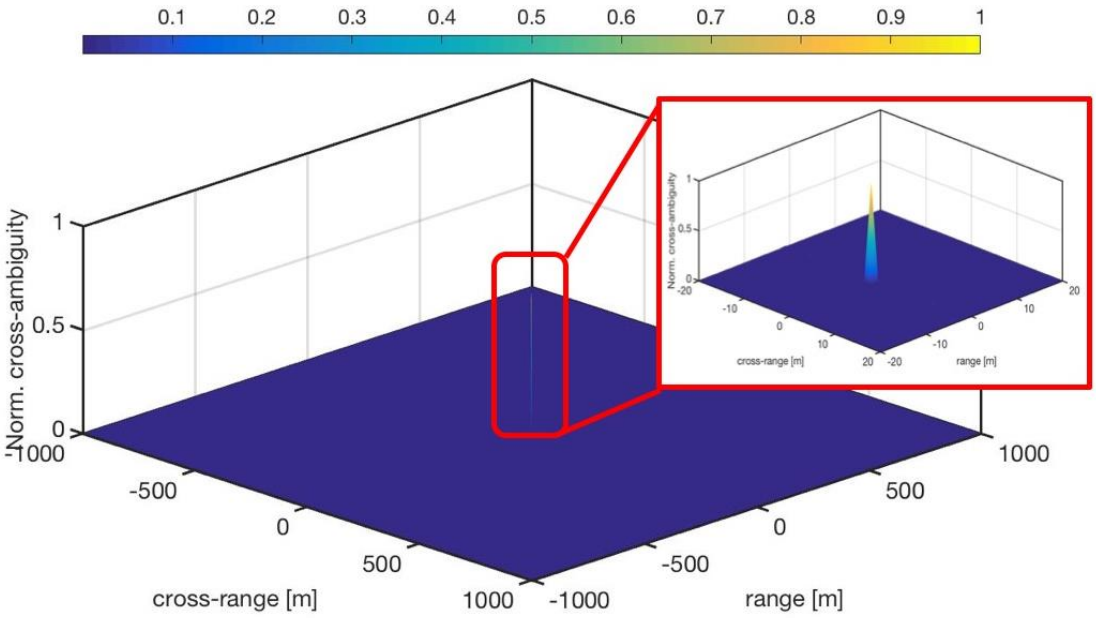

Figure 3-26: Range Cross-Range map in Search Mode for use case A

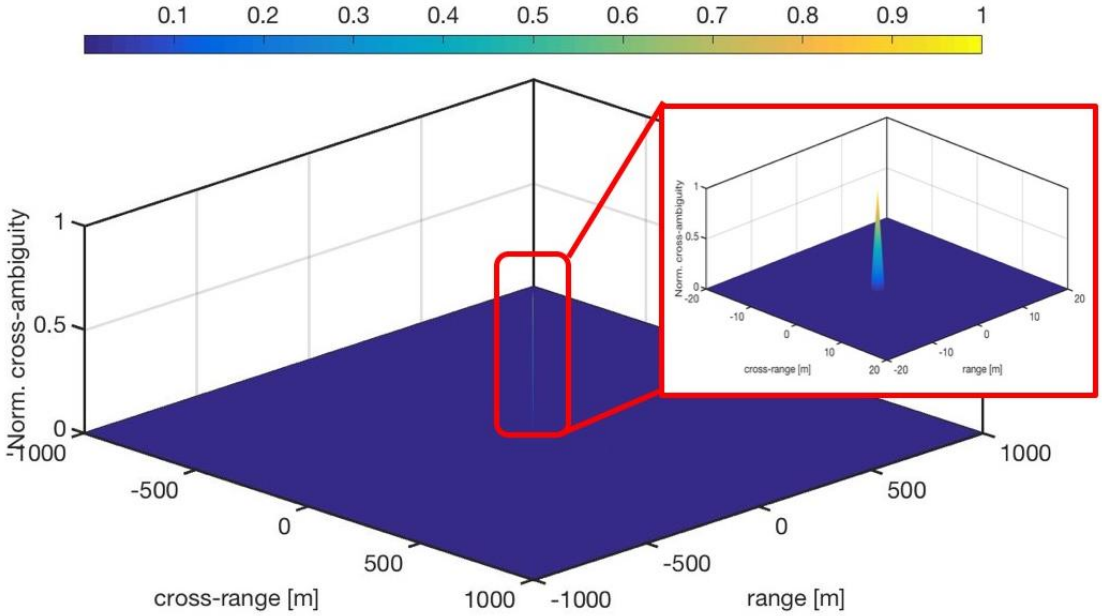

Figure 3-27: Range Cross-Range map in Search Mode for use case B

Once pre-located the targets present on the scene it is opportune switch from search to image mode enabling so a high resolution detection. In this way the dimension of the resolution cell is reduced and an operation comparable to the well known zoom function in image processing is performed. In Figure 3-28 and Figure 3-29 the outputs of image mode are depicted, computed with a resolution cell of 1.5 cm x 1.5 cm on an area of 100 m x100 m around the pre-detected target location.

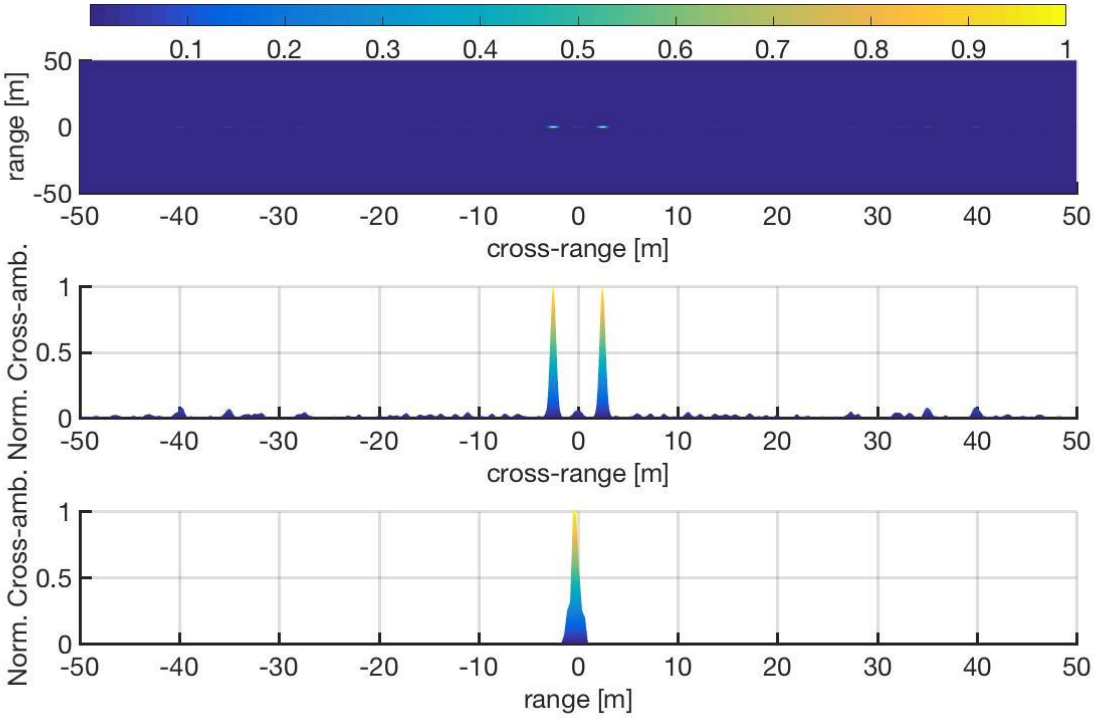

Figure 3-28: Range Cross-Range map in Image Mode for use case A

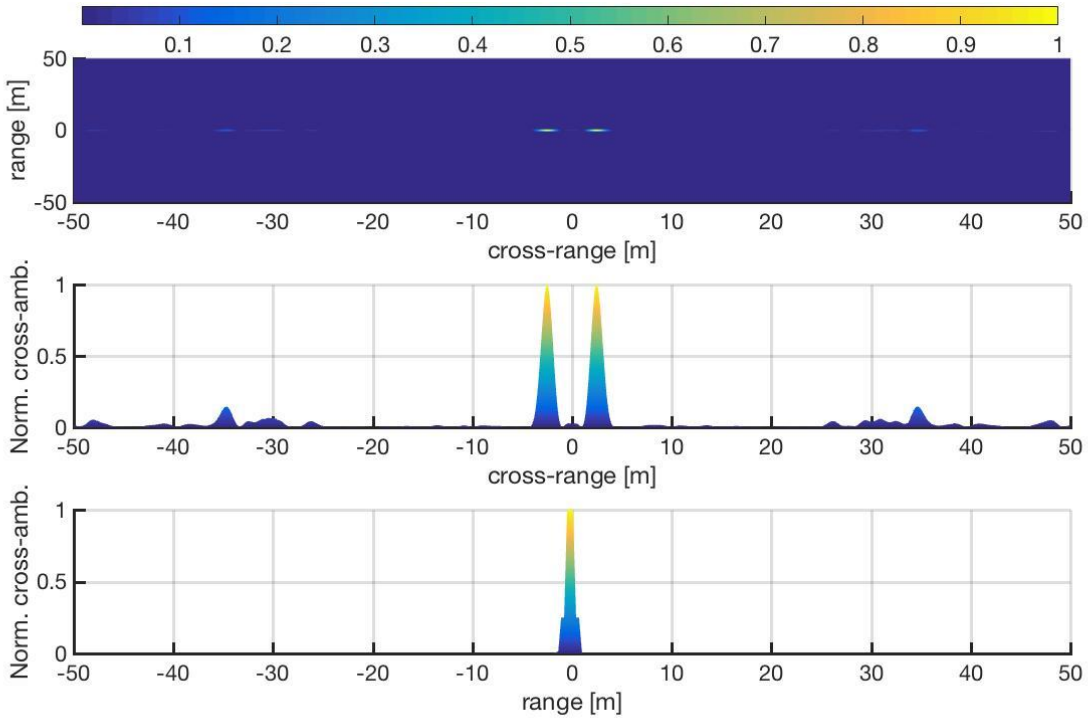

Figure 3-29: Range Cross-Range map in Image Mode for use case B

Observing cited figures, we can notice that the 2 simulated targets are successfully resolved by both MIMO configurations. Besides, as already pointed out in the section dedicated to the main lobe analysis, use case A has a slightly better resolution capability (i.e. the targets for use case A have a narrower main lobe than for use case B).

	OPTICAL HORIZON [Km]	MAXIMUM DETECTABLE TARGET RANGE (H_{TAR} 5m) [Km]	ANGULAR RESOLUTION [mrad]	SIDELOBE SUPPRESSION [dB]
CASE A	8.63 Km	17.26 Km	0.12 mrad	-16.5 dB
CASE B	13.37 Km	22.00 Km	0.14 mrad	-20.0 dB

Table 3-8: Naval scenario final performance comparison for examined installation hypotheses

In conclusion, although both examined architectures satisfy the posed angular resolution requirement, as reported in Table 3-8, use case B ensures a better side lobe suppression as well as a better optical horizon and maximum detectable range (supposing a 5 m target height). Hence, without any doubt, from the analysis emerges that the best installation solution for a coherent MIMO radar network designed specifically for naval applications is use case B.

3.3.11. Naval scenario detection test on distributed targets

Far from being an exhaustive analysis which should certainly also contemplate bi-static RCS modelling, in the following distributed targets have been taken into account in order to obtain simulations closer to reality than those done simulating ideal point-like scatterers. A complex scenario constituted by 2 distributed targets has been imagined for this scope and, as schematically sketched in Figure 3-30, the first target on the scene has been modelled with 35 point-like scatterers uniformly distributed on an area 40 m large and 60 m long, whereas the other distributed target has been modelled with 20 point-like scatterers uniformly distributed on an area 10 m large and 20 m long. The total RCS has been set to 300 m^2 for the first target and to 100 m^2 for the second one and they have been centred, respectively, in T1=(-22.5m,0) and T2= (12.5m, 5m).

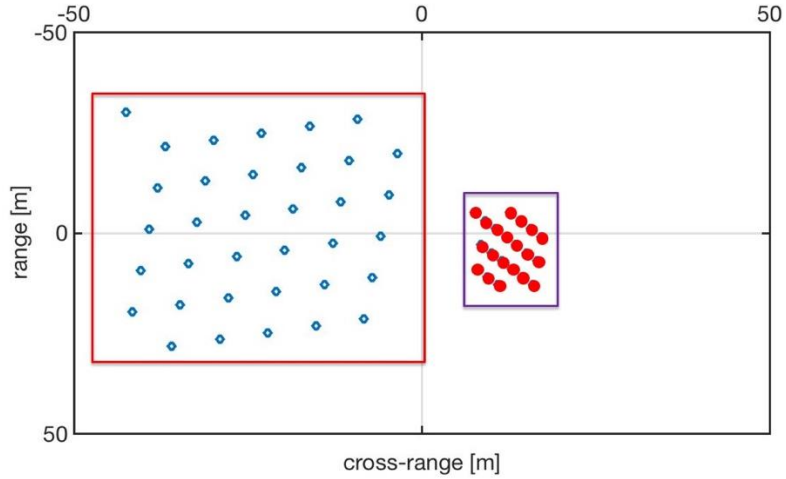

Figure 3-30: Complex naval scenario composed by 2 distributed targets

Elaborating the simulated MIMO signal matrix in image mode, the resulting range cross-range maps obtained on an area of 100 m x 100 m with a 1.5 cm x 1.5 cm resolution cell, depicted in Figure 3-31 reveal that the distributed targets are clearly detected. Furthermore, the detection statistic associated to the target having a lower RCS located on the right, as can be noticed, has got a lower intensity, since we have considered that this target has a total RCS 3 times lower than the RCS associated to the main target present on the scene.

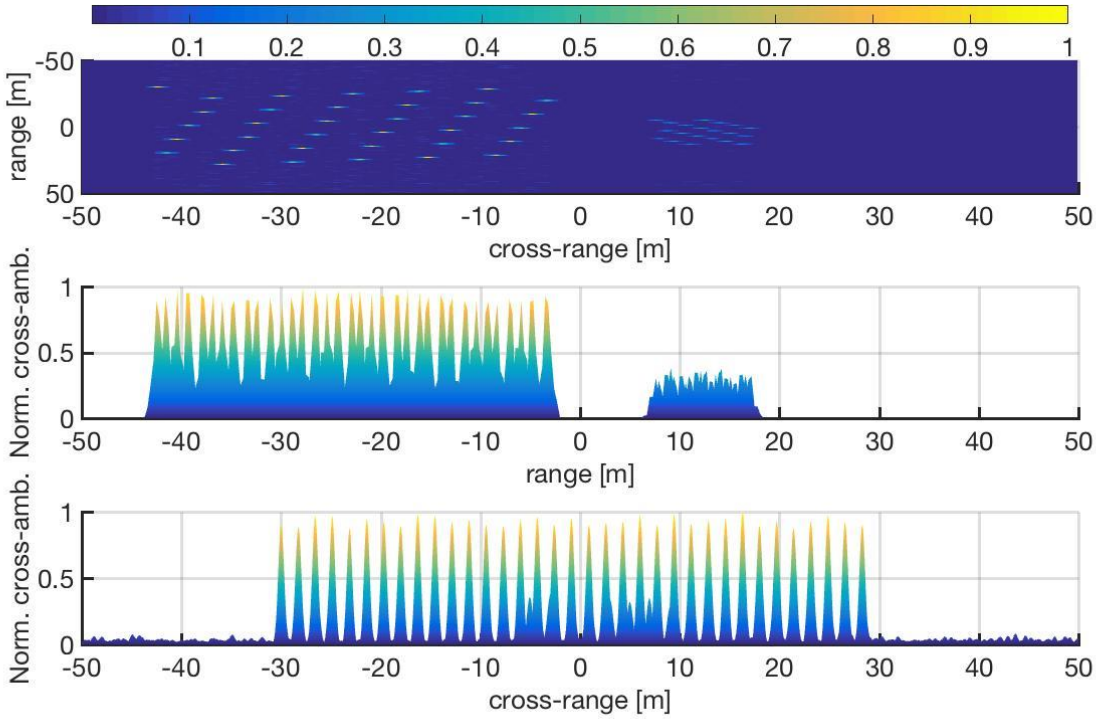

Figure 3-31: Range Cross-Range map in Image Mode for a complex naval scenario (use case B)

The outcome definitively confirms the huge potential of a coherent MIMO processing. Image mode permits, first of all, to detect multiple targets present in an area of interest, previously localized in search mode. Besides, the fine resolution cell dimension (i.e. order of the carrier frequency wavelength) provides the pre-condition for a correct classification and, eventually, for target identification.

3.4. SIDE LOBE OPTIMIZATION THROUGH DATA FUSION IN TIME DOMAIN

A main drawback of MIMO radars are significant side lobes of the ambiguity function and, as already examined in paragraph 3.3.5 and 3.3.7 those depend on the number of antenna elements used for the MIMO configuration as well as on their geometrical distribution. In paragraph 3.3.7 it has been demonstrated that, once fixed the number of TX and RX elements, a genetic algorithm can find the optimal MIMO antenna geometry, especially when installation constraints hinder to place antenna elements on the whole aperture. Moreover, from the simulative analysis there is sufficient evidence that as the number of antenna elements increases the PSLR decreases. Unfortunately, a configuration with more transmitters and receivers entails a higher system complexity and cost. For this reason, the aim of the present paragraph is to verify if it is possible to lower unwanted side lobes without changing the antenna geometry. In following two alternative possibilities are explored, leveraging in both cases on coherent data fusion of multiple data set acquired for the same scene.

In particular, in paragraph 3.4.2 a processing scheme essentially based on multiple consecutive observation acquired in time diversity is outline, whereas in 3.6 a solution based on data fusion performed on signals collected in frequency diversity is proposed.

As the ensuing processing scheme originates from a combination between MIMO processing and the well-established Synthetic Aperture Radar technique, first aforementioned technique is briefly recap, then the processing scheme which has been implemented for numerical analysis is presented and finally results, including also an evaluation of the effects due to possible errors in motion compensations, are discussed.

3.4.1. Synthetic Aperture Radar Processing

Although SAR processing has been invented more then 50 years ago, especially in the field of earth observation, this method still represents the foremost processing technique. Indeed, tens of spaceborne SAR sensors are operated today and more will be launched in next years [71]. The strength of SAR relies on the fact that, thanks to an opportune data fusion, a much higher along track resolution can be achieved with respect to the resolution obtainable implementing a standard processing without data fusion. In satellite radar systems built for earth observation across-track resolution depends, essentially, on the bandwidth of the radar signal. Instead along track resolution is related to the antenna features and is generally rather poor, due to the fact that antennas have to be small in order to satisfy demanding payload requirements. In SAR systems aforesaid limitation can be overcome, exploiting the movement of the platform. Provided that phase coherence is preserved during the whole observation time, the multiple consecutive observations of the same scene from slightly different aspect angles permit to synthetize a virtual antenna that is much longer than the real aperture antenna, used by the radar system. The antenna element spacing depends exclusively on the radar PRF and on the platform speed and, though cited array elements radiate sequentially and not simultaneously, a remarkable along-track (cross-range) resolution can be obtained. Besides surprisingly SAR resolution is independent from target distance and direct proportional to L, the physical length in along track dimension of the antenna, according to following relation:

$$\Delta r_{SAR} = \frac{L}{2} \qquad \textbf{Eq. 3-10}$$

Hence, surprisingly, the lower the antenna length, the better the resolution obtainable through SAR processing [71]. Standard SAR processing consists of the following enlisted main set of operations:

1. Range compression;
2. Motion compensation;
3. Azimuth compression on range cells, usually realized through a Fast Fourier Transform (FFT).

The resulting Range-Doppler map can be transformed into a Range-Azimuth (cross-range) map converting the Doppler frequencies to spatial coordinates, using following relation:

$$\mathrm{x} = \frac{\lambda R_0 f_D}{2v} \qquad \textbf{Eq. 3-11}$$

where λ represents the carrier wavelength, R_0 is the minimum distance between the radar and the target during the observation time, f_D the Doppler frequency and v the platform speed.
More details on SAR processing can be found in [71] [72].

At this point it is noteworthy highlighting that both SAR and MIMO approaches share the common purpose to improve the angular resolution, also referred to as along-track in spaceborne applications, and that both leverage, essentially, on spatial diversity. Furthermore, in order to get a fine resolution, it is indispensable that phase coherence is guaranteed during the observation time for SAR and among all sensors of the network for MIMO systems. While in SAR applications it is quite simple satisfy aforesaid requirement, this is not true when largely spatial distributed radar networks are deployed. In SAR systems, in fact, the same radar system acquires sequentially the whole data set so it is sufficient that the oscillator is stable (has a low PN) within the observation time. Instead in MIMO operations multiple bi-static radar channels (i.e. any transmitter-receiver combination) acquire simultaneously the same scene and, as already discussed (see paragraph 1.2), when a

distributed architecture rather than a centralized is adopted, complex synchronization algorithms are necessary to recreate, a posteriori, signal time and phase coherence.

3.4.2. SAR-like MIMO processing scheme

In extremely dynamic scenarios as the naval one the observation time, T_{OBS}, assumes values much lower than those typical for airborne or spaceborne applications, due to the fact that the target coherence is guaranteed for an extremely short period of time. In addition, the PRF has to be low enough in order to ensure the correct detection of targets at maximum operative distance and avoid, perhaps, second pulse echoes (i.e. range ambiguity). Finally, ships are much slower platforms which can just reach 1% or 10% of aircraft or satellite speed, travelling at Mach 1 (i.e. 300 m/s) and Mach 10 (i.e. 3 Km/s) respectively. For all these reasons, SAR is unquestionably inappropriate and ISAR which exploits target motion rather than platform motion has to be used in its place.

The application of SAR principles to MIMO radar networks, is an under explored research area [73] because airborne and spaceborne SAR processing already permits a fine cross-range resolution. Apparently, there is no profit in combining both techniques. However, it will be shown that this statement is incorrect. Indeed, except for some paper that has investigated the combination of MIMO and SAR in along track dimension [74], generally MIMO-SAR refers to radar systems which use a MIMO array in across-track dimension, while implementing a SAR processing in along track in order to get a fine spatial resolution in both dimensions, as, for instance, in [75].

In the ensuing proposed processing scheme MIMO and SAR are performed along the same dimension (along-track), therefore, to avoid any possible confusion with MIMO-SAR it is opportune define the method SAR-like MIMO [76].

For this analysis the considered scenario is the naval scenario already described in paragraph 3.3 (use case A). According to the outcomes discussed in section 3.3.5 to get a side lobe suppression of indicatively 20 dB a MIMO geometry with M=5 TXs and N=20 RXs with equidistant and interleaved antenna elements is necessary, thus in the following this antenna geometry is considered. In addition, the same radar waveform parameters already listed in Table 3-3 have been assumed and in order to ensure a perfect signal orthogonality the assumptions is that all transmitters operate using staggered frequencies. Besides, though theoretically the dwell time, T_{dwell}, can be much longer than for conventional radars with rotating antennas (i.e. typically 20 ms), a maximum observation time, T_{OBS}, of 0.1 s has been cautiously assumed.

An ideal point-like scatterer has been simulated 5000 m away from the MIMO antenna geometry, exactly in the middle of the array aperture at the instant $t_0 = 0$ s, as sketched in Figure 3-32.

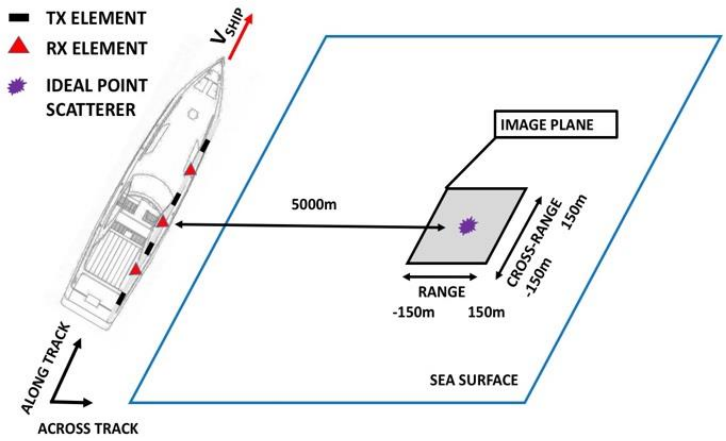

Figure 3-32: SAR-like MIMO for a naval scenario

The ship is moving in along track with speed, v , hence, after 1 PRI (i.e. 0.5 ms), the MIMO array has translated its position in the along-track direction by $\Delta S = v * T_r$. In the whole observation time T_{OBS}, in total $K = \frac{T_{OBS}}{/T_R}$ PRIs are available, that differ as they observe the same scene from slightly different observation angles.

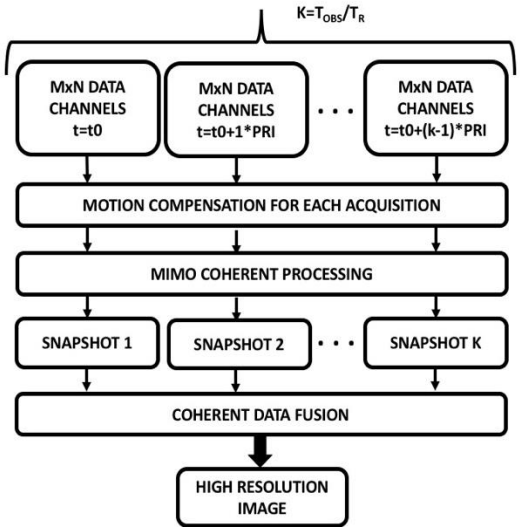

Figure 3-33: SAR-like MIMO processing block diagram

In the block diagram in Figure 3-33 the developed processing scheme is detailed. In the most favourable case, the K translated MIMO virtual array antennas do not have overlapping elements, and a synthetic array is created having KxMxN distinct antenna elements. This improved spatial information, as will be shown in next paragraph, consents to considerably reduce side lobe ambiguity, without altering the real number of TXs and RXs part of the MIMO architecture. During the data acquisition the relative position between the target and the MIMO geometry changes, hence an appropriate motion compensation is necessary to correctly process the acquired data stream. Once completed this step, for each point (x,y) on the image plane, the MIMO coherent processing block implements the log-likelihood detection function reported in Eq. 1-11. In this way in total K range/cross-range maps (in the following also referred to as "snapshots") are obtained and available for data fusion. Combining multiple snapshots (i.e. adding them) a high resolution map with lower side lobes can be obtained.

3.4.3. Results SAR-like MIMO data fusion

In this Section, the results obtained using the above defined SAR-like MIMO processing are discussed. A number of simulations summing up to 48 have been carried out varying the integration time from 1 ms to 100 ms and the nominal ship speed from 10 Km/h to 100 Km/h. From Figure 3-34, it is evident that the longer the integration time, the better the extinction ratio. Furthermore, higher speed values entail a greater translation of the MIMO antenna array and this probably causes a better data decorrelation and in the end an enhanced detection. Please note also that for an integration time of 1 ms, namely without any data fusion, the extinction ratio differs significantly from the value individuated in section 3.3.7. The apparent discrepancy is a direct consequence of the much larger area (150 m x 150 m) chosen for the evaluation of the cross-ambiguity function. The main inferable conclusion is that the grating lobes of the ambiguity function can be considerably mitigated through a coherent data fusion executed on multiple PRIs.

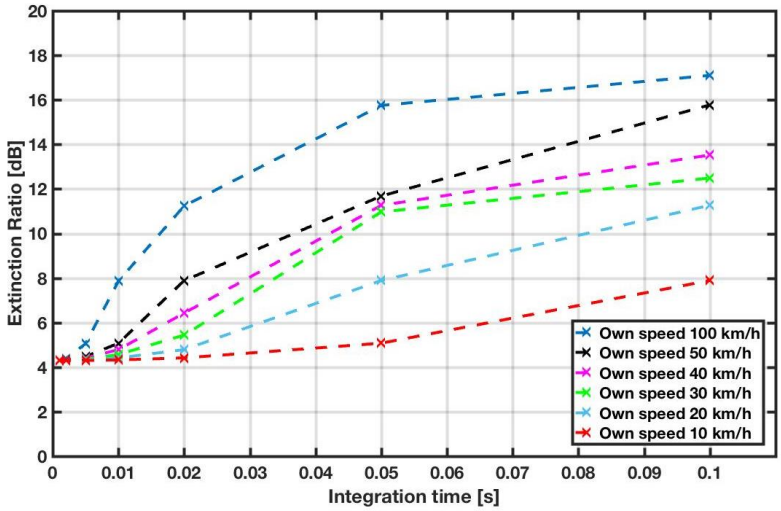

Figure 3-34: SAR-like MIMO side lobe suppression for variable integration times and platform speeds

The extinction ratio passes, in fact, from about 4 dB to almost 18 dB. The ambiguity reduction is essential, as said, to lower overall system false alarm rate in the cross-range dimension.

Figure 3-35 reports the cross-range pattern of the radar ambiguity function for a range of 5000 m assuming a ship speed equal to 50 Km/h and an integration time of 0.1 s. In particular, the red curve refers to the detection statistic obtained using a MIMO coherent processing computed on a single snapshot, while the black dashed curve refers to the MIMO SAR-like data fusion outcome achieved on multiple snapshots. The data fusion improvement is evident: until a distance of about 200 wavelengths (i.e. 6m) from the center, the two curves overlap perfectly. For higher distances, thanks to data fusion, grating lobes are effectively mitigated. Moreover, angular resolution remains unaltered and is approximately 60 cm (i.e., 20 wavelengths) in both cases, almost 3 times better than the range resolution corresponding to a radar waveform having a 100 MHz bandwidth.

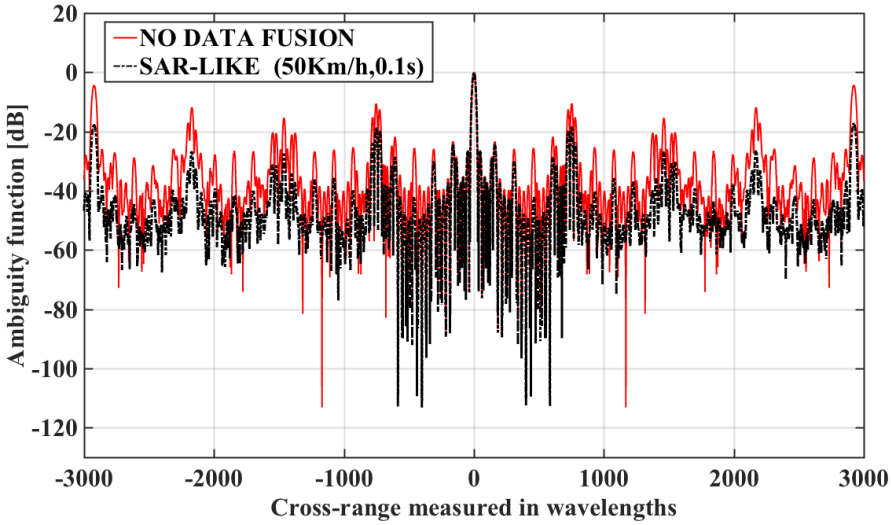

Figure 3-35: Cross-range pattern without data fusion (red curve) and with SAR-like MIMO data fusion (black dashed curve)

3.4.4. SAR-like MIMO processing: robustness to errors in motion compensation

Although it is reasonable to assume that the speed of a ship is constant over 0.1 s, numerous factors can spoil the correct estimation of this critical parameter. Inertial Navigation Systems and modern GPS, usually, provide extreme precise and accurate values. However, if the error depends on

an unknown or imprecise estimation of the target motion (which we have indeed assumed stationary), the resulting incorrect motion compensation can become a critical factor. In order to understand the robustness of the proposed data fusion scheme, the degradation caused by an imprecise motion compensation has been additionally verified. Multiple simulations have been carried out assuming a 0.1 s observation time and a nominal speed of 50 Km/h affected intentionally by a variable error on motion compensation accuracy. The results depicted in Figure 3-36 demonstrate that the method is robust since a 10% error with respect to the nominal speed has only a limited effect on detection performance. In case of no speed discrepancy side lobe suppression amounts to almost 16 dB (see red curve) and, as can be noticed there, even a 30% error still assures a 10 dB suppression which is 6 dB better than the 4 dB result achievable without implementing a SAR-like MIMO data fusion.

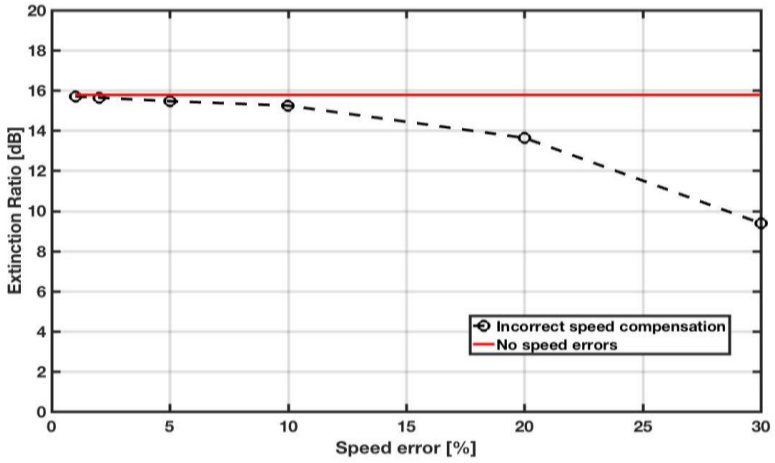

Figure 3-36: SAR-like MIMO data fusion side lobe suppression without speed compensation errors (red curve) and in presence of compensation errors (black dashed curve);

3.5. AUTOMOTIVE SCENARIO

Buyers as well as lawmaker concerns regarding road and traffic safety are pushing big car manufacturers to invest more and more resources in the research of efficient and reliable sensors [77] Currently multiple sensors including cameras, lidars and radar absolve different functions ranging from obstacle avoidance to parking aid or lane change assistant. However, the best sensors even for automotive applications are radars for their innate capacity to operate in all weather and visibility conditions. Radars can be exploited both for on board and for ground systems as, for instance, for cross-road traffic monitoring.

The trend in the automotive sector is to use higher and higher carrier frequencies; using higher frequencies implies multiple benefits: first of all, the possibility to use smaller antennas which can be better integrated in cars, secondly the opportunity to use higher fractional bandwidths supporting a fine resolution and ultimately an enhanced detection capability as current regulation sets higher limits for transmission power effectuated at higher frequencies [78]. In the past the standard for automotive applications was K-band (24GHz), whereas nowadays systems operate in W-band (77-81GHz) [79] and in the near future probably frequencies higher than 100 GHz will be used [80]. As already discussed in Chapter II managing extreme high frequencies is challenging in the RF domain and much easier in the optical domain, where signals with high fractional bandwidths can be easily generated and efficiently distributed over wide distances.

Fine range and angular resolution are required, especially by sophisticated automotive applications like autonomous driving, where a correct knowledge of the surrounding environment facilitates artificial intelligence to find constantly the optimal solution. Furthermore, sensors have to ensure a continuous monitoring of the scene because so the “reaction time” is reduced and in the end this consents to safeguard a higher security standard. As if that were not enough automotive radars are requested to be reliable even in harsh operative conditions and, otherwise than systems designed

for space or defence purposes, tough budget requirements have to be fulfilled. In the light of above delineated requirements a MIMO radar system appears to perfectly satisfy all those aspects: the coherent MIMO approach, leveraging on high fractional BWs allows to reach a fine angular resolution with a small number of antenna elements. In fact, as seen in 1.6.2, when a MIMO network with M TXs and N RXs is installed a virtual array with MxN elements is synthetized. Therefore, though a substantial lower number of antenna elements compared to a full half wavelength phased array is used, an excellent angular resolution is attainable with a substantial system cost saving. At difference to MIMO configurations with co-located antennas, when architectures with widely separated antennas are employed scanning the entire scenario with narrow beam aperture antennas is problematic. Consequently, large aperture antennas are preferred which consent multiple simultaneous acquisitions of the same scene from several aspect angles as well as a continuous monitoring.

In the following the simulative results obtained for two different automotive scenarios are presented. The main purpose of the analysis is to investigate if a MIMO approach can be also extended to vehicular and pedestrian traffic surveillance [81]. In section 3.5.1 simulations related to a ground (at cross-road) scenario are discussed; instead section 3.5.2 is dedicated to simulations done assuming to mount a MIMO system on board (on a car). Simulations have been effectuated both at 24 GHz and at 77 GHz. Thanks to the design indications emerged from the preliminary analysis an optimal MIMO configuration is individuated for both applications and in the final paragraph of this section the outcomes of a detection test effectuated on a complex automotive scenario are reported.

3.5.1. Automotive cross-road scenario

In Figure 3-37 the geometry of the considered cross-road scenario is detailed. Sensors are located on the roadway near the intersection observing the other end of the crossroad and are linearly distributed. Knowing that side lobes of the cross-correlation ambiguity function depend on the number of TXs and RXs part of the architecture, on their geometry and on the fractional BW of the radar signal, all those parameters have been studied with the aim to find a MIMO architecture appropriate to effectively monitor cross-road traffic. For the side lobe study only an ideal point-like scatterer has been simulated, located in T (x_T=0m, y_T=0m) at a distance of 30 m from the baseline. Afterwards, in place of the ideal scatterers, a complex scenario has been imagined where two targets, a pedestrian and a car are present and, as shown in Figure 3-37, aforesaid targets are both approximately 30 m faraway in range (along the y-axis) and separated by 0.5 m in cross-range (along the x-axis).

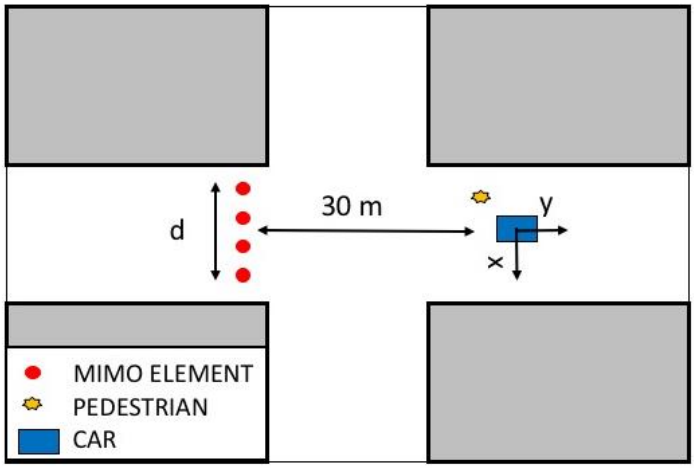

Figure 3-37: Automotive cross-road scenario

In Table 3-9 the main parameters adopted for the cross-road simulations are summarized. Several simulations have been done changing, as indicated, two parameters: the total length occupied by the linear array variable between 5 m and 15 m and the signal bandwidth changed from a minimum of 100 MHz until 5 GHz. For each run, 4 TXs and 4 RXs uniformly distributed, namely equidistant and interleaved, have been assumed and, as usual, in order to reduce the computational burden, the surveillance function is split into two phases: first in search mode potential targets are pre-located and then in image mode a high resolution map is obtained.

Parameter	Value
Carrier frequency (fc)	24 GHz & 77 GHz
Bandwidth (BW)	100MHz/200MHz/500MHz/ 1GHz/2GHz/3GHz/4GHz/5GHz
MIMO configuration	4TX x 4RX
Antenna baseline (d)	5m to 15m

Table 3-9: Automotive cross-road scenario simulation parameters

The results discussed in the following are referred to an area of 4 m x 4 m surrounding the simulated ideal point like scatterer, on which image mode has been computed. In Figure 3-38 the simulative outcomes assuming a 77 GHz carrier frequency are shown for different signal BWs and for different array lengths.

As already pointed out for the already analysed scenarios, a higher signal BW ensures lower side lobes. In fact, as shown in Figure 3-38 (bottom), the extinction ratio raises from few dBs in case lower fractional BWs are used to over 20 dB for a BW of 5 GHz and a total baseline length, d, of 15 m.

Similarly, from Figure 3-38 (top) it can be noticed that the longer the total length, d, the higher the extinction ratio. In particular, the curve related to a 5 GHz BW signal shows that the extinction ratio assumes increasing values from 7 dB till 22 dB, as the baseline is augmented gradually from 5 to 15m.

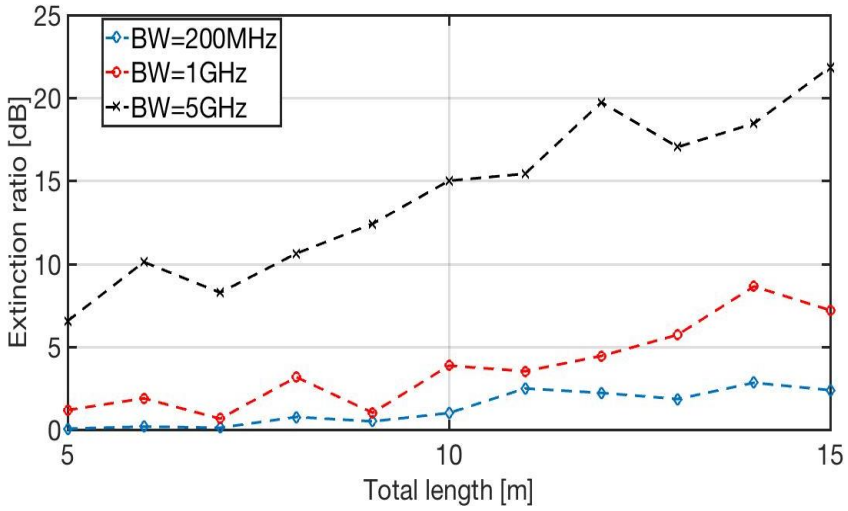

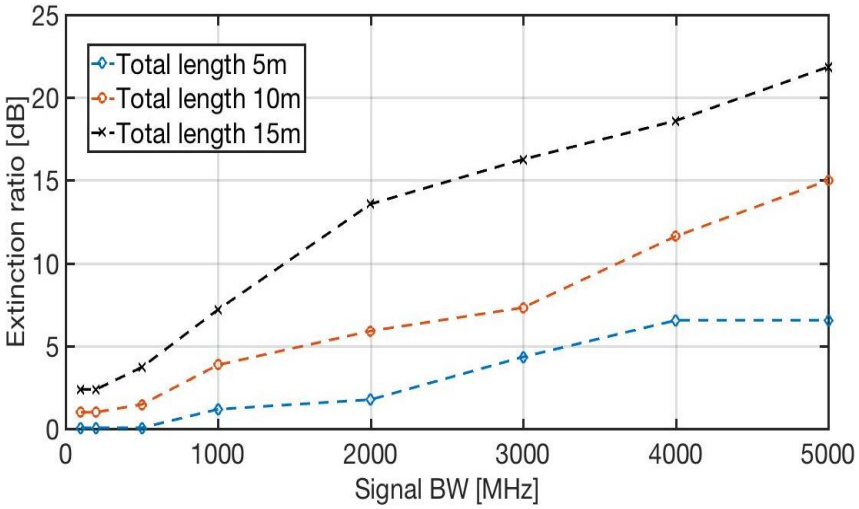

Figure 3-38: Automotive cross-road scenario side lobe suppression for simulations at 77GHz for different signal BWs (top) and variable array lengths (bottom)

In Figure 3-39 the range cross-range maps individuated assuming a 5 GHz BW signal for a 5, 10 and 15 m long baseline are shown, which qualitatively confirm the side lobe improvement as the baseline is increased.

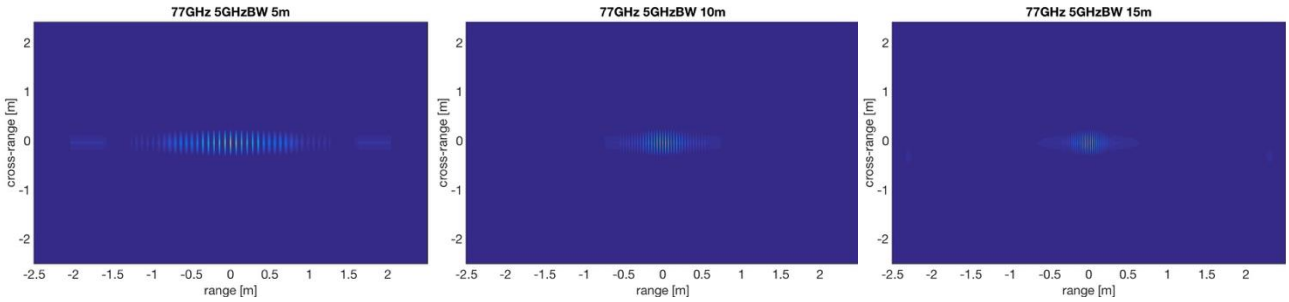

Figure 3-39: Automotive cross-road scenario range cross-range maps for simulations using a 5 GHz radar waveform at 77 GHz with variable baseline lengths 5 m (left), 10 m (middle) and 15 m (right)

The results for the same set of simulations done with a carrier frequency of 24 GHz rather than 77 GHz are depicted in Figure 3-40. The outcomes are similar to those discussed above, except for a slightly better result when a 77 GHz carrier frequency is used rather than a 24 GHz. Besides, the non monotonic increment of the extinction ratio when a 5 GHz BW signal is used and the total antenna length increases is probably associated to an overlap of MIMO virtual array antenna elements, as the geometry is varied.

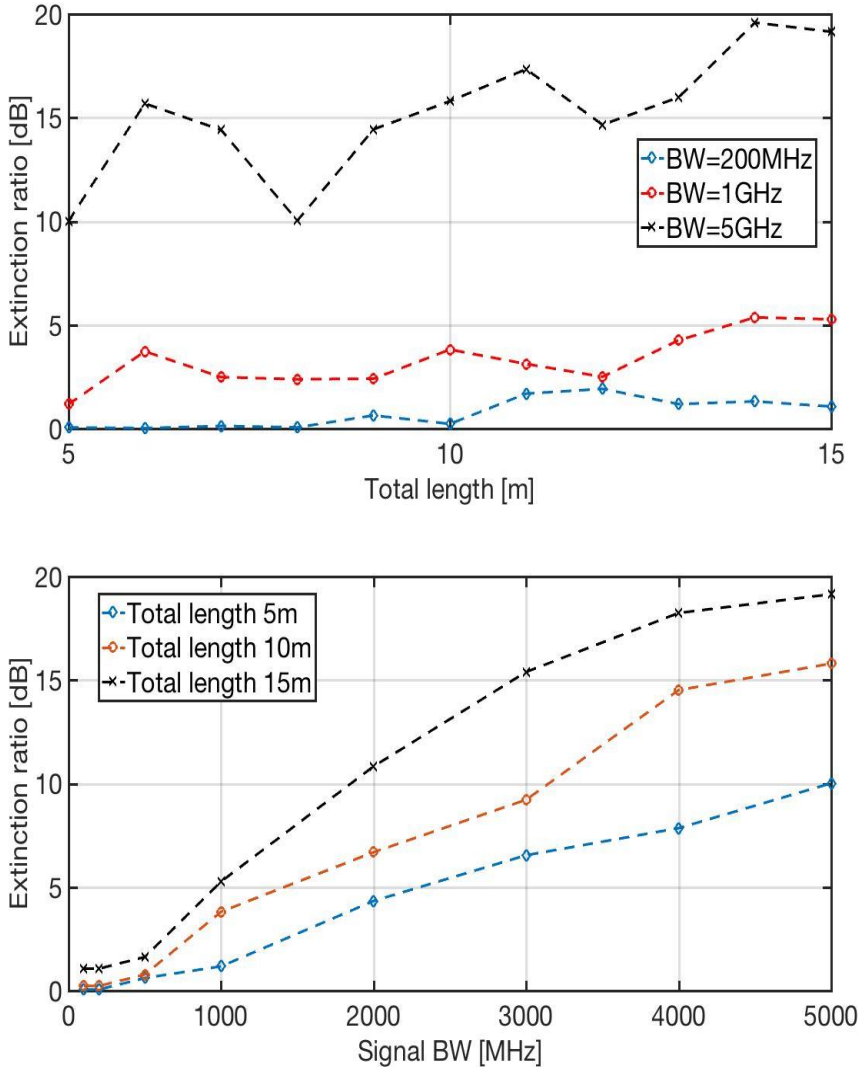

Figure 3-40: Automotive cross-road scenario side lobe suppression for simulations at 24 GHz and for variable array lengths (top) and for different signal BWs (bottom)

3.5.2. Automotive on board (car) scenario

In Figure 3-41 the geometry of the MIMO on-board scenario is sketched; this time all sensors are imagined to be placed on the front or on the side of a car. For this reason, in consideration of the typical dimension of a car a constant total length, d, of 2 m has been considered and, at difference to the cross-road scenario, the number of transmitting and receiving elements has been changed as well as the signal BW in order to understand the effect of cited parameters on side lobe suppression. Although the number of elements is variable, like in the previous scenario, they are uniformly distributed and an ideal point-like scatterer has been assumed, located in T (x_T=0m, y_T=0m) 30 m distant from the car. Finally, the individuated MIMO configuration is tested on the same complex scenario already introduced for the cross-road scenario where, as shown, two targets, a pedestrian and a car are at the same range and closely spaced in cross-range.

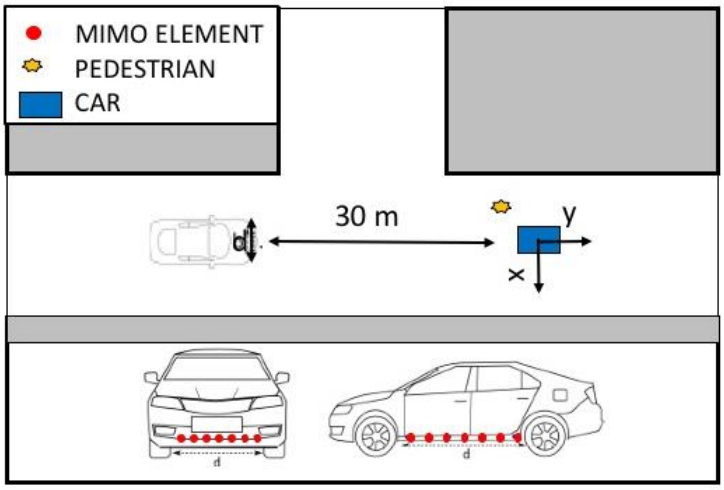

Figure 3-41: Automotive on board (car) scenario

In Table 3-10 the main simulative parameters adopted for on board simulations are summarized. As can be noticed there, two parameters have been varied: the number of TX/RX elements linearly and uniformly distributed over the 2 m total car length and the signal BW from a minimum of 100 MHz until 5 GHz. As for the cross-road scenario high resolution image mode has been computed on an area of 4 m x 4 m surrounding the simulated ideal point-like scatterer.

Parameter	Value
Carrier frequency fc	24 GHz & 77 GHz
Bandwidth (BW)	100 MHz/200 MHz/500 MHz/ 1 GHz/2 GHz/3 GHz/4 GHz/5 GHz
Number of elements	(2 to 8) TXs x (2 to 8) RXs
Total length d	2 m

Table 3-10: Automotive on board (car) scenario simulative parameters

In Figure 3-42 (top), the extinction ratio curves as the sensor element number changes, are plotted. As can be noticed changing the number of elements from 2 to 5 the extinction ratio increases, which reaches values close to 40 dB. However, differently from what expected, paradoxically a 5-element configuration ensures a superior extinction ratio than a 7-element one. This behaviour is likewise the consequence of an unfavourable geometry where MIMO virtual array antenna elements overlap.

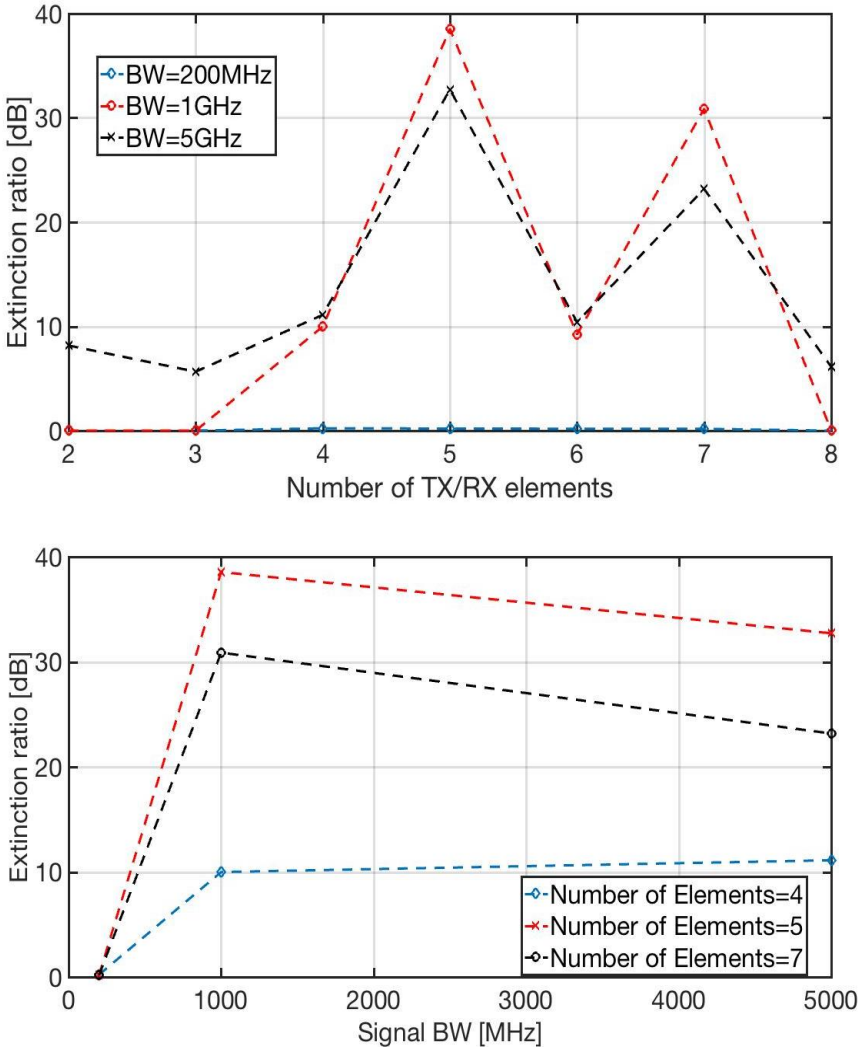

Figure 3-42: Automotive on board (car) scenario side lobe suppression for simulations at 77 GHz for variable number of TX/RX elements (top) and for different signal BWs (bottom)

The importance of signal BW is evident in Figure 3-42 (bottom), indeed, at 200 MHz, no improved detection is possible. Conversely, starting from 1 GHz, an extinction ratio better than 10 dB is ensured.

Figure 3-43 reports the same simulative outcomes depicted in Figure 3-42 obtained simulating a carrier frequency of 24 GHz. Observing aforesaid figures, it is clear that, unless the unlucky geometry with 6 TXs x 6 RXs, more antenna elements as well as a larger signal BW entail a higher side lobe extinction ratio. Furthermore, a comparison between the set of simulations done at 77 GHz and at 24 GHz emphasizes that, given a specific BW, better results are achieved at 24 GHz: in the best case for a 8 TXs x 8 RXs configuration using a 5 GHz BW the side lobe extinction ratio amounts to over 50 dB. This is a direct consequence of the fact that the extinction ratio is proportional to the fractional BW (BW/f_0). Accordingly, given a 5 GHz BW, aforesaid parameter is significantly higher at 24 GHz (BW/f_0 = 20.8%) than at 77 GHz (BW/f_0 = 6.4%).

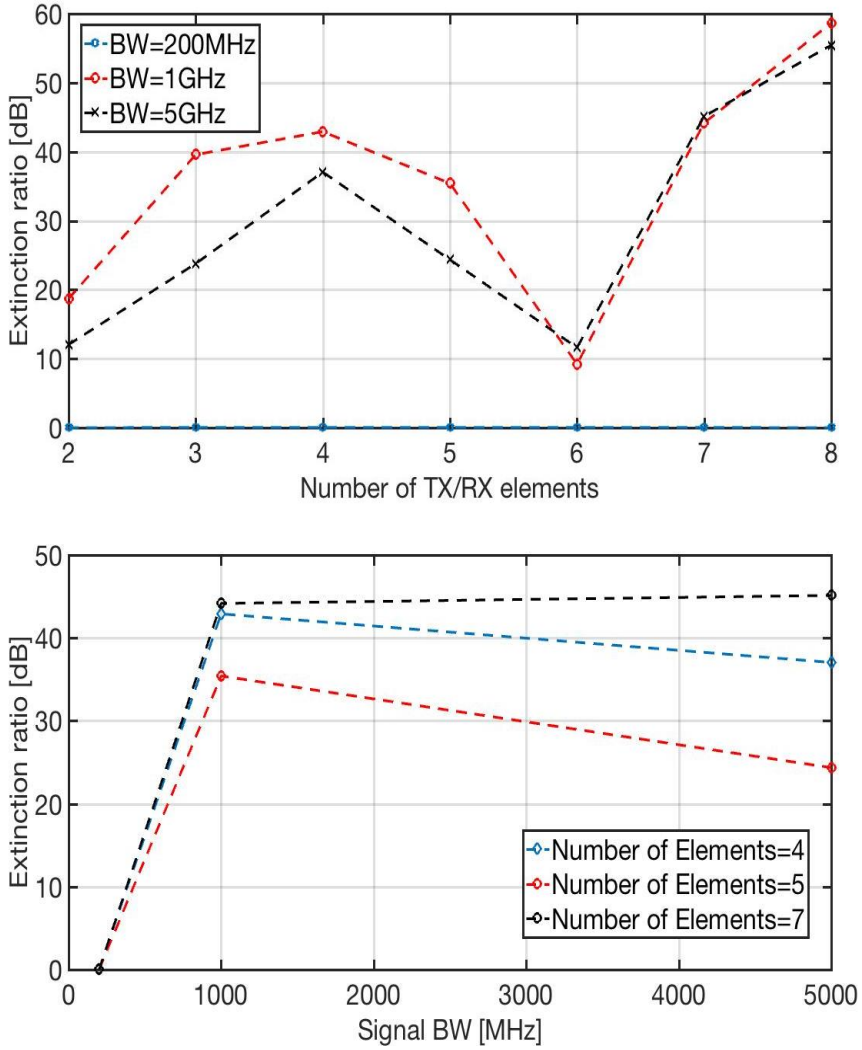

Figure 3-43: Automotive on board (car) scenario side lobe suppression simulations at 24GHz for variable number of TX/RX elements (top) and for different signal BWs (bottom)

3.5.3. MIMO detection test on a complex automotive scenario

Based on the design indications emerged from the analysis carried out a suitable MIMO configuration both for a cross-road and for an on board automotive scenario has been individuated. Here, the resulting architectures are tested on a complex automotive scenario. In Table 1-1 the main system parameters used for the test are listed. In particular, the pedestrian target has been modelled with one single scattering point over an area of 0.5 m x 0.5 m, while the car target has been modelled with 20 uniformly distributed point-like scatterers, occupying an area of 2 m x 2.5 m.

	Cross-road	**Car (On board)**
Carrier frequency fc	77 GHz	
Bandwidth (BW)	2 GHz	
MIMO configuration	4 TXs x 4 RXs	5 TXs x 5 RXs
Total length d	15 m	2 m

Car target location	(0,0) m
Pedestrian target location	(-1.5,1.5) m
Car RCS # scatterers	20
Pedestrian RCS # scatterers	1
Total car RCS_C	10 m^2
Total pedestrian RCS_P	0.5 m^2
Car dimension	2 m x 2.5 m

Table 3-11: Automotive scenario detection test simulative parameters

The range cross-range map obtained in image mode represented in Figure 3-44 (left) and Figure 3-45 (left) clearly show that the pedestrian is detected and resolved. On the contrary, in search mode, as can be noticed from Figure 3-44 (right) and Figure 3-45 (right), neither the pedestrian is detected nor the shape of the car is clearly recognizable. This confirms the importance and superiority of coherent MIMO operations with respect to non coherent MIMO, based only on amplitude information.

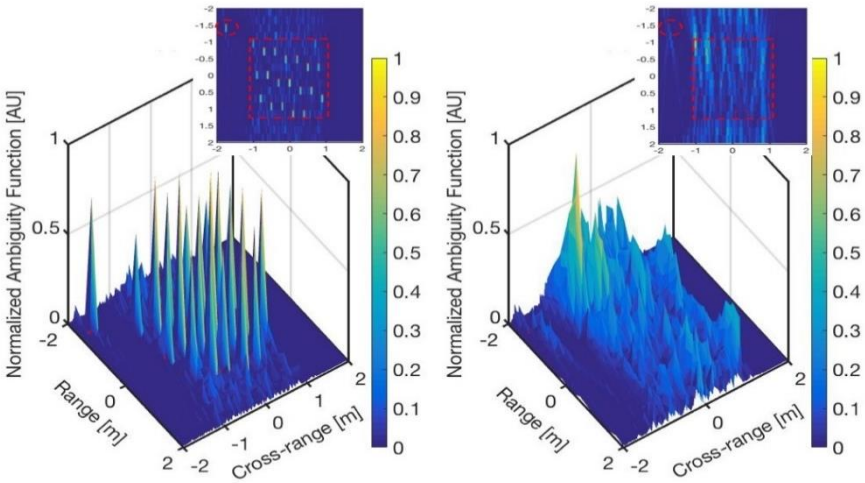

Figure 3-44: Cross-road automotive detection test range cross-range map for coherent image mode (left) and non coherent search mode (right)

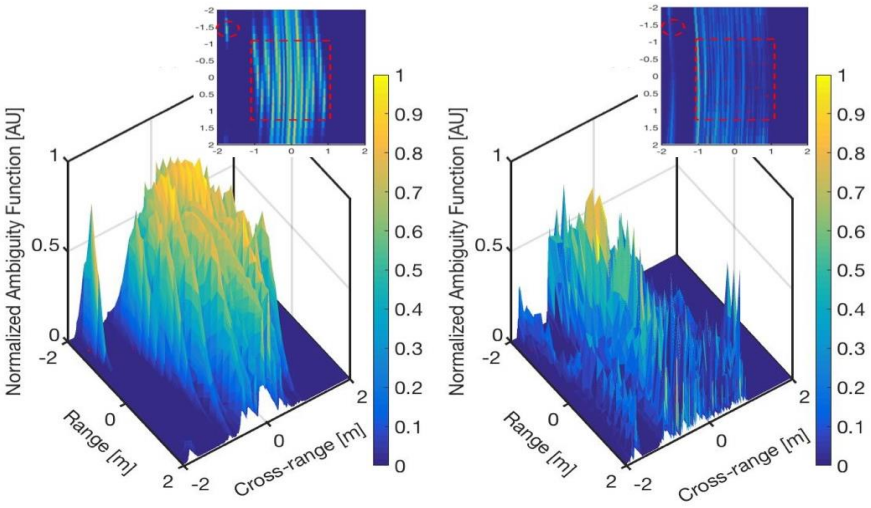

Figure 3-45: On board (car) automotive detection test range cross-range map coherent image mode (left) and non coherent search mode (right)

Despite the on board solution has 1 TX and 1 RX more than the cross-road solution and thus 25 MIMO channels rather than 16 are available for detection, the resolution guaranteed by the the cross-road radar network is much better, as appears manifest, from the comparison of Figure 3-44 (left) and Figure 3-45 (left).

It is opportune to remark that the whole analysis described above is focused on unwanted side lobe suppression and helped us in the design of a feasible architecture, whereas the resolution capability, essentially, depends on the baseline extension. Consequently, since the cross-road antenna elements are distributed on a much longer baseline (i.e. 15 m baseline against an array aperture limited by physical constraints to only 2 m) it is obvious that the cross-road resolution, as verified, results superior than the car resolution.

3.6. MULTI-BAND MIMO DATA FUSION

In paragraph 3.4 a processing scheme which leverages on multiple consecutive observation acquired in time diversity has been examined. Similarly, here, a solution based on data fusion performed on signals collected in frequency diversity is discussed with the intent to enhance side lobe suppression of the MIMO cross-ambiguity function. The basic idea which has suggested to explore this possibility descends from the simple observation that, fixed a certain antenna geometry and carrier frequency, undesired side lobes fall always at the same distance from the main peak. Aforementioned distance is function of the carrier wavelength, thus, if two or more carrier frequencies are employed, theoretically, it is conceivable to considerably lower side lobes through data fusion of data set acquired using multiple carrier frequencies.

A mandatory precondition to get the desired result, is that the same reference system is shared by the entire bi-band or multi-band system. In addition, a perfect synchronization is indispensable. Otherwise the final outcome can become worse than the single band result. In fact, an insufficient time synchronization entails a range or a cross-range localization error among bands which causes the suppression of both unwanted side lobes and target peaks. Another factor to carefully weight is the target dynamic which can cause a target cell shift during multiple consecutive observations of the scene effectuated using multi-band signals. This is a direct consequence of the narrow resolution cell foreseen in MIMO coherent image mode (i.e. in coherent image mode the cell dimension is of the order of the carrier wavelength in order to consent a correct phase compensation). For this reason, the span of time between two or more illuminations of the target in different bands should be as short

as possible. Ideally target illumination should be simultaneous, so that there in no chance that the target can migrate in a different resolution cell, jeopardizing an effective multi-band data fusion.

First the basic principle of operations is discussed and later simulative outcomes realized for the cross-road automotive scenario, already discussed in section 3.5.1, are reported. Furthermore, in section 3.6.1 an additional option has been investigated, where at difference to the previous case the two carrier frequencies are less distant and lay within the same RF band. The motivation behind the study of the latter solution originates from the consideration that in real applications, using adjacent frequencies in the same band, can lead to interesting system simplifications, as, for instance, the opportunity to share antennas and hardware components capable to manage both frequencies (i.e. amplifiers, wide-band filters etc.).

The simulative results fully confirm the validity of the multi-band MIMO approach, based on MIMO acquisitions effectuated in frequency diversity for side lobe mitigation.

3.6.1. Multi-band MIMO processing scheme

The scheme described in the present paragraph is developed with the intent to lower unwanted side lobes which represent the most critical drawback of the MIMO approach. It is evident that an enhanced radar detection is possible provided that more data are available. The increased information content consents to solve ambiguities of the MIMO cross-correlation function and, ultimately, to get a better side lobe suppression. The idea to exploit multiple observations of the scene acquired in frequency diversity rather than in time diversity, as has been done for the MIMO SAR-like approach previously examined, derives from the realization that the position of side lobes depends on two factors: the geometry of the MIMO array as well as on their distance from the baseline. Once, both those parameters are assigned it is easy to notice that side lobes move away from the main lobe as the distance increases and vice-versa. Moreover, at a fixed range the cross-range ambiguity function pattern has the same shape when diverse carrier frequencies are simulated. In particular, side lobes arise at the same distance measured in wavelengths from the main peak. Expressed in other words, if for a specific carrier frequency, f_1 , side lobes are located at $3\lambda_1$, $6\lambda_1$ and $9\lambda_1$ from the main lobe, where λ_1 is the wavelength associated to the frequency f_1 also for another carrier frequency, f_2 , side lobes fall, respectively, at a distance of $3\lambda_2$, $6\lambda_2$ and $9\lambda_2$ from the main lobe. This depends on the fact that ambiguities arise in correspondence of those angular directions where the grating lobes of the virtual MIMO array result. Cited grating lobes fall where the differential one way range between consecutive elements spaced Dpp is exactly equal to $\lambda/2$ [72].

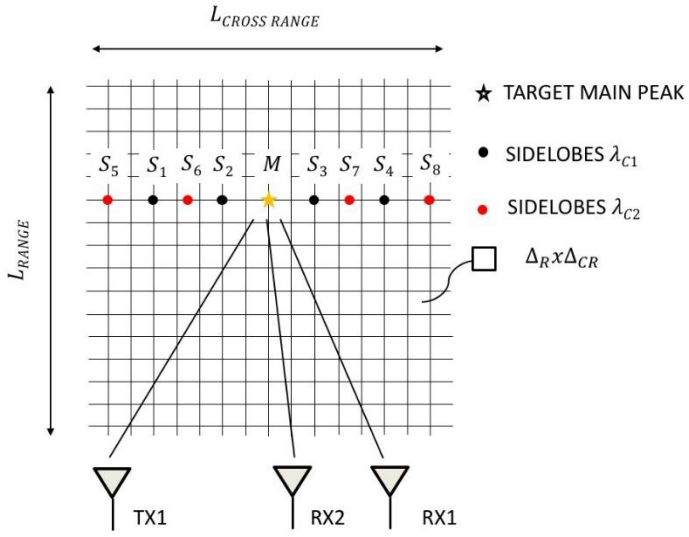

Figure 3-46: Multiband MIMO scenario

For this reason, assuming to deploy the same MIMO antenna configuration using two or more carrier frequencies side lobes fall in different positions, as schematically sketched in Figure 3-46. In particular, simulations carried out show that for a target located in M, M=(R,0), side lobes associated to the first band which has a wavelength λ_{C1} are around the main lobe M in position S1, S2, S3 and S4, respectively, at a cross-range distance $-2\lambda_{C1}R/2Dpp$, $-\lambda_{C1}R/2Dpp$, $+\lambda_{C1}R/2Dpp$, $+2\lambda_{C1}R/2Dpp$ from M. Instead, when a lower carrier frequency is selected to which corresponds a longer wavelength λ_{C2}, side lobes fall in S5, S6, S7 and S8 located at a cross-range distance $-2\lambda_{C2}R/2Dpp$, $-\lambda_{C2}R/2Dpp$, $+\lambda_{C2}R/2Dpp$, $+2\lambda_{C2}R/2Dpp$ respectively. Provided that carrier separation is large enough so that side lobes do not overlap, data fusion can effectively suppress them as both main lobes are situated in M while side lobes change their relative positions. Assuming a linear array, coarsely, selected frequencies should ensure that subsequent inequality is satisfied:

$$\frac{\lambda_{C1}R}{2D_{PP}} - \frac{\lambda_{C2}R}{2D_{PP}} > \frac{\lambda_{C1}R}{4ND_{PP}} + \frac{\lambda_{C2}R}{4ND_{PP}}$$

$$\lambda_{C2} < \lambda_{C1}\frac{2N-1}{2N+1} \qquad \textbf{Eq. 3-1}$$

$$f_{C2} > f_{C1}\frac{2N+1}{2N-1}$$

where, λ_{C1} and λ_{C2} represent the wavelengths corresponding to the selected carrier frequencies f_{C1} and f_{C2} , R the target distance from the baseline, D_{PP} the distance between two consecutive elements of the virtual MIMO array, under the assumption that cited elements are equidistant, and N the total number of virtual array elements.
In the block diagram in Figure 3-47 the developed processing scheme is depicted.

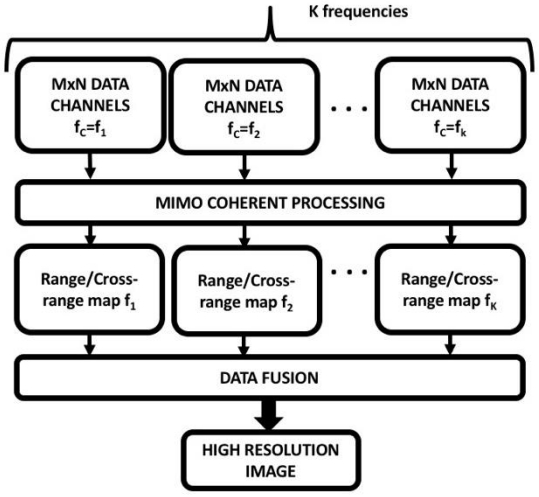

Figure 3-47: Multi-band MIMO processing algorithm block diagram

For each available band image mode is performed. The function is computed for all carrier frequencies on the same points of the grid whose spacing should be chosen in function of the smallest wavelength involved. Once all K normalized range cross-range maps are computed, data fusion can be applied, implementing an appropriate logic, which starting from the single band MIMO maps, consents to individuate a resulting multi-band map. The criterion adopted for data fusion is a key element and has pro and cons. For instance, adding up all contributes is more robust since miss detections are less common. Unfortunately, side lobe suppression is less effective too. On the other

hand, although a multiplication logic enhances side lobe mitigation, detection performance, especially in case of poor system synchronization among bands, is spoiled due to a higher miss detection rate.

3.6.2. Simulative Results Multi-band data fusion

In the next two paragraphs the outcomes of simulations effectuated applying the above outlined processing scheme are discussed. Two different scenarios are considered, each characterized by its specific parameters: in the present paragraph an automotive scenario is studied assuming to use 2 widely spaced carrier frequencies. In next paragraph, instead, 2 frequencies have been selected which, though satisfying the relation individuated in Eq. 3-1, both fall in X-band.

The results shown in the following, as anticipated, refer to the cross-road scenario introduced in section 3.5.1. In particular, simulations have been carried out assuming to implement a MIMO configuration with 4 TXs x 4 RXs having uniformly distributed antenna elements on a 15 m long baseline and to use a 2 GHz BW signal. In Figure 3-48 and Figure 3-49 the high resolution maps individuated for carrier frequency f_{C1} equal to 19.5 GHz and f_{C2} equal to 24.2 GHz are represented.

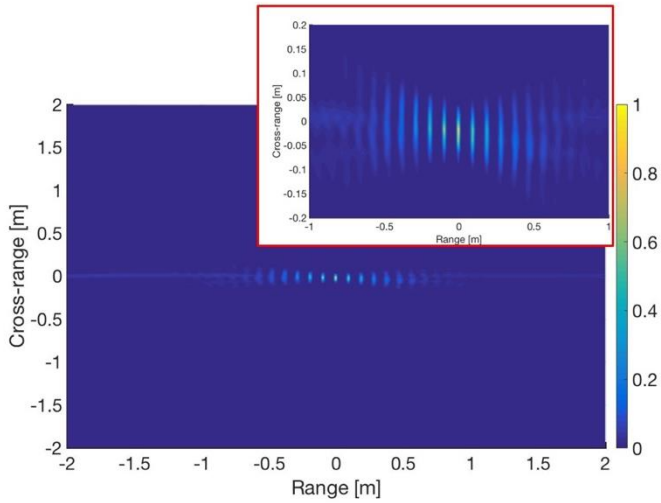

Figure 3-48: Multi-band MIMO processing cross-road scenario range cross-range map for fc1=19.5 GHz

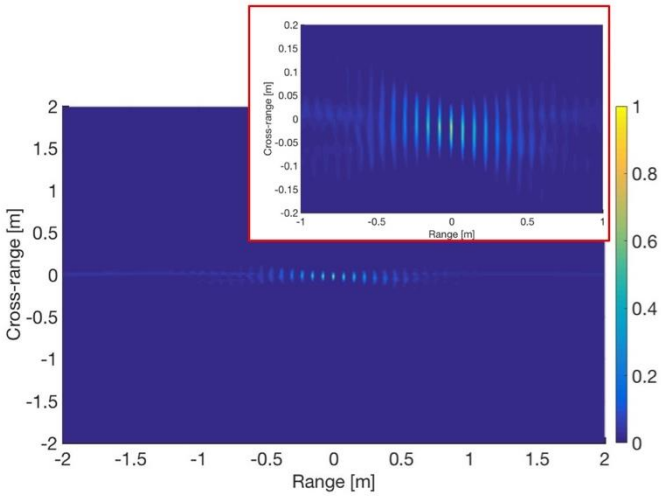

Figure 3-49: Multi-band MIMO processing cross-road scenario range cross-range map for fc2=24.2 GHz

In Figure 3-50 the ambiguity functions obtained from the combination of the two bands are shown: in Figure 3-50 a) and Figure 3-50 b) the outcomes of a multiplication data fusion logic are reported, while Figure 3-50 c) and d) refer to the corresponding outcomes achieved implementing a sum logic. From the comparison of the insets represented in Figure 3-50 c) and Figure 3-50 d) the superiority of the multiplication logic, in terms of side lobe suppression is manifest.

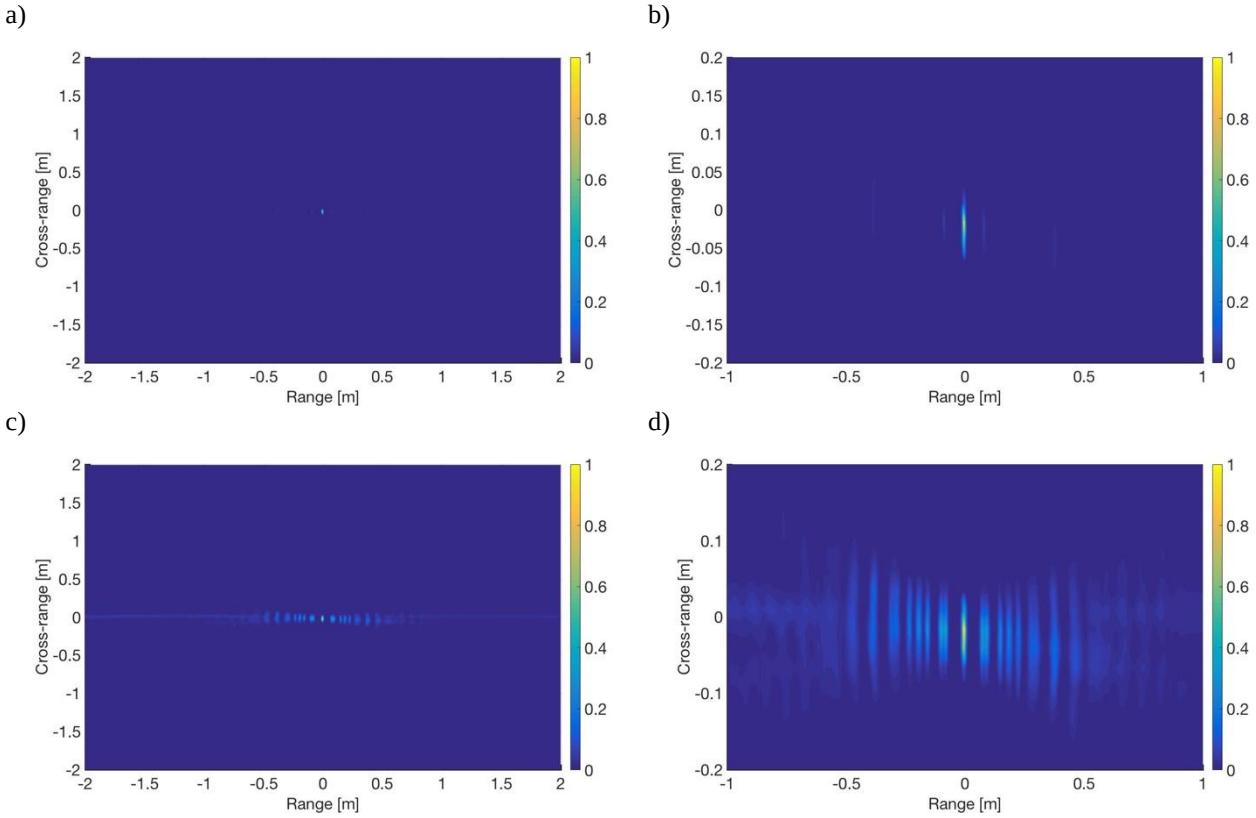

Figure 3-50: Multi-band MIMO processing for an automotive cross-road scenario range cross-range maps obtained through a multiplication data fusion logic (a), inset multiplication data fusion logic (b), sum data fusion logic (c), inset sum data fusion logic (d)

Thanks to multi-band data fusion, indeed, side lobe suppression passes from -1.2 dB and -1.3 dB on each involved band to over -12 dB. This is confirmed also by

Figure **3-51** where the cross-range pattern extracted at a range of 30 m from the baseline are plotted for each band and in case a multiplication multi-band data fusion logic is applied.

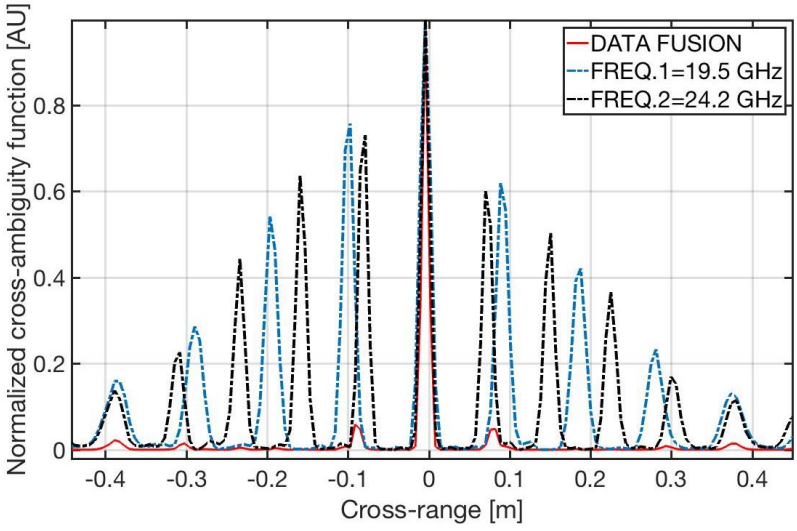

Figure 3-51: Multi-band MIMO processing for an automotive cross-road scenario cross-range pattern mono band fc1=19.5 GHz (blue dashed curve), mono-band fc2=24.2 GHz (black dashed curve) and multiplication data fusion (red curve)

As can be noticed there, side lobes are sufficiently separated so that the red curve which substantially is the product of the blue and the black curve has a side lobe peak of 0.06 at +/-0.9 cm around the center. Aforesaid peaks are much lower than the original peaks of the mono-band curves having approximately a relative amplitude of 0.75 (75% of the main peak intensity).

3.6.1. Simulative Results Multi-band data fusion for closely spaced bands

The results shown in the present paragraph refer to the coastal scenario described in paragraph 3.1. In this case multi-band simulations have been carried out assuming a MIMO configuration with 6 TXs x 5 RXs where elements are uniformly distributed over a circular baseline with a radius of 150 m and the BW of each transmitted signal is 100 MHz large. In Figure 3-52 a) Figure 3-52 b) the high resolution maps individuated, respectively, for carrier frequency f_{C1} equal to 9.0 GHz and f_{C2} equal to 10.2 GHz are represented. Figure 3-52 c) and Figure 3-52 d) show the same outcomes obtained when a multiplication and a sum data fusion logic are adopted. As already assessed for the automotive scenario, a multiplication criterion permits an enhanced side lobe suppression.

Thanks to multiband data fusion, indeed, side lobe suppression passes now from less than -1 dB (i.e. -0.45 dB and -0.5 dB) to a final value of over -8 dB.

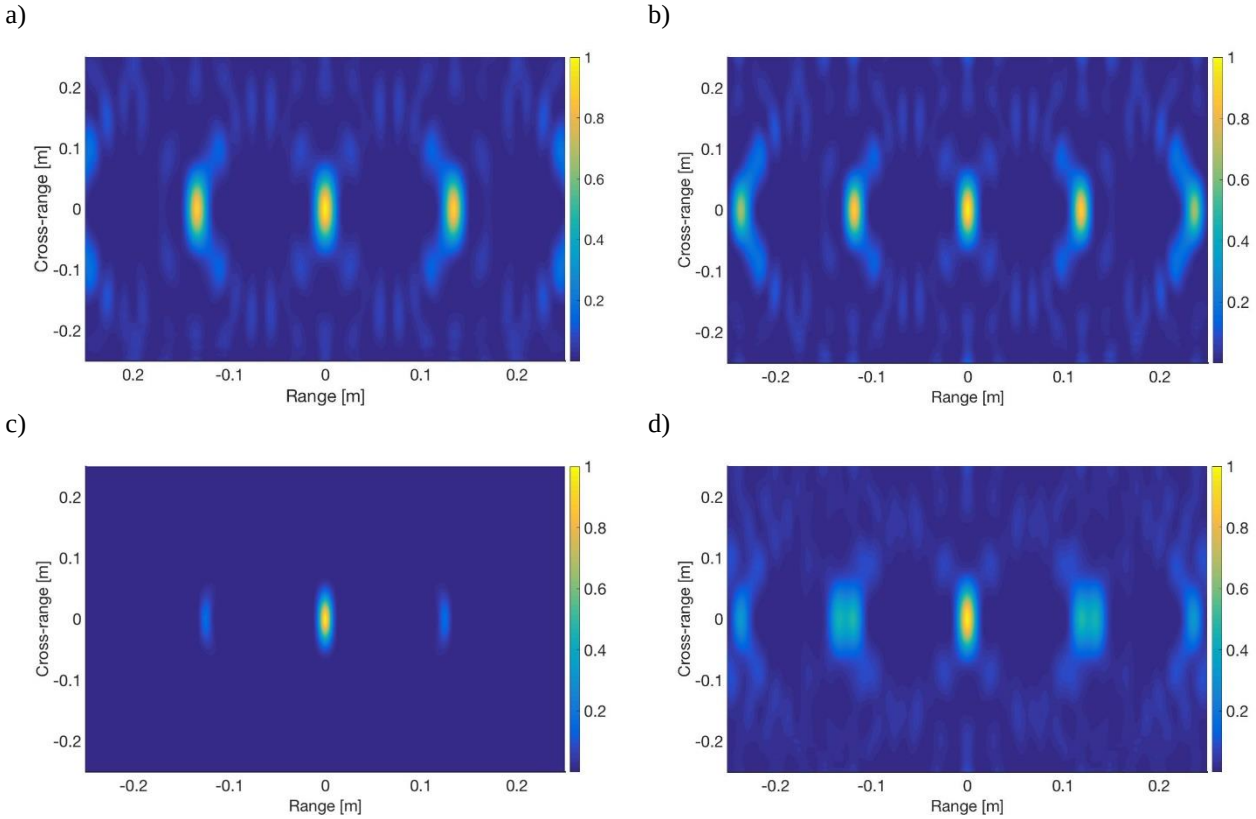

Figure 3-52: Multi-band MIMO processing coastal scenario range cross-range maps for fc1=9 GHz (a), for fc2=10.2 GHz (b), for a multiplication data fusion logic (c) and sum data fusion logic (d)

Observing the cross-range pattern extracted for a simulated point-like scatterer located at a distance of 150 m from all MIMO elements (i.e. the target is situated exactly in center of the circular antenna baseline) represented in Figure 3-53 side lobes overlap more than in the previous examined situation. This is imputable to the fact that the separation between the selected carrier frequencies is 1.2 GHz, more than 4 times lower than the 5 GHz frequency distance, supposed for the automotive scenario. Subsequently, involved wavelengths are closer and so are the side lobes of the mono-band ambiguity functions. This completely justifies the lower side lobe mitigation result achieved with respect to the automotive scenario.

Nonetheless, side lobes associated to mono-band operations are closer, the red curve related to the data fusion curve which represents the product of the blue and the black curve has a side lobe

peak of circa 0.15 shifted at +/-0.12 cm from the main lobe. Aforesaid peaks are visibly lower than the peaks of the original curves, having approximately a relative amplitude of 0.9 (90% of the main peak intensity).

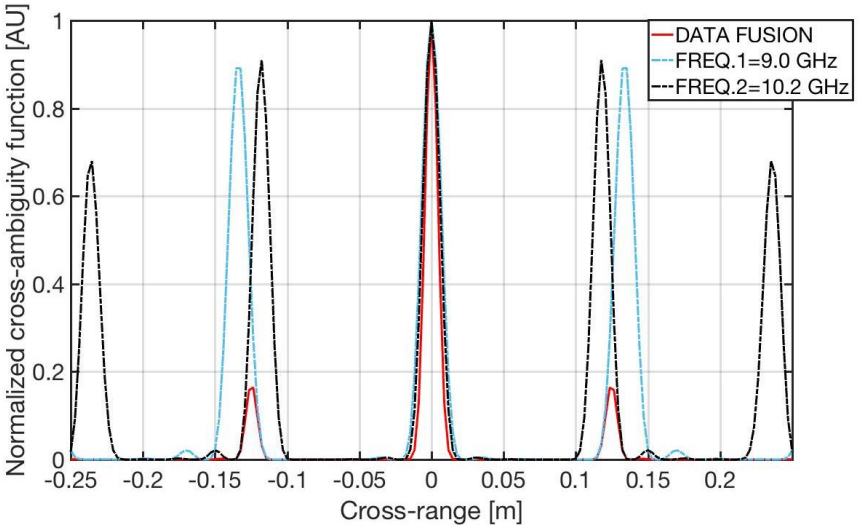

Figure 3-53: Multi-band MIMO processing for a coastal scenario cross-range pattern mono-band fc1=9.0 GHz (blue dashed curve), mono-band fc2=10.2GHz (black dashed curve) and multiplication data fusion (red curve)

4. REAL DATA PROCESSING

In this Chapter the outcomes of real data MIMO processing are reported. In total three experimental activities are described effectuated in different conditions and deploying for each experience a specific set-up. First a MIMO 1 TX x 2 RXs has been implemented with the aim to investigate the effectiveness of a photonics-based centralized radar architecture. Test done in an emulated maritime scenario have allowed to prove the strength of the employed HW solution and to individuate critical aspects as well. Thanks to the lessons learnt during aforementioned field trials, subsequently an outdoor and an indoor experiment have been realized. In particular, for the outdoor experiment a MIMO 2 TXs x 2 RXs architecture has been implemented and, as far as we know, for the first time a photonics-based coherent MIMO radar network has been tested in an outdoor environment. Instead for the indoor experiment, still ongoing, a MIMO 2 TXs x 4 RXs configuration has been used. The experimental set-up of the last two experimental activities differ completely. In fact, while in the outdoor experiment photonics is exploited also for signal generation and detection in the indoor trial campaign photonics is exclusively adopted for signal distribution among the central unit and multiple radar peripherals. Futhermore, while in the first two occasions, related to down-scaled maritime scenarios co-operative moving targets have been detected, the indoor experiment refers to an automotive application and motionless targets have been used. Despite the difficulties associated to real data processing the results are very promising, since a remarkable angular resolution improvement has been demonstrated. Finally, a good match between real data outcomes and the corresponding simulated ones, as described in the last part of the Chapter, represents a first step towards the validation of the self-developed MIMO scenario simulator.

4.1. MIMO 1 TX x 2 RXS FIELD TRIALS IN TIRRENIA (PI)

The first multistatic experimental activity has been carried out in March 2017 at the facilities of the Italian Navy in Tirrenia (Pisa). The field trials have been conducted using a modified version of the photonics-based dual band radar PANDORA described in section 2.5. In particular, the prototype has been properly modified so that, instead of operating in dual band mode (i.e. X and C band) with two monostatic RTX antennas one dedicated to X-band operations and one to C-band operations, the modified version can solely work in single band mode (i.e. only in X-band) and can manage two receivers. Therefore, a multistatic radar system having 1 TX and 2 RXs has been built.

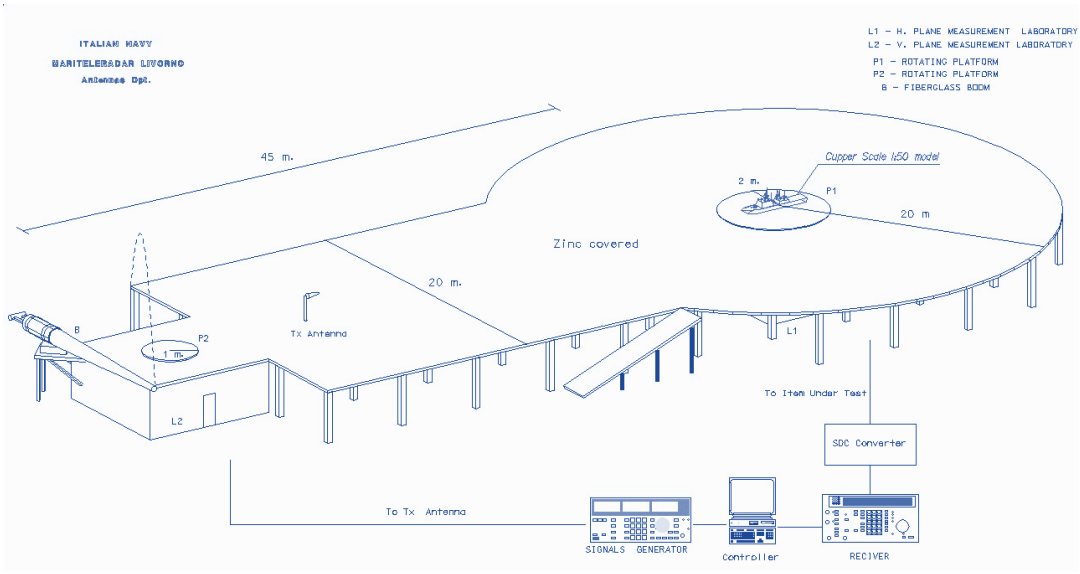

Figure 4-1: Antenna Test Range lay-out (facility of the Naval Research Centre CSSN ITE Livorno)

The experimental activity has been conducted at the Antenna Test Range of the the Italian Navy in Tirrenia (Pisa) so as to have environmental conditions as close as possible to those present in a real maritime scenario. Aforementioned facility is usually employed to get the radiation diagrams of naval antennas, prior to embark them on military ships. The uniqueness of the Test Range, as can be noticed from the lay-out depicted in Figure 4-1, is that it has got a zinc covered plane, which mimics the EM behaviour of the sea surface.

In the light of the minimal radar ranges expected for the test, less than 100 m, due to the fact the Test Range has a maximum length of circa 65 m and is about 40 m large, ultra-wideband (1 – 18GHz) Vivaldi-shaped horn antennas with 50° HPBM aperture and 12 dBi gain have been used.

The photonic core has been placed in the Laboratory L1 under the rotating platform and the two radar heads on the platform P1 (see Figure 4-1). The RX_1 has been placed close to the TX operating in a quasi monostatic configuration while the RX_2 has been placed far away from the TX realizing so a bi-static configuration with a 15 m long baseline (TX-RX_2).

Figure 4-2: Antenna Test Range field trials experimental set-up outdoor (left) and indoor equipment (right)

Moreover, in consideration of the horn antenna angular coverage, all targets have been positioned in a rectangular area, 15 m large and 25 m long. With respect to a bidimensional reference system individuated by the range axis (x-axis) disposed perpendicular to the baseline and the cross-range axis (y-axis) corresponding to the baseline axis oriented from RX_2 towards the unique TX, the target area encloses all points with a range between 15.5 m and 40.5 m and with cross-range between -7.5 m and 7.5 m. For simplicity, the area has been further divided into square cells having 5 m side, as schematically depicted in Figure 4-9.

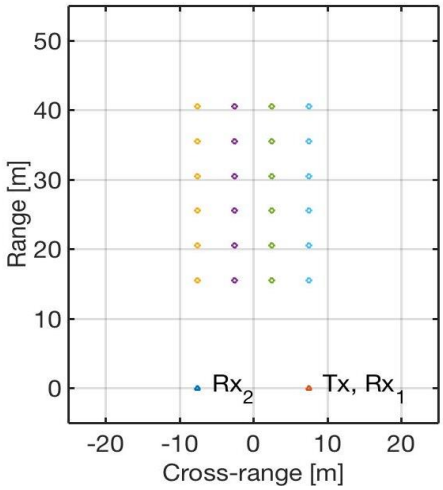

Figure 4-3: Multi-static 1 TX x 2 RXs Tirrenia field trials target geometry

Multiple data acquisitions, each 100 ms long, have been effectuated either with a single or with multiple targets, placing them on different points of the grid. In this way numerous different transmitter-target-receiver geometries have been investigated. Essentially, two kind of targets have been used: a calibrated sphere with a RCS equal to 1 m^2 (i.e. 0 dB_{sm}) and a metallic box having a RCS equal to 14.000 m^2 (i.e. 41 dB_{sm}). Furthermore, also moving targets have been used in order to facilitate radar detection, which results particularly challenging in the replicated sea clutter environment. In Table 4-1 all relevant system parameters used for the experiment are summarized.

Parameter	Value
Target Radar Cross Section	1 m^2 (0 dBsqm) Sphere 14000 m^2 (41 dBsqm) Box
Carrier Frequency	9.875 GHz (X-band)
Wavelength	0.03 m
Antenna Gain RX	15 dB
Antenna Gain TX	15 dB
Pulse duration Ti	2 µs
Pulse rep. interval Tr	50 µs (PRF=20 KHz)
Radar Non Ambiguous Range	7.5 Km
Compression gain	40
Signal Modulation	CHIRP
Signal Bandwidth	20 MHz
Radar resolution	7.5 m
Transmitted Peak Power	22 dBm (160 mW)

Table 4-1: Multistatic 1 TX x 2 RXs Tirrenia field trial main radar network parameters

4.1.1. Experimental results

First a back to back calibration (i.e. the transmitter has been connected directly to the receivers) has been performed with the aim to individuate the different system delays associated to the two available channels (CHs): CH_1 related to the $TX\text{-}RX_1$ combination and CH_2 related to the $TX\text{-}RX_2$ combination. Once individuated the system delays, that measured in samples amount respectively to 6182 samples for CH_1 and 7190 samples for CH_2 corresponding, given the 400 MHz ADC sampling frequency used for the experiment, to 2318 m and 2696 m, a standard range-Doppler processing has been performed on each available data channel.

In total 1000 PRIs have been processed, hence the expectable Doppler resolution is 20 Hz corresponding to 0.3 m/s speed resolution. From the acquisition taken with 2 targets, the metallic box placed in position B2 (cross-range=-2.5m, range=20.5m) and the sphere in C5 (cross-range=+2.5m, range=40.5m) moving away a sensitivity gap between the two channels is evident. Indeed, while in Figure 4-4 (left) the box is clearly visible and the sphere moving away at 2m/s is barely visible, processing the same data set relative to CH_2 both targets are spotted. The supposition is confirmed by the direct evaluation of the signal dynamic from which emerges that samples related to CH_1 are compressed in 5 amplitude levels, whereas for CH_2 the acquired signal occupies 55 out of 256 possible digital sample levels. This totally explicates the discrepancy noticed between the two channels.

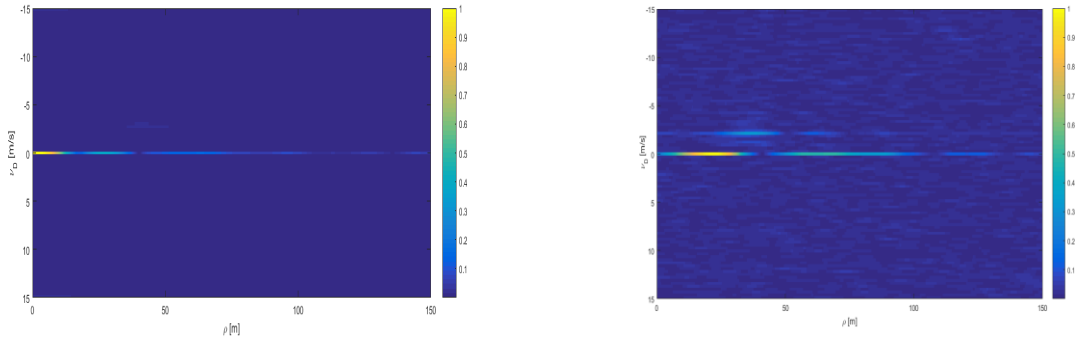

Figure 4-4: Range Doppler maps for multi-target scenario with box target in B2 and moving sphere target in C5 for CH_1 (left) and CH_2 (right)

However, despite multiple problems, including the above discussed sensibility gap among the two available channels, direct interference between the transmitter and the receivers, a limited resolution capability (i.e. 7.5 m) and extremely short radar ranges as well as a significant stationary clutter contribute due to the metallic Antenna Test Range plane (realized with the specific purpose to replicated the sea surface clutter) and clutter originated from the surrounding environment (i.e. tree clutter), a preliminary multilateration data fusion algorithm has been profitably implemented.

In order to estimate the clutter contribute within the received signal when targets are on the scene following extra data acquisitions have been taken:

- No target: Antenna Test Range without any target;
- Back-to-back: the transmitted signal is sent directly from the TX to the RX via RF cables;
- Sky: antennas are oriented upwards pointing at the sky.

In Figure 4-5 a comparison of the cross-correlation functions, computed for the three above listed acquisitions, is made. The red curve related to the the back to back acquisition, represents the ideal radar waveform auto-correlation function; the blue curve related to the sky acquisition, as can be noticed, presents a much lower intensity than the other two curves. Finally, the yellow curve associated to the no target acquisition has the highest intensity and three evident peaks: the first shifted indicatively 3 m forward with respect to the corresponding back to back peak, plus two

additional peaks located at 50 m and 100 m bi-static range, probably caused respectively by a metallic structure positioned next to the rotating plane P2 and to tall trees surrounding the Test Range platform.

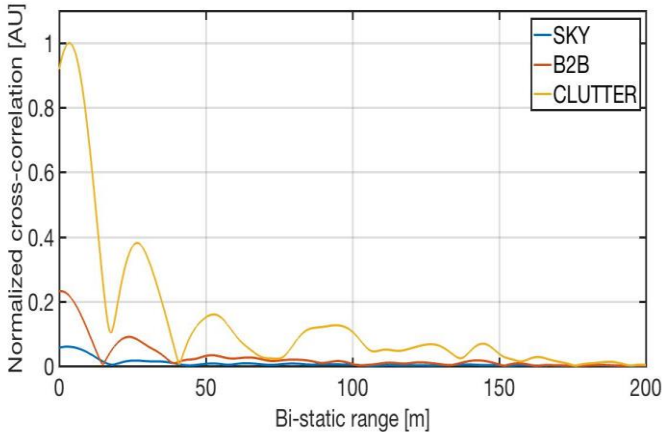

Figure 4-5: Cross-correlation functions for CH_2 for sky (blue curve) , back-to-back (red curve) and no target (yellow curve) acquisitions

In Figure 4-6 the result obtained processing the acquisition taken with 1 targets, the metallic box, placed in position B6 (cross-range=-2.5m, range=40.5m) is shown. The green circles are drawn at ranges where the relative peaks of the cross-correlation function associated to CH_1 have been spotted and, since CH_1 refers to a monostatic radar, the candidate target positions are all points equidistant to the TX-RX_1 position; hence located on a isorange circumference. The purple ellipses, instead, are drawn at the bi-static ranges where the relative peaks of the cross-correlation function associated to CH_2 have been detected. In this case all candidate positions are equidistant to the two foci of the ellipses, which coincide with the TX and the RX_2 position. The bi-static radar locates correctly the target at a bi-static range of circa 41 m while the monostatic radar cannot individuate the target. A possible explanation for the miss detection, as already pointed out is the lower receiver sensibility available for CH_1, as well as the fact that the target probably retro-scatters or reflects more energy towards the RX_2 than its retro-scatterers (back-scatters) towards RX_1, since its position falls on the symmetry axis of the TX-target-RX_2 geometry.

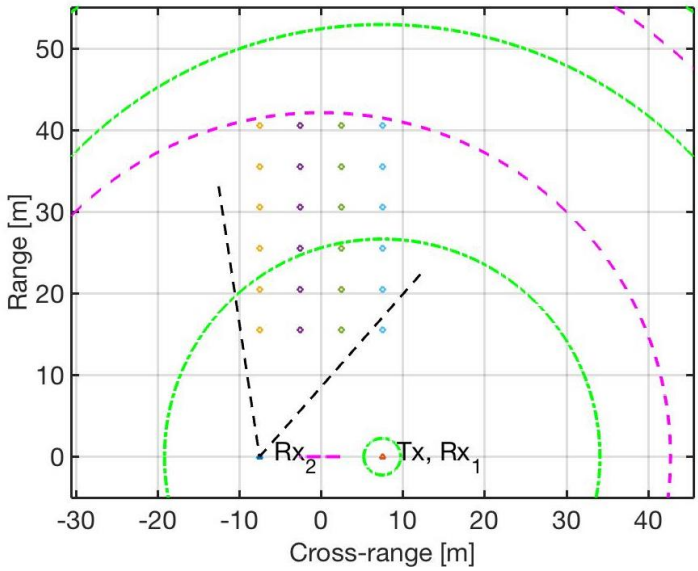

Figure 4-6: Multi-lateration data fusion for acquisition with box target in B6

In conclusion the experience has been very useful because for the first time a photonics-based multi-static radar network has been tested outdoors as well as developed processing algorithms applied on real data set. Faced problems, either concerning HW or SW aspects (i.e. RF interference, stationary clutter and bi-static RCS issues), except for the sensibility gap, have been addressed and

successfully overcome.

4.2. OUTDOOR MIMO 2 TXS X 2 RXS EXPERIMENT

In this Section an outdoor experiment carried out on a down scaled coastal scenario using a radar network developed within the NATO-funded “Multistatic and multi-band coherent radar fleet for border security (SOLE)", project is reported [82]. The discussion is organized as follows: first the experimental set-up is introduced, then the adopted processing algorithms are examined. In particular, a different processing scheme has been adopted for search mode in order ensure a superior clutter suppression, maintaining, at the same time, an acceptable processing complexity. Finally, obtained outcomes are discussed in detail.

4.2.1. Experimental set-up

The architecture of the photonics-based coherent MIMO radar network demonstrator is sketched in Figure 4-7. It is composed by a photonic core (PC) acting as central unit (CU) and by two remote radar peripherals (RPs). Each RP is connected to the PC through 3 optical fiber links: an up-conversion link for the distribution of the radar signal generated by the PC, a down-conversion link to send the echoes received from the targets to the PC for centralised processing and an additional link to exchange an unmodulated optical source between the PC and the RPs. The optical source link is exploited by the remote RPs to load the received RF signal which has to be transferred to the PC. This architecture avoids that each RP has to be equipped with a local optical oscillator keeping so the peripheral complexity low. Exploiting signal distribution implemented via OF, RPs can be sited very far away from the PC. Therefore, unprecedented wide antenna baselines can be realized.

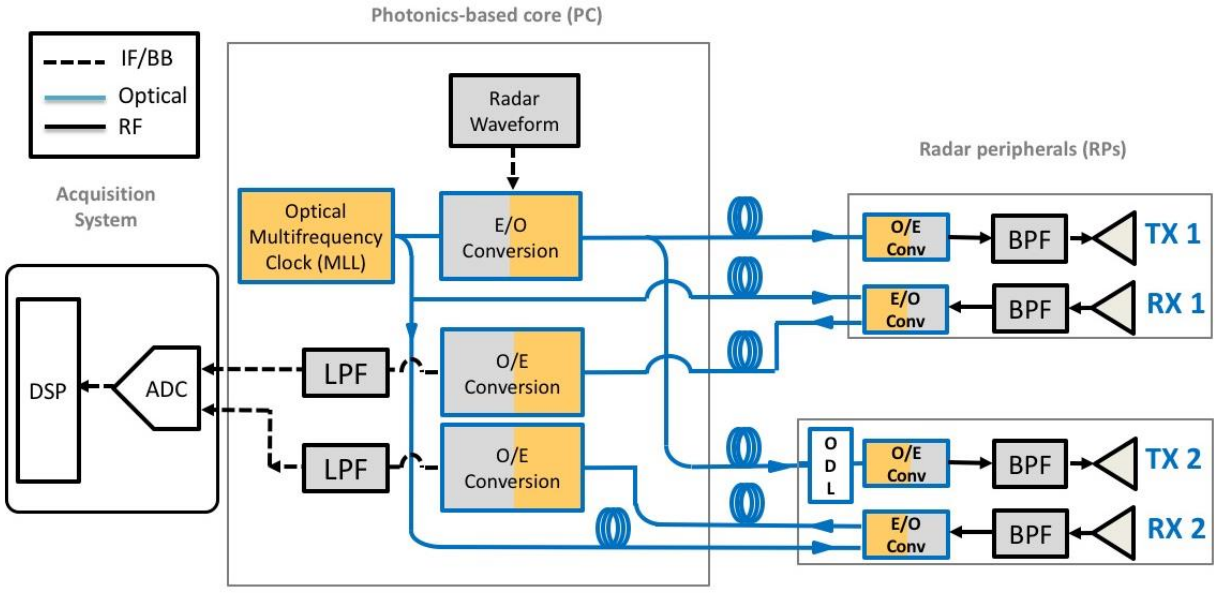

Figure 4-7: Experimental photonics-based MIMO set-up used for outdoor 2 TXs x 2 RXs experiment

Indeed, one of the key advantages of such an architectural choice consists in centralising most of the system complexity into the PC, shared among many low-complexity peripherals. Another interesting feature is the possibility of employing a single, highly stable, master optical clock, which provides the required high coherence among all the spatial distributed RF sensors. Thus, the use of many electronic LOs is avoided, along with the necessary operations of multistage frequency up- and down-conversion. Therefore, the coherence is guaranteed by the centralized shared optical master clock, without the need for complex and resource-consuming synchronization techniques to phase-lock distributed LOs. In particular, the shared optical source is a solid-state MLL, sited inside the PC.

Being the MLL output a periodic train of optical pulses, its optical spectrum is a comb of several lines, spaced by the pulse repetition rate (i. e. 400 MHz), acting as an optical multi-frequency oscillator. The intrinsic, very high phase coherence between the comb lines, as seen in Chaper II, allows to generate extremely pure RF oscillations [83]. More in general, this features enable the photonic up-conversion of the radar waveform from BB/IF to the RF domain, as well as the photonic down-conversion of signals from RF to IF. In case of up-conversion, the MLL is modulated by the digitally-generated signal thanks to an electro-optical modulator (EOM), operating its E/O conversion, and then up converted by photo detection at multiple frequencies, paced by the MLL repetition rate [60][65] [84]. After the photodiode, a microwave BPF can select the component at the desired RF frequency. As regards the down-conversion, the acquired RF signal similarly modulates the MLL, thus undergoing E/O conversion and, later, it is converted back to the electrical domain as several replicas spaced in frequency by the MLL fundamental repetition frequency. The closest replica to baseband is the signal down converted to IF [60] [55]. These processes allow for the flexible generation and the acquisition of RF signals on a very wide frequency range, up to tens or hundreds of GHz, thanks to the broadband optical spectrum of a MLL and to the electrical BW of devices, like EOMs and PDs.

As reported in Figure 4-7, the optical multifrequency master clock is employed for transmission as well as for signal generation. Therefore, its output is equally divided on two paths. The first one is modulated by the radar waveform, which is E/O converted and sent to the TXs in each RP through a span of optical single-mode fiber (SMF). On the second path, the MLL output is not modulated, but directly delivered on SMF to the RX modules in the RPs. The efficient RPs remote control is possible thanks to the SMF, that guarantees the absence of electro-magnetic interference, extremely low power losses, and a good preservation of the signal coherence, even on broad BWs [85]. It is also important underlining that, employing a single MLL for the photonic up- and down-conversion of, respectively, the generated IF and received RF signals, guarantees the preservation of the distributed signals coherence and a very precise time and phase synchronization of all involved subsystems.

The up-conversion to RF frequency of the IF signal is operated inside the TX modules of the RPs, by converting the E/O converted radar waveform back to the electrical domain. In the proposed experiment, the DAC in charge to generate the radar waveform produces a 100 ns-long rectangular pulse at IF = 100 MHz, with a BW of 100 MHz, obtained by linearly chirping the IF frequency. Monostatic range resolution is 1.5 m, as the selected radar waveform BW is 100 MHz large. Although pulses are transmitted in order to separate the TXs in time domain, actually the radar system has no blind range since both RXs receive continuously. The PRF is 20 kHz (PRI= 50 μs) thus the unambiguous range is 7.5 km. This signal is E/O converted by modulating the MLL, sent to the RPs, where it is photo detected, filtered, amplified, and eventually transmitted by the antenna. The employed PDs have an electrical BW of 10 GHz, the RF band-pass filters are centered at the RF carrier frequency, which is 9.7 GHz, and have a -3 dB BW of 100 MHz. The antennas used for transmission are Vivaldi-shaped horn antennas with a 50° HPBW, operating from 1 to 18 GHz, with a gain of 12 dBi. An ODL inserted before the O/E block associated to TX_2 is employed to realize waveform orthogonality in the time domain. The ODL is implemented by a 1 km-long SMF spool. Therefore, considering that the SMF core refractive index reduces the speed of light by 1/3 with respect to vacuum, the obtained time delay is $\Delta T = 5$ μs, which separates in time the waveforms transmitted by the two RPs. Accordingly, the unambiguous range passes from 7.5 km to 750 m.

The antennas employed by the RXs are slightly smaller than those used in transmission, have a 46° HPBM and can operate from 2 to 18 GHz providing a gain of about 12 dBi. The echoes received by the latter antennas are amplified, filtered and then E/O converted, by modulating with an EOM the unmodulated MLL output delivered to the RPs. Afterwards, the E/O converted received signals are sent back to the PC and down-converted at IF by O/E conversion thanks to two PDs. The IF signals are then low-pass filtered and acquired by a two-channel ADC at 400 MS/s.

In Table 4-2 the main radar parameters used for the experiment are listed.

Parameter Name	Parameter Value/Description
MIMO TXs	2
MIMO RXs	2
Signal Waveform	Linear Frequency Mod. (LFM) Chirp
RF	9.7 GHz
IF	100 MHz
Radar waveform PW	100 ns
Radar waveform BW	100 MHz
PRI	50 μs
TX Output Power	200 mW
Sampling speed	400 MS/s
Target RCS	1 m^2 (0 dBsm)
Horn Antenna Gain/HPBW	12 dBi
Overall System Losses	21 [dB]

Table 4-2: MIMO radar parameters outdoor 2 TXs x 2 RXs experiment

The coherent MIMO radar network has been tested in an open-field outdoor scenario and deployed, as depicted in Figure 4-8, with the TXs and RXs aligned over a 21 m-long baseline. Antennas are oriented upwards, in order to mitigate clutter and multipath returns, due to surrounding structures, buildings and vegetation. The antennas are tilted to ensure the simultaneous illumination of the target and the output power for each transmitting antenna has been set equal to 200 mW.

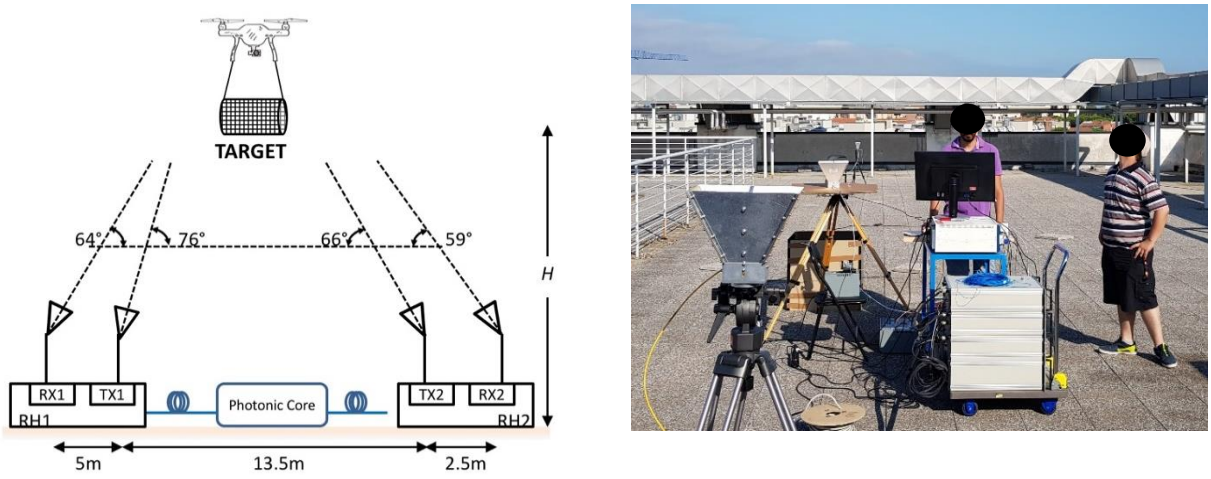

Figure 4-8: On-field deployment of the photonics-based 2TXs x 2 RXs MIMO radar network

A cylinder has been used as target in order to ensure a good RCS for any bi-static TX-RX combination. Aforesaid cylinder has been suspended below a small drone, hovering over or moving along the baseline, therefore it has been realized in tight-mesh metal net keeping so the weight within the payload limits of the drone. The target height H is in the range [15m: 20m], so that the target always results within the field of view of all antennas.

4.2.2. Processing scheme

Non-ideal conditions introduced by real environment measurements such as clutter, interferences and target RCS fluctuations afflict the acquired data set. For this reason, following the general sketch proposed in [86], the radar network signal processing has been divided into the following main sets of operations:

- **Signal conditioning:** Operations finalized to extract data channels for MIMO detection;
- **Search Mode:** Decentralized non-coherent processing with the purpose to pre-detect potential targets;
- **Image Mode:** Coherent MIMO processing for accurate target localization in case of mono-target scenario and high resolution detection in case of multi-target scenario.

In order to provide a superior stationary clutter suppression, the scheme presented in paragraph 1.8, where the algorithm in search mode is the same as for image mode, except for phase shift compensation and a detection map having a much larger resolution cell, has been modified using in search mode a decentralized non coherent processing and a multilateration data fusion approach. Image Mode is then performed only on those regions, in which the potential targets have been previously pre-located.

In the following the adopted Signal conditioning stage and the modified Search Mode are described, in detail. Instead Image Mode is not covered, as it has already been done in paragraph 1.8.

In Figure 4-9 the different areas considered by search and image modes are detailed. Both processing modes share a two-dimensional Cartesian reference system, whose center is in the middle of the antenna baseline, with the x-axis oriented towards the second transmitter, and the y-axis perpendicular to the ground plane. Consequently, the x-coordinate indicates the relative position with respect to the baseline, while the y-coordinate corresponds to the target height above the roof of the TECIP Institute, where the experimental activity has been conducted.

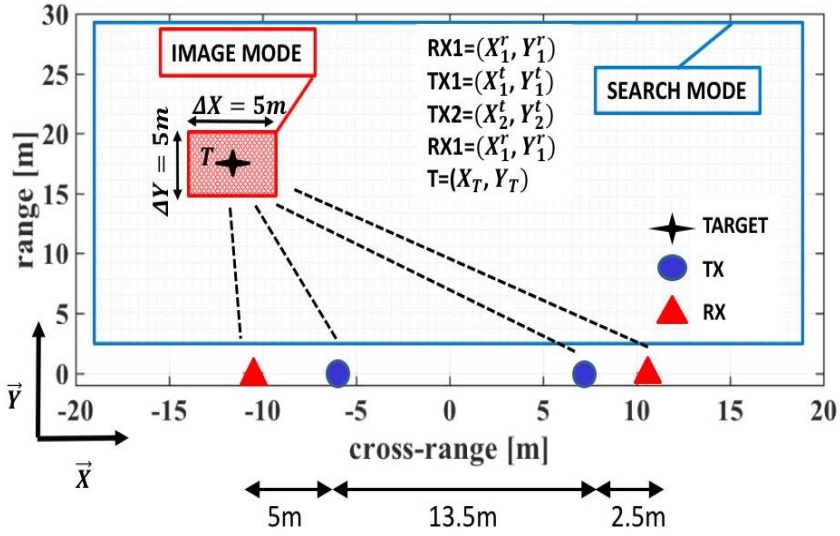

Figure 4-9: MIMO 2 TXs x 2 RXs experiment image and search mode geometry

Signal Conditioning

The data stream collected at IF by the N receivers is split into M × N channels. Since transmitter orthogonality is implemented in time domain by the means of an opportune ODL inserted as shown in Figure 4-7, for a correct data evaluation the same timing used in transmission needs to be adopted. This means that if in total M transmitters are used in time diversity each of the N data array associated to a receiver contains M channels interleaved every PRI/M. In the specific case that two transmitters are employed (M=2) to extract the 4 MIMO channels it is necessary to split each of the 2 digital data arrays, acquired by the ADCs, associated respectively to RX_1 and RX_2 into two sub arrays obtained reading, every PRI, the first or the last (PRI/2)xF_C samples (where F_C indicates the ADC sampling frequency used). As for the present experiment the ODL introduces a 5 μs delay, given the 400 MHz sampling frequency, the first 1000 samples are related to TX_1 and the ensuing 1000 samples to the remaining TX.

Successively, to maximize the SNR, the M × N channels are filtered at IF and then down-converted to BB. At this point pulse compression (i.e. matched filtering) can be performed on the received LFM signals and next standard range-Doppler processing can be applied. Finally, MTI filtering is possible on each channel allowing so an effective stationary clutter suppression.

Search Mode

As pointed out in [33], to reduce the large processing burden required by a centralized coherent processing, a pre-detection approach is used. A constant false alarm rate (CFAR) detection strategy is applied to the bistatic range-Doppler power spectral density (PSD), calculated on each channel to enhance target detection in a dense clutter environment.

In general, target detection consists in a decision test, in which a quantity, namely the detection statistic, extrapolated from the received signal is compared with an opportune threshold. Typically, target detection is performed in a given radar Range-Azimuth-Doppler cell (or in any combination of them) often referred to as the cell under test (CUT) and two alternative hypotheses can occur:

- H_1: the target is present in the CUT;
- H_0: the target is not present in the CUT.

CFAR detectors are all those detection algorithms which keep the probability of false alarm (i.e. false positive) below a fixed level [86] [87]. Despite various techniques do exist, they share the same detection principle described as follows.

The signal in the CUT is compared with a threshold, which is the product between the clutter power, Z, and a scaling factor, T, which depends on the desired probability of false alarm.

Usually, the clutter power around the CUT is estimated from K neighbouring cells, also called training cells, whereas N_G guard cells are important to avoid target masking in the adjacent cells. In the Cell-Averaging (CA) CFAR, for instance, clutter power corresponds to the mean signal power from the K training cells.

For the present analysis a CA-CFAR square–law detection strategy is applied to the bistatic range-Doppler PSD , $X_{k,l}(\tau, f_D)$, calculated for each available MIMO channel, where $k = 1, \dots, M$ and $l = 1, \dots, N$. The detection threshold Λ is computed from a finite reference window of K Range-Doppler cells surrounding the CUT. Then, the statistic Y is compared with the threshold such that:

$$Y = X_{k,l}(\tau, f_D) \underset{<_{H_0}}{\overset{>^{H_1}}{}} \Lambda = T \cdot Z, \qquad \textbf{Eq. 4-1}$$

where T is a deterministic constant scale factor that depends on the desired constant false alarm probability, P_{FA}, and Z is the noise power estimate. For the $K/2 + N_G/2$ range cell Z is given by:

$$Z = \frac{1}{K} \cdot \left(\sum_{k=0}^{K/2-1} X(k) + \sum_{k=K/2+N_G+1}^{K+N_G+1} X(k) \right). \qquad \textbf{Eq. 4-2}$$

Under the assumption that all samples are independent and identically distributed with exponential distribution, the P_{FA} can be calculated as:

$$P_{FA} = (1 - T)^{-K} \qquad \textbf{Eq. 4-3}$$

Once an opportune threshold is individuated, hard decisions can be taken on the Range-Doppler PSD of each MIMO channel.

The time delays corresponding to positive detections can be transformed into Cartesian coordinates to define a target position, given by the intersection of isorange ellipsoidal crown-like areas, as shown in Figure 4-10.

When individual bistatic range values are available, a common method to estimate the target position is multilateration. Given a single target illuminated by all the M×N channels, the set of decentralized range measurements should intersect in an area. Employing an "AND" decision logic (i.e. a target is declared present when it is correctly detected by all the channels) the potential target can be pre-located in an area enclosed by the intersections of cited iso-range ellipsoidal crowns.

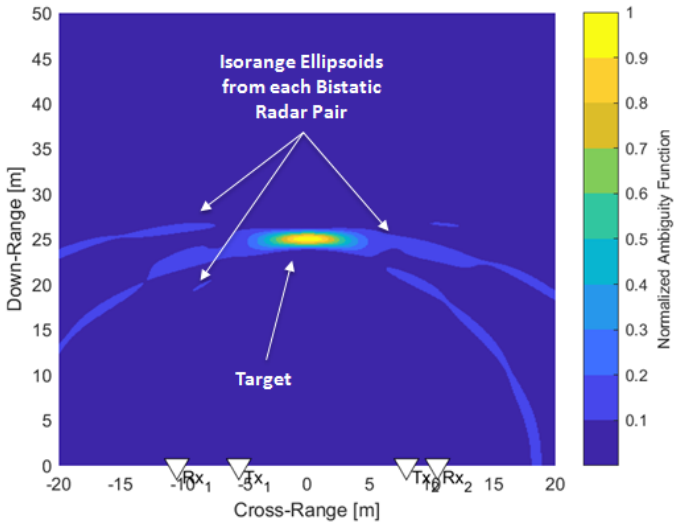

Figure 4-10: Outdoor MIMO 2 TXs x 2 RXs experiment search processing simulations: a target in the range cross-range map is pre-located where iso-range ellipsoids formed by each channel intersect

Image Mode

The implemented photonics-based coherent MIMO 2 TXs x 2 RXs radar network ensures an excellent phase coherence. As depicted in Figure 4-7, the same IF frequency generated by the MLL oscillator is first used in transmission for up-conversion of the signal from BB to RF and, afterwards, for signal down-conversion from RF to BB. Moreover, the optical oscillator is characterized by a very low PN curve [83].

A coherent MIMO processing can be applied since the negative effects on MIMO coherent detection performance, due to oscillator instability, are negligible. For the proposed system architecture, in fact, the temporal jitter, which is obtained integrating the PN, introduced by the optical oscillator on the spectral window of interest [20 Hz : 200 MHz] (CPI=50ms), is in the order of magnitude of 10^{-12} s, while the angular jitter is in the order of 10^{-2} rad, one order smaller than the upper phase jitter limit individuated in [32]. For further details see section 1.7 and 1.3.

4.2.3. Experimental results: Mono-target Search Mode

In the top-images of Figure 4-11 the range/radial speed PSD are depicted for all four bi-static radar channels. The PSD has been evaluated on a 25 ms long observation time, corresponding to 500 PRIs. Subsequently a CA-CFAR detector is applied to the PSDs computed for each MIMO channel, with the following parameters: $K\tau$ =16 and Kf_D=8 and $P_{FA} = 10^{-5}$, where $K\tau$ and Kf_D are the number of training cells along range and radial speed, respectively, while the number of guard cells, N_G, on both dimensions is set to 4.

Instead in the bottom-images of Figure 4-11 for each channel the detection maps obtained applying the above defined CA-CFAR detector on the corresponding PSD maps are shown. The target is correctly spotted by all 4 bi-static radars, with slightly different radial speeds depending on the transmitter-target-receiver geometry and relative motion. As can be noticed there only on the TX_1-RX_1 channel a false alarm is erroneously detected, located at a bistatic range of about 40 m.

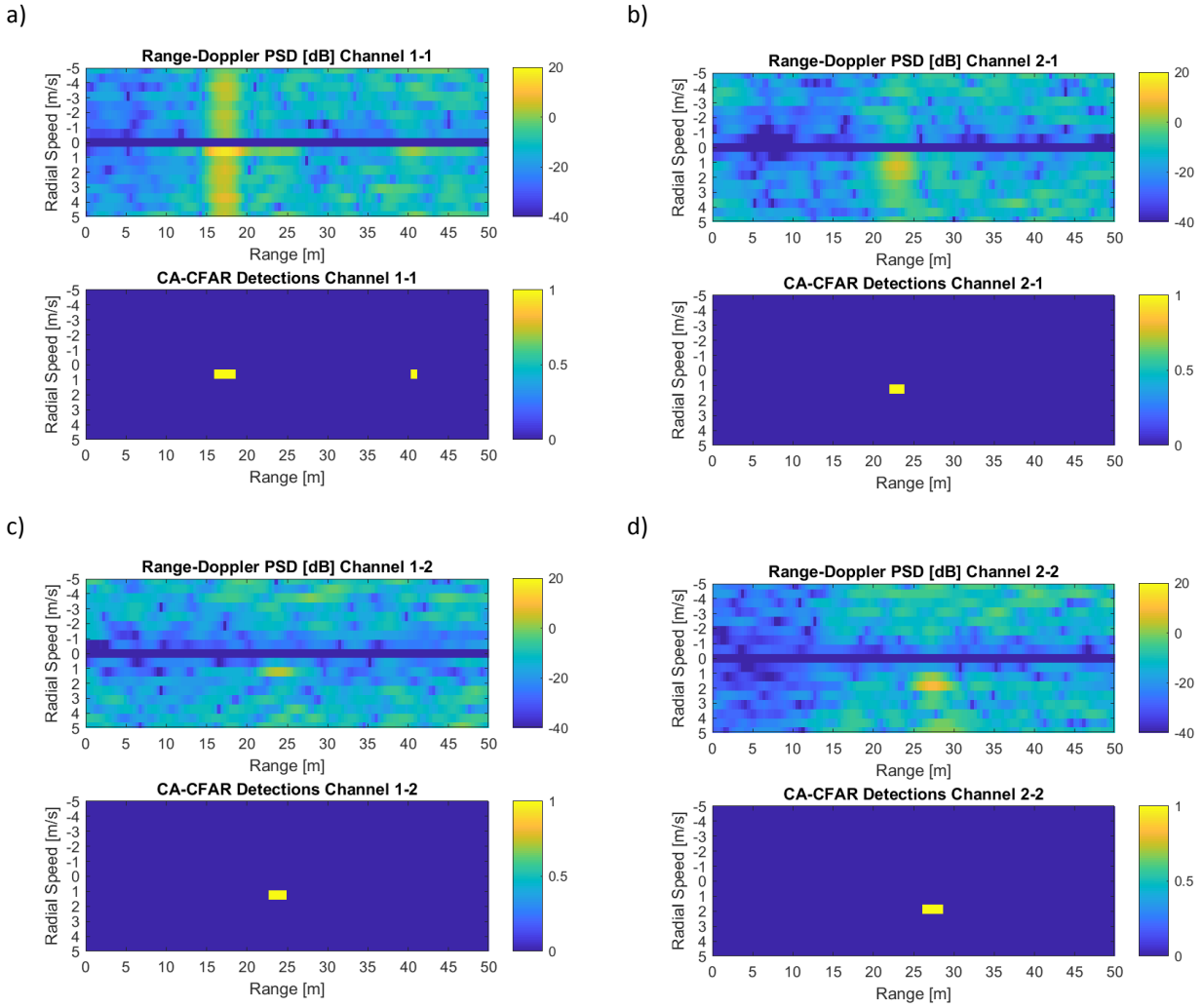

Figure 4-11: Range-Doppler PSD maps (top) and CA-CFAR detection outputs (bottom) for MIMO CH1-1 (TX_1-RX_1) (a); MIMO CH2-1 (TX_2-RX_1) (b), MIMO CH1-2 (TX_1-RX_2) (c) and MIMO CH2-2 (TX_2-RX_2) (d)

Combining the multiple detection maps, a cumulative range/cross-range map based on multilateration can be obtained. In Figure 4-12 the resulting map is depicted. The ellipsoidal crowns represented there in light blue individuate all iso-range points having the same bi-static range from the considered TX-RX couple, as the candidate target detected by the CA-CFAR detector. The area in which all isorange ellipses overlap, extends for about 3x3 m around the central point having coordinates D= (-12 m, 16.5 m).

It has to be remarked that during data acquisitions the target height has been constantly measured using a laser range finder. Furthermore, after data acquisition, GPS positions (red circles)

extracted from the drone log-file have also been evaluated and both measures confirm that the area of intersect is compatible with the individuated target position.

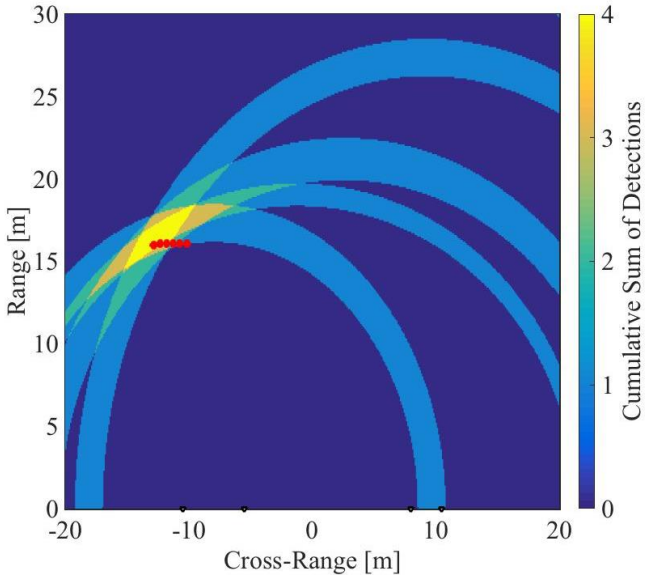

Figure 4-12: Multilateration Search mode range cross-range map (red dots represent GPS drone positions)

4.2.4. Experimental results: Mono-target Image Mode

Search mode consents to delimit the possible target area to an ambiguous region of about 3 m in range and 3 m in cross-range. By knowing this a priori information on target location, MIMO processing in Image Mode can be applied on an area of 5 m x 5 m around D. In order to limit noise and interfering signal effects for each channel the same signal conditioning used also for Search Mode has been implemented, exception made for Doppler processing and MTI filtering.

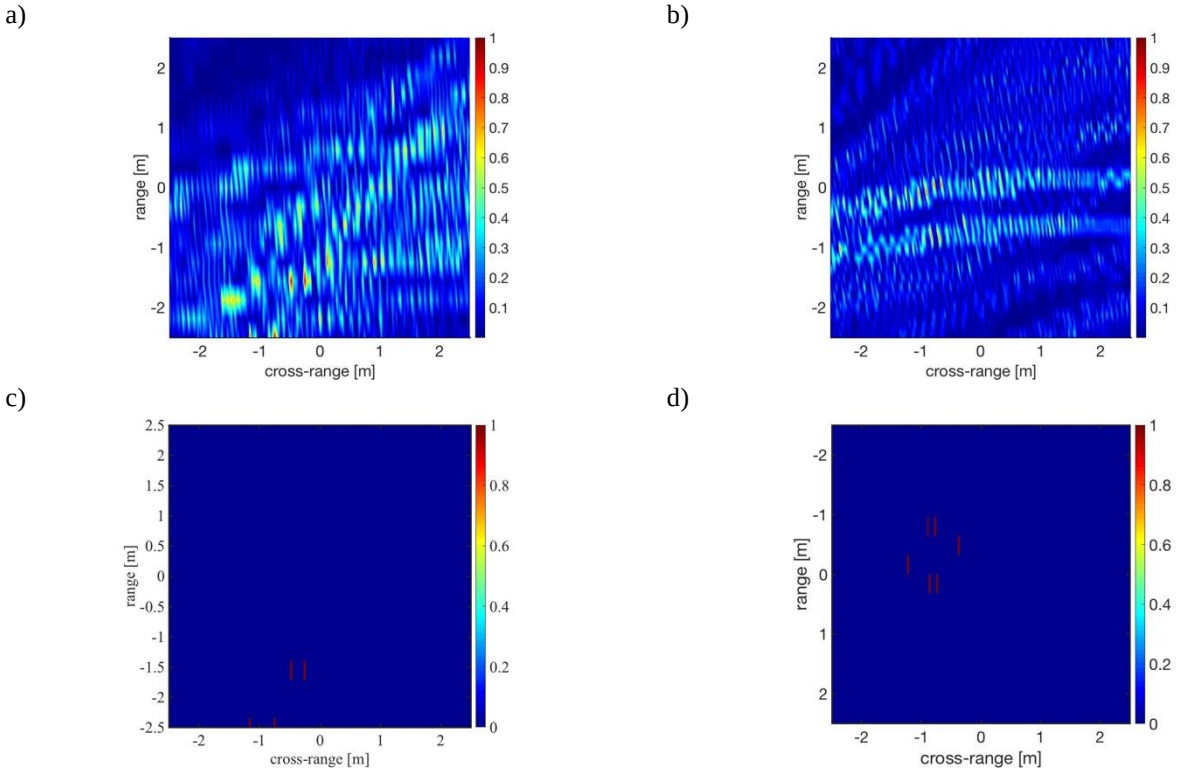

Figure 4-13: Image Mode range cross-range map first acquisition (a), second acquisition (b); detection map first acquisition (c) and second acquisition (d)

Next the coherent MIMO cross-ambiguity function has been computed on 161x16 samples, which are spaced by one wavelength in cross-range (i.e. 3 cm) and ten wavelengths in range (i.e. 30 cm). The resulting cross-ambiguity function is shown in Figure 4-13 (a). Although the target peak is visible, as expected due to the minimal 2x2 MIMO architecture used for the experiment, side lobes with a very high intensity level, are also present. For this reason, it is opportune extract a detection map applying a simple threshold detector on the individuated MIMO cross-ambiguity function rather than the CA-CFAR detector illustrated for search mode. The outcome of this operation is depicted in Figure 4-13 (b) and consents to clearly spot the cooperative target in a square area with size 0.5 m x 0.5 m centered in T=(-0.25m, -1.25m). Furthermore, it has to be underlined that the metallic cylinder used as target had a radius of 17 cm and a height of approximately 30 cm, which could explain the detection of 2 points spaced 30 cm in cross-range. Unfortunately, two additional point like areas are present on the map related to extremely high side lobes which in real operations would have increased the overall false alarms rate. Processing a different PRI, 2 objects are detected spaced approximately 50 cm in height: the object positioned at a higher quote seems to be larger than the lower one. Perhaps in this acquisition also the drone has been detected. The metallic cylinder target, in fact, was suspended approximately 50 cm below the drone, see Figure 4-13 (b-d). In conclusion, thanks to coherent MIMO processing detection precision has been increased by a factor 20 lowering the ambiguity area from an initial 3 m x 3 m area, found in search mode, to a much smaller one having a 10 cm size along both dimensions [82].

4.2.1. Experimental results: Multi-target detection

In the light of the successful result achieved on a mono-target scenario a further experiment has been effectuated involving multiple targets with the aim to test the angular/cross-resolution capability of the MIMO radar network. This time two targets have been used; each one suspended below a commercial drone. The targets, as in the mono-target experiment described previously, are two cylinder having a radius of 17 cm and a height of 50 cm realized in tight-mesh metal net. Though hovering at the same altitude between 15 and 20 m, due to security reasons, it has not been possible bring them closer than 3 m in cross-range. At difference to the mono-target case a standard search mode has been preferred rather than a CA-CFAR detection on each available channel followed by a multilateration data fusion. In particular, both Search mode and Image mode have been computed on the same area with a spatial sampling spacing of 10 cm along range and cross-range dimension. Hence as the cross-ambiguity function has been evaluated on an area with a size of 15 m in range and 20 m in cross-range both resulting range cross-range maps consist of 150 x 200 samples.

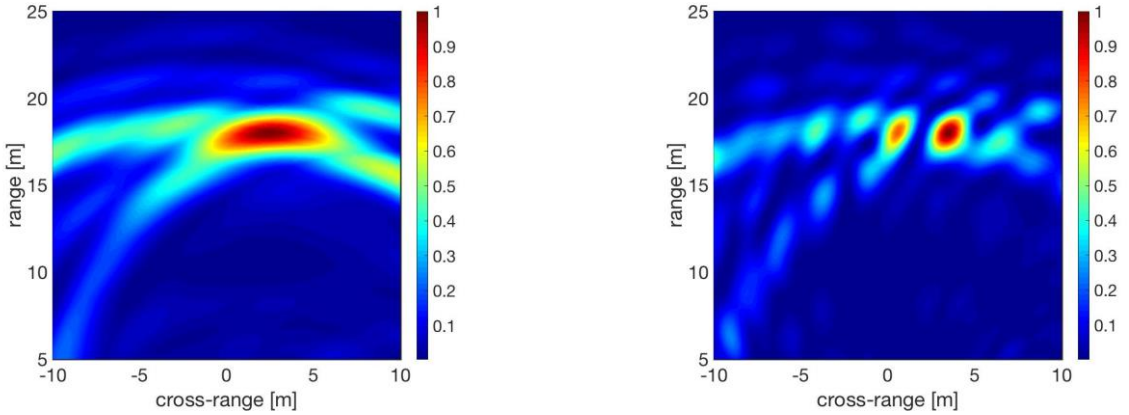

Figure 4-14: Multi-target Search Mode range cross-range map (left) and Image Mode range cross-range map (right)

Although the maps shown in Figure 4-14 are obtained for the same area and with the same resolution cell they deeply differ: Figure 4-14 (left), indeed, refers to Search Mode, whereas Figure 4-14 (right) to Image Mode output. While in Search Mode the two targets are not distinguishable

Image Mode, which exploits also phase information, consents to correctly separate both targets present on the scene. In particular, thanks to coherent processing, the two cylinders can be clearly detected: the first one is in T1= (0.5m, 18m) and the second one in T2=(3.5m,18m). Compared to the angular resolution ensured by the horn antennas used for the experiment which, given the 50° HPBW, is about 15 m at 18 m, a remarkable resolution improvement has been achieved.

4.3. INDOOR MIMO 2 TXS X 4 RXS EXPERIMENT

The experimental activity reported in this Section which has started in April 2019 at the TECIP Institute of Sant'Anna School in Pisa and is still in progress. At difference to the previous field trial campaign, an increased multi-static MIMO radar network has been set-up consisting of 2 TXs and 4 RXs and all tests have been effectuated indoors. Furthermore, the HW architecture realized for this activity differs totally from the version analysed previously as photonics is exploited merely for signal distribution. The Section is organized as follows: first the new set-up is introduced, investigating especially two major aspects Long-Wavelength Vertical-Cavity Surface-Emitting Lasers (LW-VCSEL), utilized for Radar Over Fiber (RaOF) purposes and patch antennas, which have been designed and realized internally, then the MIMO geometry is introduced as well as the main parameters related to the radar waveform and finally real data processing outcomes are discussed. For a better comprehension of the whole design process also preliminary results, extremely helpful for system development and characterization and for SW debugging, are presented. In the end, before drawing the conclusions, a comparison between real data outcomes and corresponding numerical outcomes is done in order to validate the self-developed MIMO scenario simulator.

4.3.1. Indoor experimental set-up

In the present section the set-up realized specifically for the indoor experiment is briefly outlined. With respect to the set-up examined in paragraph 4.2 two substantial changes have been made: first optical components are used exclusively for signal distribution, whereas in the former scheme photonics was also utilized for distributed signal generation and reception, and ad hoc developed patch antennas have been employed for signal reception rather than horn antennas.

In Figure 4-15 the set-up employed for the indoor MIMO test is detailed. As reported there, a Fujistsu 60 GSa/s DAC directly generates the RF signal which undergoes an electro-optical conversion operated by a LW-VCSEL. The resulting optical signal can be delivered to a remote transmitter using SMF. At the transmitter stage, a photodiode operates the inverse conversion from the optical to the electrical domain and, eventually, after an opportune amplification the signal is transferred to the TX antenna. At the receiver side, a Low Noise Amplifier amplifies the signal in order to correctly modulate in direct modulation (DM) mode the RX VCSEL, which consents to effectively distribute the acquired signal back to the central node. Here, prior to DSP an ADC provides signal digitization. For this purpose, four channels, one for each receiver, of a 40 GS/s real time oscilloscope have been exploited. Although 2 TXs and 4 RXs have been used for the MIMO experiment, for simplicity, only a single transmitting and receiving chain are represented in the reported block diagram. The 2 TX antennas are ultra-wideband (1 – 18GHz) Vivaldi-shaped horn antennas with 50° HPBM aperture and 12 dBi gain, while in reception, as anticipated, ad hoc developed patch antennas have been used, better detailed later on.

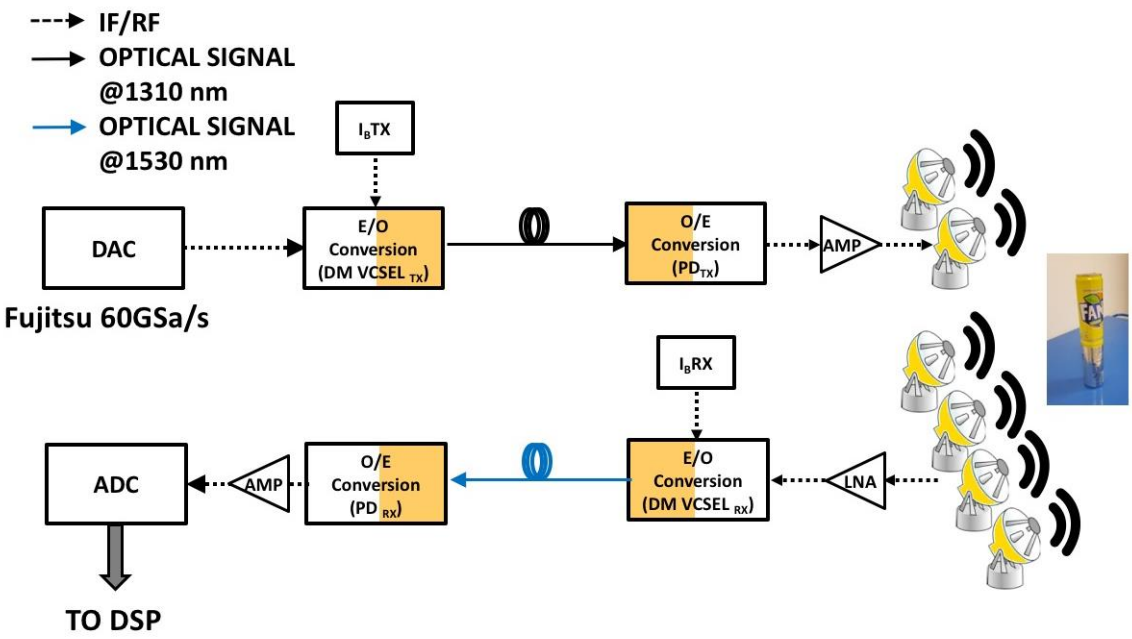

Figure 4-15: MIMO indoor 2 TXs x 4 RXs experimental set-up

Long Wavelength Vertical Cavity Surface Emitting Lasers

LW-VCSELs represent a promising class of new laser sources. Compared to classical horizontal-cavity lasers like Distributed Feedback lasers (DFB) those optical sources have several appealing features such as a better robustness to high temperatures, a superior power efficiency and the possibility to be directly integrated on Si-based transceivers. All those features combined with an extremely competitive price are pushing the sector to explore the possibilities offered by those innovative optical sources. VCSELs have been already successfully employed for optical sensing [89],[90], for optical digital transmission [91] on short ranges as well as for RoF applications [92],[93]. In particular, LW-VCSELs with an emission wavelength of 1.3 μm when operated in DM mode enable a distortion-free transmission of broadband signals over SMF up to several kilometers. As this technological solution consents to distribute large bandwidth signals up to 20 GHz over long distances with a low attenuation, such optical components seem to be eligible for the realization of spatial distributed centralized multistatic radar networks.

Although large distances can be covered by a system based on VCSELs for signal distribution, a goal of the experiment is to prove that those components are effectively adequate for the implementation of a Radar over Fiber (RaoF) system. In fact, it has to be said that in the indoor experiment described here, since transmitters, receivers and antennas are separated by a few meters, also conventional RF technology could have been used to interconnect all elements. However, once demonstrated the feasibility of the MIMO radar demonstrator, further tests are planned in an outdoor scenario with an increased antenna baseline. For this reason, 20 m-long SMF fiber patches have been already adopted for signal distribution.

The VCSEL structure is based on Vertilas' unique InP Buried Tunnel Junction (BTJ) design and features a very short optical cavity. In order to obtain a user-friendly demonstrator an ad hoc Printed Circuit Board (PCB) has been designed for properly driving and modulating the laser. Thanks to the PCB, depicted in Figure 4-16, a 6.5 mA bias current can be applied to VCSELs to which corresponds, coarsely, a 2 mW optical power output, as shown in Figure 4-17.

Figure 4-16: MIMO indoor 2 TXs x 4 RXs experiment VCSEL PCB

Despite the actual die chip frequency response has been measured to be 18.5GHz [94], the measured response of the packaged VCSEL on PCB is approximately only half of that. Indeed, from Figure 4-18 we deduce that the -3 dB BW is ~9 GHz. Most of the BW reduction is due to the sub-optimum TO-can pigtail VCSEL packaging. Vertilas is currently working on a packaging optimization to minimize impedance mismatching and leakage and parasitic currents.

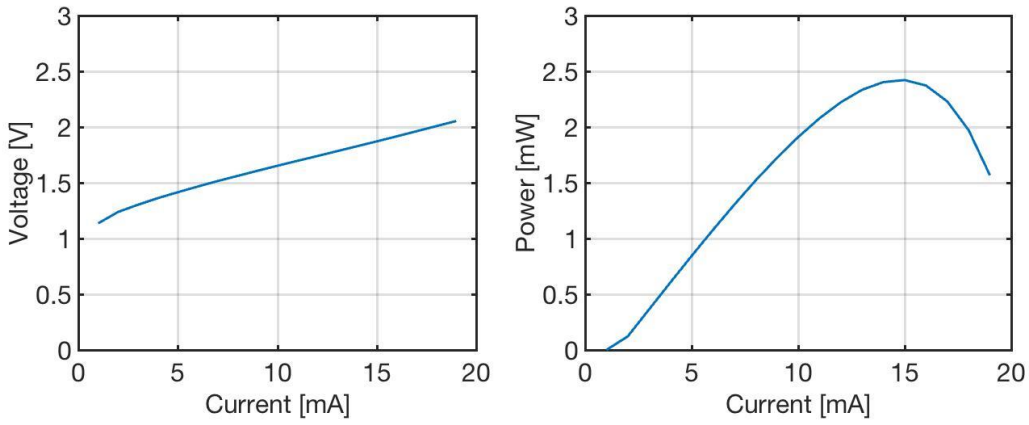

Figure 4-17: MIMO indoor 2 TXs x 4 RXs experiment VCSEL diode voltage (left) and emission optical power (right)

Nevertheless, selecting a 8.5 GHz carrier frequency for the radar system which results also ideal for the patch antennas, as will be better explained in next paragraph, this anomaly is irrelevant and 1 GHz large signals centered around 8.5 GHz can be employed for radar detection [95].

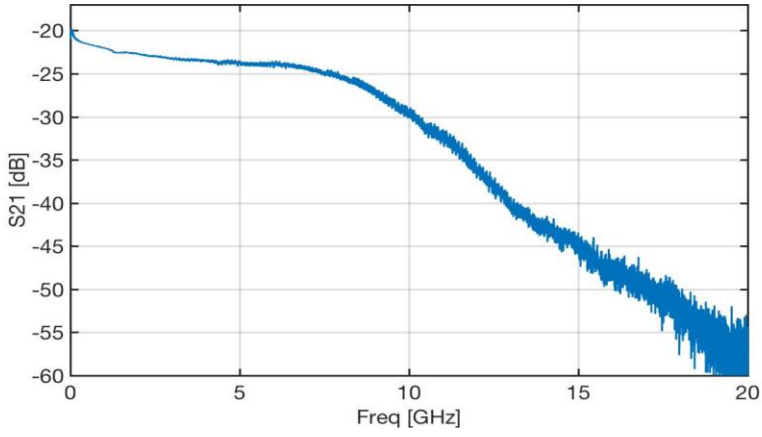

Figure 4-18: MIMO indoor 2 TXs x 4 RXs experiment VCSEL frequency modulation response

In [96] the same VCSELs has been adopted for the realization of an UWB VCSEL-based radar-over-fiber system. The system architecture used for this experimental activity is similar to the architecture detailed in Figure 4-15. However, only a single TX and RX have been employed as the purpose is to demonstrate that the proposed low-cost VCSEL-based solution for radar signal distribution is suitable to manage UWB radar waveforms. It is opportune to point out that different patch antennas than those used for the MIMO experiment, which are described in the following, have been adopted. In particular, antennas used for this activity provide a 6 dBi gain and can operate in the frequency range 6–11 GHz, so that 3 GHz-bandwidth UWB signals with a carrier frequency of 7.5 GHz can be transmitted. As shown in Figure 4-19, where the cross-correlations functions obtained for different measurments are reported, the -3 dB peak associated to each target (see black and red curves) is about 13 cm large. Therefore, likewise the system can distinguish two targets whose two-way (i.e. bi-static) relative distance is about 13 cm, equivalent to 6.5 cm one–way distance. Measurments confirm cited resolution capability, indeed, two targets having a two-way relative distance of 11 cm have been correctly resolved [96].

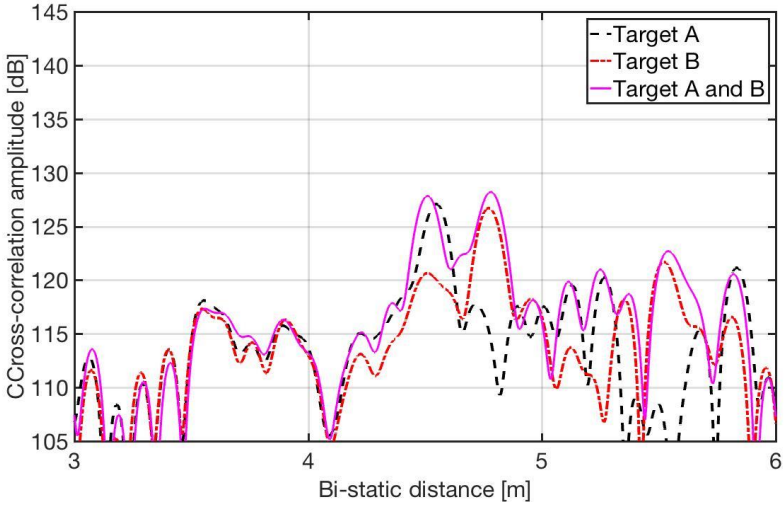

Figure 4-19: UWB VCSEL-based radar-over-fiber bi-static radar cross-correlation functions for target A located at 4.55 m bi-static distance (black curve), for target B located at 4.77 m bi-static distance (red curve) and target A + B (purple curve);

Patch Antennas

MIMO operation foresees that the same target can be observed simultaneously from different view angles. Therefore, unlike conventional mono-static radars large aperture antennas are more indicated than high directivity, high gain antennas. Patch antennas appear very promising as they have twofold benefits: they are inexpensive and have a small form factor. For those reasons it is easier to arrange them in arrays, this way ensuring the desired antenna gain and better integrate the resulting arrays in a complex system as, for instance, in a ship hull or on a car bumper.

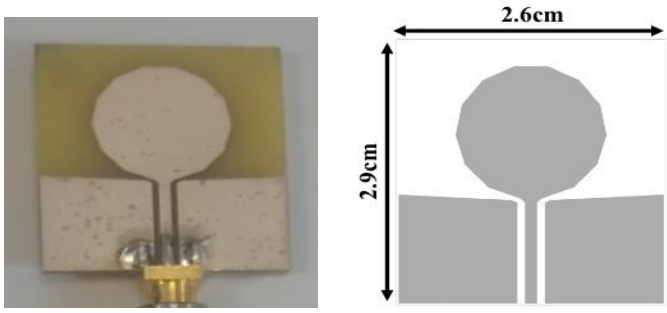

Figure 4-20: Self-developed RX patch antenna

The antennas specifically designed for this activity, depicted in Figure 4-20, are circular patch antennas, measuring 2.6 cm × 2.9 cm (see antenna layout in Figure 4-20 right), and are realized on a FR4 substrate. The antenna is fed using a co-planar waveguide feed line. In Figure 4-21 the simulated antenna gain and return loss obtained through High Frequency Electromagnetic Field Simulator (HFSS) are shown. According to simulations done, the antenna is matched at 8.5 GHz and 10 GHz where the return loss reaches -35 dB. At these frequencies the resulting gain should be approximately 3.5 dBi and 5 dBi respectively. In order to verify the real performance of the built patch antenna, a characterization of the component has been done at the facilities of the CSSN ITE of the Italian Navy.

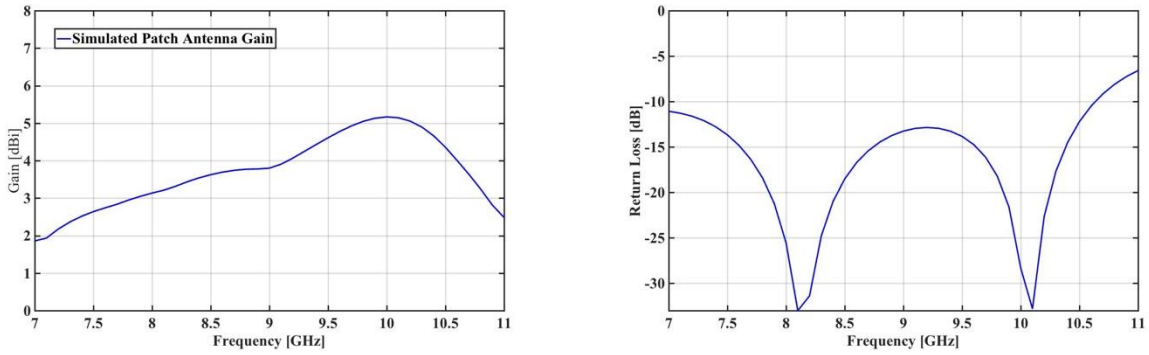

Figure 4-21: Self-developed RX patch antenna simulated antenna gain (left) and return loss (right)

In Figure 4-22 the layout of the shielded anechoic chamber where the characterization has been performed is represented. The measurements confirm the results of HFSS simulations.

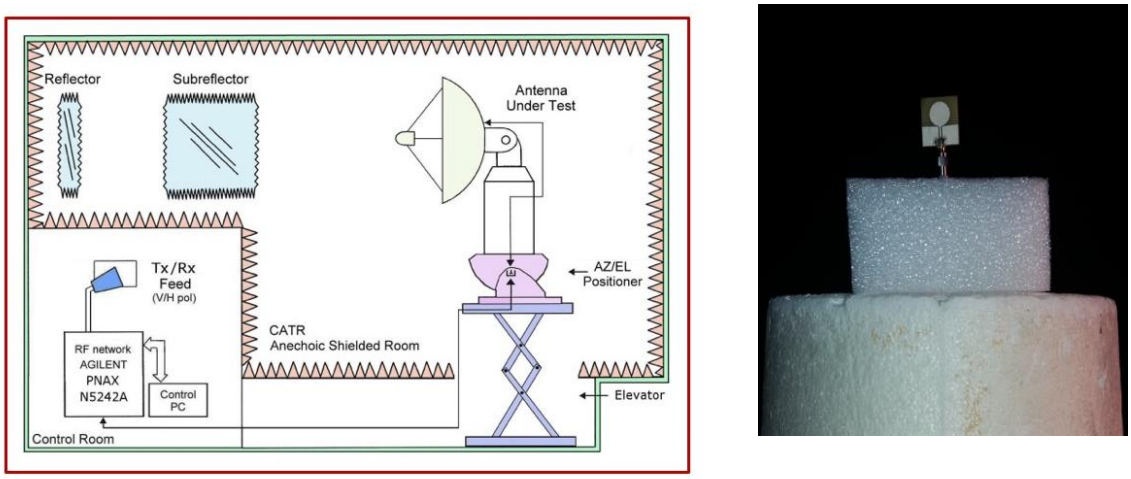

Figure 4-22: Anechoic chamber layout (left) and patch antenna characterization (right)

However, due to the instability of the dielectric constant of the antenna substrate and the poor surface finish the actual matched frequency is 1 GHz large around 8.5 GHz (see Figure 4-23) and the measured gain at this working frequency is less than 3 dBi instead than expected 5 dBi (see Figure 4-24).

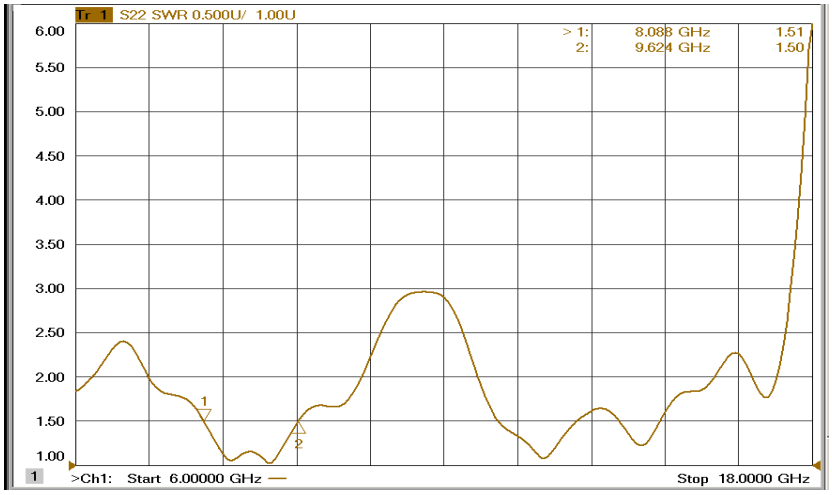

Figure 4-23: Patch antenna measured return loss

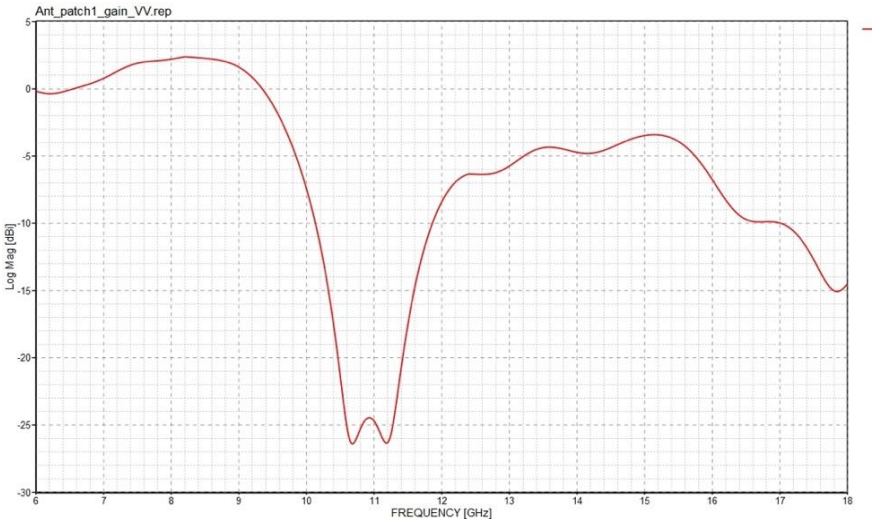

Figure 4-24: Patch antenna measured antenna gain

As expected, the antenna –3dB beam width is higher than 60°, as it can be deduced from Figure 4-25. Although the bandwidth and gain of the antenna could be improved by using a stable substrate such as Rogers 4350b and by increasing the size of the radiating patch of the antenna, the developed antenna is good enough to manage a 1 GHz BW signal centred around 8.5 GHz, ensuring a sufficient Field of View for the indoor MIMO radar experiment.

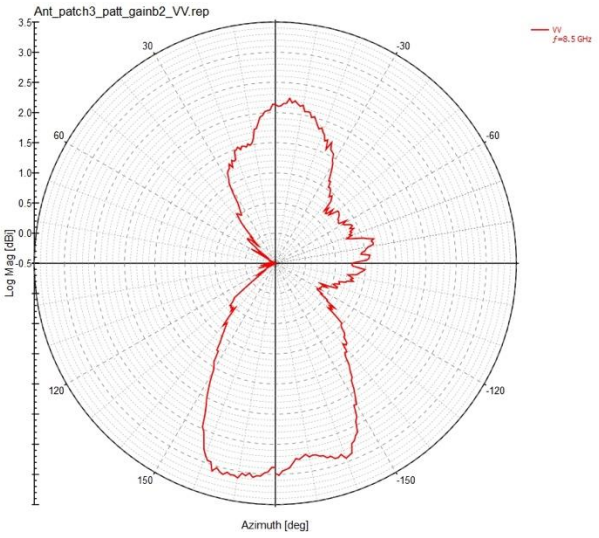

Figure 4-25: Patch antenna radiation diagram

4.3.2. Radar waveform

Since the RaoF VCSEL link introduces indicatively a 30 dB attenuation of the incoming RF signal, a frequency-modulated continuous-wave (FM-CW) signal has been selected as radar waveform so that continuous signal transmission is feasible. Therefore, while maximizing the transmitted radar power, ultra-wide bandwidth signals can be generated. As the MIMO architecture is constituted by 2 TXs, 2 linearly chirped pulses with 1 GHz BW have been used. The TX_1 transmits an up-chirp with a frequency increasing linearly from 8 to 9 GHz, whereas the TX_2 transmits a down-chirp with a frequency decreasing from 9 to 8 GHz, as can be noticed from Figure 4-26, where the spectrograms of the radar waveforms are depicted.

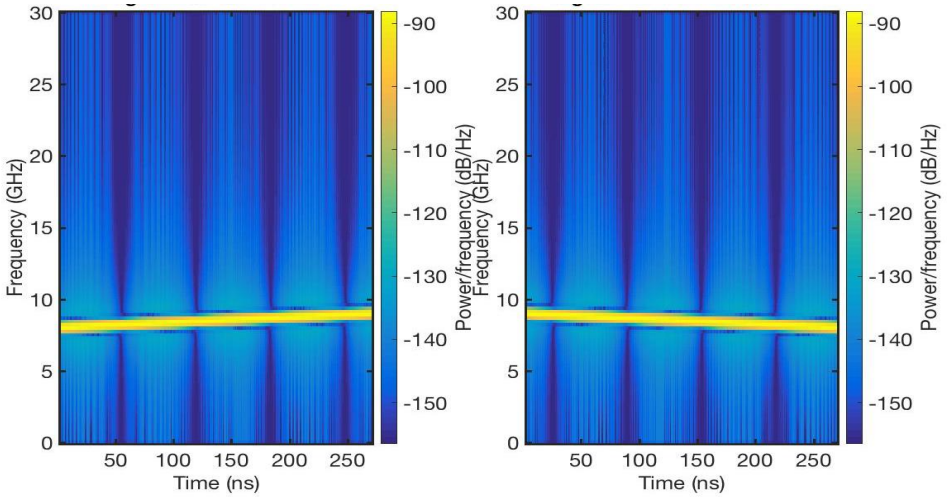

Figure 4-26: Radar waveform spectrogram associated to TX_1 up-chirp (left) and to TX_2 down-chirp (right)

Furthermore, the aforementioned signals have been separated also in time domain in order to limit mutual interferences and ensure perfect signal orthogonality. In particular, the 2 waveforms are interleaved so that each TX is active for one PRI and is silent for the following PRI, when it is the turn of the other TX to send its signal. In consideration of the dimension of the test room where the experiment takes place, a non ambiguous range of about 41 m is sufficient, leading to a 273 ns long PRI. For simplicity the acquired signals are interpolated at 60 GHz so that the received signals and the reference signal generated by the DAC have the same sampling frequency. Consequently, at 60 GHz a PRI is 16384 samples long. In Figure 4-27 the signals acquired respectively by the receiver

RX_1 and RX_2 during a back-to-back calibration (i.e. the transmitter in connected directly to the receiver) are represented together with their amplitude spectrum (see Figure 4-28), which confirms that the generated signal has a BW of 1 GHz around the 8.5 GHz RF carrier frequency.

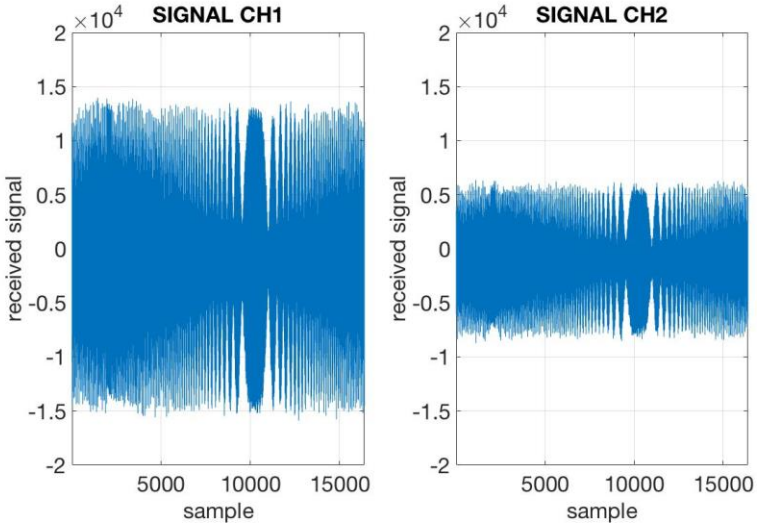

Figure 4-27: Back-to-back calibration received signal on CH_1 (TX_1-RX_1) (left) and on CH_2 (TX_2-RX_2) (right)

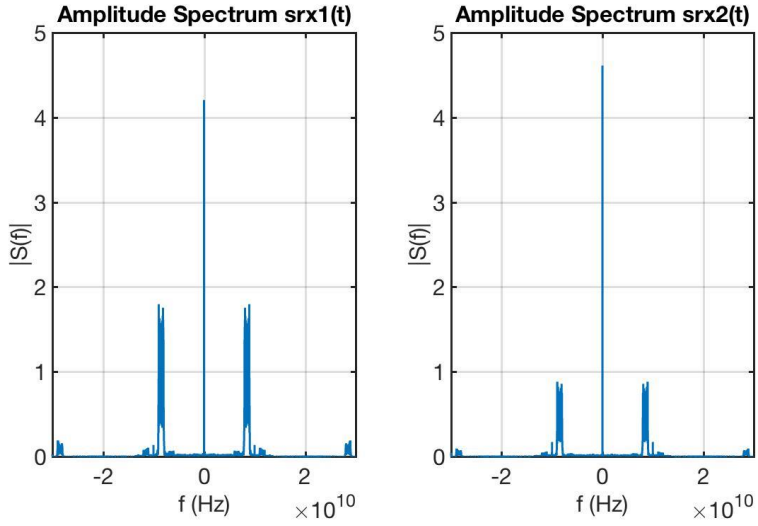

Figure 4-28: Back-to-back calibration amplitude spectrum received signal on CH_1 (TX_1-RX_1) (left) and on CH_2 (TX_2-RX_2) (right)

Although the theoretical bi-static range resolution associated to a 1 GHz signal is 30 cm, the real resolution identified operating a cross-correlation between the acquired back-to-back signal and the generated reference signal results to be only 40 cm, probably due to non linearities within the generation/detection scheme (see Figure 4-29).

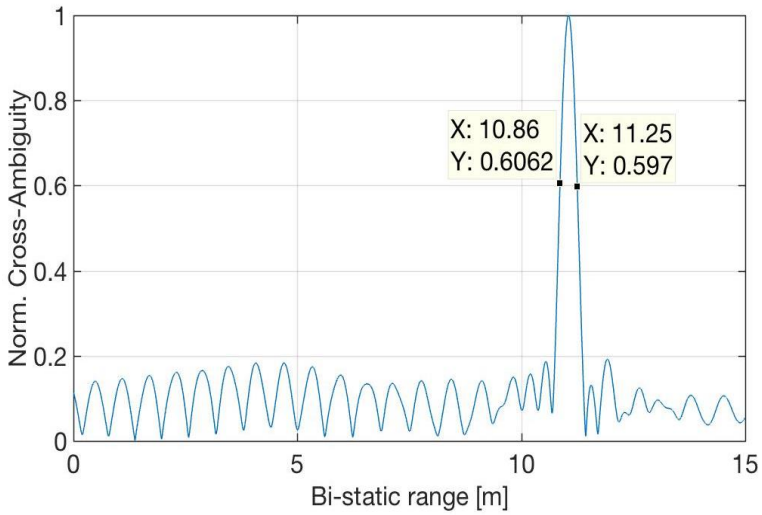

Figure 4-29: Back-to-back calibration cross-correlation function for CH_1 (TX1-RX1)

The system has been designed with the aim to detect a target with a RCS of 1 m^2 at 10 m distance. Therefore, from power budget analysis, a 7.5 dBm launch power (i.e. effective isotropic radiated power) is adequate. Nonetheless, as will be seen in the following, a much smaller target has been used for the trials, a metallic can with a radius of 2.5 cm and a height of 15 cm. Accordingly, the target RCS, which can be determined through equation Eq. 4-4, is indicatively 7 dB inferior than the assumed 0 dBsm. For this reason, horn antennas have been used in transmission instead than the initially planned patch antennas, achieving so an extra gain of circa 9 dB.

$$\sigma_{CYLINDER} = \frac{2pi \cdot rh^2}{\lambda} \qquad \textbf{Eq. 4-4}$$

Thanks to test conducted in back-to-back configuration the dynamic range of the system has been determined. Despite a 120 dB attenuation introduced placing a variable attenuator between the transmitter and the receiver, after DSP, the signal has still been correctly detected with a 3 dB side lobe suppression. Conversely, the lower attenuation limit has been found at 50 dB in this case, keeping the same ADC scale (200mV/div on the real-time oscilloscope employed as ADC), the signal amplitude occupies almost the full ADC scale. Therefore, based on aforementioned test, the system has got a dynamic range better than 70 dB.

In Table 4-3 the main system parameters employed for the MIMO indoor experiment are listed.

Parameter Name	Parameter Value/Description
MIMO TX	2
MIMO RX	4
Signal Waveform	Linear Frequency Mod. (LFM) Up/Down-Chirp
Carrier Frequency	8.5 GHz
Chirp Bandwidth	1 GHz

Pulse Repetition Interval (PRI)	270 ns
Output Power	5 dBm
Sampling Frequency	60 GHz
Target RCS (omnidirectional)	-7 dBsm (metalic can)

Table 4-3: Main radar parameters MIMO indoor 2 TXs x 4 RXs experiment

4.3.1. System characterization and calibration

Prior to discuss in next paragraph the results of the investigation it is useful to present the main outcomes obtained during the system characterization phase. Here, we report hardware in the loop test effectuated with the finality to validate processing algorithms and find suitable calibration techniques. Each channel (i.e. any transmitter-receiver combination) is acquired by the DAC with a different time delay, due to different cable lengths inserted between each DAC channel to the associated antenna and vice versa, from the receiving antenna to the ADC (i.e. oscilloscope channel). For this reason, an accurate channel calibration of the whole MIMO system has to be done in order to accurately compensate channel time shifts which can determine detection errors.

Starting from the hardware configurations, shown in Figure 4-30, where as sketched, opportune time delays have been inserted amidst the multiple transmitter receiver links a 2x2 and a 2x4 MIMO radar network have been emulated.

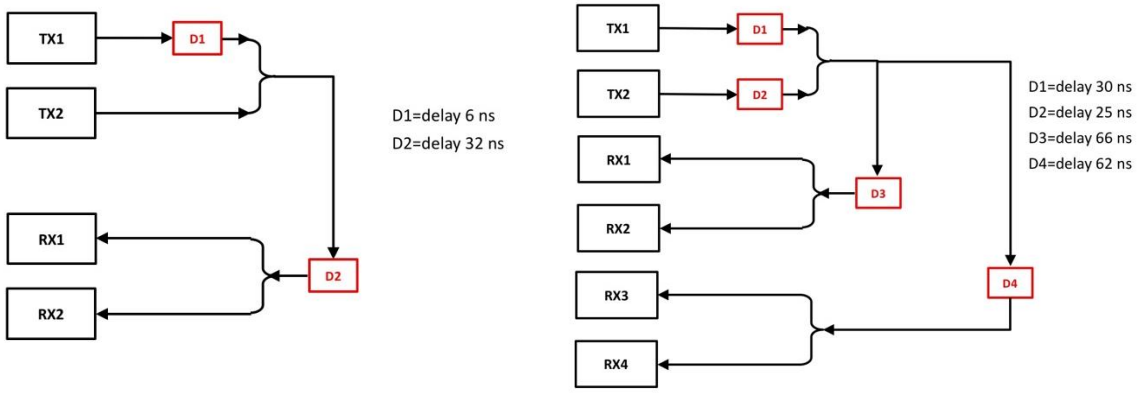

Figure 4-30: Hardware in the loop test emulated target for a MIMO 2 TXs x 2 RXs configuration (left) and for a MIMO 2 TXs x 4 RXs configuration (right)

Based on the delays of aforementioned architectures two suitable physical MIMO geometries, represented in Figure 4-31, have been determined.

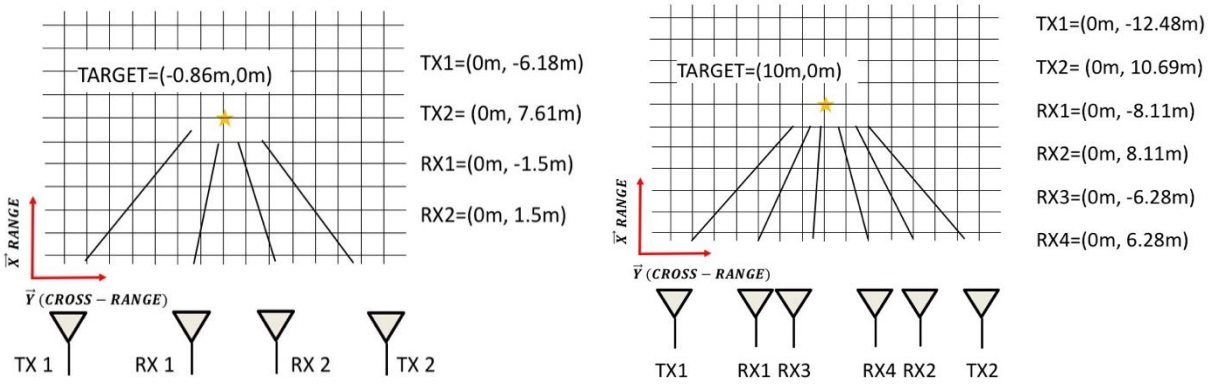

Figure 4-31: Hardware in the loop test possible physical MIMO geometries corresponding to emulated target delays MIMO 2 TXs x 2 RXs configuration (left) and MIMO 2 TXs x 4RXs configuration (right)

The cross-correlation functions computed for each channel confirm the validity of the processing as the bi-static target distances are compatible with the inserted time delays. In particular, for the 2 TXs x 2 RXs MIMO architecture the cross-correlations depicted in Figure 4-32 show that for both TX_1-RX_1 and TX_1-RX_2 the peak of the function is at a bi-static range of about 11 m, instead for the remaining channels the peak is positioned at about 9 m.

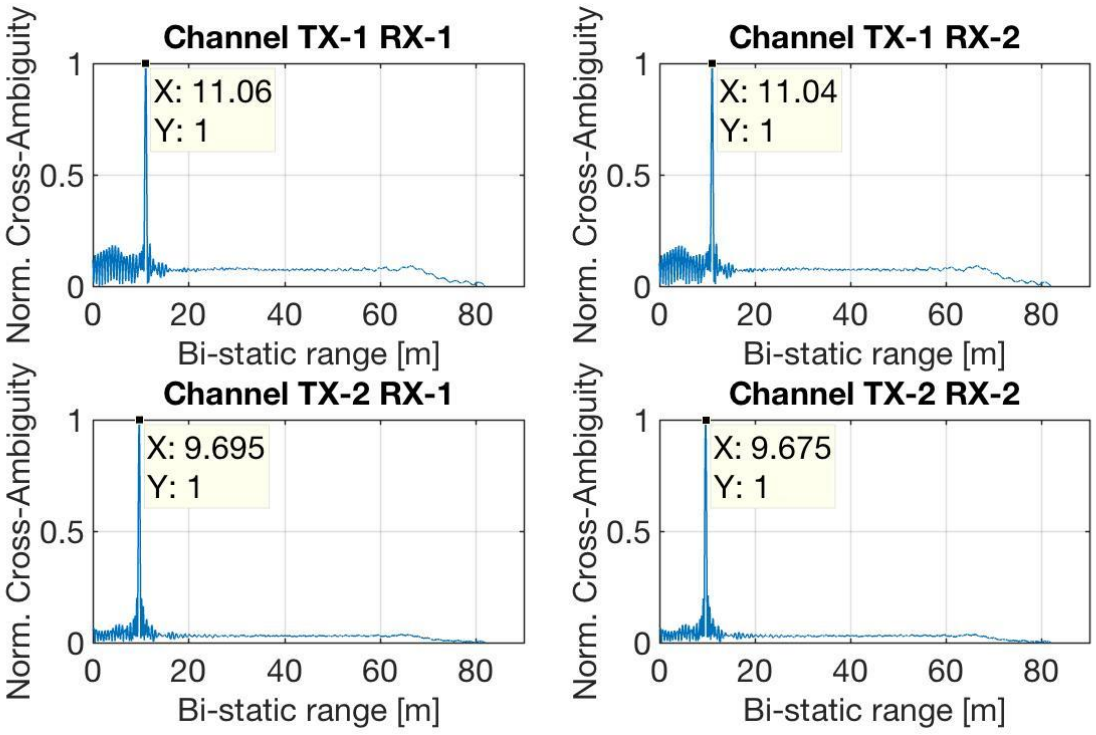

Figure 4-32: Hardware in the loop test 2 TXs x 2RXs MIMO configuration cross-correlations for each channel

Unlike the MIMO 2 TXs x 4 RXs test, represented in Figure 4-33, the peaks do not match exactly, due to an imprecise calibration compensation.

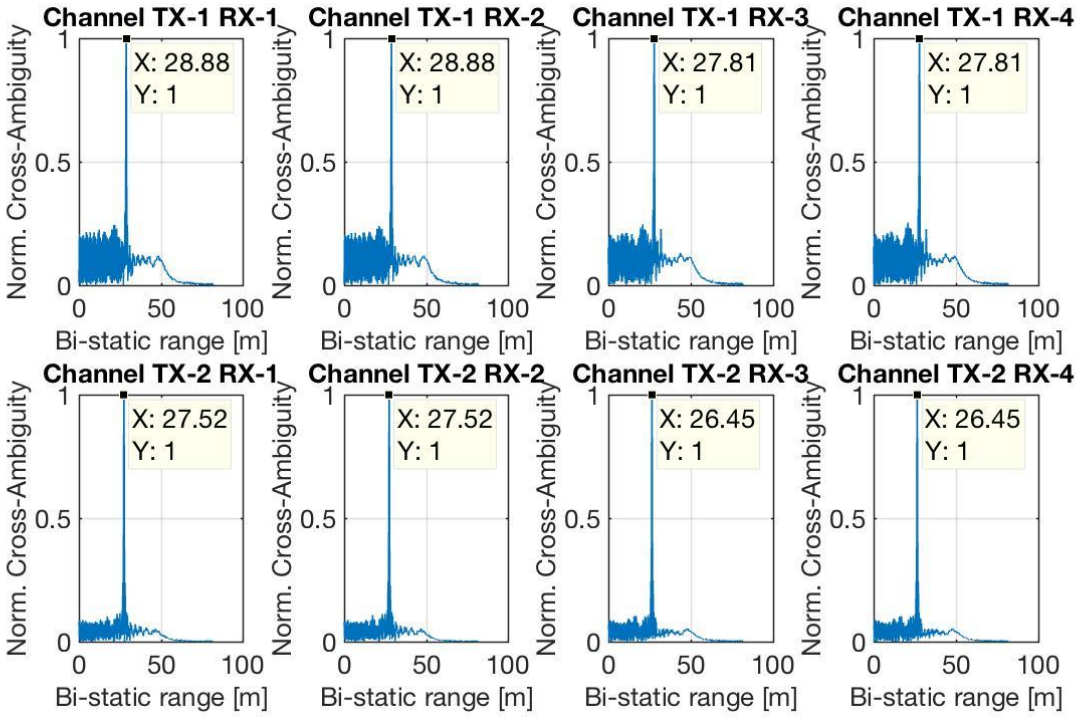

Figure 4-33: Hardware in the loop test 2 TXs x 4 RXs MIMO configuration cross-correlations for each channel

Completed positively this preliminary operation both a coherent and a non coherent MIMO processing have been applied. The resulting maps obtained through the log-likelihood detector in Eq. 1-11 are depicted in Figure 4-34 and in Figure 4-35. In both cases the target is correctly detected in T1=(0.86m,0m) and T2=(10m,0m), since the maps are centered around position T1 and T2 respectively and in addition the superiority of coherent processing is likewise confirmed.

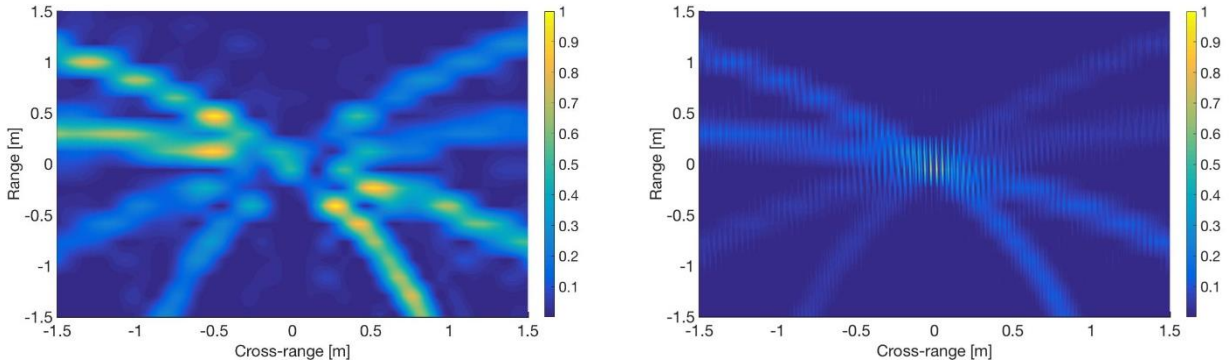

Figure 4-34: Hardware in the loop test 2 TXs x 2 RXs MIMO configuration range cross-range maps non coherent (left) and coherent processing (right)

Besides from the maps other two aspects are evident: the ellipses associated to each channel have different intensities and, especially for the 2 TXs x 4 RXs test, they do not overlap exactly in the same point. The observed anomalies are explainable by the fact that the channels are not equalized (in other terms each RaOF VCSEL couple ensures a different channel attenuation) and residual calibration errors are present accountable for time shift, to which correspond bistatic distance errors. In conclusion, the test endorses the validity of the developed processing algorithms and emphasises the need to equalize channel amplitude and to recover time delays through an accurate channel calibration.

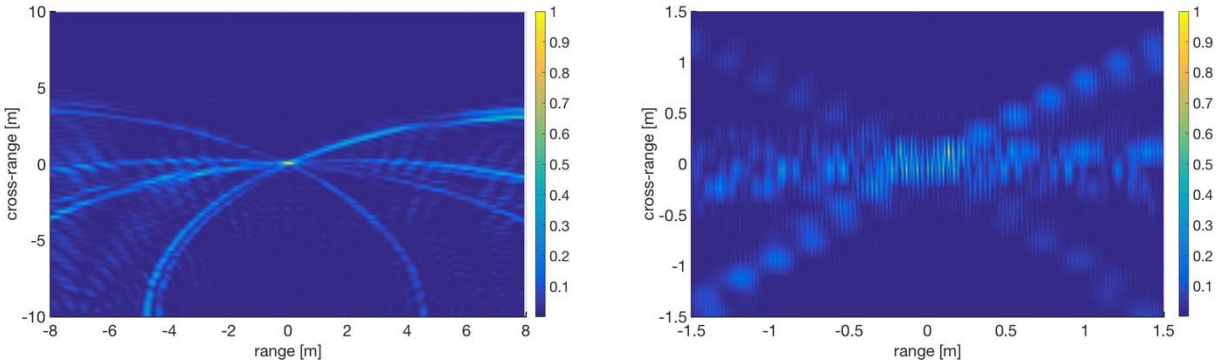

Figure 4-35: Hardware in the loop test 2 TXs x 4RXs MIMO configuration range cross-range maps non coherent (left) and coherent processing (right)

4.3.2. Experimental results

This section is dedicated to the discussion of the outcomes descending from real data processing; first the set-up utilized is briefly described then trials with a single and multi-target scenario finalized to determine the angular resolution capability are discussed and in the end a comparison is effectuated between the expected detection capability of the implemented MIMO radar network, as it results from numerical analysis, and performance achieved on experimental data.

Indoor test layout

The experiment has been carried out, as said, indoors in a test room having a size of approximately 7 m x 12 m (see Figure 4-36). Although no equipment is in the room, metallic objects such as the window, and air conditioning diffusers contribute to generate clutter which significantly obstructs detection operations. Unfortunately, corner reflectors usually employed for monostatic radar test are not appropriate for MIMO radars with widely separated antennas.

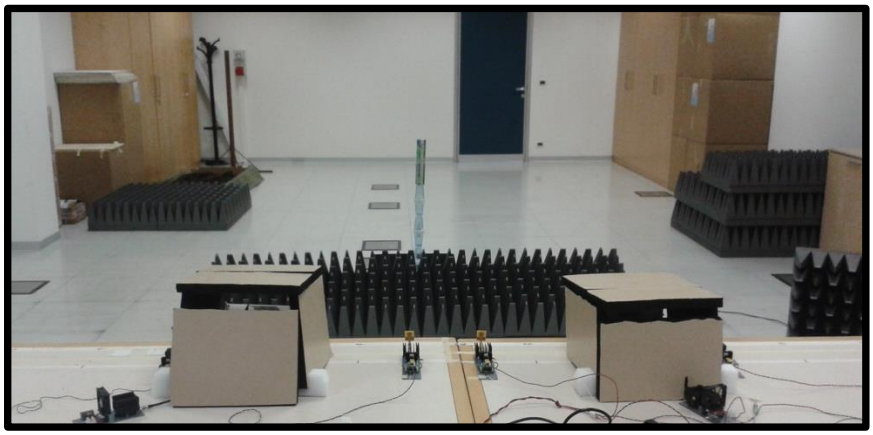

Figure 4-36: 2TXs x 4 RXs MIMO experiment indoor test layout

In this case, indeed, targets having a cylindrical symmetry on the horizontal plane are more indicated. Thanks to cylindrical symmetry the target shown in

Figure **4-37** has a bi-static RCS with a lower angular variability compared to a planar surface, subsequently on each channel an acceptable SNR level can be guaranteed.

At this point it has to be remarked that MIMO theory reviewed in [25] has been developed under the assumption that targets are ideal point-like scatterers. Of course real targets are always distributed rather than point-like, for instance, the can depicted in mentioned figure has a diameter of 5 cm. Smaller targets have been also considered for the experiment, which better meet the assumption.

However, the ensuing target RCS decrease entails an insufficient SNR level for radar detection. On the contrary, often in order to have a higher SNR a target constituted by two cans, one placed above the other, has been used. During the dissertation the importance of antenna geometry for MIMO radars has been repeatedly highlighted and in general the best configuration is the one where transmitters and receivers are uniformly distributed, namely interleaved and equidistant over the whole baseline.

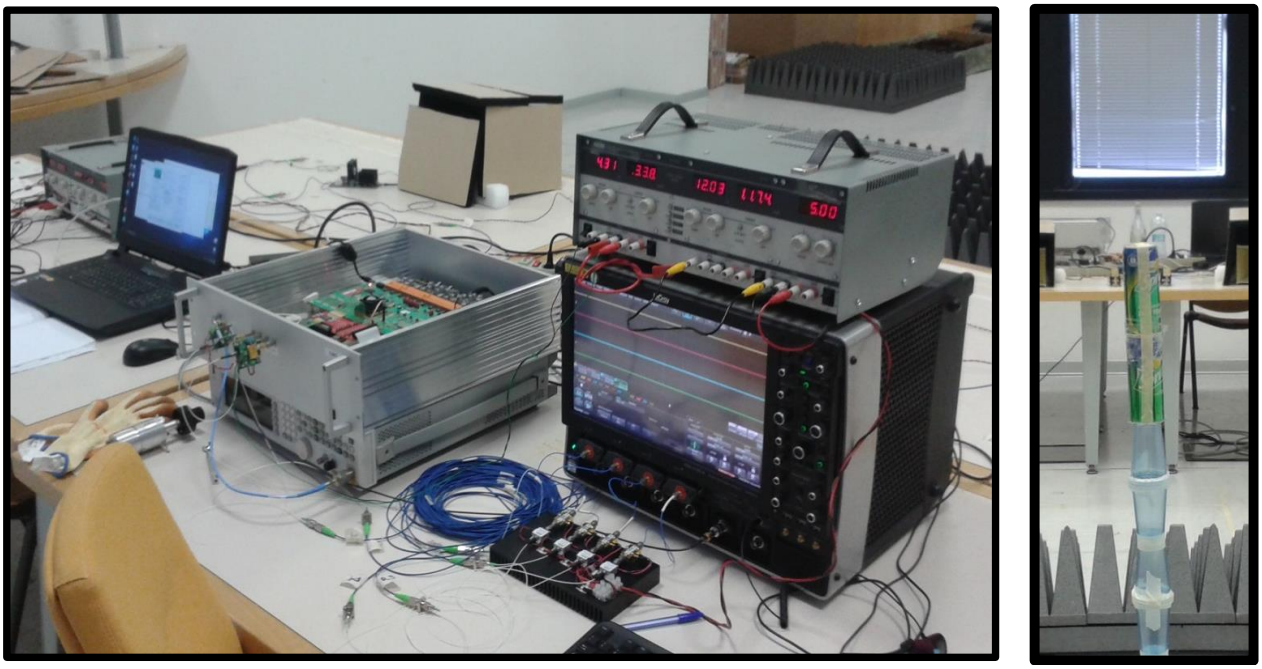

Figure 4-37: 2 TXs x 4 RXs MIMO experimental set-up: DAC, Oscilloscope and DSP (left) and 2-can target (right)

Nevertheless, for practical reasons other geometries have been explored which consent to uncouple more efficiently the receivers from the transmitters or, for instance, larger baseline so to enhance angular resolution. Therefore, in the following prior to discuss the results the implemented MIMO architecture is briefly presented. Moreover, with the aim to further optimize the system configuration ensuing measures have also been adopted:

- absorbing panels have been inserted between the TXs and RXs, as can be noticed from Figure 4-36, with the aim to further enhance RF uncoupling;

- as transmitters use more directive horn antennas they have been tilted (rotated symmetrically) towards the center of the room, where targets are placed, consenting so a better illumination of the area of interest.

Mono-target detection test

The finality of this set of test is to verify that the system is capable to individuate the presence of a target, independently form its relative position to the baseline. In particular, the target is moved in range and cross-range. In Table 4-4 the main target and antenna parameters for this test are listed. As already anticipated, some metallic elements within the laboratory determine a high clutter environment. Even tough those elements cannot be physically removed, a digital clutter suppression can be performed. For this reason, in addition to data acquisitions where the target is on the scene also acquisitions without the target have been taken. Since, luckily unwanted clutter is stationary, a significant enhancement can be obtained just subtracting for each channel the signal associated to the empty room from the target data set.

Parameter Name	Parameter Value/Description
Target type	Can
RCS	-4 dBsm (2 cans: each 5cm diam. x 15cm height)
TX positions	TX-1 (0m, -1.50m) TX-2 (0m, +1.50m)
RX positions	RX-1 (0m,-1.00m) RX-2 (0m,-0.50m) RX-3 (0m,+0.50m) RX-4 (0m,+1.00m)

Table 4-4: MIMO indoor 2 TXs x 4 RXs experiment main antenna and target parameters

The positive impact of clutter suppression is clearly recognizable observing

Figure **4-38**, which shows the radar maps determined with and without applying aforesaid measure respectively.

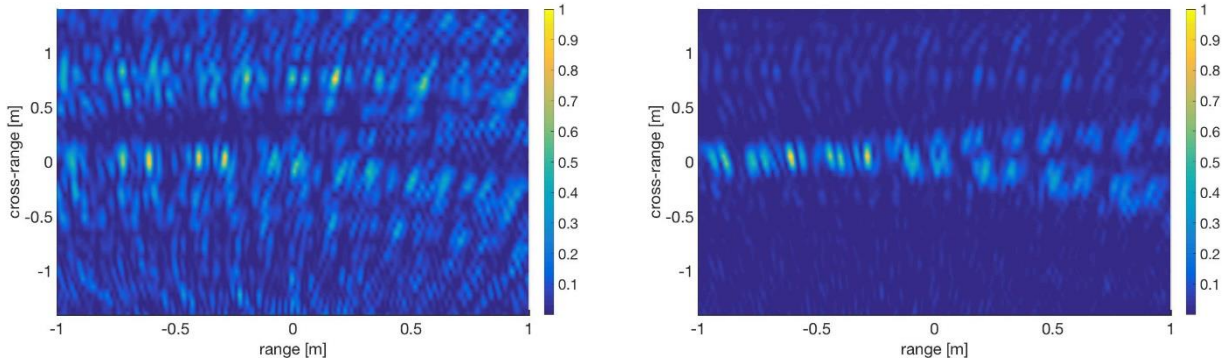

Figure 4-38: 2 TXs x 4 RXs MIMO experiment range cross-range maps without (left) and with (right) digital clutter suppression

In the light of the considerable enhancement achieved, in the following outcomes always include digital clutter suppression. In Figure 4-39 the range cross-range maps and the cross-range patterns computed for each mono-target test are reported.

Aforesaid maps are determined employing a MIMO coherent processing (i.e. high resolution image mode) and focus on an area with an extension of 2 m in cross-range (along the antenna baseline) and 3 m in range centered around position (4.2 m, 0 m). Spatial sampling is performed with a spacing of 2 λ (i.e. 7 cm) in range and 0.1 λ (0.35 cm) in cross range. Thus, in total, each high resolution map has 43 x 567 cells.

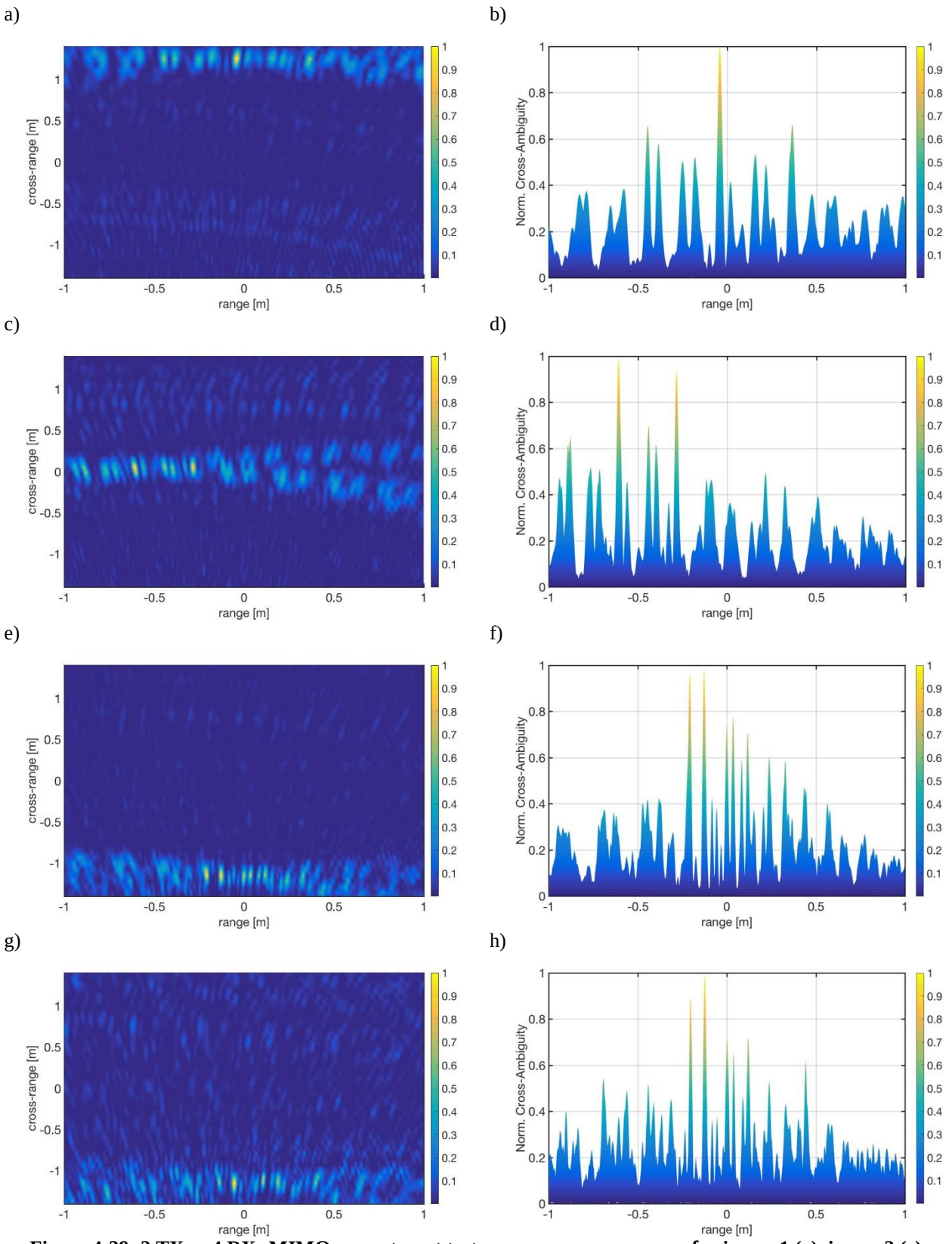

Figure 4-39: 2 TXs x 4 RXs MIMO mono-target test range cross-range maps for image 1 (a), image 2 (c), image 3 (e), image 4 (g) and cross-range pattern for image 1 (b), image 2 (d), image 3 (f), image 4 (h)

In Table 4-5 the main outcomes resultant from the analysis are summarized.

Image	Target Position	Relative Position	Detected Correctly Range	Detected Correctly Cross-range	Side lobes suppression	Notes
1	(5.4m, 0m)	(1.2m, 0m)	YES	YES	-3dB	Side lobes at +/-0.4m from main lobe
2	(4.2m, 0m)	(0m, 0m)	YES	YES	0dB	Side lobes at +0.3m from main lobe
3	(3.0m, 0m)	(-1.2m, 0m)	YES	NO	NOT APPLICABLE	Main lobe shifted -0.2m in cross-range
4	(3.0m, 0.1m)	(-1.2m, 0.1m)	YES	NO	NOT APPLICABLE	Main lobe shifted -0.3m in cross-range

Table 4-5: MIMO 2 TXs x 4 RXs experiment mono-target detection results

In conclusion, the radar system demonstrates a high reliability in determining the correct target range while in cross-range, especially for lower distances from the baseline, the cross-range measure is not exact. For the last 2 images analysed, where the target range distance is only 3 m, from the baseline, main lobes are shifted from the expected position. This behaviour could be a direct consequence of two factors:

- Target position is closer to antenna near field region with heavy repercussion on signal phase;
- Point-like assumption on target worse than for higher ranges, as, for instance, 4.2 m or 5.4 m;

Multi-target resolution test

The finality of this set of test is to verify that the system allows to successfully resolve two targets close to each other in the cross-range dimension. For this test the same parameters already detailed in Table 4-4 are applicable.

a)

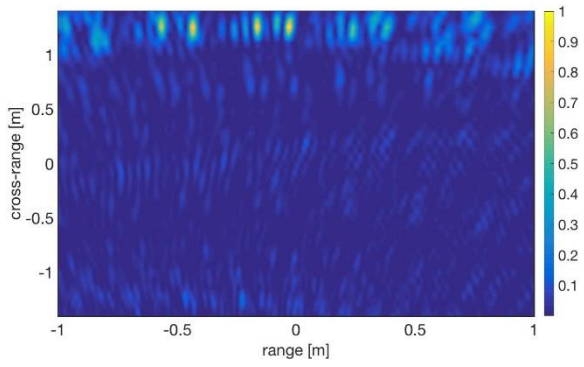

b)

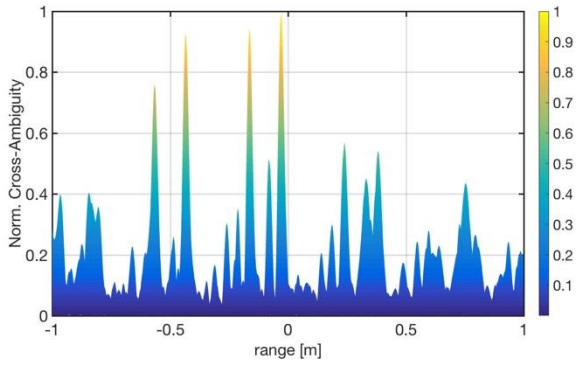

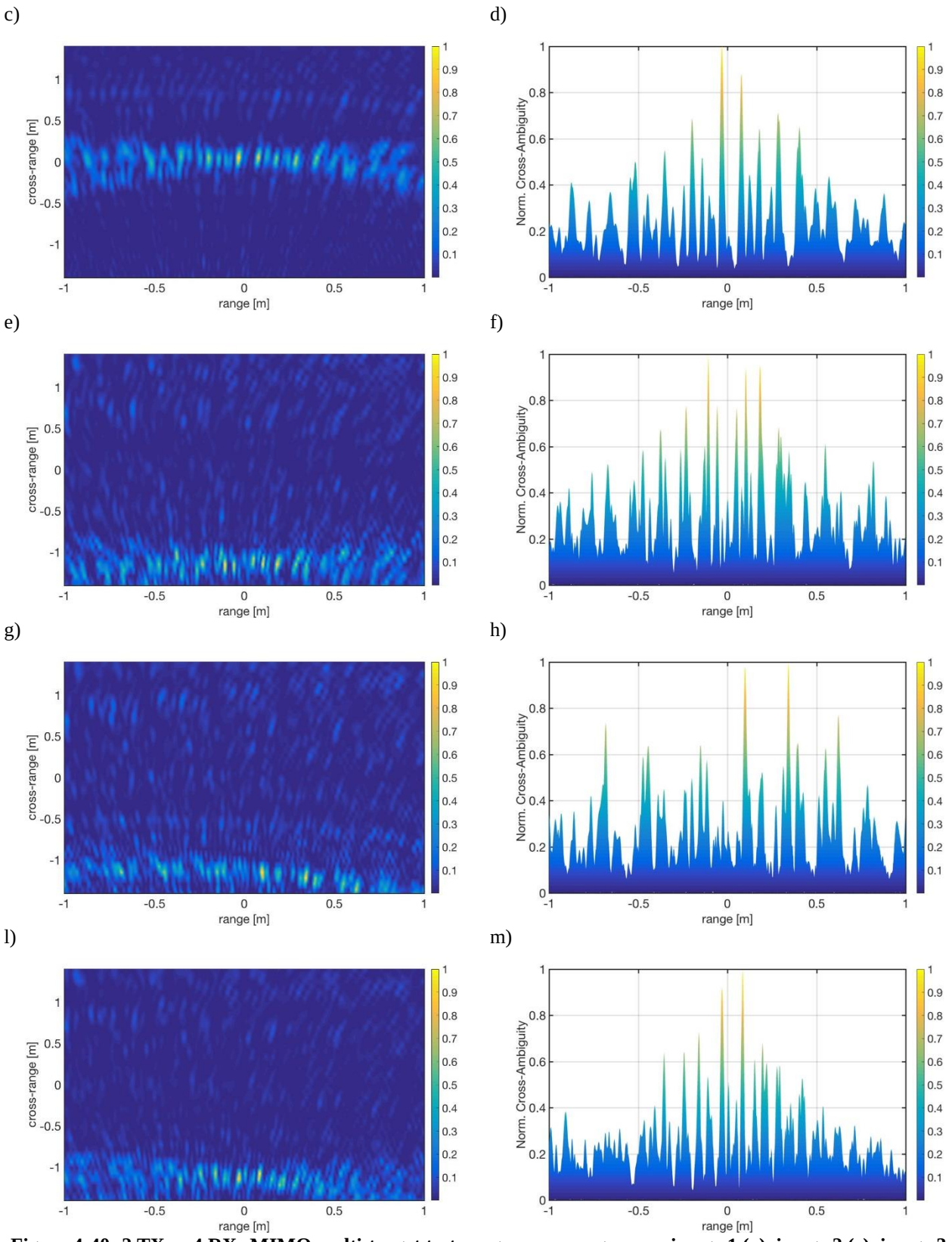

Figure 4-40: 2 TXs x 4 RXs MIMO multi-target test range cross-range maps image 1 (a), image 2 (c), image 3 (e), image 4 (g), image 5 (l) and cross-range pattern for image 1 (b), image 2 (d), image 3 (f), image 4 (h), image 5 (l)

Similarly, to mono-target test the results presented are achieved performing a high resolution image mode and cross-ambiguity function is computed exclusively on an area with an extension of 2 m in cross-range (along the antenna baseline) and 3 m in range centered around position (4.2m,0m).

As spatial sampling is done with a spacing of 2 λ (i.e. 7cm) in range and 0.1 λ (0.35cm) in cross range, thus in total each high resolution map has 43x567 cells.

Image	Target Position	Relative Position	First Target Detected	Second Target Detected	Side lobes suppression	Notes
1	(5.4m,0m) (5.4m, -0.2m)	(-0m, 1.2m) (1.2m, -0.2m)	YES	YES	-3dB	Grating lobes at -0.5m
2	(4.2m,0m) (4.2m, 0.1m)	(0m, 0m) (0m, 0.1m)	YES	YES	-2dB	None
3	(3.0m, 0m) (3.0m, 0.1m)	(-1.2m, 0m) (-1.2m, 0.1m)	NO (correct range detection)	NO (correct range detection)	NOT APPLICABLE	Two shifted peaks at +/- 0.1m in cross-range
4	(3.0m, 0m) (3.0m, 0.2m)	(-1.2m, 0m) (-1.2m, 0.2m)	NO (correct range detection)	NO (correct range detection)	NOT APPLICABLE	Two shifted peaks at +0.1m and +0.4 in cross-range
5	(3.0m,0m) (3.0m, 0.3m)	(-1.2m, 0m) (-1.2m, 0.3m)	NO (correct range detection)	NO (correct range detection)	NOT APPLICABLE	Two shifted peaks at +/- 0.05m in cross-range

Table 4-6: MIMO 2 TXs x 4 RXs experiment multi-target detection results

From Table 4-6, where all outcomes are summarized we infer that the system has a remarkable angular resolution since at a distance of 4.2 m two closely spaced targets, 10 cm far away one from each other are clearly resolved. Nevertheless, when the range is decreased to 3 m despite the better SNR available on each channel, side lobes raise to such an extent that cross-range resolution is spoiled. Probably the reasons behind this apparent incongruity are the same already individuated, also accountable for the reduced cross-range detection accuracy when a single target is situated at lower ranges (i.e. 3 m from the baseline). Other co-factors which can have an additional negative impact are:

- Insufficient system calibration (i.e. incorrect channel time delay estimation);
- Errors in the antenna positions used for MIMO computation.

Finally, a further reason is the minimal MIMO configuration deployed which ensures a reduced side lobe suppression. This factor is further investigated in next paragraph dedicated to a comparison between results achieved processing real data set and corresponding simulative outcomes.

4.3.3. Real data and simulative outcomes comparison

The purpose of the comparison outlined here is, first of all, to validate the developed MIMO scenario simulator and, in case a sufficient correspondence is found, cited design tool can be exploited to enhance current system performance assessed on mono-target and multi-target scenarios.

Starting from the antenna configuration, specified in Table 4-4, simulations have been effectuated replacing the distributed can target with an ideal point-like scatterer located in the same position. At difference to real environment measures, ideal conditions are assumed; thus neither clutter nor amplitude or phase noise contributes have been included. Besides slightly different parameters with respect to the experimental outcomes former discussed are adopted: the cross-ambiguity function is calculated on a smaller area with a lower spatial sampling. In particular, the image area now has a size of 2 m in cross-range (along the antenna baseline) and 2 m in range centered around the simulated target position and spatial sampling has a spacing of 2 λ (i.e. 7 cm) in range and 0.5 λ (1.25 cm) in cross range, so, in total, each high resolution map is made by 29 x 160 cells. Thanks to these simplifications the computational effort is reduced indicatively by a factor 6 and, subsequently, data processing is considerably speed up.

The first two cross-range pattern, depicted in Figure 4-41 a) and b), are related to a multi-target scenario where two targets located in A=(5.2m, 0m) and in B=(5.2 m, 0.2m) are present. Despite the high side lobes the cross-range pattern simulated at distance of 5.2 m from the antenna baseline has two peaks, exactly where targets are expected to be, namely at 0 m and -0.2 m in cross-range (see Figure 4-41 a)). Observing the same output achieved processing the equivalent real data set depicted in Figure 4-41 b) the target peaks are located in the right position and also the side lobe shape seems very similar. A couple of high side lobes, indeed, falls at cross-range 0.25 m and 0.35 m and another one at cross-range -0.45 m and -0.55 m. While the first side lobe couple has also the same relative amplitude the only difference can be found in the much higher intensity of the latter individuated side lobe couple. All in all, it is evident that there is a good match between the two pattern. Conversely, for a mono-target scenario with a target in position C=(0 m,3 m) the cross-range pattern, shown in Figure 4-41 c) and d) respectively, are completely different.

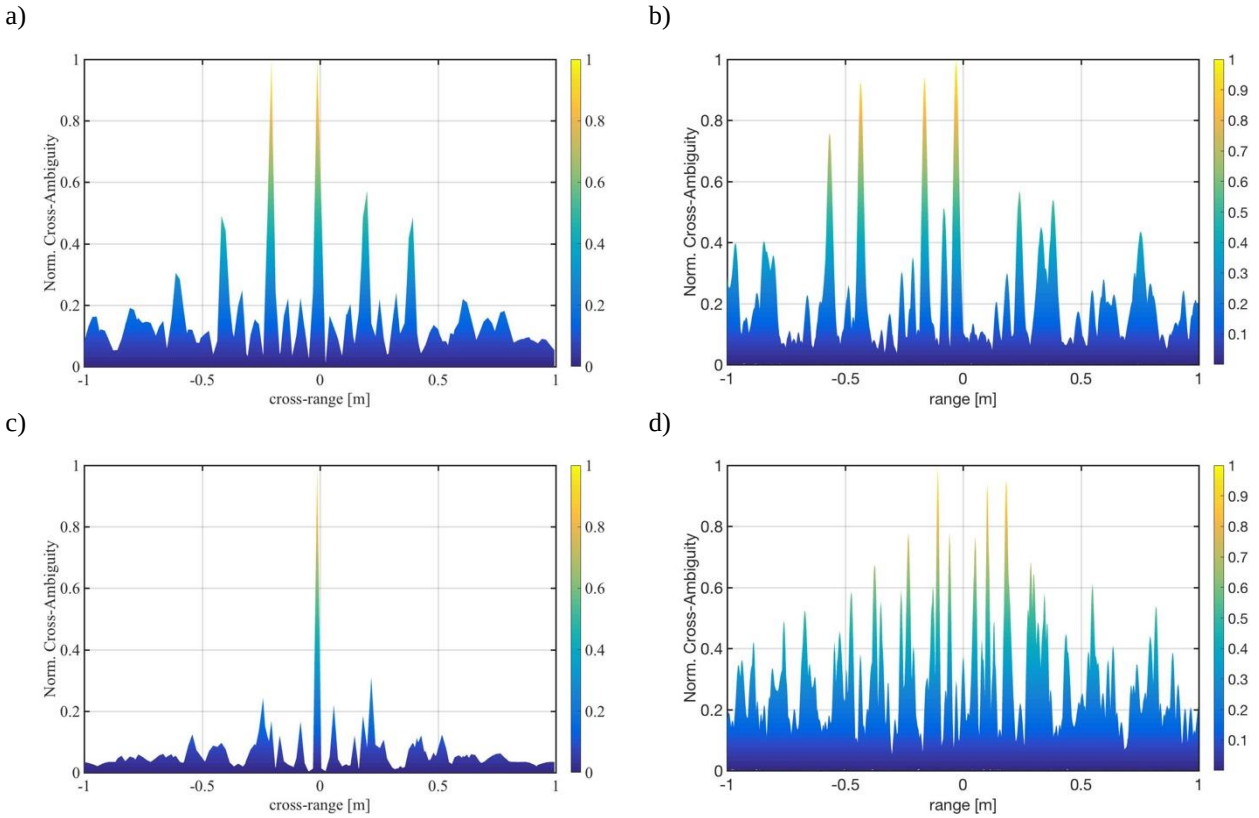

Figure 4-41: 2 TXs x 4 RXs MIMO real data against simulated data comparison cross-range pattern for multi-target equivalent simulated scenario (a), multi-target real scenario (b), mono-target equivalent simulated scenario (c), mono-target real scenario (d)

In real data processing a detection is though, as multiple main peaks are present and side lobes are very high at difference to the simulated scenario where only one peak is present and side lobes

are lower than -6 dB. Assuming that the cause of this deviation depends on the non point-like dimension of the real target, which we remember has a height of circa 30 cm (two cans) and a diameter of 5 cm the focus moves to the multi-target test with the aim to evaluate if MIMO configurations with more antenna elements can lead to a better ambiguity function side lobe suppression. In Figure 4-42 a) and b) the same output is determined simulating this time, instead than a MIMO 2 TXs x 4 RXs configuration, a 4 TXs x 4 RXs and a 6 TXs x 8 RXs respectively. Outcomes reveal that side lobes are lower than -13 dB with a net gain of over 7 dB with respect to the initial 2 TXs x 4 RXs geometry.

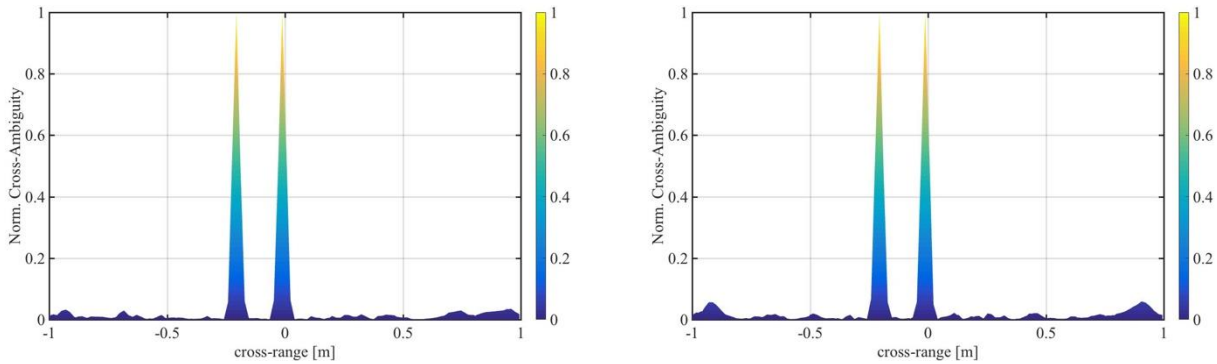

Figure 4-42: Multi-target simulations cross-range pattern for a MIMO 4 TXs x 4 RXs configuration (a) and MIMO 6 TXs x 8 RXs configuration (b)

Unfortunately, due to HW constraints such as the maximum available number of channels on the oscilloscope, used as ADC, which limits to 4 the maximum number of receivers, the current set-up cannot be upgraded without introducing major modifications. For this reason, at the moment data fusion techniques, discussed in section 3.4 and in 3.6 are explored in order to effeùctively mitigate the MIMO side lobe issue.

5. CONCLUSIONS

Fostered by the remarkable results already achieved by my research group in the field of photonics-based radar detection, in this work I have envisaged the chance to apply photonics also to multi-static radar systems and in particular to a novel class of radars, known as MIMO radars. Therefore, I have developed the MIMO simulator, outlined in Chapter I, with the specific purpose to find out the strengths and weaknesses of spatial distributed radar networks and to accomplish a preliminary feasibility check of the conceived system architecture as well. As the numerical analysis, individually carried out, considering different operative scenarios essentially confirms that a centralized photonics-based radar architecture can be adopted for coherent MIMO operations, cited design solution has been deeply investigated with the ambitious goal to prove its effectiveness. Subsequently, supported by my colleagues I have contributed to the development of the experimental set-up tested both in a down-scaled coastal scenario, and indoors, on an on-board automotive scenario. Thanks to profitable teamwork and excellent professional skills existing within the group, the remarkable localization accuracy and resolution capability, reported in Chapter IV, have been assessed. The experimental outcomes definitively witness the robustness of the proposed architecture and more generally demonstrate that photonics could result an enabling technology for the development of MIMO radars.

Simulations carried out clearly show the superiority of coherent MIMO detection with respect to analogous non coherent operations, since additional phase information can significantly reduce detection ambiguity. However, in consideration of the extremely high carrier frequency usually adopted by radars, the radar cross-ambiguity function has to be computed with a high spatial sampling in order to implement an appropriate phase shift compensation. Typically, radar carrier wavelengths for the examined applications are of the order of some cm, hence it is not practical to explore large areas using such fine resolution cell. For this reason, it is advisable to split the surveillance function into two steps: in search mode potential targets are first pre-located and, afterwards, coherent image mode can be performed on small areas already individuated in search mode for target imaging or identification purposes. In this way, the whole area of interest is continuously monitored in low resolution and high resolution coherent MIMO processing is realized on demand on limited portions of the scene, so as to keep the computational burden at acceptable levels.

The uttermost drawback of MIMO coherent processing are significant side lobes of the radar cross-ambiguity function. Several factors, such as fractional signal bandwidth, signal-to-noise ratio and antenna geometry, affect their intensity and disposition. Essentially a MIMO radar implements a virtual sparse array; thus, unlike a phased array, it is not surprising that side lobes have a high intensity. However, simulations have consented to verify that in general the higher the signal bandwidth and the total number of antenna elements foreseen by the MIMO architecture, the lower the side lobe amplitude.

Unfortunately, increasing those parameters implies a higher system cost and complexity level. For this reason, along the dissertation, various solutions have been investigated, all finalized to enhance side lobe suppression, given a fixed MIMO architecture.

Especially in naval and automotive applications, physical constraints often impede to install antennas in some specific area of the platform. When this happens, it is not possible to distribute sensors uniformly, which usually represents the best installation solution in terms of side lobe suppression, and it is opportune to perform an antenna geometry optimization. For the naval scenario, since an exhaustive search for the optimum solution is not conceivable, as the sparse array is wide with respect to the carrier wavelength, which implies a considerable number of candidate positions, this kind of analysis has been effectuated by investigating a statistic and a genetic approach. The best result has been achieved by the genetic algorithm leveraging on the MIMO scenario simulator for the computation of the PSLR fitness function. The optimal antenna geometry obtained by the means of cited algorithm is 3 dB better than the optimal solution found through a statistical approach and 13 dB better than a non-optimal solution.

When the MIMO radar network is embarked on a moving platform SAR-like data fusion, can lead to an enhanced side lobe suppression. Leveraging, in fact, on the same principle at the root of SAR processing, it is possible to reduce detection ambiguity through coherent integration of sequentially acquired data in spatial diversity. Provided that target and MIMO network coherence is guaranteed for the entire observation time (T_{OBS}), assuming to use M TXs and N RXs a virtual array formed by MxNxK elements is realized, where K represents the ratio between the observation time and the radar waveform pulse repetition interval (T_R). Simulations outcomes, assuming realistic parameters for a naval scenario, confirm that in this way a side lobe suppression enhancement as high as 14 dB can be achieved. Moreover, a sufficient robustness to estimation errors of the platform speed has also been verified.

Finally, a completely different approach has been explored based on multiple observations of the scene acquired in frequency diversity rather than in spatial diversity. The basic idea is that, though antenna geometry is fixed, side lobe peaks fall in different positions around the main lobe, depending on the carrier wavelength. Accordingly, combining multiple range cross-range maps obtained using different carrier frequencies leads to a resulting detection map with mitigated side lobes. The method appears very simple and powerful, at the same time, even when a minimal MIMO architecture is deployed and suitable, especially, for an automotive case, where carrier frequencies can be better separated. Simulations done show that the initial -1 dB side lobe suppression on each mono-band MIMO map can be lowered until -12 dB, with a remarkable net gain of over 10 dB, when multi-band data fusion is performed.

In total, 3 scenarios have been analysed addressing, at first, more theoretical aspects when the coastal scenario has been examined and, gradually, more practical ones when the remaining naval and automotive scenarios have been covered. Despite each situation has its own specific system parameters and design requirements, it turns out that adopting a coherent MIMO radar network appears to be always advantageous, since a superior angular resolution can be ensured, much higher than the current standard. For instance, in the naval case, where a practical solution has been outlined, by evaluating also the impact of unknown sensor displacement, imputable to structural ship deformations, angular resolution passes from 10 mrad to indicatively 0.1 mrad with a noteworthy increment by a factor 100.

MIMO approach has an intrinsic drawback which represents, at the same time, its major strength: all elements of the MIMO configuration need to “see” the target simultaneously. The only way to satisfy this requirement, especially when a largely distributed network is deployed, is through low directional antennas. Unfortunately, a lower directivity implies even a lower antenna gain, which is a vital factor in radar applications to get high radar ranges. Nonetheless, the apparent disadvantage to use low gain antennas can be balanced thanks to longer CPI times, as, unlike in conventional radars, neither rotating nor electronic beam scanning antennas are used. Even under the worst hypothesis that signal orthogonality is realized using time diversity, more pulses can be integrated so that the initial antenna gain disadvantage can be balanced and sometimes even higher SNRs can be reached.

It has to be underscored that for the scenarios examined in the present study radar power budget is unquestionably not an issue, as the maximum target range is limited respectively to tens of km for maritime applications and tens of m for automotive applications. Hence, by suitably selecting all radar parameters, standard detection can be easily guaranteed.

On the other hand, changing radar paradigm from a conventional monostatic to a MIMO distributed radar network, entails several benefits in addition to fine angular resolution, far better than the resolution associated to the sole signal bandwidth. Although the following aspects have not been addressed, it has to be pointed out that the possibility to observe the scene with different aspect angles represents a strategic advantage in the detection of low RCS or stealth targets (diversity gain) and facilitates also the discrimination of slow-moving targets.

Additional minor benefits due to the proposed architecture are:

- Large aperture antennas assure a continuous surveillance of the scenario unlike conventional radars with rotating or electrical beam scanning antennas, where monitoring is discontinuous (ubiquitous monitoring) [31];
- Better fault tolerance and graceful degradation due to the particular system architecture composed by multiple distributed TX and RX antennas;
- Better system integration, especially when antennas with a small form factor, such as patch antennas, are used;
- Spatial sensor distribution allows to effectively solve EMI issues between conflicting systems (EMI optimization).

Despite MIMO radars with widely separated antennas can ensure all those advantages, issues hard to solve in the RF domain, still impede the spreading of this innovative radar class. In fact, depending on the network topology, which can either be distributed or centralized, different requirements have to be ensured. Essentially the main challenge for a centralized architecture is an efficient signal distribution, whereas a distributed one needs a tight time and phase synchronization. Realizing an efficient signal distribution can be easily achieved in the optical domain; consequently, both implemented photonics-based demonstrators adopt a centralized architecture.

Based on the design indications emerged from the whole numerical analysis accomplished and, encouraged by the outcomes of the phase noise analysis, suggesting that a MLL optical oscillator is eligible for the implementation of a centralized coherent MIMO radar network, first an outdoor experiment has been carried out using a minimal MIMO 1 TX x 2 RXs configuration. Successively, given the positive results obtained, other experimental activities using more transmitters and receivers (i.e. 2 TXs and 2 RXs and a 2 TXs x 4 RXs architecture) have been realized. For each test a specific set-up has been implemented and, in particular, for the last experiment photonics is exploited exclusively for signal distribution.

The activities have consented to test the implemented MIMO detection algorithms on real data set as well as to validate the developed simulator comparing its outcomes with the corresponding results from real data processing.

Although a minimal MIMO architecture deployed for the outdoor trials and the difficulties typical of an open-field environment, in which background clutter, electromagnetic interferences, RCS fluctuations and multipath are all elements that degrade radar performance, a single target has been correctly pre-located with an ambiguity of 3 m in both range and cross-range dimension. Subsequently, in high resolution image mode the target localization precision has been lowered to ~10 cm, about 10 times better than the range resolution capability ensured by a radar waveform with a signal bandwidth equal to 100 MHz. Moreover, a cross-range resolution of, at least, 3 m has been demonstrated, as two targets spaced 3 m along cross-range have been successfully resolved. Unfortunately, for security reasons, as the targets were carried by two drones, it has not been possible to further reduce the target distance in cross-range. However, the result reached by the first photonics-based MIMO coherent radar network tested in an open field environment is very promising, especially, if the cross-range resolution obtained is compared with the angular resolution provided by

the horn antennas used for the experiment (equal to 15 m for the considered distance from the baseline). Indeed, an increment by a factor 5 has been achieved.

Indoors test confirm the remarkable angular resolution capability of a coherent MIMO radar network with widely separated antennas. In fact, two targets both located at a range of 4.2 m and spaced only 10 cm apart in cross-range have been distinguished.

Finally, test finalized to verify the reliability of the simulator show a good match between numerical outcomes and those obtained by processing real data, confirming the validity of the developed tool.

In conclusion, the experiments endorse the huge potential of a coherent MIMO processing and the effectiveness of a photonics-based approach for the implementation of a centralized radar network with widely separated antennas.

Moreover, the research activity has consented to individuate ensuing aspects which should be better investigated:

- Bi-static and distributed target RCS: MIMO theory has been developed for point-like scatterers; however real targets are distributed, so it is mandatory to evaluate how this factor impacts on radar detection;
- High clutter environment: the use of large aperture antennas, as noticed during experiments carried out, entails a target detection in a high clutter background; thus efficient techniques need to be developed (i.e. MIMO CFAR detector) to address this upcoming issue;
- Diversity gain: based on RCS target models first a numerical analysis and afterwards field trials should be conducted in order to prove the potential improvement arising from radar detection performed exploiting data acquired in spatial diversity;
- 2D-3D radar detection: during the dissertation only 2-D scenarios have been considered. Although this is a reasonable assumption for maritime applications, indoor test reported related to an automotive case have revealed that a 2-D model is a limiting assumption and that a 3-D model would be more indicated, enabling perhaps a fine elevation localization.

At the same time, more sophisticated MIMO configurations should be investigated as well as proposed data fusion techniques finalized to lower radar cross-ambiguity function side lobes. Ultimately, field trials in a relevant maritime scenario should be planned in order to definitively prove the remarkable detection capability of this innovative photonics-based radar architecture including possibly also system robustness and reliability tests. These final tests could take place at the facilities of the Vallauri Institute, the Research Centre for Telecommunications and Electronics of the Italian Navy, located in Livorno.

LIST OF PUBLICATIONS

Conference Papers

Ghelfi P., Scotti F., Serafino G., **Lembo L.**, Hussain B., Onori D., Falconi F., Porzi C., Malacarne A., Bogoni A., "The photonic revolution in radars", AFCEA, Rome, ITALY, October 2017.

Lembo L., Ghelfi P., Bogoni A., "Analysis of a Coherent Distributed MIMO Photonics-Based Radar Network", European Radar Conference (EuRAD) 2018, Madrid, Spain, September 2018.

Lembo L., Serafino G:, Scotti F., Ghelfi P., Bogoni A., "Microwave Photonics in Radar", IEEE Photonics Conference (IPC 2018), Reston, USA, October 2018.

Lembo L., Ghelfi P., Bogoni A., "Photonics-based coherent MIMO radar networks" Asia Communications and Photonics Conference (ACP) 2018, Hangzhou, China, October 2018.

Lembo L., Maresca S., Serafino G:, Amato F., Scotti F., Ghelfi P., Bogoni A., "In-Field Demonstration of a Photonic Coherent MIMO Distributed Radar Network" 2019 IEEE Radar Conference, Boston, USA, May 2019.

Lembo L., Serafino G., Scotti F., A. Malacarne, Ghelfi P., Bogoni A., "Photonics for Radar systems", PhotonIcs & Electromagnetics Research Symposium (PIERS 2019), Rome, Italy, June 2019.

Lembo L., Ghelfi P., Bogoni A., "Antenna Position Optimization of a MIMO Distributed Radar Network through Genetic Algorithms", International Radar Symposium (IRS) 2019, Ulm, Germany, June 2019.

Maresca S., Serafino G., Scotti F., Amato F., **Lembo L.**, Bogoni A, Ghelfi P., "Photonics for Coherent MIMO Radar: an Experimental Multi-Target Surveillance Scenario", International Radar Symposium (IRS) 2019, Ulm, Germany, June 2019.

Lembo L., Malacarne A., Ghelfi P., Bogoni A., "SAR-Like Multi-Input Multi-Output Radar for Naval Applications", European Radar Conference (EuRAD) 2019, Paris, France, October 2019.

Malacarne A., Maresca S., Scotti F., Hussain B., **Lembo L.**, Serafino G., Bogoni A., Ghelfi P., "A Radar over-fiber System based on Directly-Modulated Uncooled VCSELS", European Conference on Optical Communication (ECOC) 2019, Dublin, Ireland, September 2019.

Malacarne A., Maresca S., Scotti F., Hussain B., **Lembo L.**, Serafino G., Bogoni A., Ghelfi P., "A ultrawide-band VCSEL-based radar-over-fiber system", 2019 IEEE

International Topical Meeting on Microwave Photonics (MWP) 2019, Ottawa, Canada, October 2019.

Journals

Serafino G., Amato F., Maresca S., **Lembo L**., Ghelfi P., Bogoni A., "Photonic approach for on-board and ground radars in automotive applications" IET Radar, Sonar & Navigation, Vol. 12, n. 10, pp. 1179-1186, 2018;

Ghelfi P., Scotti F., Serafino G., **Lembo L.**, Hussain B., Onori D., Falconi F., Porzi C., Malacarne A., Bogoni A., "Towards a New Generation of Radar Systems Based on Microwave Photonic Technologies, IEEE/OSA Journal of Lightwave Technology, Vol. 37, pp.643-650, 2019.

Books

Bogoni, A., Ghelfi, P., Laghezza, F. et al, Photonics for Radar Networks and Electronic Warfare Systems, Scitech Publishing, 2019;

G. Galati et al, Radar Evolution: the Italian Accademic Contribution", CNIT Technical Report-02, 2018.

REFERENCES

[1] Barton, D.K., Radar Technology Encyclopaedia, Artech House, London 1997.

[2] Griffiths, H., Klein Heidelberg–The First Modern Bi-static Radar System, IEEE Transactions on Aerospace and Electronic Systems, Vol. 46, No. 4, October 2010.

[3] Ingss, M. et al, NetRad multistatic sea clutter database, IEEE International Geoscience and remore Sensing Symposium (IGARSS), July 2012

[4] Derham, T. et al, Realization and Evaluation of a Low Cost Netted Radar System, IEEE Radar 2006.

[5] Moo, P., Overview of Naval Multifunction RF Systems, European Radar Conference (EuRAD) September 2018.

[6] Willis, N. J., Bistatic Radar, 2nd Ed. SciTech Publishing, 2005.

[7] Bilal, H et al, Performance Analysis of Auto-Regressive UWB Synthesis Algorithm for Coherent Multi-Band Radars, International Radar Conference (IRC) 2017.

[8] Baker, C. J, An introduction to multistatic radar. 2009. NATO-SET 136 Lecture Series Multistatic Surveillance and Reconnaissance: Sensor, Signal and Data Fusion.

[9] Chernyak, V. S. Fundamentals of Multisite Radar Systems: Multistatic Radars and Multistatic Radar Systems. 1st. s.l. : CRC Press, 1998.

[10] Hanle, E. Survey of bistatic and multistatic radar 1986, IEEE Proceedings on Communications, Radar and Signal Processing, Vol. 133, p. 587–595.

[11] Breault, T. L., The Effects of Crystal Oscillator Phase Noise on Radar Systems Report FEI-Zyfer, Inc.

[12] Hee, T. H., Hajimiri, A., Oscillator Phase Noise: A Tutorial, IEEE J. Solid-State Circuits, vol. 35, no. 3, pp. 326-336.

[13] Auterman, J. L., Phase stability requirements for a bistatic SAR, 1984. Proceedings of the IEEE National Radar Conference. p. 48–52.

[14] Weiss, M., Time and phase synchronization aspects for bistatic SAR systems, 2004. Proceedings of the European Synthetic Aperture Radar Conference. p. 395–398.

[15] Wang, W. Q., Multi-Antenna Synthetic Aperture Radar. London, UK : CRC Press, 22013.

[16] J.Choi, B., DCS: distributed asynchronous clock synchronization in delay tolerant networks, 2012, IEEE Transactions on Parallel and Distributed Systems, Vol. 23, p. 491–504.

[17] Leng, M., Distributed clock synchronization for wireless sensor networks using belief propagation, 11, 2011, IEEE Transactions on Signal Processing, Vol. 59, p. 5404–5414.

[18] Amemiya, M. e al., Time and frequency transfer and dissemination methods using optical fiber network. Proceedings of the 2005 IEEE International Frequency Control Symposium and Exposition.

[19] Predehl, Katharina e al, A 920-kilometer optical fiber link for frequency metrology at the 19th decimal place." Science., et. 2012, Science, Vol. 27, p. 441-444. 336.6080.
[20] Capmany, J., Microwave photonics combines two worlds, Nature photonics Vol. 1, June 2007
[21] Godrich, H., Target Localization Accuracy Gain in MIMO Radar-Based Systems, IEEE Transactions on Information Theory, Vol. 56, N°. 6, June 2010.
[22] Chernyak, V., Multisite Radar Systems Composed of MIMO Radars, IEEE Aerospace and Electronics Systems Magazine, December 2014.
[23] Bathurst, J.N., Design Considerations for a Shipboard MIMO Radar for Surface Target Detection, European Radar Conference 2018.
[24] Rao, S., MIMO Radar, Texas Instruments Application Report SWRA554A– May 2017.
[25] Haimovich, A. M., MIMO radar with widely separated antennas, IEEE Signal Processing Magazine January 2008.
[26] Escot-Bocanegra, D., Indoor Measurement of Bistatic High Resolution Range Profiles of Scale Model Aircraft Targets, European Radar Conference, Sept 2018, Madrid, Spain
[27] Frankford M, Numerical and Experimental Studies of Target Detection With MIMO Radar, IEEE Transactions on Aerospace and Electronics, Vol. 50, No. 2, April 2014.
[28] Lehmann, Nikolaus H., High Resolution Capabilities of MIMO Radar, IEEE Signals System and Computers 2006.
[29] Steinberg, B, The Peak Sidelobe of the Phased Array Having Randomly Located Elements, IEEE Transactions on Antenna Propagation, Vol. a-20, No. 2, March 1972.
[30] Steinberg, B, Sidelobe Reduction of Random Arrays by Element Position and Frequency Diversity, IEEE Transactions on Antenna Propagation, Vol. a-31, No. 6, Nov 1983.
[31] Skolniek, M., System Aspect of Digital Beam Forming Ubiquitous Radar, Naval Research Laboratory, vol. NRL/MR/5007—02-8625, June 2002.
[32] Pasya, I. et al, Detection Performance of M-Sequence-Based MIMO Radar Systems Considering Phase Jitter Effects", IEEE Phased Array Systems & Technology, 2013.
[33] Lembo, L. et al, Analysis of a Coherent Distributed MIMO Photonics-Based Radar Network, European Radar Conference (EuRAD) 2018.
[34] Mizuno, T., Miyamoto, Y., High capacity dense space division multiplexing transmission, Optical Fiber Technology, vol.35, pp. 108-117, February 2017.
[35] Bogoni, A., Ghelfi, P., Laghezza, F., Photonics for Radar Networks and Electronic Warfare Systems, Scitech Publishing, 2019.
[36] Capmany J., Microwave photonics combines two worlds, Nature photonics Vol 1 June 2007.
[37] Fu, Jianbin e Shilong Pan, A fiber-distributed bistatic ultra-wideband radar based on optical time division multiplexing. 2015. IEEE 2015 International Topical Meeting on Microwave Photonics.
[38] Chi, H., Yao, J.P., An approach to photonic generation of high frequency phase-coded RF pulses, IEEE Photonics Technology Letters, vol. 19, no. 10, pp. 768–770, 2007.
[39] Lin, I.S., McKinney, J.D., Photonic synthesis of broadband microwave arbitrary waveform applicable to ultrawideband communication, IEEE Microwave and Wireless Components Letters, vol. 15, no. 4, pp. 226–228, 2005.

[40] Nanzer, J. A., et al., Photonic Signal Generation for Millimeter- Wave Communications, Johns Hopkins apl Technical Digest, vol. 30, no. 4, pp. 299-308, 2012.
[41] Yilmaz, T. et al., Toward a Photonic Arbitrary Waveform Generator Using a Modelocked External Cavity Semiconductor Laser, IEEE Photonics Technology Letters, vol. 14, no. 11, pp. 1608-1610, 2002.
[42] Chou, J., Han, Y. and Jalali, B., Adaptive RF-Photonic Arbitrary Waveform Generator, International Topical Meeting on Microwave Photonics, pp. 1226-1229, 2002.
[43] Ghelfi, P., Scotti, F., Laghezza, F., Bogoni, A., Phase Coding of RF Pulses in Photonics-Aided Frequency-Agile Coherent Radar Systems, IEEE Journal of Quantum Technology, vol 48, no. 9, pp. 1151-1157, 2012.
[44] Ghelfi, P., Scotti, F., Laghezza, F., Bogoni, A., Photonic Generation of Phase-Modulated RF Signals for Pulse Compression Techniques in Coherent Radars, IEEE Journal of Lightwave Technology., vol. 30, no. 11, pp. 1638-1644, June 2012.
[45] Seeds, A.J., Lee, C.H., Naganuma, M., Guest editorial: Microwave photonics. IEEE Journal of Lightwave Technology, vol. 21, no 12, pp 2959–2960, 2003.
[46] Cox, C.H., Ackerman, E. I., Microwave Photonics: past, present and future, International Topical meeting on Microwave Photonics, pp 9-11, 2008.
[47] Capmany, J., Novak, D., Microwave Photonics combines two worlds, Nature Photonics, vol. 1, no. 6, pp. 319-330. 2007.
[48] Yao, J., Microwave photonics, IEEE Journal of Lightwave Technology, vol. 27, no. 22, pp. 314-335, 2009.
[49] Yu, J. , Jia, Z. , Wang, T., Chang, G.K., Centralized Lightwave Radio-Over-Fiber System With Photonic Frequency Quadrupling for High-Frequency Millimeter-Wave Generation, IEEE Photonics Technology Letters, vol. 19, no. 19, pp. 1499-1501, 2007.
[50] Bohémond, C., Rampone, T., Sharaiha, A., Performances of a Photonic Microwave Mixer Based on Cross-Gain Modulation in a Semiconductor Optical Amplifier, IEEE Journal of Lightwave Technology, vol. 29, no. 16, pp. 2402-2409, 2011.
[51] Ghelfi, P., Scotti, F., Laghezza, F., Onori, D., Bogoni, A, Photonics for Radars Operating on Multiple Coherent Bands, J. Lightwave Technol., vol. 33, no. 2, pp. 500-507, 2016.
[52] Valley, G.C., Photonic analog-to-digital converters, Optics Express, vol. 15, no 5, pp. 1955-1982, 2007.
[53] Juodawlkis, P. W., Twichell, J. C., Betts, G. E., Hargreaves, J. J. et al, Optically sampled analog-to-digital converters, IEEE Transaction on Microwave Theory and Techniques vol. 49 no. 10, pp. 1840–1853, 2001.
[54] Laghezza, F., Scotti, F., Ghelfi, P. , Bogoni, A, Photonics-Assisted Multiband RF Transceiver for Wireless Communications, IEEE Journal of Lightwave Technology, vol. 32, no. 16, pp. 2896-2904, 2014.
[55] Laghezza, F., Scotti, F., Ghelfi, P., Pinna, S., Serafino, G., Bogoni, A, Jitter-Limited Photonic Analog-to-Digital Converter with 7 effective bits for wideband radar applications, IEEE Radar Conference, pp. 1-5, 2013.
[56] Capmany, J. Ortega, B., Pastor, D., A tutorial on microwave photonic filters, IEEE Journal of Lightwave Technology, vol. 24, no. 1, pp. 201-229, 2006.
[57] Shen, H., Khan, M.H., Fan, L., Zhao, L., Xuan, Y., Ouyang, J. Varghese, L.T., Qi, M., Eight-channel reconfigurable microring filters with tunable frequency, extinction ratio and bandwidth, Optics Exp., V. 18, n. 17, pp. 18067-18076 (2010).

[58] Cox, C., et al. Limits on the Performance of RF-Over-Fiber Links and Their Impact on Device Design IEEE Transactions On Microwave Theory And Techniques, Vol. 54, No. 2, February 2006.
[59] Futatsumori, S. , Morioka, K., Kohmura, A., Okada, K., Yonemoto, N., Design and Field Feasibility Evaluation of Distributed-Type 96 GHz FMCW Millimeter-Wave Radar based on Radio-Over-Fiber and Optical Frequency Multiplier, Journal Lightwave Technology, v.34, n.20, 2016.
[60] Ghelfi, P., Laghezza, F., Scotti, F., Serafino, G., Capria, A., Pinna, S., Onori, D., Porzi, C., Scaffardi, M., Malacarne, A., Vercesi, V., Lazzeri, E., Berizzi, F., Bogoni, A., A fully photonics-based coherent radar system, Nature, vol. 507, no. 7492, pp. 341–345, 2014.
[61] Zhang, F., Guo, Q., Wang, Z., Zhou, P., Zhang, G., Sun, J., Pan, S., Photonics-based broadband radar for high resolution and real-time inverse synthetic aperture imaging, Opt. Exp., V.25, N.14, 2017.
[62] Nagatsuma, T., Horiguchi, S., Minamikata, Y., Yoshimizu, Y., Hisatake, S., Kuwano, S., Yoshimoto, N., Terada, J., Takahashi, H., Terahertz wireless communications based on photonics technologies, Opt. Exp., V.21, N.20, 2013.
[63] Laghezza, F., Scotti, F., Ghelfi, P., Bogoni, A., Photonics-Assisted Multiband RF Transceiver for Wireless Communications, IEEE J. Lightwave Technol., vol. 32, no. 16, pp. 2896-2904, 2014.
[64] Scotti, F., Laghezza, F., Serafino, G., Pinna, S., Onori, D., Ghelfi, P., Bogoni, A., In-field experiments of the first photonics-based software-defined coherent radar, J. Lightwave Technol., vol. 32, n. 20, pp. 3365-3372, Oct. 2014.
[65] Scotti, F., Laghezza, F., Serafino, G., Banchi, L., Malaspina, V., Ghelfi, P., Bogoni, A., Field evaluation of a photonics-based radar system in a maritime environment compared to a reference commercial sensor, IET Radar Sonar Navig., 9, 8, pp. 1040–1046, 2015.
[66] Scotti, F., Laghezza, F., Bogoni, A., Field trial of a photonics-based dual-band fully coherent radar system in a maritime scenario, IET Radar Sonar Navig. Vol. 11, n. 3, 2017.
[67] Scotti, F., Laghezza, F., Ghelfi, P., Bogoni, A., Multi-Band Software-Defined Coherent Radar Based on a Single Photonic Transceiver, IEEE Trans. Microwave Theory Techn., vol. 63, no. 2, pp. 546-552, 2015.
[68] Dalle Mese, E., Appunti al corso di tecnica radar, Servizio Editoriale Università di Pisa, 2006.
[69] Carr, J., An Introduction to Genetic Algorithms, May 2014.
[70] Lembo, L., Ghelfi, P., Bogoni A., Antenna Position Optimization of a MIMO Distributed Radar Network through Genetic Algorithms, International Radar Symposium (IRS) 2019, Ulm, Germany, June 2019.
[71] Moreira, A., et al, A tutorial on Synthetic Aperture Radar, IEEE Geoscience and Remote Sensing Magazine, Vol. 1, pp 6-43, March 2013.
[72] Tomiyasu, K., Tutorial Review of Synthetic-Aperture Radar (SAR) with Applications to Imaging of the Ocean Surface, Proceedings of the IEEE, Vol. 66, pp.1585-1585, May 1978.
[73] Wang, W. Q., MIMO SAR imaging: Potential and challenges, IEEE Aerospace and Electronic Systems Magazine, Vol.28, pp.18-23, 2013
[74] Cristallini, D. et al, Exploiting MIMO SAR Potentialities With Efficient Cross-Track Constellation Configurations for Improved Range Resolution, IEEE Transactions on Geoscience and Remote Sensing, Vol. 49 No.1, January 2011
[75] Tarchi, D. et al, MIMO Radar and Ground-Based SAR Imaging Systems: Equivalent Approaches for Remote Sensing, IEEE Transactions on Geoscience and Remote Sensing, Vol.51, N.1, January 2013.

[76] Lembo, L., Malacarne, A., Ghelfi P., Bogoni A., SAR-Like Multi-Input Multi-Output Radar for Naval Applications, European Radar Conference (EuRAD) October 2019.
[77] Selling autos by selling safety," The New York Times, January 1990.
[78] European Telecommunications Standards Institute, "ETSI EN 302 264-1 V1.1.1, June, 2009.
[79] Menzel, W., Millimeter-wave radar for civil applications, Proceedings of the 7th European Radar Conference, Sept. 2010.
[80] Köhler, M, Hasch, J., Blöcher, H.L., et al., Feasability of automotive radar at frequencies beyond 100 GHz, International Journal of Microvawe and Wireless Technologies, vol. 5, n.1, 2013.
[81] Serafino, G., Amato, F., Maresca, S., Lembo, L., Ghelfi, P., Bogoni, A., Photonic approach for on-board and ground radars in automotive applications, IET Radar, Sonar & Navigation, Vol. 12, n. 10, pp. 1179-1186, 2018.
[82] Lembo, L., Maresca, S., Serafino, G, Amato, F., Scotti, F., Ghelfi, P., Bogoni, A., In-Field Demonstration of a Photonic Coherent MIMO Distributed Radar Network, 2019 IEEE Radar Conference, Boston, USA, May 2019.
[83] Serafino, G., Ghelfi, P., Perez-Millan, P. et al., Phase and amplitude stability of EHF-band radar carriers generated from an active mode-locked laser, J. Lightwave Technol., vol. 29, no. 23, Dec. 2011.
[84] Ghelfi, P., Scotti, F., Nguyen, A. T., Serafino, G. and Bogoni, A., Novel architecture for a photonics-assisted radar transceiver based on a single mode-locking laser, in IEEE Photonics Technology Letters 23 (10), 5720509, pp. 639-641.
[85] Williams, P. A., Swann, W. C., and Newbury, N. R., High-stability transfer of an optical frequency over long fiber-optic links, Journal of Optical Society of America, B 25, pp. 1284-1293, 2008.
[86] Richards, G.A., Fundamentals of Radar Signal Processing, 2nd Ed., McGraw-Hill, 2014.
[87] Gandhi, P. and Kassam, S. A., Analysis of CFAR Processors in Nonhomogeneous Background, IEEE Transactions on Aerospace and Electronic Systems, vol. 24, pp. 427-445, July 1988.
[88] Maresca, S., Serafino, G., Scotti, F., Amato, F., Lembo, L., Bogoni, A., Ghelfi, P., Photonics for Coherent MIMO Radar: an Experimental Multi-Target Surveillance Scenario, International Radar Symposium (IRS) 2019, Ulm, Germany, June 2019.
[89] Larsson, A., Advances in VCSELs for Communication and Sensing," in IEEE Journal of Selected Topics in Quantum Electronics, **17**(6), pp. 1552-1567, Nov.-Dec. 2011. DOI: 10.1109/JSTQE.2011.2119469
[90] Amann, M., Long Wavelength VCSELs for Sensing Applications, 2007 International Nano-Optoelectronics Workshop, Beijing, 2007, pp. 75-76
[91] Malacarne, A., Neumeyr, C., Soenen W. et al., Optical Transmitter Based on a 1.3-μm VCSEL and a SiGe Driver Circuit for Short-Reach Applications and Beyond, Journal of Lightwave Technology, 2018, **36**(9), pp. 1527-1536, DOI: 10.1109/JLT.2017.2782882
[92] Nanni, J., Pizzuti, F., Tartarini G. et al., VCSEL-SSMF-based Radio-over-Fiber link for low cost and low consumption wireless dense networks, 2017 International Topical Meeting on Microwave Photonics (MWP), Beijing, 2017, pp. 1-4.
[93] T. Thow, A.E. Kelly and N. Raphael, Analogue RF over fibre links for future radar systems, 2017, Proceedings of the SPIE: The International Society for Optical Engineering, 10103, 101030Y. DOI:10.1117/12.2250548

[94] Malacarne, A *et al*., Performance Analysis of 40-Gb/s Transmission Based on Directly Modulated High-Speed 1530-nm VCSEL, in *IEEE Photonics Technology Letters*, vol. 28, no. 16, pp. 1735-1738, 15 Aug.15, 2016.

[95] Malacarne, A., Maresca, S., Scotti, F., Hussain, B., Lembo, L., Serafino, G., Bogoni, A., Ghelfi, P., A Radar over-fiber System based on Directly-Modulated Uncooled VCSELS, European Conference on Optical Communication (ECOC) 2019, Dublin, Ireland, September 2019.

[96] Malacarne, A., Maresca, S., Scotti, F., Hussain, B., Lembo, L., Serafino, G., Bogoni, A., Ghelfi, P., A ultrawide-band VCSEL-based radar-over-fiber system, 2019 IEEE International Topical Meeting on Microwave Photonics (MWP) 2019, Ottawa, Canada, October 2019.